MINERAL, FLUID AND THERMAL EVOLUTION IN VEINS FROM LATE OROGENIC COAL BASINS OF THE CANTABRIAN ZONE (VARISCAN, NW SPAIN)

INAUGURAL-DISSERTATION
zur
Erlangung der Doktorwürde
der
Naturwissenschaftlich-Mathematischen Gesamtfakultät
der
Ruprecht-Karls-Universität
Heidelberg

vorgelegt von
Ldo. Geología Fernando Ayllón
aus Santander (Spanien)

-2003-

View to the east of the Ciñera-Matallana coal basin from the summit of Alto La Peña (Llombera)

"There is no problem so awful that you can't add some guilt to it and make it even worse!"

Bill Watterson, "Calvin and Hobbes"

"It is a popular delusion that the scientific enquirer is under an obligation not to go beyond generalisation of observed facts...but anyone who is practically acquainted with scientific work is aware that those who refuse to go beyond the facts, rarely get as far"

Thomas Henry Huxley

"Truth in science can be defined as the working hypothesis best suited to open the way to the next better one"

Konrad Lorenz

Para Ana,

por mantener siempre viva mi ilusión

ACKNOWLEDGEMENTS

AGRADECIMIENTOS

DANKSAGUNG

a) ich erkläre hiermit, daß ich die vorgelegte Dissertation selbst verfaßt und mich dabei keiner anderen als der von mir ausdrücklich bezeichneten Quellen und Hilfen bedient habe,

b) ich erkläre hiermit, daß ich keiner anderen Stelle ein Prufüngsverfahren beantragt bzw. die Dissertation in dieser oder anderer Form bereits anderweitig als Prüfungsarbeit verwendet oder einer anderen Fakultät als Dissertation vorgelegt habe.

Heidelberg, den 17/02/2003

CONTENTS

CHAPTER 4: VEIN MINERALOGY AND TEXTURAL RELATIONS

CHAPTER 5: FLUID INCLUSION ANALYSIS

CHAPTER 6: ORIGIN OF MINERAL PHASES AND FLUID SOURCES

CHAPTER 7: FLUID INCLUSION RE-EQUILIBRATION

CHAPTER 8: FLUID-TEMPERATURE DISTRIBUTION AND VEIN EVOLUTION

CHAPTER 9: DISCUSSION AND TECTONO-THERMAL HISTORY

ABSTRACT

The detailed study of syn-tectonic mineral veins and textural features of fluid inclusions is a useful approach for reconstructing the fluid and thermal evolution in diagenetic and very low-grade metamorphism environments. Here, mineralised fissures within the clastic sedimentary rocks of the Ciñera-Matallana and Sabero Stephanian pull-apart coal basins (Cantabrian Zone, Variscan of NW Spain) are investigated. These bedding perpendicular fissures (cm-wide) formed in sandstones synchronous with folding and faulting during bedding-parallel slip. Three stages of infilling and mineral growth are recognised within the veins, reflecting different fracture-opening events under different fluid, thermal and tectonic regimes at hydrostatic pressure conditions:

Stage 1 was related to the temperature rise during burial before thermal peak conditions were attained (during Permian times). Euhedral quartz crystallised from a heterogeneously trapped, immiscible H_2O-CH_4-CO_2 ($\pm$ NaCl) fluid mixture. P-T conditions evolved from 73°-110°C and 15-56 MPa to 87°-129°C and 10-27 MPa. At a late stage of quartz growth saddle dolomite precipitated. Materials for mineral precipitation were derived locally from the detrital fraction within the Stephanian rocks, and transported into solution by advection of large volumes of gas (CH_4-CO_2) and water formed in response to progressive maturation of the coal.

Stage 2 also occurred under burial conditions, with lower temperature diagenetic dissolution-precipitation reactions controlling mineral growth. Brittle reactivation of veins caused microcracking of the large quartz crystals and extensive dedolomitisation. Ferroan blocky calcite precipitated at 60° to 100°C from a H_2O-NaCl-$CaCl_2$-CH_4 fluid with total salinities from 20.5 to 31.9 eq.wt%, also preserved as secondary inclusions in the vein quartz. This fracture re-opening and fluid flow event was related to the infiltration of marine water during Cretaceous tectonic subsidence, subsequently modified and expelled during late tectonic reactivation (Alpine Orogeny).

Stage 3 was linked with uplift and exhumation of the basin fill. Late calcite and authigenic kaolinite formed in response to low-temperature diagenetic and weathering reactions of the Stephanian rocks. Mineral precipitation was controlled by a constant supply of meteoric water (T < 50°C), that circulated preferentially along fault structures reaching the deeper parts of the stratigraphic section.

Shortly after the Stage 1 of vein evolution, diorite sills were emplaced into the basinal sequences and small veins containing quartz and kaolinite formed within some of these intrusives. The hydrothermal quartz also crystallised from an immiscible H_2O-CH_4-CO_2 ($\pm$ NaCl) fluid at 164°-296°C and 3-48 MPa, and is considered to be the product of extensive mineral alteration as the cooling magma intruded along coal seams.

A variety of thermally re-equilibrated fluid inclusions are reported in fissure quartz within the clastic rocks. Five textural types of re-equilibration were recognised in progressive order of inclusion modification: scalloped, hairy, annular-ring shaped, haloes and decrepitation clusters. These textures resulted from a combination of brittle fracturing and dissolution and re-precipitation of quartz, with preferential loss of water. Decrepitation of fluid inclusions in vein quartz throughout the entire basin reflects the wide extent of the thermal peak. Short-lived, high temperatures are related to the intrusion and alteration of the diorites in the basin, which further enhanced degassing and dehydration of the coal. The generated fluid probably circulated by advection through the already formed fissure network.

LIST OF ABBREVIATIONS

CZ = Cantabrian Zone

CMB = Ciñera-Matallana basin

SB = Sabero basin

SGL = Sabero-Gordón fault line

IC = illite crystallinity

VR = vitrinite reflectance

CAI = conodont colour alteration index

PPL = plane polarised light

CL = cathodoluminescence

SEM = scanning electron microscopy

EDX = energy dispersive X-ray

T = temperature

P = pressure

V_m = molar volume

X = molar fraction

Tm = final melting temperature

Th = total homogenisation temperature

Ph = homogenisation pressure

Tm_{car} = final melting temperature of carbonic phase

Th_{car} = total homogenisation temperature of carbonic phase

XRD = X-ray diffraction

cal1 = early vein calcite

qtz1 = vein quartz

cal2 = main vein calcite

cal3 = late vein calcite

py = vein sulphide minerals

kln = vein authigenic clay (kaolinite)

qtz2 = hydrothermal vein quartz in diorite

LPE = Law of Proportional Effect

CSD = Crystal size distribution

α = mean of the natural logarithms of the crystal sizes

β^2 = variance of the natural logarithms of the crystal sizes

Ma = million years

MPa = mega Pascals

cm^3mol^{-1} = cubic centimeter per mol

PDB = Pee Dee Fm Belemnite

°C = degrees Celsius

eq. wt% = equivalent weight percentage

SMOW = standard mid-ocean water

CHAPTER 1: INTRODUCTION

1.1. THEME, OBJECTIVES AND STRUCTURE OF THE WORK

Fluid-rock interaction has been a subject of increasing importance for Earth scientists in recent years. Crustal fluids are comprised mostly of aqueous solutions containing electrolytes and gases, and their flow allows transport of matter and heat on a wide range of scales. Fluid-flow in the Earth's crust plays an essential role in geological processes such as the formation of geothermal systems, sandstone and carbonate diagenesis, heat and chemical transfer along active faults, hydrocarbon reservoir evolution and formation of ore deposits (Parnell, 1994; Garven, 1995; Morad, 1998; Worden and Morad, 2000; McCaffrey et al., 1999). The motive of this study was to investigate tectonically controlled fluid evolution and associated mineral growth in sedimentary basins characterised by high palaeogeothermal gradients. For this purpose, the Ciñera-Matallana (CMB) and the Sabero (SB) Coalfields, two Stephanian pull-apart basins of the Variscan orogen in NW Spain, were selected as suitable case studies.

The thermal history of a sedimentary basin is not only the result of sedimentation and progresive burial, but is also influenced by the subsequent geotectonic evolution.The characterisation and timing of thermal events underwent within basinal successions is of great importance in mineral and hydrocarbon exploration. In coal basins, the reconstruction of the thermal history can be best achieved by combining several methods on the same sequence. Data referring to fluid activity may be directly correlated with different analytical techniques diagnostic of the thermal maturation of rocks, such as illite crystallinity of pelitic rocks (IC) and the vitrinite reflectance (VR) of organic matter (Kisch, 1987). During Carboniferous-Permian times numerous coal-bearing basins were deposited all around the globe. Well studied examples include the Pennsylvanian anthracite fields of the Appalachians, the Ruhr Coalfield (NW Germany), the Midland Valley (Britain), the South Wales Coalfield, the South African Coalfields and the Bowen Basin (Queensland, NW Australia). In these Permo-Carboniferous basins, the temperatures required to reach the actual coal ranks are unlikely to have developed by burial within a normal continental geotherm (Teichmüller and Teichmüller, 1986; Snyman and Barclay, 1989; Daniels et al., 1990; White, 1991; Bevins et al., 1996). They share several common features:
- Coal ranks ranging from low bituminous to anthracite grades
- Early development of coalification in respect to the basin history, being either pre- and/or syn-orogenic
- High palaeogeothermal gradients (> 50°C/Km)
- Coal seams tend to record higher temperatures than surrounding mudstones

In the Pennsylvania, South Wales and the Bowen Basins, such characteristics have been interpreted to result from the flow of high temperature fluids along coal seams and tectonic structures (Daniels et al., 1990; Gayer et al., 1991, 1997 & 1998; Uysal et al., 2000). The fluid flow is envisaged to have been driven by orogenic compression or associated with magmatic activity, which constitutes one of the main agents of thermal maturation and coalification.

The importance of tectonic structures in focussing the flow and distribution of crustal fluids, especially at shallow burial depths, has been widely recognised (Sibson, 1994; McCaffrey et al., 1999). During dilation of the crust major fluid migration occurs along extensional faults. Strike-slip fault systems also provide a major control on cross-formational fluid flow, allowing interactions between otherwise separate flow regimes (Muchez and Sintubin, 1997). Such different fluid systems are likely to leave an imprint in the rock record, associated with the extensional activity. In a compressional tectonic regime, fluids are considered to migrate upward and laterally, often along thrust faults, from the orogenic wedges into adjacent foreland basins (Oliver, 1986; Garven, 1995). As a consequence of rock deformation, mineral veins are usually formed in both extensional and compressional regimes (Fitches, 1987; Fisher and Byrne, 1990; Swierczeswska et al., 2000). The mineral phases contained in such fissures typically precipitate from a range of different fluid events, often with distinct compositions and varying confining pressures and temperatures (Muchez et al., 1995; Svensen et al., 2001).

Fluid inclusions preserved in minerals represent the only reliable source of obtaining direct information regarding fluid composition and the conditions of mineral forming solutions (Roedder, 1984). The importance of fluid inclusions in the study of fluid-related cementation in clastic sequences and the transition from diagenesis to very low-grade metamorphism has been widely recognised (Burrus, 1987a; Burley et al., 1989; Walderhaug, 1994; Frey et al., 1980; Mullis et al., 1994). Determining the preserved fluid composition and fluid pressure-temperature (P-T) conditions is of key importance in discriminating between internal and external fluid sources within the basin sequences and allows the possible mechanisms of heat and mass transfer to be evaluated. Despite the importance of fluid inclusion studies, only a few investigations of mineral veins within coal basins have been published. The results of Kisch and Van den Kerkhof (1991) in the Pennsylvania anthracite fields and of Alderton and Bevins (1996) in South Wales imply that:

• Fluid systems trapped within the vein mineral inclusions were generated mostly from the thermal maturation of the basinal rocks
• Peak fluid temperatures and pressures are slightly lower than those inferred from coal rank indicators

This investigation focuses on the study of the tectonic-related vein mineralisations present in the Ciñera-Matallana and Sabero basins. The characterisation of mineral-fluid compositions and fluid conditions within these fissures provides an excellent record of the different fluid systems that circulated within the basinal successions. Special attention is given to the description and understanding of processes in these strike-slip basins, which have undergone the transition from diagenesis to very-low grade metamorphism. The main objectives of this dissertation are to:

- establish the field relations between fluid-related mineralisations and deformation-induced structures
- describe the mineral growth sequence
- characterise the composition and P-T conditions of the mineral-related fluid systems
- discuss the possible origin of minerals and fluids
- evaluate the role of the fluids in the thermal history of the basinal rocks with this pull-apart setting, particularly in relation to the anomalously high palaeogeothermal gradients

The framework of the thesis is structured as follows:

-Chapter 2 provides a brief description of the geological features of the CMB and SB and the field relations of the sampled veins.

-Chapter 3 is a detailed explanation of the different analytical methods applied in this study, in order to provide the background to the results and interpretation.

-Chapter 4 presents a description of the different mineral phases found within the veins, the mineral growth sequence and the features of crystallisation.

-Chapter 5 characterises in detail the fluid inclusion types preserved in the different vein minerals. Several fluid systems are interpreted and the fluid trapping conditions and their relative timing is unravelled.

-Chapter 6 integrates the obtained mineral and fluid data with information available from previous studies to assess the processes responsible for the formation of the different fluid systems and the precipitated minerals.

-Chapter 7 focuses on the re-equilibration textures of fluid inclusions in vein quartz of the CMB, formed as a consequence of changes in the temperature and pressure conditions in the fissure environment following quartz crystallisation.

-Chapter 8 outlines the distribution of fluid temperatures within the basin sequences and summarises the fluid-thermal-mineral evolution within the veins.

-Chapter 9 discusses the fluid-thermal history of the basins and presents a tectonothermal reconstruction of events

1.2. FLUID-ROCK INTERACTION AND STEPHANIAN BASINS IN THE CANTABRIAN ZONE

1.2.1. Geology and thermal evolution of the Cantabrian Zone

The CMB and the SB are located in the south of the Cantabrian Zone (CZ; Fig. 1). This area constitutes the external zone of the Variscan orogenic belt in the NW of the Iberian Peninsula, and it is situated in the core of the Iberic arc, as defined by the different Palaeozoic major tectonostratigraphic zones. Two different successions can be recognised in relation to the Variscan deformation: one pre-orogenic and one syn-orogenic. The pre-orogenic sequence is formed by Lower Palaeozoic siliciclastic rocks, with some carbonate beds, and by alternating Devonian carbonate and clastic formations (2 to 3 km thickness). The syn-orogenic Carboniferous pile (of up to 8 km thickness) is interpreted as a foreland basin sequence (Julivert, 1978; Marcos and Pulgar, 1982), the siliciclastic content of which increases upwards. Both successions were complexly folded and thrusted under a thin-
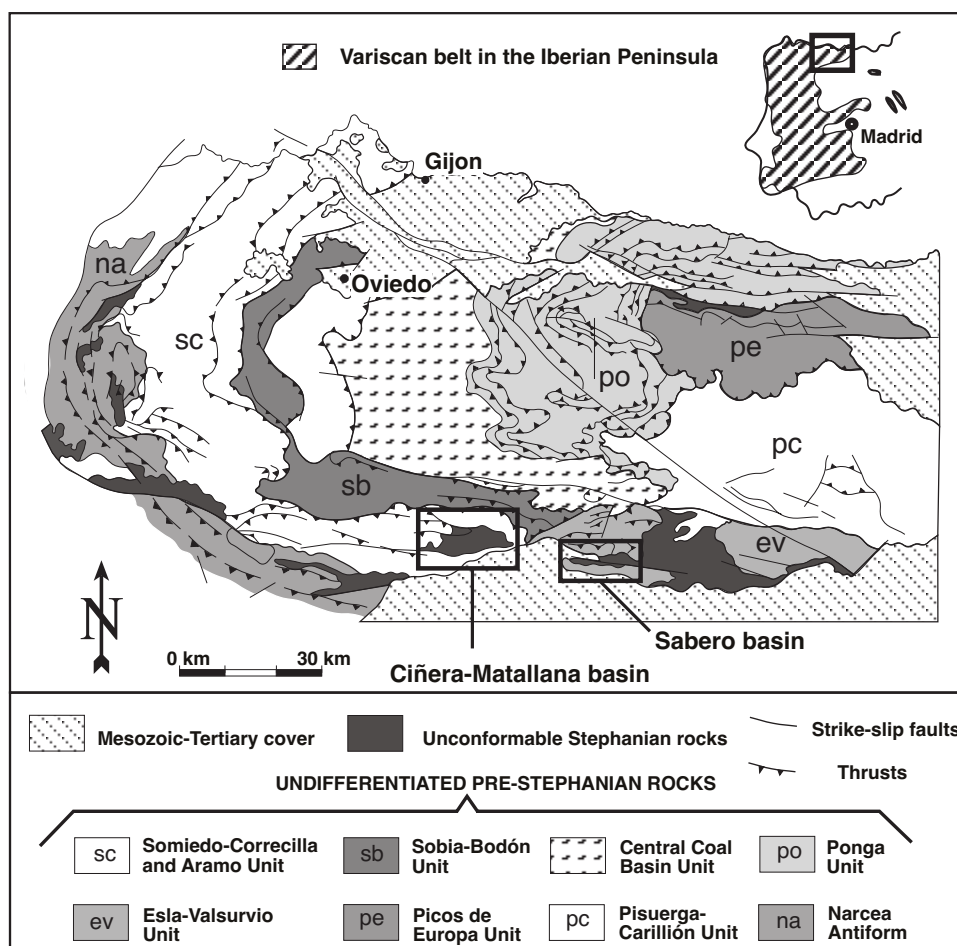
Figure 1. Geological sketch map of the Cantabrian Zone showing the main thrusts and the Variscan tectonostratigraphic units (after Pérez-Estaun et al., 1988). Note the distribution of the discordant Stephanian rocks within pull-apart basins around the curved structure (Asturian arc). The framed areas enclose the Ciñera-Matallana and Sabero coal basins.

4

skinned tectonic regime between Westphalian B and Stephanian times (Julivert, 1971). The tectonic transport directions of the different tectonostratigraphic units converge towards the centre of the arc (Pérez-Estaún et al., 1988).

The CZ is essentially regarded as a non-metamorphic unit. Several studies dealing with illite crystallinity (IC), vitrinite reflectance (VR), cleavage development and conodont colour alteration index (CAI) have been published over the last twenty years (Brime and Pérez Estaún, 1980; Brime, 1985; Aller et al., 1987; Alonso and Brime, 1990; Keller and Krumm, 1993; Colmenero and Prado, 1993; García López et al., 1997; Bastida et al., 1999; García López et al., 1999; Brime et al., 2001). They have shown the distribution and main features of the "metamorphic" zones within the transition from diagenesis to metamorphism, formed during two episodes of low-T metamorphism in the CZ (Fig. 2). The first episode, of Carboniferous age, was related to the regional metamorphism of the Variscan of NW Iberia. It is represented in small areas of the W, NW and SW parts of the CZ, where epizonal conditions are reached, and it is also present as a burial metamorphism that reaches anchizonal conditions in the basal part of some nappes, with the thermal
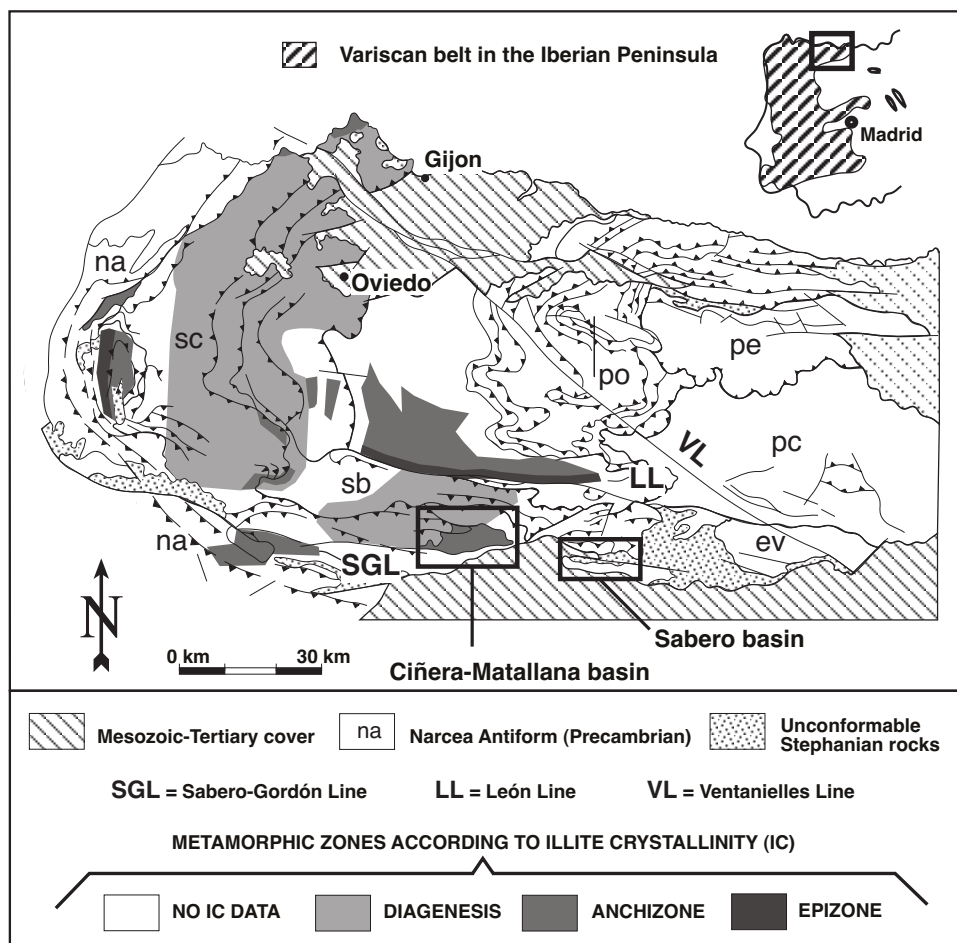
Figure 2. Geological sketch map showing the main metamorphic zones of the Cantabrian Zone according to the illite crystallinity index (after García López et al., 1999). Note that the Ciñera Matallana basin falls within the anchizonal field, in contrast with the surrounding diagenetic rocks of Palaeozoic age.

peak occurring prior to their emplacement. The second episode, of late-Variscan/ Permian age, occurs in two different forms: a diastathermal metamorphism, mainly developed in the central and in the southeastern parts; and a local contact metamorphism associated with small igneous intrusions. Many of these areas that approach very-low to low-grade metamorphic conditions are localised in the vicinity of major strike-slip faults.

1.2.2. Thermal "anomalies" in Stephanian rocks

Stephanian coal-bearing clastic sequences rest unconformably over the older Palaeozoic rocks and were deposited in small pull-apart basins with faulted margins (see Fig. 1). The age of these basins young towards the west-northwest, from uppermost Westphalian-Stephanian A (Guardo) to Stephanian C (Villablino, Rengos). In the south and south-west of the CZ these basins are distributed along strike-slip, deep reaching faults, formed as a consequence of transtensional movements which migrated westward with time during the late stages of the orogeny.

The basin sediments generally have high VR indexes (Fig. 3), which in many occasions are higher than the Carboniferous foreland and intrathrust coal basins in the same region. Many are intruded by small igneous sills and dykes. In their study of the rank distribution in the coal basins of the CZ, Colmenero and Prado (1993) consider the rank to depend on the structural location of the coalfields. The highest ranks being linked to hydrothermal heat flows related to the presence of major deep faults. Porosity and the degree of compaction of the Stephanian sediments play an important role in the coalification process. Relatively uncompacted and uncemented sediment would facilitate fluid circulation, whereby heat transfer would be more effective under these conditions (Duddy et al., 1994). Therefore, any related fluid activity that may reflect anomalous thermal gradients can be expected to have left an imprint upon the stephanian clastic deposits, either during or after their deposition.

1.2.3. Significance of fluids in the thermal evolution of the Cantabrian Zone

The role of fluids in the thermal processes related to low-T metamorphism in the Cantabrian Zone has been suggested to be of importance. They have been invoked as the most likely agents for heat transfer, at least in the second metamorphic episode of the CZ. Raven and Van der Pluijm (1986), based on a general study of CAI for the whole CZ, postulated that hydrothermal fluids circulated through the deep-reaching strike-slip faults (mainly the Leon Line, the Sabero-Gordón Line and the Ventanielles-Cardaño Line), associated with igneous activity, and were the main cause of heating. Studies dealing with small polymineralic ore deposits and large-scale dolomitization also indicate the significance of fluid flow. All published investigations relate the large variety of Palaeozoic small ore deposits in the south of the CZ with fault systems or with small-scale magmatisc intrusions (Paniagua et

al., 1988, 1988a 1993, 1995, 1997; Paniagua, 1998; Luque-Cabal, 1990; Crespo et al., 2000). Large-scale dolomitization, affecting largely Namurian limestones, is also interpreted to be linked to fracture-controlled fluid flow along steep systems associated with thrusts and/or with strike-slip faults (Gómez Fernández et al., 2000; Spiro et al., 1995; Tornos and Spiro, 2000; Grimmer, 2000; Gasparrini et al., 2001, 2002). Such case studies provide the only direct evidence of fluid activity in the Carboniferous of the CZ, in the form of fluid inclusion and stable isotope data. Mineralisation took place in the late Variscan (293-262 Ma, absolute dating results for ore deposits), associated with an extensional stress regime, and is regarded as shallow/-epithermal, with fluid temperatures $\leq$ 100-300°C and pressures < 500 bars (mainly hydrostatic conditions). Up to the present day, no investigations dealing with fluid compositions and the conditions within the Palaeozoic sedimentary sequence and the discordant Stephanian rocks (other than ore deposits) have been undertaken.
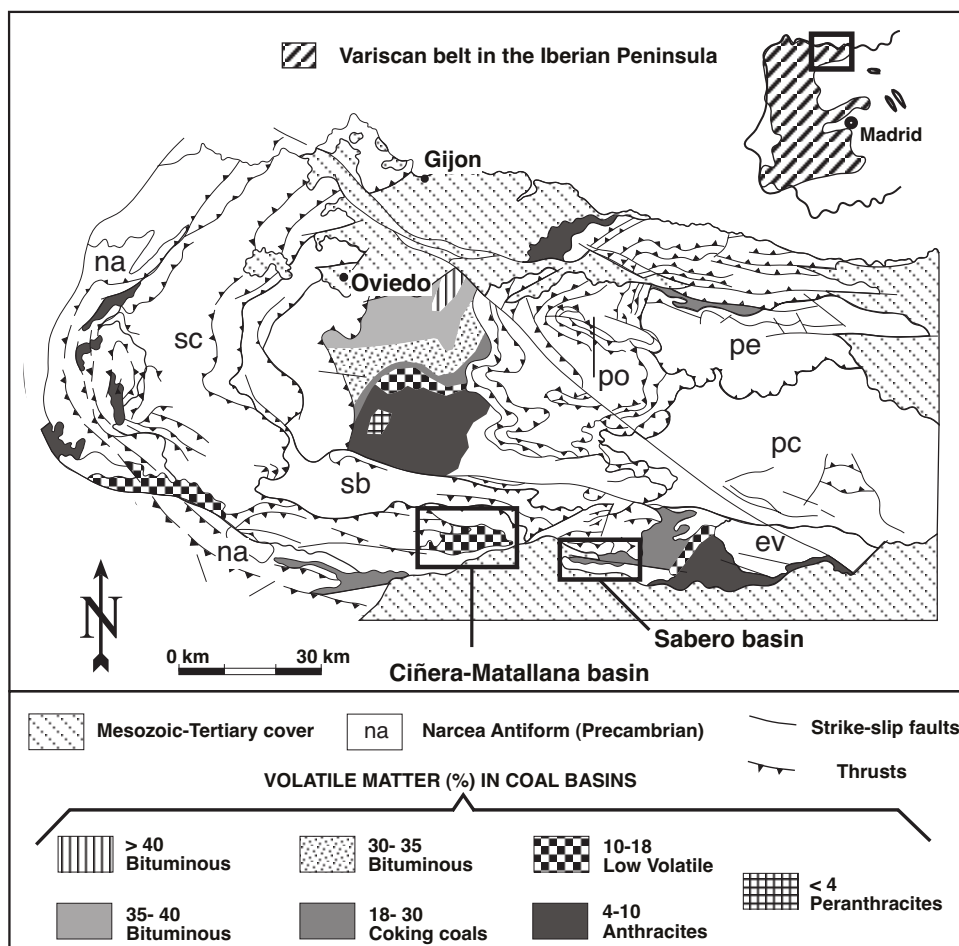
Figure 3. Geological sketch map showing the volatile matter content of the different coalfields of the Cantabrian Zone (after Colmenero and Prado, 1993). Note that the highest coal ranks (lower volatile contents) are reached within the Stephanian basins around the Asturian arc and in the south of the Central Coal Basin, close to the northern margin of the León Line.

1.2.4. Associated projects at the University of Heidelberg

This investigation was undertaken within the framework of the Graduiertenkolleg Program on Fluid-Rock Interaction (GRK 273). A variety of PhD projects have been running during the last years at the University of Heidelberg concerning the study of fluid-rock interaction processes and the thermal evolution of the Palaeozoic sequence in the southern part of the Cantabrian Zone. A list of the PhD contributions directly relevant to this study are given as follows:

- "Paläotemperatur-Anomalien in spät-Variskischen Kohlebecken am Beispiel des Ciñera-Matallana Beckens, Kantabrisches Gebirge, NW Spanien" (2002) by Kai Frings. This project, complementary with the one presented here, focused on the study of the IC, VR and anisotropy of the magnetic susceptibility (AMS) of the Ciñera-Matallana basin.
- "Fluidassoziierte Brekzien als Monitor dolomitisierender und dedolomitisierender Lösungströme in der Kantabrischen Zone (Nordspanien)" (2000) by Jörg Grimmer.
- "Large-scale hydrothermal dolomitization in the SW of the Cantabrian Zone (NW Spain): timing, controls and origin of the dolomitising fluids" (2003) by Marta Gasparrini.
- "Spätdiagenetische Prozesse in den Karbonaten der unterdevonischen La Vid Gruppe, Kantabrisches Gebirge (NW Spanien)" (2002) by Jochen Schneider

Published work by the author regarding the subject of this thesis includes:

- Ayllón F, Bakker RJ, Warr LN (2003) Re-equilibration of fluid inclusions in diagenetic-anchizonal rocks of the Ciñera-Matallana coal basin (NW Spain). Geofluids, 3, 49-68.
- Ayllón F, Bakker RJ, Warr LN (2001) Heterogeneous trapping and re-equilibration of fluid inclusions in diagenetic/anchizonal rocks, Ciñera-Matallana coal basin (NW Spain). XVI ECROFI European Current Research on Fluid Inclusions, Porto 2001. Abstracts (Noronha F, Doria A, Guedes A; Eds). Faculdade de Ciencias do Porto, Departamiento de Geologia, Memoria 7, 11-14. University of Porto.
- Ayllón F, Bakker RJ, Warr LN and Brime C (2000) A fluid inclusion study of syn-deformation carbonate-quartz veins in the Stephanian rocks of the Cantabrian Zone, NW Spain". DMG 2000, Heidelberg (Germany). European Journal of Mineralogy, 12, No. 1, 6.

CHAPTER 2: GEOLOGICAL SETTING AND FIELD RELATIONS

2.1. INTRODUCTION

The Sabero (SB) and Ciñera-Matallana (CMB) basins were selected as field areas for this study. These pull-apart, intramontane coal basins are located along the Sabero-Gordón fault line, one of the major, E-W trending, strike-slip fault systems of the Cantabrian Zone (Fig. 2). They were deposited during the later stages of the Variscan Orogeny (Stephanian) and subsidence was accompanied by igneous activity. Both areas are thought to have been connected during Stephanian to early Permian times, in a similar way as the SB is linked with the eastern border of the Guardo-Cervera late Westphalian coalfield. The precise extension of the original basin is unknown (Martínez-García, 1990; and references within). An extensive literature is available concerning different aspects of the geology of the area (Wagner and Artieda, 1970; Wagner, 1971; Galán et al., 1978; Heward, 1978; Knight, 1983; Méndez Cecilia, 1985; Marschik, 1991; Bieg and Burger, 1992; Villegas, 1996; Knight et al., 2000). Coal mining has been taking place for about a century and it is still active in the CMB. The relative small size of these coalfields is to some degree compensated by good exposure (abandoned open cast mines and trenches are common place), which allows for detailed sampling and field work.

2.2. SABERO BASIN

The sequence of this coalfield is exclusively continental except for some thin horizons of marine origin. On the basis of fossil flora, sedimentation occurred during the late Stephanian A (Barruelian) and continued up to the middle Stephanian B (300-296 Ma). The basin forms a structurally isolated unit, elongated E-W for 11-10 km and up to 3-4 km wide in the N-S direction (Fig. 4). The total thickness of the succession is in excess of 2000 m, and is composed of conglomerates, sandstones, shales and siltstones, with intercalated coal seams.

Stratigraphy

Knight (1983) has subdivided the succession into eight lithostratigraphical units, four of which are mappable as formations. The depositional environment of the sediments was that of alluvial fans and associated facies, with sediment provenance coming mostly from the south throughout the whole sequence. The two youngest units (Única and Perla beds) are restricted to the western end of the basin and a thrust level bounds its base (Casetas

thrust fault).

<u>Alejico beds</u> (0-300m): located in a small synform in the NE corner of the basin, older strata are more folded than the younger ones, possibly reflecting early syn-sedimentary deformation. Steep fluvial conglomerates evolve to a fluvial flood plain with coal seams of limited extension.

<u>Raposa Fm</u> (100-600 m): comprised of sand-bearing shales, sandstones with some small coal seams and seat-earth horizons. A marine interval is present immediately above the basal conglomerate. It represents the continuation of the palaeotopographic infill of a broad valley with onlap towards the west.

<u>Gonzalo Fm</u> (100-140 m): grey-blue shales with ostracodes and lamelibranquia, lacustrine shales, medium grained sandstones with cross-lamination, ripples and cross-stratification (turbiditic features).

<u>Sucesiva Fm</u> (60-155m): two coal seams mark the base and the top of the formation, respectively, with shales and sandstone between,containing cross-stratification and seat-earth horizons. The facies evolves from lacustrine to fluviatile flood plain.

<u>Quemadas Fm</u> (up to 300 m): it represents an increase in subsidence and widespread flooding. Blue lacustrine shales at the base evolve into alternations of sandstones and shales. Black limolites and argillites with rich bivalve fauna form the top level, representing a restricted marine environment.

<u>Herrera beds</u> (over 200 m): they occupy the faulted core of the Sabero syncline and are bounded by two major faults (La Llama and Olleros). They contain the thickest coal seams of the basin and have been object of intense exploitation, though their outcrop is rather restricted. According to Knight et al (2000),"the principal mined sequence has suffered intense tectonic deformation, with at least three major thrust fault repetitions of the main seams and apparent subsequent refolding in association with latter fault movements".

<u>Ùnica beds</u> (230-250 m): coarsening upwards lake infill, with up to five thin coal seams deposited in a flood-plain environment. In the upper parts of the sequence, thick and extensive in-river sandstones were formed.

<u>Perla Beds</u> (up to 550 m): thick, siltstone-dominated sequence with some substantial fluviatile sandstones in the upper part, rootlet beds, occasional lacustrine intervals and only one widespread identifiable coal seam (middle of the unit). Available outcrops are limited.

Structural outline

The present day limits of the coalfield are a reflection of the tectonic structure and do not represent the original basin outline. The basin has been folded and thrusted into an asymmetrical syncline with a thrusted southern limb (cross sections in Fig. 4). Two principal areas are distinguished, divided by the Casetas thrust. In the east, a west plunging syncline (synclinorium) is reflected by the occurrence in the north and south of the area of the same
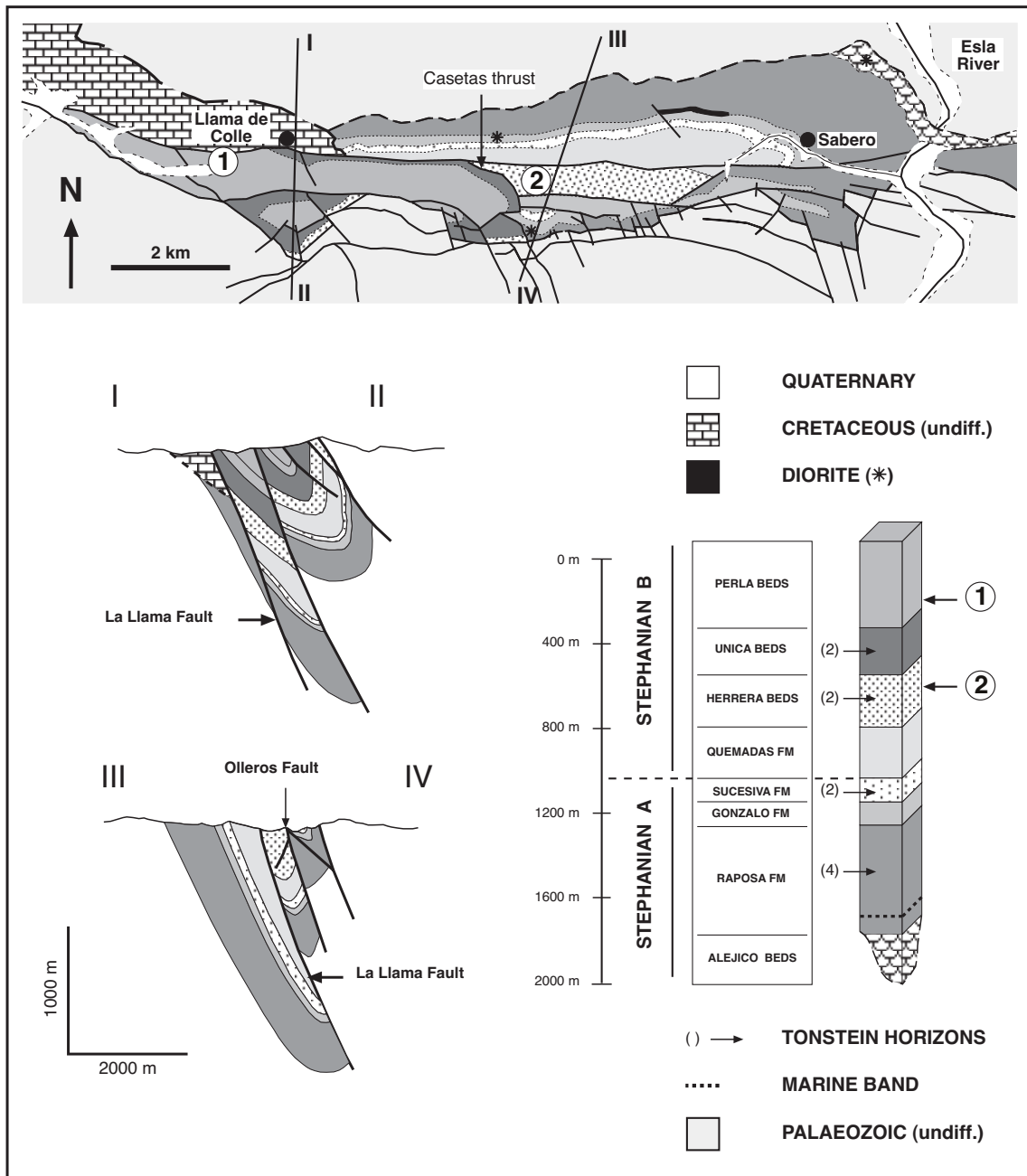
Figure 4. Geological map, cross-sections and stratigraphic column of the Sabero coal basin. The points 1 and 2 signalled in the map and column correspond to outcrop localities investigated in this study (see Table 1, page 18). Modified from data of Knight (1983) and Knight et al. (2000).

sequences younging towards the centre of the coalfield. The Herrera beds occupy the tightly compressed core of the structure. The northern limb has a constant dip toward the south of 60-70° and is relatively undisturbed, but to the south the structure becomes more complicated with the presence of several minor synclines and small south-dipping thrusts. The hanging wall of the Casetas thrust, which contains the two youngest units of the basin, occupies the western part of the coalfield. It has a rather complex structure and is not well resolved. A steep (65°) south-dipping, E-W oriented major feature, La Llama fault (associated to the Sabero-Gordón Line), crosscuts the coalfield and also displaces

unconformably overlying Cretaceous rocks in the west. During its latest movement in the Alpine orogeny this fault acted as a thrust plane, producing a downthrow displacement of about 400 m to the north (Helmig, 1965).

2.3. CIÑERA-MATALLANA BASIN

This small pull-apart basin forms a complex half-graben structure, extending 12 km (E-W) along strike and 6 km across (Fig. 5). The preserved 1500 meters thick basin fill consists of clastic continental rocks: conglomerates, sandstones and shales, with intercalated coal seams; constituting a coarsening upwards sequence. On the basis of the fossil flora the sediments have been dated as Stephanian B (298-294 Ma). Transtensional, syn-sedimentary movements along the strike-slip Sabero-Gordón fault zone (SGL) controlled the basin subsidence (Wagner, 1971; Villegas, 1996). This is reflected in great lateral facies changes and thickness variations in the two basal formations (San Francisco and Pastora). Tectono-sedimentary conditions were more stable during the deposition of the upper sequences, which, in general, show good lateral continuity.

Stratigraphy

Six formations are identified in the coalfield (after Wagner, 1971; Heward, 1978; and Villegas, 1996). Most of the boundary levels between formations are marked by coal seams.

San Francisco Fm (0-400 m): constitutes the first palaeo-valley fill during the initial stages of basin formation and is mainly formed by torrential conglomerates and coarse-grained sandstones, with some thin coal seams of minor extent and of variable thickness. Its occurrence is restricted to the northeastern and western margins of the basin.

Pastora Fm (85-200m): swamp facies with important coal deposits in the western side of the basin (up to 20 m), intercalated with fluviatile coarse grained sandstones and conglomerates with major and abrupt lateral facies changes. In the central parts of the palaeovalley an elongated lake formed, depositing organic rich shales. Six tonstein horizons (kaolinitized ash layers) have been identified in this formation.

Cascajo-Roguera (150-175 m): the base of this formation is an excellent stratigraphic marker, constituted by organic rich shales characterised by the presence of the fossil Leaia baenschiana (phyllopod), as well as fish scales and floating plant debris. The deposition of this sequence reflects the expansion of the lacustrine facies throughout the basin, and the termination of major coal accumulations. The sequence is made up largely of sand-bearing shales and fine-grained sandstones. The upper parts of this formation shows fluviatile (plane parallel and cross stratification) and swamp facies.

San José Fm (75-90 m): very regular thickness and abundant fossil content. Formed by immature sandstone beds with frequently interbedded organic-rich lacustrine shales. Five

coal seams (four at the top of the sequence) occur, each 50 to 60 cm thick. The upper coal seam forms an excellent stratigraphic marker, with abundant and characteristic fossil flora.

Bienvenidas Fm (350-380 m): this formation does not markedly vary from the previous San José. Thicker sandstones packets with channelled bases and transported plant debris, and fluviatile conglomerates are common. Up to five intercalated coal seams (30 to 120 cm thick) can be recognised.

Matallana Fm (up to 275 m): facies dominantly fluviatile. Thick (tens of meters) coarse-grained sandstone beds with abundant plant debris (including tree trunks), alternating with carbonaceous shales, seat-earth horizons and some faunal-bearing lacustrine levels. It contains three coal seams with good lateral continuity, between 70-100 cm in thickness.

Structural outline

As for the SB, the present day limits of the coalfield are mostly due to the tectonic structure and do not reflect the shape of the original basin. The western half of the basin contains three main eastward plunging synclines (cross section I-II, Fig. 5), with vertical to steeply south-dipping axial planes and shallow E-W oriented axes plunging towards the east. These are separated by poorly developed anticlines formed along pre-existing, complexly faulted, horst blocks. In the eastern part of the basin, the structure is simpler and the synclines tend to merge into a large synclinorium with shallower dipping limbs (cross section III-IV, Fig. 5). Fault planes strike preferentially E-W in direction. As a result of late Variscan compressive/transpressive deformation, metre- to decametre-scale thrusts and folds were formed. In many cases the coal beds acted as detachment horizons and are strongly sheared, such as the coal-rich Pastora Formation. In some localities the discordant surface between Stephanian and older Palaeozoic rocks also acted as principal slip planes. The Sabero-Gordón fault was reactivated during the Alpine uplift of the Cantabrian Mountains in Miocene times, and caused renewed deformation of the Stephanian rocks (Alonso et al., 1995; Villegas, 1996; Pulgar et al., 1999). Many of the observed south-dipping thrusts are considered to have been formed during this period.
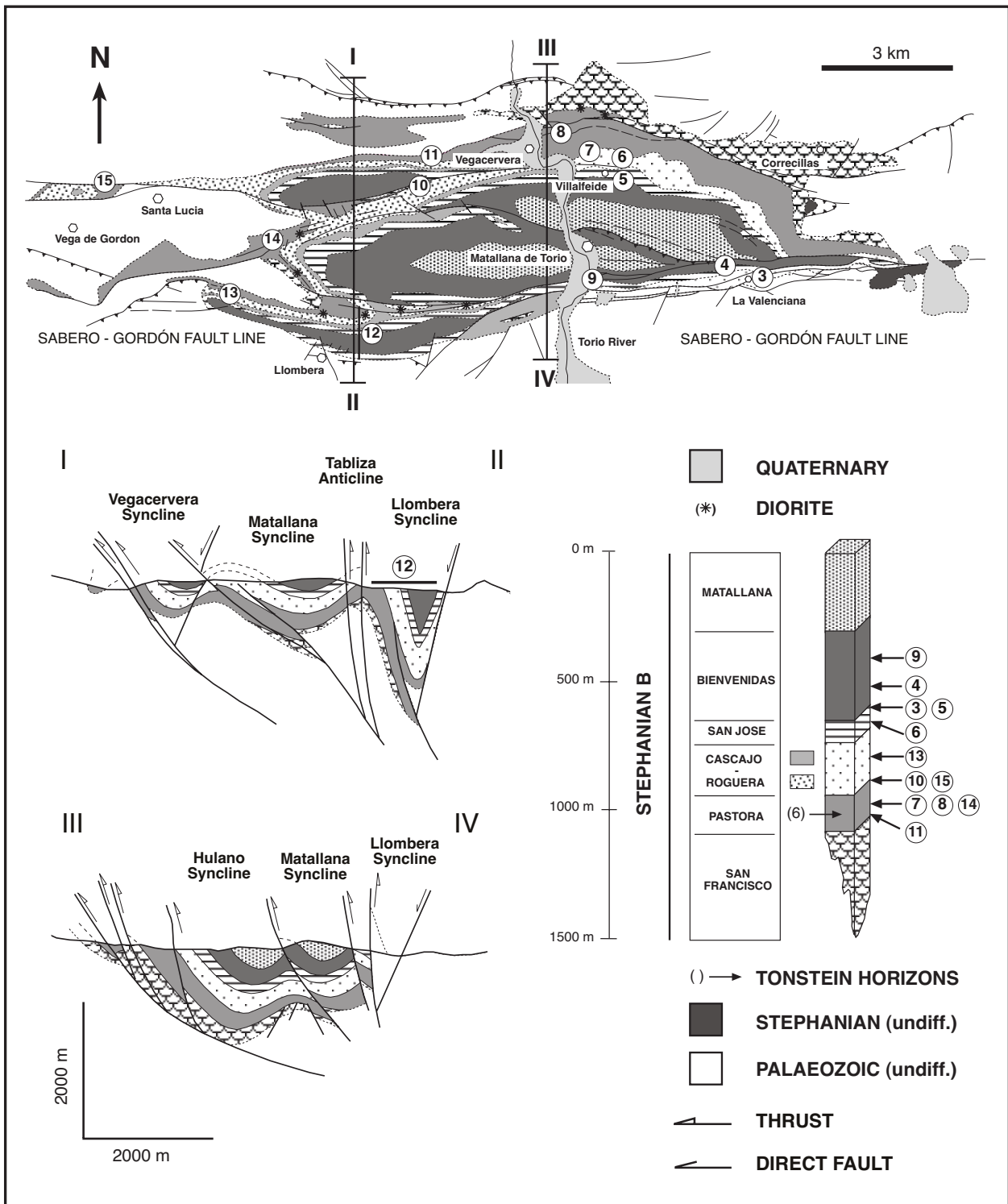
Figure 5. Geological map, cross-sections and stratigraphic column of the Ciñera-Matallana coal basin. The points 3 to 15, marked in the map and stratigraphic column, correspond to outcrop localities investigated in this study (see Table 1, pages 18-19). Modified from Wagner and Artieda (1970), Alonso et al. (1990) and Villegas (1996).

2.4. IGNEOUS ROCKS

2.4.1. Diorite intrusions

Sedimentation in the Stephanian basins was followed by the intrusion of magmatic sills and dykes ranging from 1 to 15 meters in thickness, locally reaching up to 20 m in the SB and up to 30 m in the CMB (Knight, 1983 and Méndez Cecilia, 1985). In both coalfields these rocks are located preferentially within the basal formations: from San Francisco to the top of San José in the CMB and in the Alejico, Raposa, Sucesiva and Gonzalo formations of the SB. In the SB the igneous rocks are exposed along the northern and southern boundaries of the coalfield, occasionally following preferred horizons for distances of up to 1 km (mapped sill in Fig. 4). The outcrops in the south, where the magmatic material intruded through sandstones, show the best preservation of the original igneous mineralogy and textures. In the CMB the intrusive rocks crop out along the southern flank of the Matallana Syncline, within the hinge zone and in the southern flank of the Tabliza anticline as well as on the NE side of the basin (Bardaya mine, Fig. 5). Sills and dykes have also been encountered at depth in both Stephanian sequences in open cast and underground mine workings, and in exploration boreholes within the CMB (Knight, 1983, Méndez Cecilia, 1985; Villegas, 1996).

The intrusive rocks of both basins have mineralogical and chemical affinities with the igneous rocks located in other Stephanian coalfields of the CZ and in Palaeozoic rocks of the Palentian Zone. Although these rocks have not yet been dated, associated magmatic activity and ore deposits within the CZ are of Permian age, ranging from 293 to 262 Ma. (Loeschke, 1982; Corretgé and Suárez, 1990; Crespo et al., 2000 and references within). In several localities it can be observed that they were folded and faulted together with the Stephanian sediments. They are dioritic in composition (being slightly more basic in the SB), with microporfidic textures, and are locally more acidic where assimilation of the country rock occurred. The primary mineralogy, when recognisable, comprises a plagioclase groundmass (andesine/oligoclase), with hornblende, pyroxene and biotite phenocrysts. Characteristically they preferentially penetrated along coal beds, assimilating wall rock and producing metric thick, natural coke aureoles (Fig. 6). In these cases the intrusive bodies were completely altered to a pale coloured assemblage of carbonates, quartz, iron oxides, epidote, actinolite, chlorite, sericite and kaolinite. The alteration minerals pseudomorphose the original magmatic textures, though quartz also occurs in crosscutting joints in some of the more altered sills (see chapter 4). The resulting rock is deeply weathered when exposed.
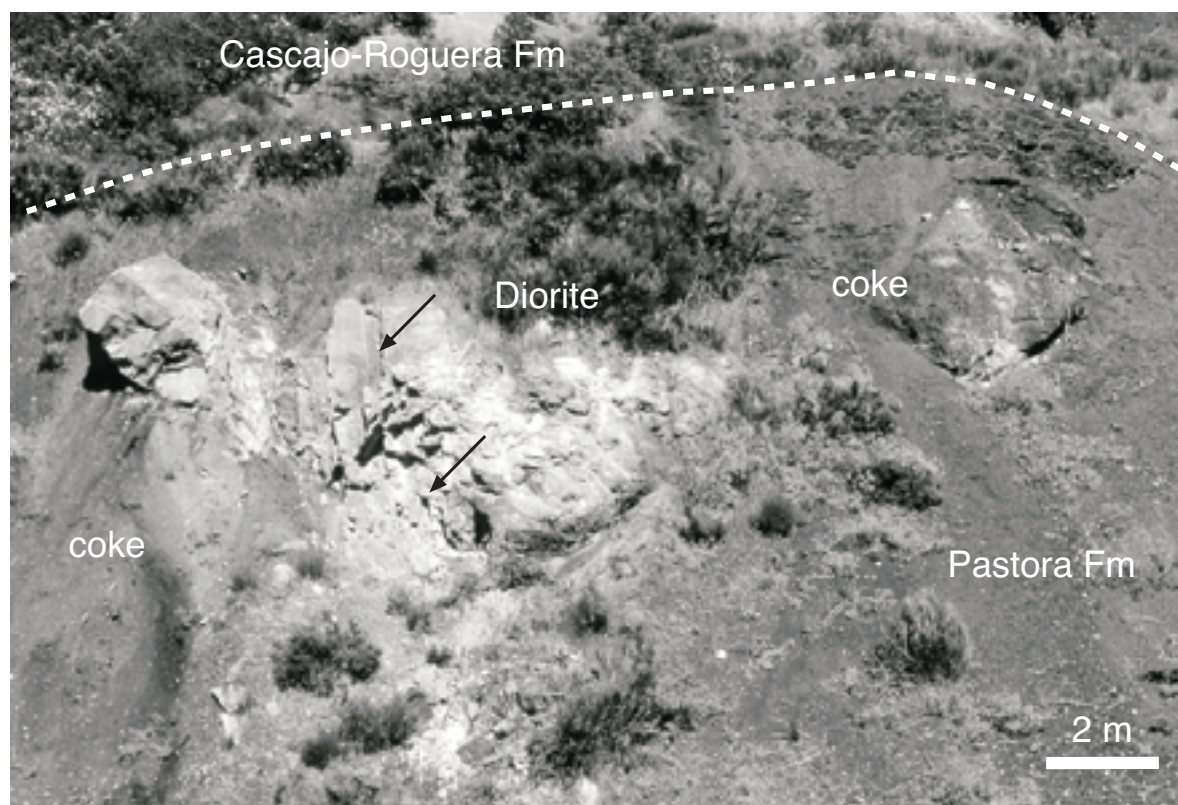
Figure 6. Diorite intrusion within a coal seam on top of Pastora Fm, Tabliza anticline (locality 12b). The coal has been completely transformed into coke, forming an irregular aureole around the diorite. Arrows point to quartz filled fractures within the diorite.

2.4.2. Pyroclastic tonsteins

Sixteen tonstein horizons have been described in the two Stephanian coalfields (Bieg and Burger, 1992; Knight et al, 2000). These bands have served as the means of resolving structural and stratigraphic problems, especially important in the SB. Their character, compositions and petrographical features are very similar and entirely consistent with a pyroclastic origin. The main constituent is kaolinite, both as matrix and as fragmentary crystals and phenocrysts (pseudomorphs of biotite and feldspar). A common source area for these volcanic ashes has been proposed, although good correlation between both basins has not been achieved. The ten horizons in the SB (Fig. 4) occur as kaolinite coal-tonsteins. In the CMB there are a total of six bands, all within the Pastora Fm (Fig. 5); three kaolinite tonsteins, one kaolinite/illite transition tonstein and two illite tonsteins (illite forms the pseudomorphs).

There is no exclusive relation between the tonsteins character, the degree of diagenesis and the coal rank. Many factors may influence the mineral transformations in the volcanic ashes: hydrothermal metasomatism, temperature rise, original composition, chemical and biochemical processes (Bohor and Triplehorn, 1993). The degree of kaolinite to illite transformation appears depending on deformation, with alteration intensity increasing in areas of tectonic compression.

2.5. PALAEOTHERMAL CONDITIONS

Only data concerning the volatile content of coal is available for the SB (Fig. 3). The values oscillate between 30 and 18 % volatiles (coking coals), which is well into the catagenesis level of organic matter maturation and within the diagenetic domain (Barnes et al., 1990). Recent investigations on the tonstein mineralogy and illite crystallinity of pelitic rocks (Knight et al., 2000; Frings pers. com.) confirm the predominantly diagenetic character of these rocks and the lower thermal gradients experienced in this coalfield with respect to those of other Stephanian basins.

In CMB basin the metamorphic grade of the sedimentary rocks determined by illite crystallinity (IC) indicates high diagenetic to local upper anchizonal grade conditions (Galán et al., 1978; Frings, 2002), which is generally higher than the diagenetic conditions of the surrounding Palaeozoic sequence (Fig. 2; García López et al., 1999). Low volatile coals (10-18 % volatile matter) and semiantracites constitute the coal seams, which corresponds with the transition between the catagenesis and metagenesis stages of organic matter maturation. Under these conditions the generation of dry gas (essentially methane) and progressive moisture loss from the coal is expected. According to Méndez Cecilia (1985), there exists a general increase in the thermal maturation of the coal seams with stratigraphic depth. Mean vitrinite reflectance values increase from 1.3% in the Matallana Formation to 2% in the San Francisco Fm. However the highest reflectance values (up to 2.6%) were recorded in the Pastora Formation, due to the fact that this formation contains most of the igneous sills/dykes present in the coalfield. Based on these data a palaeogeothermal gradient of 60 to 70°C/km was proposed for the Stephanian basin, similar to other Stephanian coal basins across the Cantabrian Zone. In the Palaeozoic basement estimated palaeogeothermal gradients are only about 35°C/km (Brime et al., 2001).

2.6. VEIN OCCURRENCE IN THE STEPHANIAN SEDIMENTS

Fieldwork undertaken in both coal basins has shown that deformation related quartz-carbonate mineralisations occur in the Stephanian sedimentary sequences, associated with small- and medium-scale structures. The opening of cm-wide fissures occurred synchronous with folding and faulting and was associated with the formation of closely spaced joint systems (Fig. 7 and 8).

Locality	Samples	Position	Formation	Description	Vein Mineralogy
1a	1, 2, 3, 4, 5	N 42°50.733′ W 05°15.827′ 840 m South of SG Line	Perla Beds (mine N of Veneros)	Thrusted section (coal beds are the slip planes) with veins in associated extensional fracture systems	(qtz1) cal2 dolm (relics) kaolinite pyrite/chalcopyrite
1b	6	N 42°50.162′ W 05°15.881′ 865 m	Perla Beds (mine N of Veneros)	Fracture in vertical sst beds besides sheared coal seam	dolm cal2 kaolinite pyrite/chalcopyrite
2	7, 8, 9, 10	N 42°49′51.3′′ W 05°12′00.6′′ 1183 m	Herrera Beds (South of Sotillos de Sabero)	Veins associated with fractures in sst beds besides sheared coal seam	(qtz1) cal2 dolm kaolinite
3	23, 24, 25	N 42°51′35′′ W 05°28′33′′ 1120 m	San José (La Valenciana mine)	Faulted section with numerous sheared coal beds and associated veining.	qtz1 cal2 dolm (relics) kaolinite
4	26	N 42°51′44′′ W 05°28′59′′ 1275 m	Bienvenidas/ San José (La Valenciana Valley)	Fractures cut by a bedding-parallel normal fault plane in alternating sst and coal beds	cal1 qtz1 cal2 dolm (relics) kaolinite
5	28	N 42°52.698′ W 05°30.880′ 1050 m	Limit San José- Bienvenidas	Fracture system in homoclinal fold in sst	qtz1 cal2 dolm (relics)
6	29, 30	N 42°52′52′′ W05°30′43′′ 1060 m	San José	Veins associated with a vertical dipping fault	cal2 dolm (relics) kaolinite
7	31	N 42°53.006′ W 05°31.187′ 1000 m	Pastora	Veins in fracture system perpendicular to bedding in sst	qtz1 dolm (altered)
8	32, 33, 34	N 42° 53′23.8′′ W 05°31′50.7′′ 1205 m	Pastora	Fractures associated with fault propagation folds in sst beds alternated with coal seams	qtz1 cal2 dolm (relics) cal3 kaolinite

Table 1. Location and description of the vein-bearing sampled outcrops in Sabero (SB) and Ciñera-Matallana (CMB) coal basins (see also Fig. 4 and 5). sst = sandstone; cal1/2 = calcite; qtz1 = quartz; dolm = saddle dolomite.

Vein samples were selected from fifteen localities associated with structures occurring in different stratigraphic units throughout the basins (Table 1 and Fig. 4 and 5). As it can be seen from the sampled outcrop locations, veins are much less abundant in rocks of the SB than in those of the CMB.

Locality	Samples	Position	Formation	Description	Vein Mineralogy
9	27	N 42°51´36´´ W 05°30´59´´ 1010m	Bienvenidas (Mina Picalín)	Vein associated with a normal fault in sandstone beds	qtz1 cal2 dolm (relics) cal3 kaolinite
10	36, 37, 38	N 42°52´49.0´´ W 05 33´34.9´´ 1140m	Contact of Pastora and Cascajo-Roguera	Vein set in faulted sst besides two sheared coal seams (50 cm to 1m thickness)	qtz1 cal2 dolm (relics) cal3 kaolinite
11	35	N 42°53.141´ W 05°33.525´ 1000 m	Pastora	Cross-cutting veins in vertical conglomerate beds at the base of the discordance of the coalfield	dolm cal2 cal3 kaolinite
12a	39, 40, 41, 42, 43, 44	N 42°51´00´´ W 05°34´55´´ 1230m	Bienvenidas (hinge zone of Llombera Syncline)	Vein set in the upper limb of a parasitic antiform	qtz1 cal2 dolm (relics) kaolinite pyrite chalcopyrite
12b	45, ign12	N 42°51´12´´ W 05°34´50´´ 1250 m	Contact of Pastora and Cascajo-Roguera (Tabliza anticline)	Centimetre vein filling in orthogonal cross-cutting fractures to a dioritic intrusive body	qtz2 kaolinite
12c	46, 47, 48, 49, 50, 51	N 42°51´12´´ W 05°34´50´´ 1250 m	Pastora (Tabliza anticline)	Fault-related vein along fault plane in shales	qtz1 cal2 dolm (relics) pyrite chalcopyrite kaolinite
13	52	N 42°51.272´´ W 05°36.918´´ 1100 m	Cascajo-Roguera	Vein in the hinge of an anticline	cal2 dolm (relics)
14	53, 54, 55, 56, 57	N 42°52.055´ W 05°36.074´	Pastora Fm (open cast mine along Matalla syncline)	Vein sets in fold propagation folds, extensional vein systems and implosion breccias. Host rocks are sst and conglomerates	white calcite pyrite chalcopyrite kaolinite
15	60	N 42°52´36.2´´ W 05°39´53.0´´ 1220 m	Cascajo-Roguera	Fractures in bended syncline	qtz1 cal2 dolm (relics)

Table 1 (continued).

In the latter basin veins are found throughout the area, whereas in the SB they are restricted to a few outcrops within the Herrera, Única and Perla beds. Veining is particularly significant in sandstone and conglomerate beds alternating with shales, organic rich pelites and coal-bearing strata (Fig. 7 and 8). This association of lithologies appears to be important, as in other deformed areas where the coal-bearing strata are absent no significant mineralisation took place and vein quartz did not form.
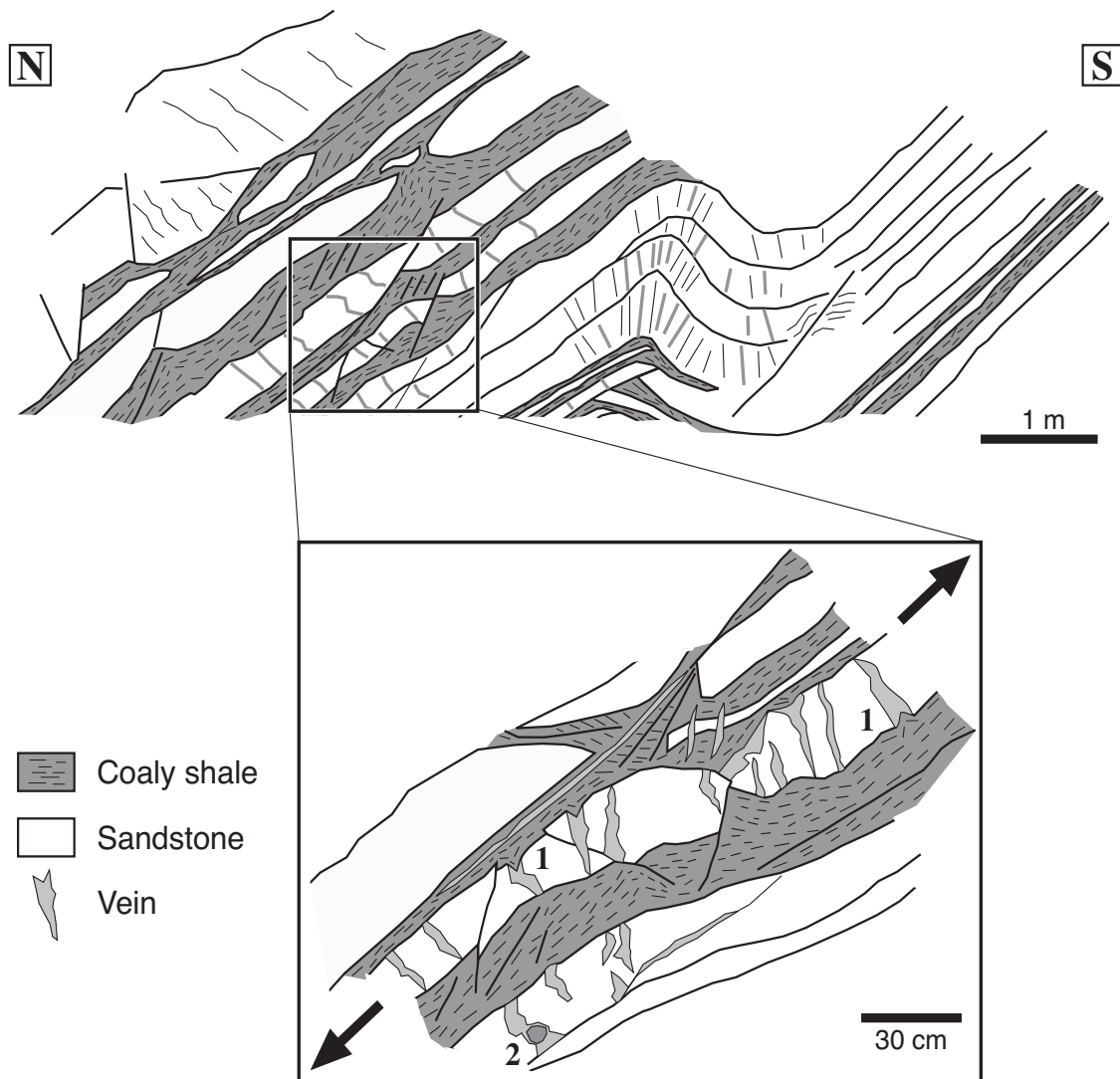
Figure 7. Outcrop from locality 12a, situated due south of the hinge zone of the Llombera Syncline, Bienvenidas Fm (Table 1 and Fig. 5). This parasitic antiform illustrates the type and scale of the fold-related deformation structures present in the coalfields. Quartz-carbonate veins occur in extensional fractures, synchronous with folding, in the upper limb and in the hinge zone. A closer view to the upper thinned limb (arrows indicate the direction of extension) shows that the veins are mostly restricted to the extended sandstone beds and are generally perpendicular to the bedding, with the adjacent coaly shales moving into some of the fractures (**1**). Ocassionally large pyrite and chalcopyrite crystals have grown in the fractures (**2**).

a

N   S

Coaly shale   Sandstone   Vein

2 m

b

N   S

Coal

Sandstone

Vein

2 m
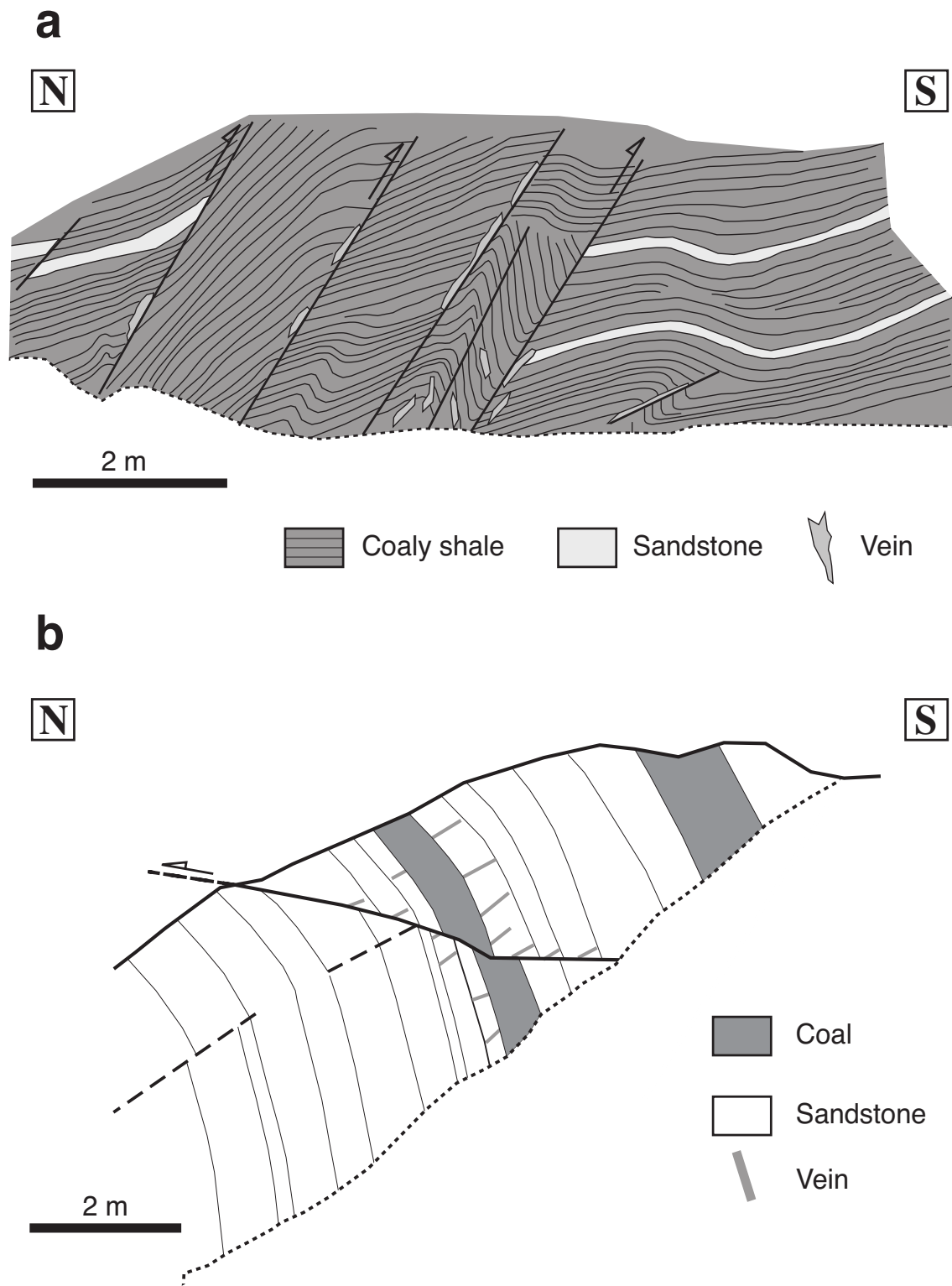
Figure 8. Type and scale of the fault-related deformation structures present in the coalfields. Sketch (a) shows several small steep reverse faults in coal-bearing shales of the Pastora Fm within the Tabliza anticline (outcrop from locality 12b). Veins formed along the fault planes and within bedding-parallel jogs. Sketch (b) illustrates vein development where a small inverse fault cuts vertically dipping strata of the Bienvenidas Fm (outcrop from locality 9). Quartz-carbonate veins occur in extensional fractures perpendicular to bedding, within sandstone beds above and below the coal seam.

Mineral growth occurred within steeply dipping bedding perpendicular fissures, and to a minor extent also along bedding-parallel veins and slickencryst surfaces. The dominant deformation mechanism responsible for the formation of the mineralised fissures was bedding parallel slip, focused along preferential incompetent horizons that accommodate much of the compressive stresses during shearing (Fig. 9).
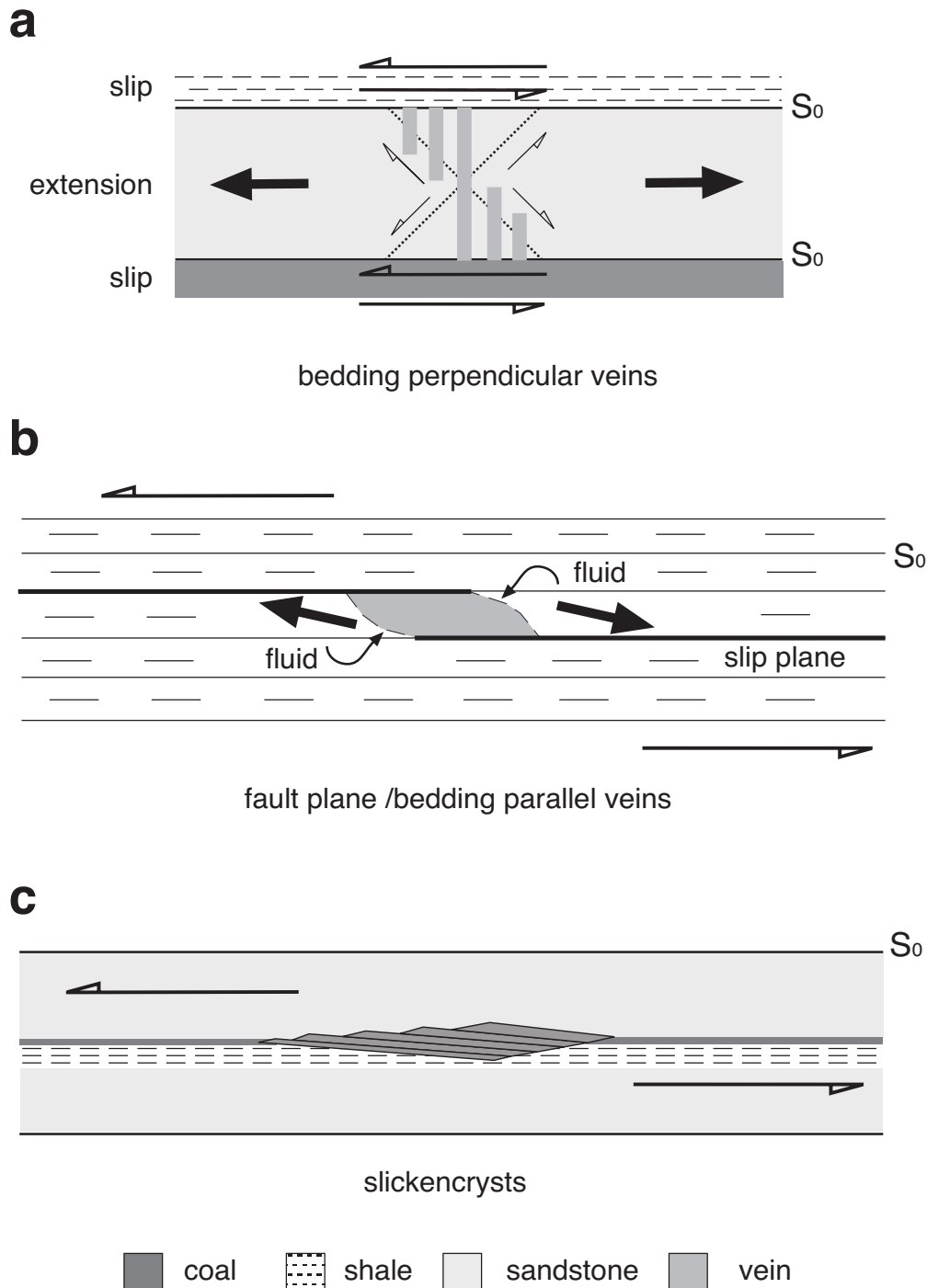
Figure 9. Sketches illustrating the kinematic model for the formation of the mineralised fissures in the Stephanian siliciclastic rocks (not to scale). Bedding-parallel slip accommodated mainly the compressional deformation; thick arrows indicate the direction of extension. (a) Bedding perpendicular veins, (b) veins parallel to bedding and along slip/fault planes, and (c) mineralised slickencryst surfaces.

In coal-basin setting, the slip horizons are along the coal seams and the shales (see Cole et al., 1991; Frodsham and Gayer, 1997). The intercalated and more competent sandstone beds undergo horizontal extension and develop sub-vertical fractures as a consequence (Fig. 9a). The presence of conjugated joint systems in many of the deformed outcrops, even in those without veins, is also consistent with this mechanism of formation. In many occasions mobilisation of under and overlaying shale and coal into the fissures can be observed (see detail in Fig. 7). Bedding-parallel veins, formed mostly within pelitic rocks, and mineralised slickencryst surfaces within fault planes, represent dilational jogs within detachment planes formed by rotation and sliding during slip motions (Fig. 9b and 9c).

CHAPTER 3: ANALYTICAL METHODS

This investigation is based on the study of 60 vein samples selected from 15 localities (Table 1). The veins were collected retaining their orientation in order to estimate kinematic directions of mineral growth, according to the method of Paschier and Trouw (1998). Rock sections were cut perpendicular to bedding and retaining portions of the wall rock to document the relations vein mineral-host rock. Table A1 (Appendix) gives a detailed list of the analytical methods applied to the sample material, which are summarised as follows.

3.1. PETROGRAPHY

3.1.1. Transmitted and reflected light microscopy

Petrographic microscopy of rock samples was the first step of this analytical study. Thin sections (30 μm and 60-50 μm) from vein samples were analysed in detail under transmitted and reflected light for mineral identification and fluid inclusion petrographic relations. Sections were also used for cathodoluminescence (CL) and scanning electron microscopy (SEM) analyses. Double polished (100-120 μm) sections for fluid inclusion microthermometry were only prepared from the same rock slice, when inclusions were first observed and characterised in thin section.

3.1.2. Carbonate staining

The optical properties of calcite ($CaCO_3$) and dolomite ($MgCa(CO_3)_2$) are similar and therefore may prove difficult to distinguish optically. A simple chemical staining technique was employed to differentiate calcite from dolomite and the ferrous iron (Fe^{+2}) content of both minerals. Two staining solutions were prepared following the procedure described by Dickson (1965):

- Solution A: 100 ml HCl 1.5% (15 ml of pure acid brought to 1 litre with water) mixed with 0.2 gr. of Alizarin red-S. This solution serves to distinguish calcite from dolomite.
- Solution B: 100 ml HCl 1.5% mixed with 2 grams of Potassium Ferricyanide. This solution is used to distinguish ferran from non-ferran minerals.

Both solutions were mixed together in a ratio of A/B = 3/2. 60 rock slabs (47 veins from Stephanian rocks) were prepared and polished using 400 μm powder. Samples were immersed in the mixture of the two solutions for 30 to 45 seconds, agitating them slightly to remove the small gas bubbles from the surface. Afterwards, the stained slabs were

washed under running water for a few seconds and then dried. The colours formed after staining are (Adams et al., 1984): (1) Calcite = pink to red-brown; (2) Ferroan calcite = mauve to blue; (3) Dolomite = colourless; (4) Ferroan dolomite = very pale blue. During staining only the crystals exposed at the surface react with the staining solution, and the intensity of the colour is partly related to the intensity of the etching with acid. Fine-grained crystal fabrics with many crystal boundaries tend to etch more rapidly and thus show deeper colours than coarse crystal fabrics with fewer crystal boundaries.

3.1.3. Cathodoluminescence

The principle of cathodoluminesce is based on the known property of many mineral species, non-luminescent in the pure state, to luminescence when "activated" under electron bombardment by the presence of small concentrations of impurities (Pagel et al., 2000). The term "cathodoluminescence microscopy" refers to the microscopic observation of minerals and rocks in thin section while under electron bombardment (Barker and Koop, 1991). In this study, cathodoluminescence properties of vein calcite and dolomite have been investigated in order to obtain extra information concerning the growth relations and history of the carbonate minerals. Luminescence of calcite and dolomite is attributed to the presence of Mn^{2+} as an activator ion, whereas Fe^{2+} is believed to be the most important quencher ion (Machel and Burton, 1991; Machel et al., 1991).

Observations were performed with a **Citl cold cathode** apparatus of the type **CCL 8200mk3** at the Geological-Palaeontological Institute, University Heidelberg (Germany). Thin sections (30 μm) were placed on a glass tray supported on an X-Y bearing carriage in a vacuum chamber with an upper window for microscopic observations. An electron beam is generated and deflected on the specimen by means of an obliquely arranged gun. Beam voltage of 20 kV and current of 400 to 600 A were used. Transmitted light and cathodoluminescence images were photographed in 200 ASA film with an **AGFA RSX (II)** camera. Observations and photographic recording were performed in a darkened room, under a red photographic "safe light", which provides illumination without disturbing the essential "night vision".

3.1.4. SEM imaging and EDX identification

Scanning electron microscopy (SEM) images from minerals were obtained using a **LEO-32** facility, housed at the Institute of Environmental Geochemistry, University Heidelberg. For more detailed information on the method and technical descriptions the reader is referred to Welton (1984) and references within. Previous to analysis the thin sections (30 to 60 μm) were coated with carbon by vacuum evaporation. The coating allows a clear image to be obatined, acting as an insulating material, minimising interference from evaporating substances and increasing secondary element emission. For study, sections

were attached to a SEM specimen plug. A thin line of Silpaint was added to provide an electrical conection for the sample to the plug.

The SEM image is formed by an internally generated electron beam. The accelerated electrons are de-magnified and focused through a series of electromagnetic lenses into a finely focused beam, which bombards the sample. The interaction of the primary electron beam with the sample produces simultaneously various forms of radiation: secondary electrons, characteristic X-rays, Auger electrons, backscatter electrons and "Bremsstralung" (continuous or background) X-rays. In this study back-scattered electron images (BSE) of vein minerals, mostly authigenic clays, were obtained. Besides the comparison of characteristic mineral morphologies, mineral identification was confirmed by determination of elemental composition using the energy dispersive X-ray system (EDX).
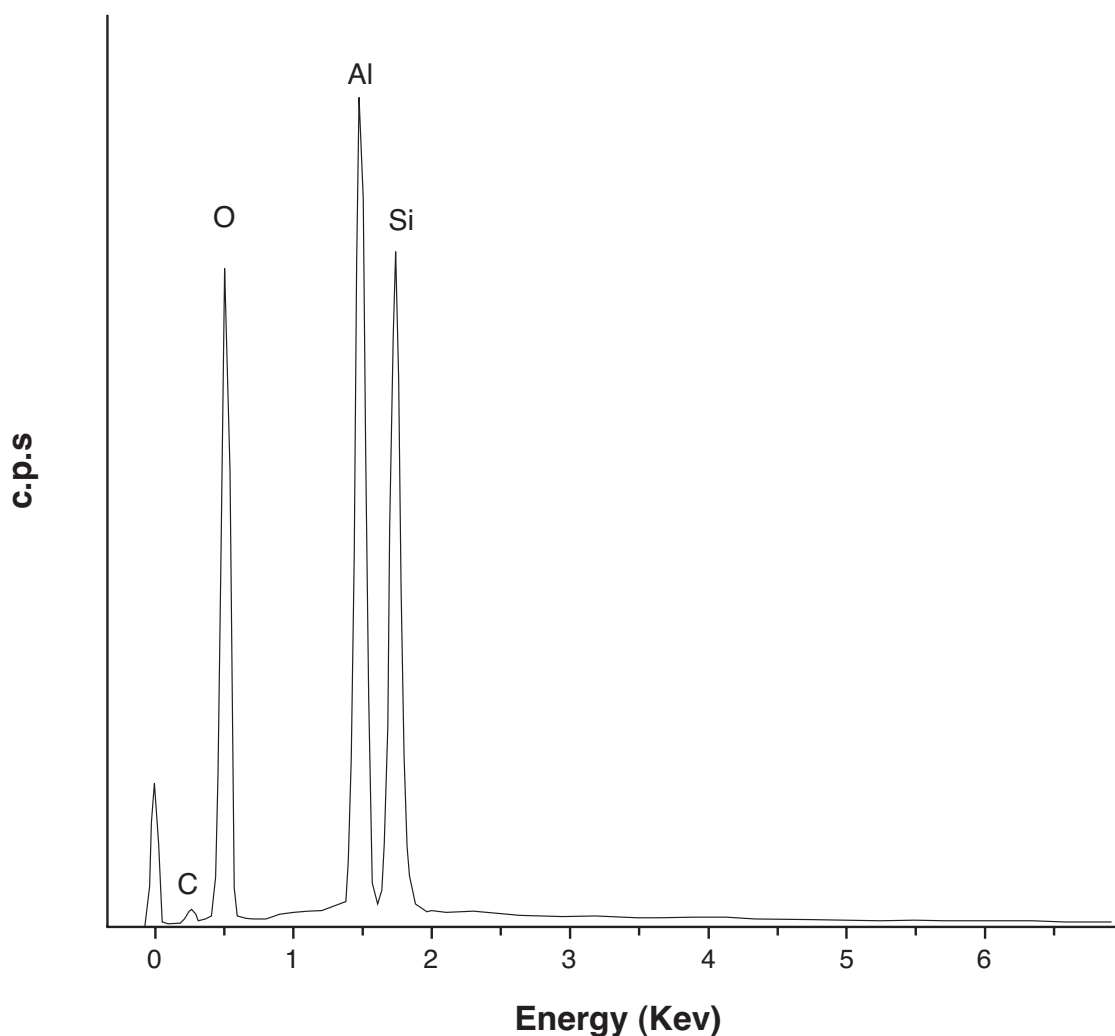
Figure 10. Energy Dispersive X-ray (EDX) spectrum of kaolinite: $Al_4[Si_4O_{10}](OH)_8$. Sample 36, locality 10.

For EDX analysis, all X-rays generated from a selected area in the SEM image (generally at high magnifications) are collected and separated by a multi-channel pulse height analyser. Any major element in the sample (above $Z = 11$, sodium) will yield a peak

27

on the graph at its unique energy level. The element identification is done automatically by the computer, lining up the peak apex with the energy scale at the bottom of the graph and then comparing the obtained number with X-ray energy reference values. The relative concentrations of the elements are then compared with the chemical formula of the suspected mineral, as the peak heights are roughly proportional to their concentration (Fig. 10).

3.2. FLUID INCLUSIONS

Fluid inclusion analysis forms the core of the investigations undertaken in this study. There exists an extensive body of scientific literature dedicated to the study of fluid inclusions in minerals. For an introduction to the basic principles of the method and further information on the different analytical techniques applied here the reader is referred to Hollister and Crawford (1981), Roedder (1984), Shepherd et al. (1985) and Andersen et al. (2001). Goldstein and Reynolds (1994) and Mullis (1987) provide more specific insights on the study of fluid inclusions applied in diagenetic and low-temperature metamorphism environments.

Inclusions preserved in minerals represent entrapped portions of fluids present during different stages of the rock evolution. Therefore, they constitute the only direct means of characterising the fluid phases involved in geological processes. The first and more important step, before any analytical technique is applied, is to evaluate the textural relationships between fluid inclusions and the host mineral at room temperature. This evaluation leads to the selection and grouping of inclusions into assemblages or associations that can be further investigated (Goldstein and Reynolds, 1994; van den Kerkhof and Hein, 2001). As a general rule, inclusions may form either contemporaneously with precipitation of a certain mineral (primary) and/or after its crystallisation is partially (pseudosecondary) or totally completed (secondary). Analytical procedures and interpretation of the data obtained allow better definition of each group and further constrain the properties of each association of inclusions. Linking the various generations of fluid inclusions preserved in rocks with the mineralogical evolution is a key approach in elucidating fluid-rock interaction and rock history.

3.2.1. Microthermometry

Thermometric analysis (microthermometry) is the most popular and widely used non-destructive analytical technique for studying fluid inclusions. The method relies on careful observation and recognition of the phase changes that take place in inclusions during heating or cooling. Depending upon fluid composition this may involve solid-, liquid- and vapour-phase transformations. By accurately measuring the temperature at which these

changes take place it is possible, with reference to simple fluid systems (up to 4 components), to derive estimates (semi-quantitative) of the P-V-T-X state of the fluids at the time of trapping. As already noticed by Sorby (1858), the correctness of this approach relies on the assumption that inclusions have behaved essentially as volumetrically closed systems after fluid entrapment. At room temperature the inclusions are generally multiphase systems which hold liquid-, vapour- and/or solid-phases. During microthermometry runs in this study, the most important phase transformations reported are:

T_h = total homogenisation temperature. It defines the final transition of all the phases present in an inclusion, either at room- or at low-temperature, to a homogeneous phase of unique density. It can take place into the liquid- or into the vapour-state.

T_m = final melting temperature. This temperature defines the total disappearance of a solid phase, nucleated at low temperatures in one inclusion, into a liquid phase. Ice, different salt hydrates, clathrates and solid CO_2 have been here analysed.

Some of these phases (mostly salt hydrates) fail to nucleate at first instance during microthermometric cooling. This phenomenon is termed metastability (Roedder, 1984) and can be overcome by submitting the measured inclusions to several cooling-heating cycles, by cooling to temperatures < -100°C and by maintaining low temperatures for relative long periods (tens of minutes). Single crystals of the different phases are generally obtained, facilitating identification and improving the accuracy of measurements.
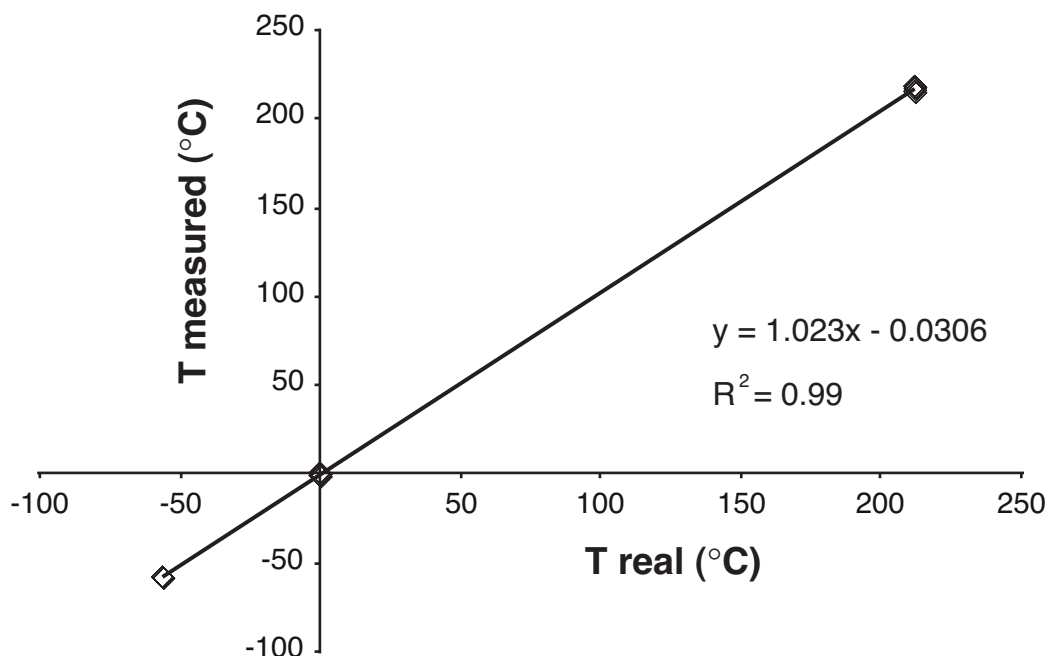
Figure 11. Calibration curve of the Linkam TH600 Microthermometry Stage (Geological-Palaeontological Institute, University Heidelberg) with the standard temperatures of CO_2 critical point, ice final melting and $AgNO_3$ melting. See Table 2.

Microthermometric measurements were made using either a Linkam TH600 (Geological-Palaeontological Institute, University Heidelberg) or a Linkam MDS 600 (Department of Mineralogy and Petrology, University of Leoben). Calibration was performed using synthetic (H_2O-CO_2) fluid inclusions supplied by SYNFLINC at the triple point of CO_2 (-56.6 °C), the melting point of ice for H_2O (0.0 °C), the melting temperature of CO_2-H_2O clathrate (+9.9 °C) and the critical point of H_2O (374.0 °C). Additionally, the melting point of the chemical standard $AgNO_3$ at 1 bar (210 °C) was used. The heating rate used was 5°C/min, and as homogenisation was approached, the rate was reduced down to 2°-1 °C/min. An example of the measured temperatures for some of the above transitions is reported in Table 2. The calibration curve obtained plotting the real vs. the measured values is presented in Fig. 11. The accuracy of the data presented in this study is approximately ± 0.4 °C below -60 °C, ± 0.3 °C between -60 to 30 °C and ± 2.5 °C in the range of 30 to 220°C.

Date	Phase (°C)	T measured(°C)
28.07.2000	H_2O (0)	-0.3
	CO_2 (-56.6)	-57.8
	$AgCO_3$ (212)	214.8
15.08.2000	H_2O (0)	-0.4
	CO_2 (-56.6)	-57.9
	$AgCO_3$ (212)	215.9
09.12.2000	H_2O (0)	-0.3
	CO_2 (-56.6)	-58
	$AgCO_3$ (212)	215.3
01.03.2001	H_2O (0)	-0.1
	CO_2 (-56.6)	-58
	$AgCO_3$ (212)	217.5
27.05.2001	H_2O (0)	-0.4
	CO_2 (-56.6)	-57.6
	$AgCO_3$ (212)	218.3
27.07.2001	H_2O (0)	0
	CO_2 (-56.6)	-57.4
	$AgCO_3$ (212)	218
19.09.2001	H_2O (0)	0.4
	CO_2 (-56.6)	-58.5
	$AgCO_3$ (212)	219
20.10.2001	H_2O (0)	0.3
	CO_2 (-56.6)	-57.8
	$AgCO_3$ (212)	216

Table 2. Temperature calibration data for the Linkam TH600 stage (Geological-Palaeontological Institute, University Heidelberg).

3.2.2. Raman Microspectrometry

Energy changes in a beam of light interacting with, for example, a fluid contained in an inclusion, are induced by the inelastic collisions of vibrating polyatomic molecules or molecular groups: this is called the Raman scattering effect. Molecular groups have a number of vibrational modes corresponding to specific energy states of the molecule in question. Raman scattering is a weak effect (10^{-3} to 10^{-6} of the irradiated light energy), and thus a monochromatic laser beam is normally required to study it. The interaction of the incident light with the vibrational modes in the sample causes losses and gains of energy in the incident beam, referred to as Stokes and anti-Stokes scattering, respectively. A Stokes Raman spectrum is a plot of the intensity of scattering vs. the energy loss, expressed in wave numbers relative to the source (Δv cm^{-1}, the Raman shift), i.e., the changes in wave number compared to that of incident light. The peaks in the spectrum correspond to the energies of the vibrational modes of different species in the sample. This technique is non-destructive, but the laser may induce reactions in the inclusions or the mineral analysed, if organic phases are present (such as petroleum). Details on the theory of Raman scattering and its application in Earth sciences can be found in the reviews by McMillan (1989), McMillan and Hofmeister (1988) and Roberts and Beattie (1995). Gardiner and Graves (1989) is a useful handbook for practical Raman spectrometry.

Gas, liquid and solid phases in fluid inclusions were analysed by a Raman microprobe LABRAM-800 at the Department of Mineralogy and Petrology, University of Leoben. Two different wavelengths for the excitation laser radiation were used: 632.8 nm (red laser) for measurements on calcite and 532.2 nm (green laser) for quartz. The less energetic red laser source is used to avoid fluorescence in calcite, and because the penetration depth of the red laser is smaller, only fluid inclusions close to the surface can be analysed. Mole fractions of gas species in the inclusion's vapour phase were calculated using a formula derived from Placzek's polarizability theory (Dubessy et al., 1989; Burke, 2001):

$$X_a = [A_a / (\sigma_a)] / \sum [A_i / (\sigma_i)]$$

X_a, A_a and σ_a are, respectively, the molar fraction, the peak area and the Raman cross-section for species **a**; A_i and σ_i are the appropriate values for all species present in any given fluid inclusion. $\sigma_{CH4} = 7.5$; $\sigma_{CO2} = 2.5$ (sum of the two peaks); $\sigma_{C2H6} = 13$; $\sigma_{C3H8} = 18$. Values are taken from Table 2 in Burke (2001). The instrument efficiency number is taken as unity for all components. Raman values for identified gas phases, salt hydrates and minerals can be found in the appendix.

3.2.3. Combined Raman and microthermometry

Accurate identification of ice, salt hydrates (e.g. hydrohalite) and clathrate crystals, formed in fluid inclusions during cooling runs (down to -196 °C), was achieved following the method described by Dubessy et al. (1982), Samson and Walker (2000) and Bakker (2001a). A Linkam stage (TMS 93) was attached to the Raman microprobe. Recognition of the types of salt hydrates allows determination of the components dissolved in undersaturated fluid inclusions. This method also enables accurate estimation of the true melting temperatures of phases that are difficult to establish, for example, eutectic melting temperatures.

3.2.4. Thermodynamic calculations and computer programs

The bulk fluid composition and density of fluid inclusions are obtained by the following approach. First, microthermometry (clathrate and ice melting temperatures) and Raman microspectrometry data are used to determine the compositions of the aqueous and vapour phases at relatively low temperatures, treating each as a separate subsystem of a typical fluid inclusion. Second, a reference P-T condition is specified, at which the relationship between fluid composition and density (or molar volume) is known. Finally, the compositional information of each phase is combined via mass- and volume-balance equations, all valid for the reference P-T condition. These were calculated using the computer packages "CLATHRATES" (Bakker, 1997), including the programs ICE and CURVES, and "FLUIDS" (Bakker, 2001b), including AQSO1, AQSO2, BULK and ISOC. The extra observational data required for this last step is the volume fraction of the vapour bubbles, estimated from video images by measuring area percentages at room temperature.

For measurements involving clathrate melting temperatures, the programs ICE and CURVES were used. The equation of state from Duan et al. (1992a,b) was applied to calculate the fugacity of CH_4 and CO_2 at clathrate melting temperatures. The quadruple point Q1 for several gas compositions and the low density of a vapour-like CH_4-rich gas mixture were calculated with CURVES. The programs AQSO1 and AQSO2 were used to calculate salinities in binary H_2O-NaCl systems (Bodnar, 1993) and ternary H_2O-NaCl-$CaCl_2$ systems (Naden, 1996), respectively. Bulk fluid properties of individual fluid inclusions were calculated using the program BULK. For the pure H_2O system the equations of Haar et al. (1984) and Wagner and Pruss (1993) have been adopted, and for mixtures of CO_2-CH_4 homogenisation conditions the model of Thiery et al. (1994) was applied, which combines the equations of state according to Soave (1972) and Lee and Kesler (1975). In complex H_2O-CH_4-CO_2-NaCl mixtures, the Henry constant according to Rettich et al. (1981) and Carroll et al. (1991) was used to calculate CH_4 and CO_2 solubilities, respectively. Setzmann and Wagner (1991) equation was adopted for pure CH_4 isochore calculations and Krumgalz et al. (1996) to calculate the density of electrolyte bearing aqueous solutions.

3.3. X-RAY DIFFRACTION

X-ray diffraction (XRD) is the scattering of X-ray electromagnetic radiation by the electrons around the nuclei of the atoms composing the unit cell of a crystal/mineral phase. The wavelength of X-rays and the structural spacing of crystals have both dimensions about 10^{-8} cm. The diffraction pattern produces a spectrum characteristic for each mineral phase. A full description of X-ray diffraction methodology, analytical settings and applications can be found in Brindley and Brown (1980) and Moore and Reynolds (1997).

To generate diffraction spectra high-energy electrons are released from a heated filament in a Röntgen X-ray tube and bombard a Cu anode, which reacts by emitting X-rays. The resulting radiation emerges from a thin, beryllium window, focused to produce a sub-parallel beam and then directed to the sample. When the crystals in the sample reach an appropriate angle, they will diffract the X-rays according to Bragg´s Law :

$$n\lambda = 2d \sin \theta$$

Where **n** = integral number of wavelengths; λ = wavelength of the X-rays; **d** = lattice spacing (in angstroms); and θ = angle of diffraction. The diffracted beams pass first to a crystal monochromator, having the function of filtering the unwanted radiation, and then enters the detector. In the resulting spectrum of the X-ray diffraction pattern the horizontal scale is calibrated in $°2\theta$ and the vertical scale displays the intensity of the diffracted radiation.

X-ray diffraction (XRD) measurements were performed at the Geological-Palaeontological Institute, University Heidelberg, in order to aid determination of the mineral paragenesis of the vein material made by standard petrographic microscopy. All X-ray determinations were carried out on a **Bragg-Brentano-Diffractometer** of the type **Siemens D 500**, with a Cu Röntgen X-ray tube (CuKα) and graphite monochromator operated at 40 kV and 30 mA. For the purpose of mineral identification diffraction patterns were compared with a set of standard patterns compiled by the Joint Committee on Powder Diffraction Standards (JCPDS).

Powder preparates

Duplicate powder samples were prepared from the same slabs of rock used to make thin and double polished sections. Rock pieces of vein minerals and host rock were initially crushed by hand using a metal mortar to reduce the samples to mm-fragments. The material was then grounded with a tungsten disc mill, and reduced to a powder of 600-μm grain size. The powder so obtained was scanned in the 2θ range from 2 ° to 50° with increments of 0.02°[2θ]/sec, using aperture diaphragms of 1° and a detector slit of 0.15°.

Texture preparates

The mm-sized rock fragments were also used for preparation of textured slides. Material was ultrasonically treated for 3 hours in a water bath at 35 kHz. The < 2μm clay fraction was separated by centrifugation. X-ray slides (3 x 3 cm) were prepared by the pipette-on-slide method, keeping the specimen thickness as constant as possible (> 5 mg/cm^2). Measurements were performed using the same conditions as for random powder samples.

Kaolin polytype identification

For determination of the kaolin mineral polytype 10 representative texture samples were heated between 460 and 540°C at intervals of 20°C. Samples were maintained in the oven for one hour at each temperature and after every step they were extracted and irradiated at room temperature. The X-ray slides were scanned in the 2θ range from 2° to 20° with increments of 0.02°[2θ]/sec.

3.4. STABLE ISOTOPE ANALYSIS

Principles

For a complete description of the foundations, analytical techniques and applications of stable isotopes the reader is referred to Hoefs (1997), Sharp (1999) and Valley et al. (1986), and references therein. Isotopes are atoms whose nuclei contain the same number of protons but a different number of neutrons. The atomic weight of each naturally occurring element is the average of the weights contributed by its various isotopes. The term stable refers to those isotopes that are not radioactive. In most cases, one stable isotope is predominant, the others being present only in trace amounts. Certain differences exist in physicochemical properties due to isotope mass differences. The chemical properties of molecules differing only in isotopic substitution are qualitatively the same, but quantitatively different. These differences in chemical properties can lead to considerable isotope effects in chemical reactions.

The partitioning of stable isotopes between two substances or two phases of the same substance with different isotope ratios is referred to as isotope fractionation. The main phenomena producing isotope fractionations are isotope exchange reactions and kinetic processes; the latter depend primarily on differences in reaction rates of isotopic molecules. Other factors are the chemical composition and the crystal structure. Fractionation mechanisms are specific for any given element.

Mass spectrometry methods are the most effective means of measuring isotope abundance. A mass spectrometer separates charged atoms and molecules by their mass

as they move through magnetic and/or electrical fields. The accuracy with which absolute isotope abundance can be measured is substantially poorer than the precision with which relative differences in the isotope abundance between two samples can be determined. Nevertheless, the determination of absolute isotope ratios from standards is very important, because these numbers form the basis for the calculation of the relative differences, the δ-values. The δ-values can reflect the fractionation mechanisms and processes predominant for each specific element during geological evolution.

In carbonate minerals and rocks oxygen isotope ratio ($\delta^{18}O$) provides a useful tool for the study of water/rock interaction, as this ratio shifts for both phases away from their initial values during interaction. Carbon isotope ratios ($\delta^{13}C$) can be used to trace the carbon source and the carbonate evolution during diagenesis and very low-temperature metamorphism.

Analytical procedure

Measurements of the stable isotopes $\delta^{13}C$ and $\delta^{18}O$ in both dolomite and calcite were performed in the Institute of Geology, University of Erlangen-Nürnberg. Powder preparations were obtained by drilling the vein carbonate crystals from polished rock slabs (400 μm). The powder was poured directly into the glass containers of the carrousel preparation line. The carbonate powders were reacted with 100% phosphoric acid (density >1.9 g/cm^3); Wachter and Hayes, 1985) at 75°C in an online carbonate preparation line (**Carbo-Kiel** - single sample acid bath) connected to a **Finnigan Mat 252 mass-spectrometer**. All values are reported in per mil relative to V-PDB Standard (Cretaceous belemnite of the Pee Dee formation) by assigning a $\delta^{13}C$ value of +1.95‰ and a $\delta^{18}O$ value of -2.2‰ to NBS19 (equivalent Marble Standard). Values for oxygen are reported as well in per mil relative to SMOW (Standard Mean Ocean Water). Oxygen isotopic compositions of dolomites were corrected using the fractionation factors given by Rosenbaum and Sheppard (1986). Reproducibility was checked by replicate analysis of laboratory standards and is better than $\pm$ 0.02 for $\delta^{13}C$ and $\pm$ 0.04 for $\delta^{18}O$ (1σ). Though in the studied samples vein calcite contains entrapped fragments of dolomite, these do not represent more than 5-10 vol. % of the total (estimated from thin section). The short reaction time (10 minutes) and low temperature of the phosphoric acid (75°C) lead to conclude that no significant amount of dolomite derived $\delta^{18}O$ and $\delta^{13}C$ was incorporated in the measured CO_2 (gas). Therefore, the obtained isotopic values are considered to be representative for the calcite phase.

CHAPTER 4: VEIN MINERALOGY AND TEXTURAL RELATIONS

4.1. VEINS IN CLASTIC SEDIMENTARY ROCKS

4.1.1. Mineral phases

Typically, the studied veins show little variation in mineralogy, irrespective of structural association and stratigraphic position (Fig. 12 and Table 1). They contain quartz (qtz1), saddle dolomite (dolm), ferroan calcite (cal2), pyrite/chalcopyrite (py) and an authigenic clay fraction dominated by kaolinite (kln) with minor illite/smectite (ill/sm) . This has been confirmed by transmitted and reflected light microscopy, SEM mineral identification in thin sections, and by X-ray analysis separated from the clay size fraction of the vein samples (Figs. 13, 23, pages 39 and 50; and appendix, Table A2). The main difference between the veins in the coalfields arises in the quartz content, absent from most of samples collected in the SB. Quartz is also absent in samples from localities 6 and 14 in the CMB.

Quartz (qtz1)

This mineral occurs mainly as large euhedral crystals (up to 10 cm in size), with well-developed growth zones marked by inclusion clouds. Smaller crystals (mm size) show typical arrays of pseudosecondary fluid inclusion trails along the c-axis (normal to the crystal borders) and are generally arranged perpendicular to the vein walls. In many veins the large prismatic qtz1 crystals show evidence for remobilization and brittle deformation in the form of cal2 filled microfractures (Fig. 12). A few deformed crystals show weak undulose extinction and deformation lamellae, along crystal borders, wherein contact with cal2 crystals occurs. This phase of quartz mineralisation is particularly important regarding the study of fluid inclusions and fluid trapping conditions.

Saddle dolomite (dolm)

All the dolomite formed in the veins has been identified as saddle dolomite (Radke and Mathis, 1980; Spötl and Pitman, 1998). Only in samples 6 and 9 from the SB, and in sample 51 from the CMB, is this mineral preserved as entire millimetre- to centimetre-sized crystals of euhedral/subhedral spear-shaped form showing sweeping undulose extinction. The dolomite occurs as a void-filling product in the remaining open space within the veins and has a characteristic brown colour, reflecting iron oxidation during widespread dedolomitisation. This process produced embayments and border corrosion of remaining

dolomite crystals. Under cathodoluminesce it is distinguished by its non-existing or very dull luminescence, diagnostic of the iron content (Fig. 14a-b, page 40). In the rest of the studied samples only tiny entrapped fragments of dolm remain within the ferroan calcite, and within fluid inclusions, outlined by their higher relief and their brown alteration colour. Identification was qualitatively confirmed by Raman microspectrometry.
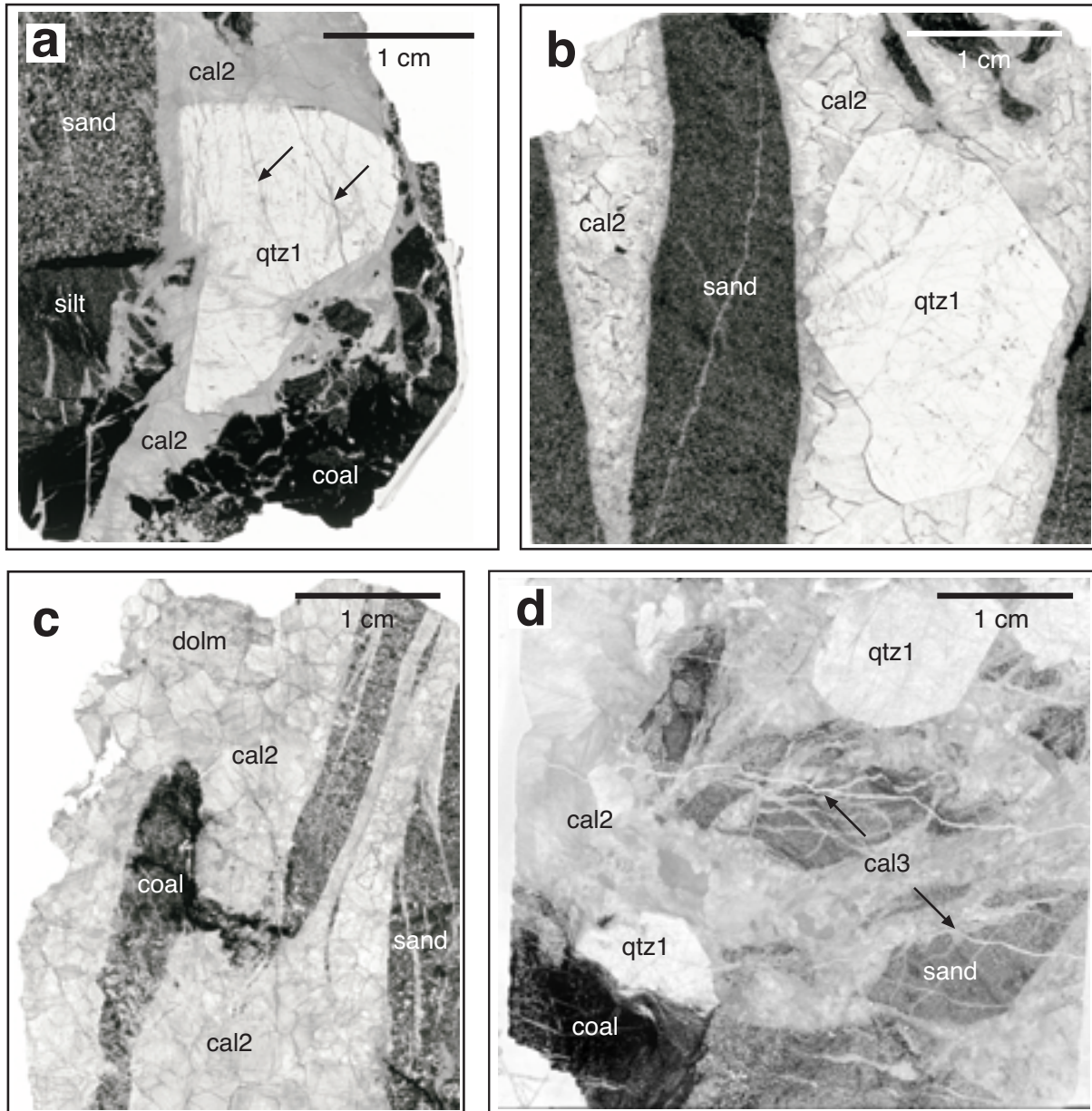
Figure 12. Photomicrographs of double polished sections (100-120 μm thick) from veins in the Stephanian sedimentary rocks of the Ciñera-Matallana and Sabero basins, illustrating mineralisation and deformation features (Table 1). (a) Fault related vein, sample 26 -locality 4-. (b) Fold related vein, sample 42 -locality 12a-. Arrows point to calcite (cal2) filled cracks. (c) Fault related vein, sample 6 -locality 1b-. (d) Fault related vein, sample 36 -locality 10-. Qtz1, dolm, cal2 and cal3 (arrows in (d)), refer to quartz, saddle dolomite and calcite respectively. sand = sandstone, silt = siltstone.
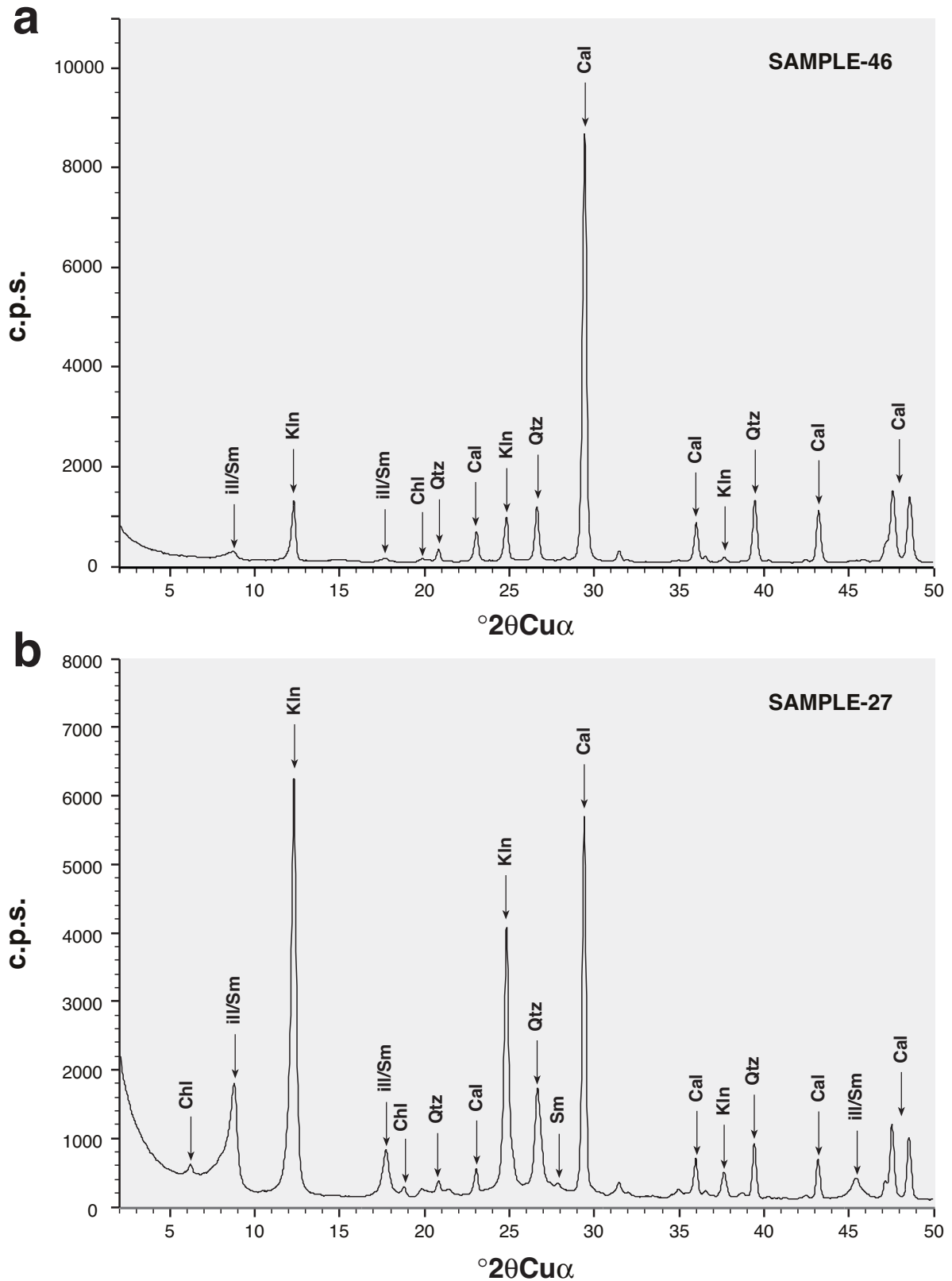
Figure 13. X-ray diffractograms of two texture preparates (clay fraction < 2μm) from different vein samples of the clastic rocks of the CMB. Sample 46 (a) contains only vein minerals; whereas sample 27 (b) has vein material and surrounding host rock (sandstone). Note how the clay mineral content increases significantly when host rock fragments are included, but no difference in the mineral paragenesis is observed. Abbreviations of mineral names after Kretz (1983).
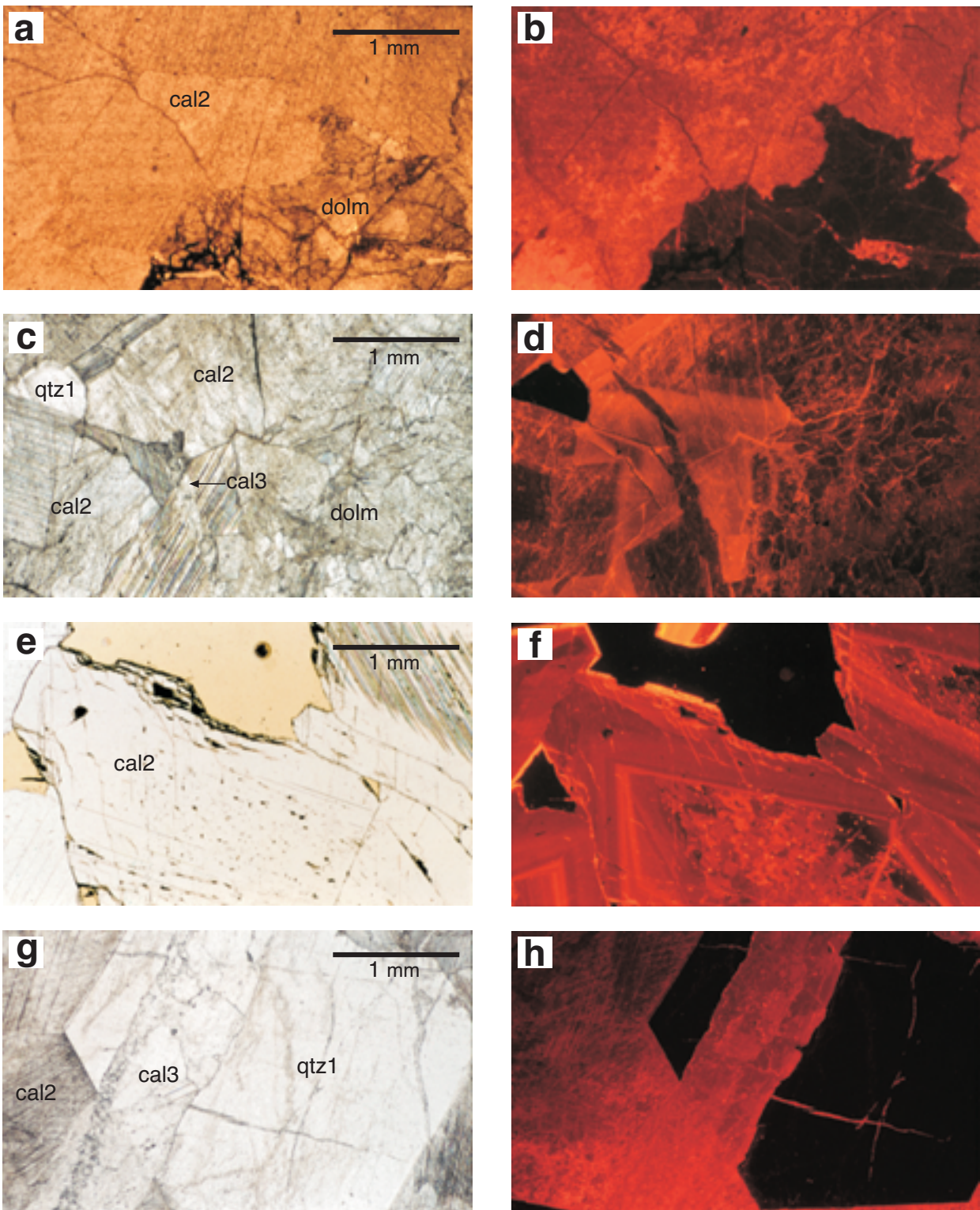
Figure 14. Photomicrographs of thin sections (30 to 60 μm) under transmitted plane polarised light (PPL) and cathodoluminescence (CL) showing the relations among the carbonate minerals.

a-b) Dissolution of dolm, with crystal borders embayment and corrosion. Sample 6, Sabero.

c-d) Progressive dedolomitisation which has almost obliterated dolm. Cal3 is represented as thin, cross cutting, dull brown luminescent band. Sample 32, Ciñera-Matallana.

e-f) Relatively undeformed cal2 crystals present a cloudy core, containing dolm relict fragments. The outer clear areas of the crystals are well defined by dark red / orange zones. Sample 48, Ciñera -Matallana

g-h) Under PPL cal3 is clearer than cal2, but its luminescence colours are the same as for this last phase. Cal3 CL bands parallel the qtz1 fractured borders. Sample 36, Ciñera-Matallana.
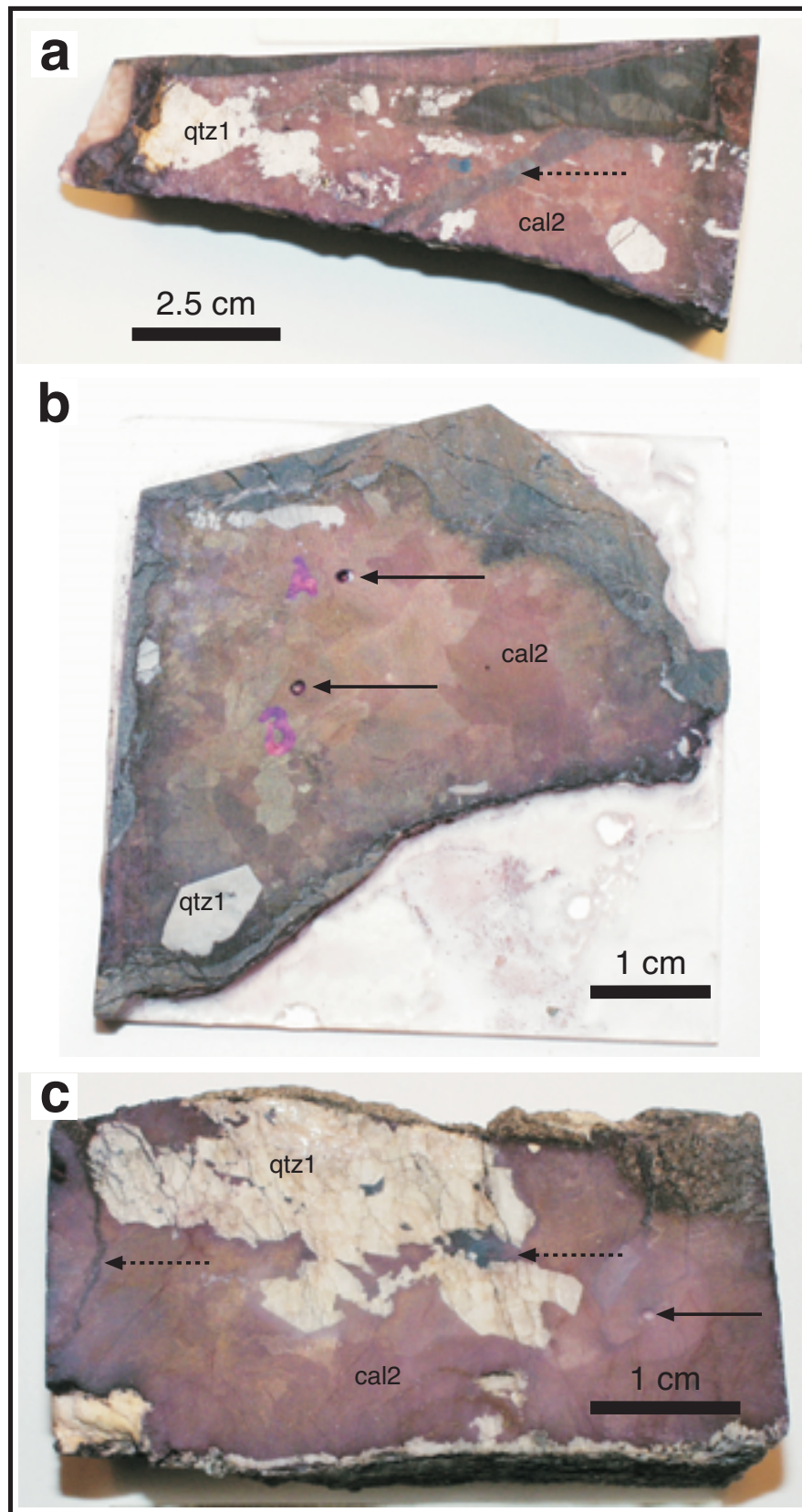
Figure 15. Photographs of stained polished hand specimens from mineralised fissures in the studied Stephanian basins. (a) Sample 3 -locality 1a-, Sabero. (b) Sample 36 (locality 10), Ciñera-Matallana. (c) Sample 27 (locality 9), Ciñera-Matallana. Dashed arrows point to areas with a more bluish staining colour, characteristic for cal3. Solid arrows point to areas drilled in order to obtain powder for $\delta^{13}C$ and $\delta^{18}O$ stable isotope analysis of cal2.

Ferroan blocky calcite (cal2)

The ferroan calcite (cal2) is commonly the most important mineral by volume with the exception of samples 31 and 51 (localities 7 and 12b, respectively), where it is absent. This phase is characterised by its blocky habit and white to slightly pink colour in hand specimens, probably due to the presence of entrapped altered dolm fragments. Staining of polished vein material shows that this calcite is homogeneously ferroan, presenting a characteristic mauve colour, regardless of distance between localities, structural association and stratigraphic position (Fig. 15). In thin section this mineral exhibits mm-sized crystals of blocky habit and a cloudy, dirty appearance. Under CL it presents a dull luminescence, sometimes patchy (probably due to meteoric alteration), evolving to clearer orange-coloured zones towards grain boundaries (Fig.14c-d). Many cal2 crystals, especially those in veins related to fault structures, present abundant deformation-induced, closely-spaced and narrow straight twins, usually less than 5 mm wide (Type I of Burkhard, 1993; see also Paschier and Trouw, 1998). A number of these grains also show interpenetrated borders and occasionally small stylolite surfaces. In the less deformed crystals a core with tiny dolomite fragments surrounded by clearer calcite can be commonly observed. This outer area shows zoning in CL, with alternating dark brown-orange bands, whereas the core zones have a dull patchy luminescence (Fig.14e-f).

Sulphides (py)

Pyrite (py) and chalcopyrite (Ccp) have been identified within the veins by reflective light microscopy. They are present as small (mm sized), disseminated single crystals of euhedral habit within cal2 and around vein minerals grain boundaries (Fig. 16a). Occasionally they reach centimetre sizes (see detail in Fig. 7, page 20). These two sulphide minerals are also present within mm-thick coal horizons and disseminated in host rocks adjacent to mineralised fissures (Fig. 16b).
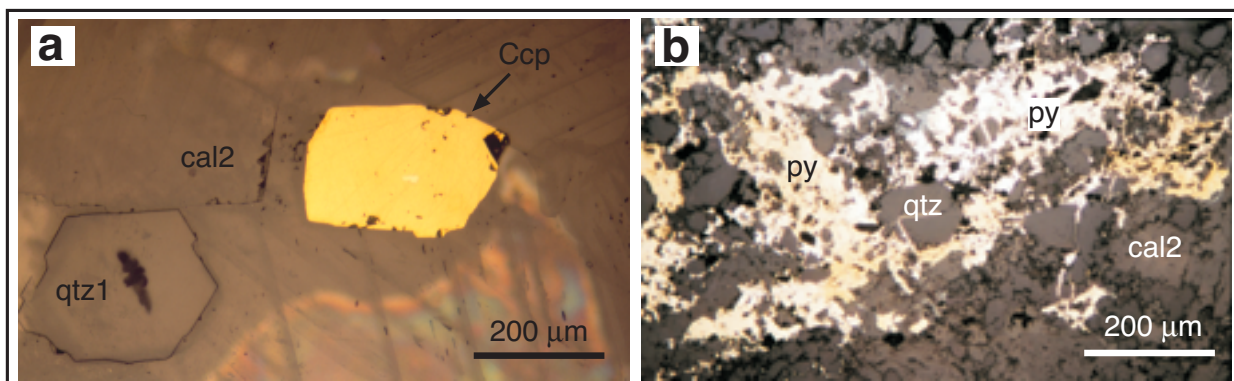
Figure 16. Reflected light images of sulphide minerals in veins from the clastic Stephanian rocks. (a) Chalcopyrite (Ccp) crystal, sample 42. (b) Disseminated pyrite (py) cementing host-sandstone nearby a mineralised fissure, sample 6.

Late calcite (cal3)

A third calcite type, cal3, is recognised within small veins cutting the host rock and the whole vein assemblage (Fig. 12d and Fig. 14g-h). These clear crystals are only weakly twinned and virtually inclusion-free. In the stained polished vein samples, cal3 is characterised by a more bluish colour (see Fig. 15), but crystals do not show distinct CL features and have essentially the same luminescence colours as cal2. This phase is present in samples in which the vein minerals are more deformed, particularly those associated with fault structures.

Authigenic clay minerals (kln)

Within the clay fraction, kaolin group minerals are by far the most important. The kaolin phase occurs as microporous clusters of authigenic crystals filling volumes between crystal boundaries (calcite-calcite, but also cal2-qtz1 and mineral-host rock). This mineral is also present intergrowing with cal3 and generally it replaces both qtz1 and cal2 (Fig. 17). The mineral habit observed under transmitted light microscopy and SEM consists of vermicular crystals, comprised of disorderly appearing stacks of thin euhedral plates. Smaller crystals of blocky morphologies are also common and many times they surround vermicular crystals. The kaolin clusters are also characterised by a dark blue luminescence colour under CL (Fig. 18). This phase is specially abundant in fault related veins, along cal2-host rock contact surfaces and fissure walls, within pore spaces in vein minerals and as haloes around entrapped host-rock fragments. The kaolin present in the veins is always in the form of the low temperature polytype kaolinite. Though small crystal size make it impossible to distinguish the kaolin polytypes based on optical properties, the dominant crystal morphologies described above are those typical of the low temperature kaolinite variety (Ehrenberg et al., 1993). This is confirmed by the disappearance of the 7.14 Å XRD peak at temperatures $\leq 500°C$ (Fig. 19 and Table 3). Dickite, the high temperature polytype, resists temperatures up to 550-650°C (Brown and Brindley, 1980; and references within). The remaining peak intensity in some of the samples at 520-540°C (all < 10% of the initial intensity) is attributed to the presence of minor ammounts of chlorite.
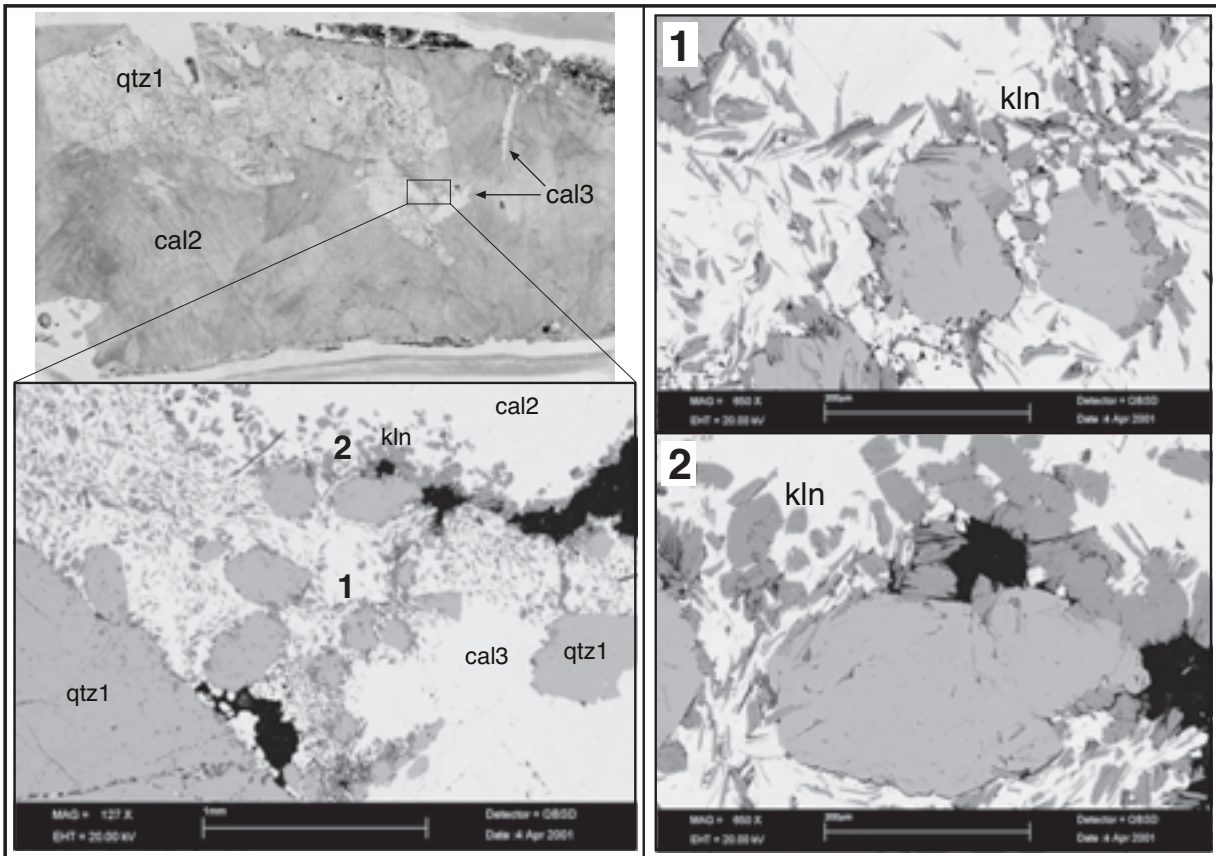
Figure 17. SEM back scattered electron images from a thin section illustrating the growth of authigenic pore filling kaolinite (kln), together with late calcite (cal3), in veins from the Stephanian clastic sediments. Both phases replace qtz1 and cal2 (1). Many kaolinite crystallite packages have a fan-shaped morphology (2), typical for the low temperature polytype. Sample 27 (locality 9), Ciñera-Matallana.
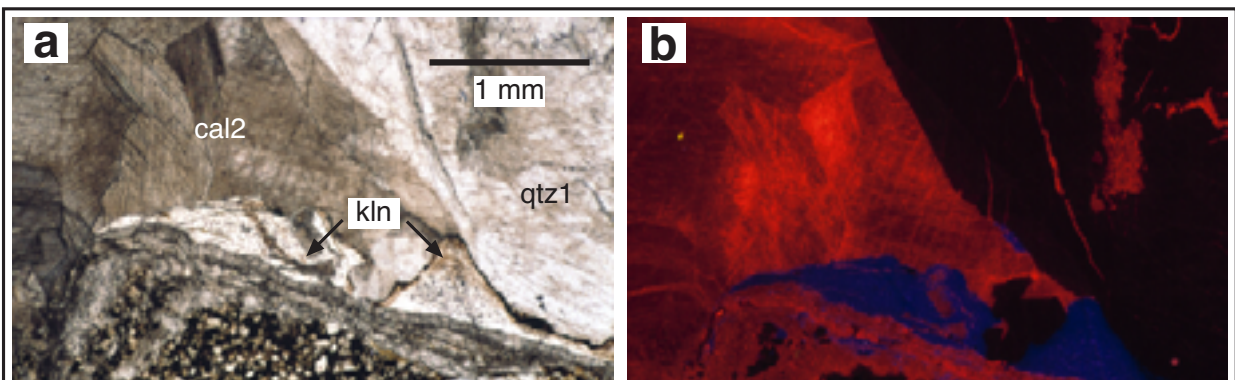
Figure 18. Photomicrographs of authigenic pore filling kaolinite (kln) under (a) transmitted plane polarised light and (b) cathodoluminescence. Note the diagnostic deep blue luminescence colour. Sample 36, locality 10.
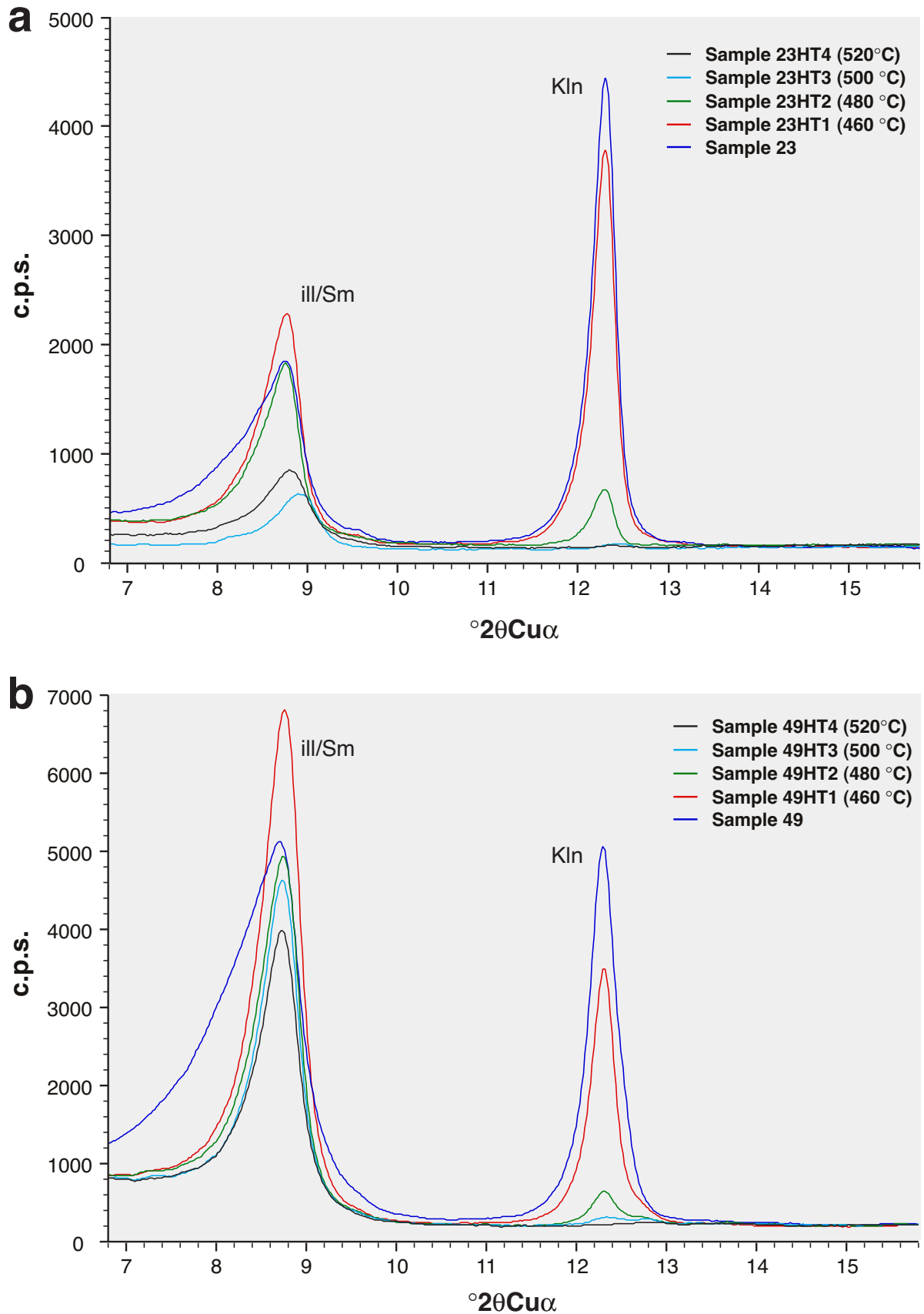
Figure 19. X-ray diffractograms showing the authigenic kaolinite main peak (kln) of two heated texture preparates (clay fraction < 2μm) at progressive temperature intervals. Both the 7.14 Å (°2θ =12.3) peaks disappear at 500°C, which confirms the low temperature kaolinite as the dominant polytype. (a) sample 23, locality 3; (b) sample 49, locality 12c.

a

Sample	Kaolin 7.14 Å peak intensity (counts)					
	25°C	460°C	480°C	500°C	520°C	540°C
Ign-Sb1*	1787	702	197	109	98	0
Ign12*	3967	2320	969	614	305	103
Ign14*	5303	2671	1040	637	362	186
can10	1135	696	99	0	-	-
can23	5012	4243	646	0	-	-
can25	1695	1433	275	79	0	-
can34	1957	1682	144	0	-	-
can35	1595	1180	188	0	-	-
can36*	3727	3252	1497	792	421	90
can37	5130	4803	943	211	0	-
can46*	1416	1205	546	324	150	96
can49	5535	3848	575	0	-	-
can54*	10502	10023	4348	2754	1414	460

b

Sample	Kaolin 7.14 Å peak intensity (%)				
	460°C	480°C	500°C	520°C	540°C
Ign-Sb1*	39	11	6	5	0
Ign12*	58	24	15	8	3
Ign14*	50	20	12	7	3
can10	61	9	0	0	0
can23	85	13	0	0	0
can25	85	16	5	0	0
can34	86	7	0	0	0
can35	74	12	0	0	0
can36*	87	40	21	11	2
can37	94	18	4	0	0
can46*	85	39	23	11	7
can49	70	10	0	0	0
can54*	95	41	26	13	4

Table 3. Temperature stability of the kaolin mineral polytype in the veins of the sedimentary and igneous rocks of the CMB and the SB. The results are given as absolute values (table 3a) and as percentage calculated with respect to the intensity of the reflections obtained before heating (table 3b). See text for explanation. * = chlorite bearing sample.

4.1.2. Mineralisation history

The mineral growth sequence determined in this study is outlined in Fig. 20. After the initial opening of the fissures certain amounts of calcite (cal1) were precipitated, followed by the growth of large euhedral quartz (qtz1). Cal1 is only preserved as small relics within few qtz1 crystals in sample 26 (locality 4), and therefore has not been characterised above. The quartz directly surrounding this calcite shows growth-zones that parallel their contacts. During and after the last stages of qtz1 growth, ferroan saddle dolomite was precipitated (dolm), filling the remaining void space in the veins. Some qtz1 crystals have growth zones delimited by trails of small dolomite crystals. Following this early mineralisation both vein and wall rock suffered brittle deformation, with brecciation of host rock and fracturing of detrital grains. Large vein-qtz1 crystals were microcracked and sometimes detached from the vein walls (Fig. 12). Following brittle deformation, calcite (cal2) precipitated dedolomitising and almost totally replacing dolm. The textural features of calcite (see above) indicate that deformation occurred after crystallisation. Together with cal2, small amounts of sulphide minerals (py) formed, and were probably accompanied by precipitation of authigenic kaolinite (kln). The third type of calcite, cal3, subsequently formed in microfissures, cutting the host rock and the whole vein assemblage. Kaolinite continued to grow after all the other mineral phases have already been formed, as it replaces all of them.
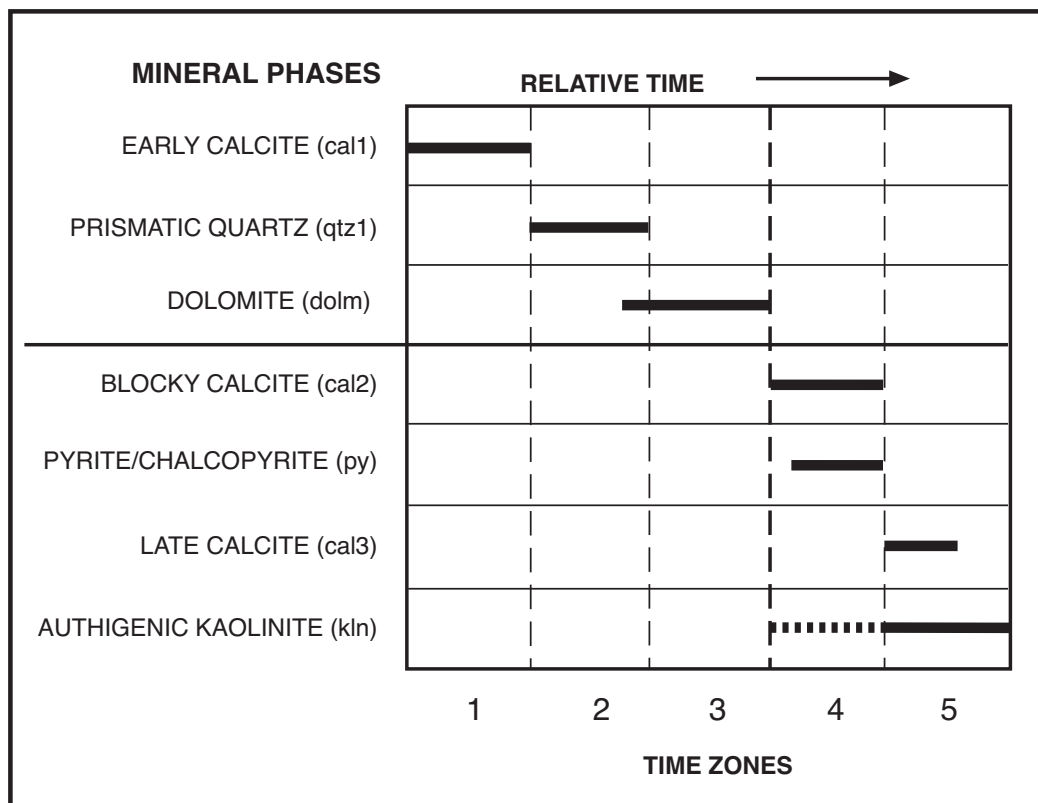
Figure 20. Diagram showing the relative sequence of mineral growth for the veins in the sedimentary rocks of the Ciñera-Matallana and Sabero coalfields. See text for details.

4.1.3. Features of mineral growth

The absence of fibrous crystals indicates that vein filling occurred within open fissures, with no strain increments or syn-growth deformation (Wilson, 1994). Initial crystallisation took place within fluid-filled cavities in a relatively stress-free environment, enabling formation of euhedral prismatic crystals by a free face growth that displaced the fluid. The resultant open texture, with large variations in dihedral angles, allowed passage of further fluids, facilitating fracture reactivation and mineral precipitation within the veins. The mobilisation of material from the overlying and/or underlying shales (also coal) into the veins, which can be observed in many cases (see detail in Fig. 7, page 20), also confirms the existence of open fractures.

Some fragments of wall rock sandstone remain attached to euhedral qtz1 and both show microcracking and mobilisation within the veins. Qtz1 contact surfaces with the host rock fragments are irregular and closely follow the boundaries of sand grains. The fact that this fracturing followed grain boundaries rather than breaking through individual grains suggests the sands were only weakly cemented at this stage (Fisher and Byrne, 1990). This is in contrast to cal2 and cal3 crystallisation that follows cracks in detrital grains, producing sharp contact surfaces between the calcite and the host rock.
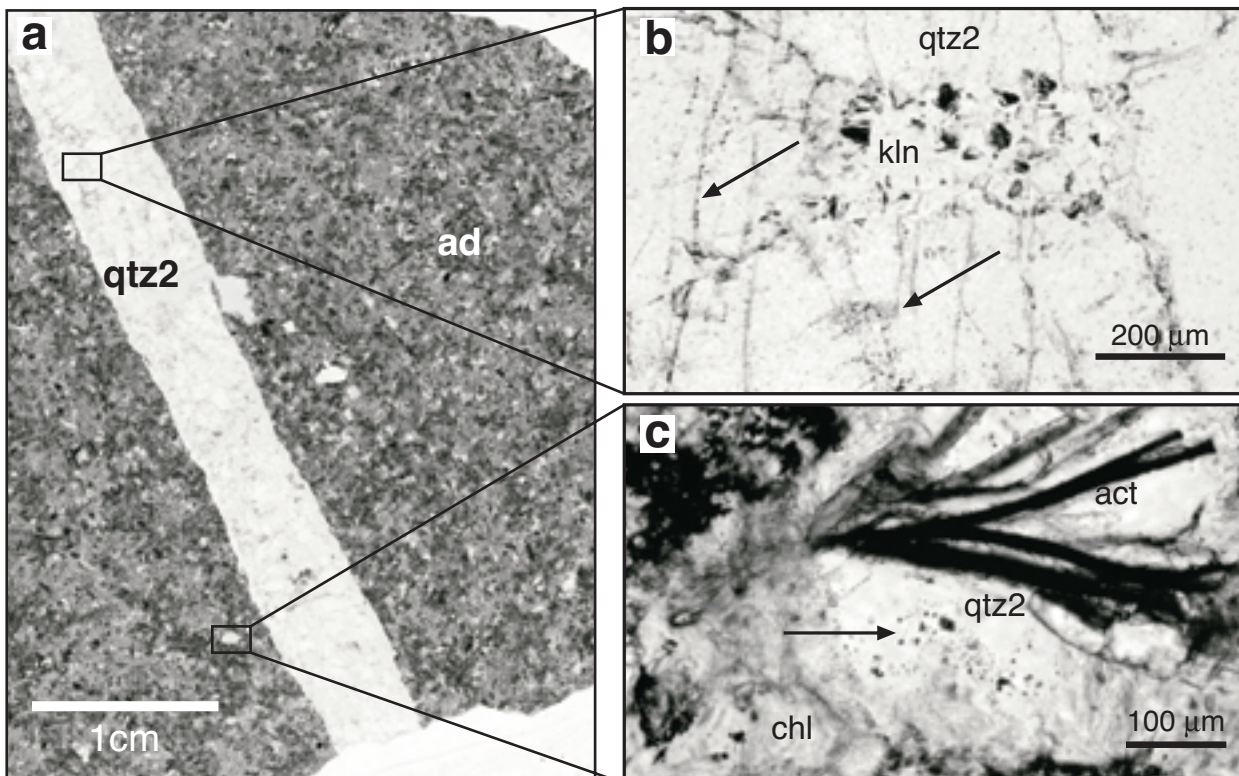
Figure 21. (a) Photomicrograph of a 60-50 μm thin section from a quartz vein (qtz2) in a diorite intrusion (ad), locality 12b, Tabliza Anticline. (b) Alteration of qtz2 to kaolinite (kln). The arrows point to fluid inclusion assemblages distributed in small clusters within qtz2 crystals and along vertical crosscutting trails. (c) Pore filling qtz2 with a vapour-rich inclusion assemblage (arrow). act = actinolite; chl = chlorite.

4.2. VEINS IN DIORITES

Minor quartz mineralisations (qtz2) are found in most altered igneous rocks that have intruded through coal beds (e.g. intrusion in Alejico beds and in the Tabliza anticline, Fig. 6, page 16). Qtz2 is present as mm to cm wide veins infilling crosscutting joints, as cavity-filling nodules that resemble vesicles, and within small pores in the altered diorites (Fig. 21). The mineralised joints do not propagate into the adjacent sediments, but they do occur in igneous rocks that appear undeformed. The fissures/joints crosscut the previously formed alteration minerals of the host rock. Qtz2 crystals within veins are subhedral to anhedral (many elongated), have a chaotic orientation, and coarsen towards the centre of the fractures. In the nodules the mineral fabric is inequigranular and interlobate. All these features indicate that qtz2 formed as a late alteration product, which is common during very low-grade metamorphism and hydrothermal alteration processes in mafic rocks (Winkler, 1979; Alt, 1999).

As in the previously described veins, a late stage kaolinite is abundant in the vertical quartz fissures, filling pores and cracks along qtz2 crystal boundaries (Fig. 22). The mineral habit observed under transmitted light microscopy and SEM is very similar to that of the kln phase in the mineralised fissures of the clastic rocks. X-ray analyses of the clay size fraction of 4 samples confirm that kln is the dominant authigenic clay mineral, with minor illite/smectite and that there are no variations in the mineral paragenesis described in chapter 2 (Fig. 23). As with the veins in the sedimentary rocks the kaolinite is in the form of the low temperature polytype (Table 3). Significantly, it is absent in the qtz2 nodules and very rare within the altered igneous rock (Fig. 21c and 23a).
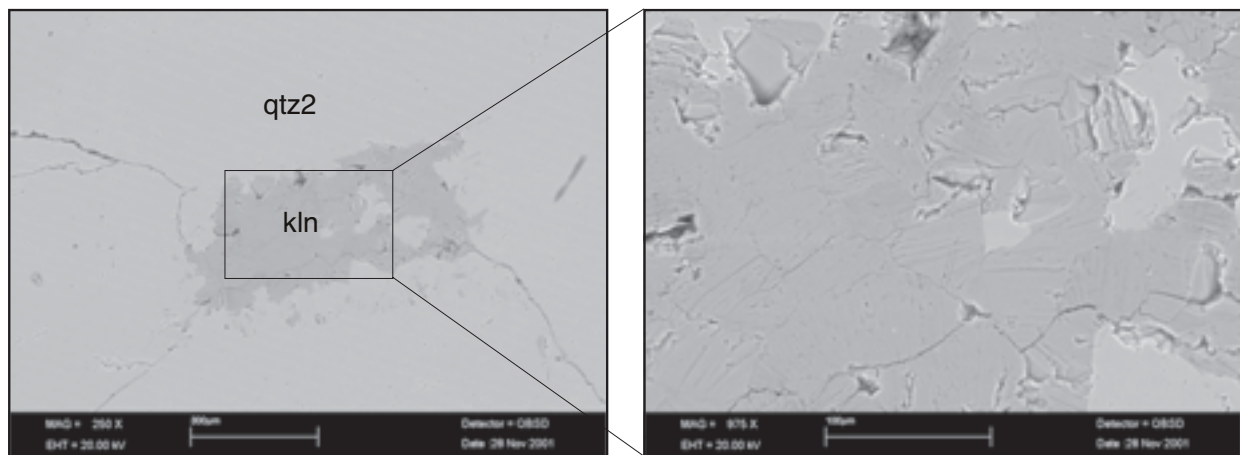
Figure 22. SEM back-scattered electron images from a thin section illustrating kaolinite growth within qtz2 veins in dioritic rocks as a late alteration product, partially replacing quartz (qtz2). Sample ign12, locality 12b.
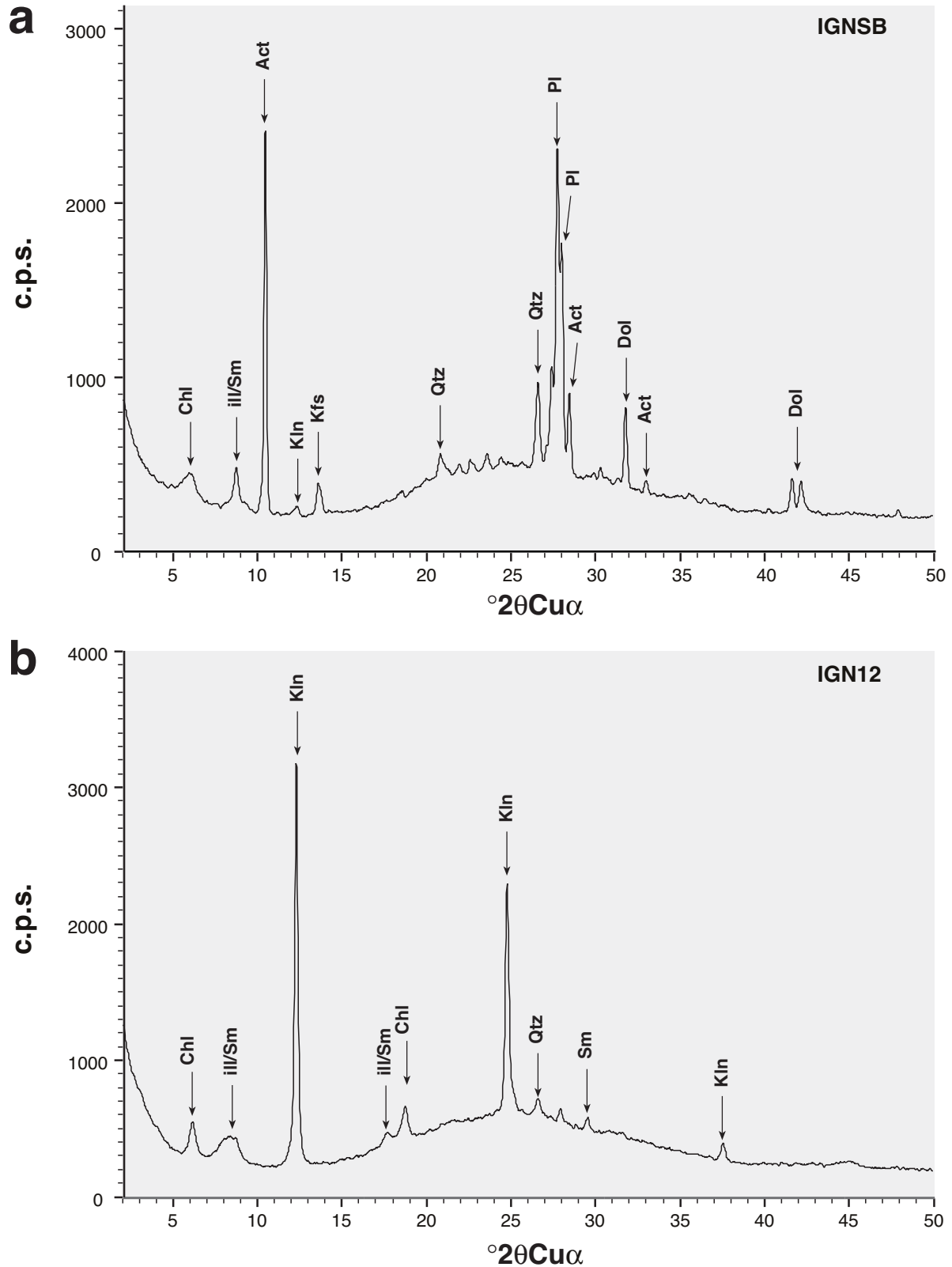
Figure 23. X-ray diffractograms of two texture preparates (clay fraction < 2μm) from dioritic rocks within the Stephanian sediments. (a) Altered diorite, sample ignSB -Alejico beds-. (b) Qtz2 vein, sample ign12 (locality 12b). In contrast to the sedimentary rocks (Fig. 13b), kaolinite is almost absent within the altered diorite itself.

CHAPTER 5: FLUID INCLUSION ANALYSIS

5.1. FLUID INCLUSIONS IN VEINS FROM THE CLASTIC SEDIMENTARY ROCKS

In the Ciñera-Matallana and Sabero coal basins, at least six types of fluid inclusion assemblages are recognised within the 3 cement generations of the syntectonic quartz-carbonate veins: one in cal1, three in qtz1, and another two in cal2. Detailed fluid inclusion analyses reported here were made for the best constrained samples, but correlation with samples from other localities is supported by preliminary petrographic observations. Only inclusions in cal2 could be measured in vein samples from the SB basin. A summary of the data obtained is presented in Table 4 and a complete database of the microthermometry and Raman microspectrometry results is included in the Appendix (Tables A3 to A13). The characteristics of these inclusions are outlined as follows, in order of their formation.

		qtz1 type 1	*qtz1* type2	*qtz1* type3	*cal2* type 1c	*qtz2* type 1q-2q
Number		67	91	83	114	26
Liquid		0 - 100	0 - 100	95 - 100	90 - 100	18 - 92
T_h **(aq)**		73 / 110 (110)	87 / 129 (120)	40 / 98 (55)	60 / 137 (80)	150 / 296
T_m **(ice)**		-3.5 / -1.0 (-1)	-3.9 / 0.0 (-1)	-41.0 / -7.2 (-40)	-39 / -4.9 (-20)	-2.4 / 0.0 (-2)
T_m **(cla)**		-	-3.0 / +12.1	-30.0 / -25.0	-	-5.2 / +16.2
T_m **(hh)**		-	-	-47.0 / -1.2	-27.0 / -7.2	-
T_m **(hyd)**		**-**	**-**	-7.2 / -6.0	-35.8 / -30.2	-
T_m **(car)**		-105.4 / -82.5 (-83)	-89.0 / -73.0 (-81)	-	-	-
T_h **(car)**		-78.8 / -72.3 (-75)	-76.8 / -59.0 (-75)	-	-	-
Raman	CH_4	0.24 - 1.00 (1)	0.40 - 1.00 (1)	0.96 - 1.00 (1)	1.00	0.78 – 0.89
	CO_2	0.00 - 0.76 (0)	0.00 - 0.60 (0)	0.00 - 0.04 (0)	-	0.11 - 0.28
	C_2H_6	0.00 - 0.02 (0)	0.00 - 0.03 (0)	-	-	-
	C_3H_8	0.00 - 0.01 (0)	minor	-	-	-
	C_2H_4	minor	minor	-	-	-
Raman low T		H_2O (ice+liq)	H_2O (ice+liq)	H_2O (ice+liq) Hydrohalite	H_2O (ice+liq) Hydrohalite	H_2O (ice+liq)
Trapped Minerals		Mg- calcite Calcite	Mg- calcite Calcite	Kaolinite	Dolomite	Kaolinite

Table 4. Summary of microthermometry and Raman results for five fluid inclusion types in vein minerals of the Ciñera-Matallana basin. All temperature results are given as ranges in °C (mode in brackets). Number = total number of inclusions measured. Liquid = volume percentage of the aqueous phase (filling degree). Th (aq) = total homogenisation of aqueous inclusions, always into the liquid phase, only measured for inclusions with a liquid vol. % < 100. Tm = final melting temperature. cl = clathrate; liq = liquid; hh = hydrohalite; hyd = unidentified salt-hydrate phase. For gas-rich inclusions: Th (car) = homogenisation temperature of the CH_4-rich carbonic gas mixture; Tm (car) = melting temperature of gas-mixture. Raman = molar fractions of detected gas phases (mode in brackets). Raman low T = phases detected at temperatures below 0°C.

5.1.1. Relict calcite (cal1) inclusions

This phase contains mainly flat, small (1-5 μm) all-liquid aqueous inclusions. Few inclusions show less than 5 vol.% vapour bubbles ($Th_{liq} = 76 – 89°C$). Pure water (ice melts at 0°C) is the only component identified. The molar volume varies between 18 (all liquid) and 18.65 cm³mol⁻¹.

5.1.2. Vein quartz (qtz1) inclusions

The three types of inclusion assemblages in vein quartz are distinguishable by distribution within the crystals (Fig. 24) and by filling degree. Type 1 inclusion assemblages are located within growth zones of the quartz. Inclusions are typically large (up to 10's of μm) and vapour-dominated (Fig. 25a). Generally they are irregularly shaped, but in some assemblages negative crystal shapes occur. Type 2 inclusions are distributed along crosscutting trails and as small clusters within the quartz crystals (Fig. 24). Shapes are semi-regular to highly irregular, with sizes ranging up to 50 μm (Fig. 25b).
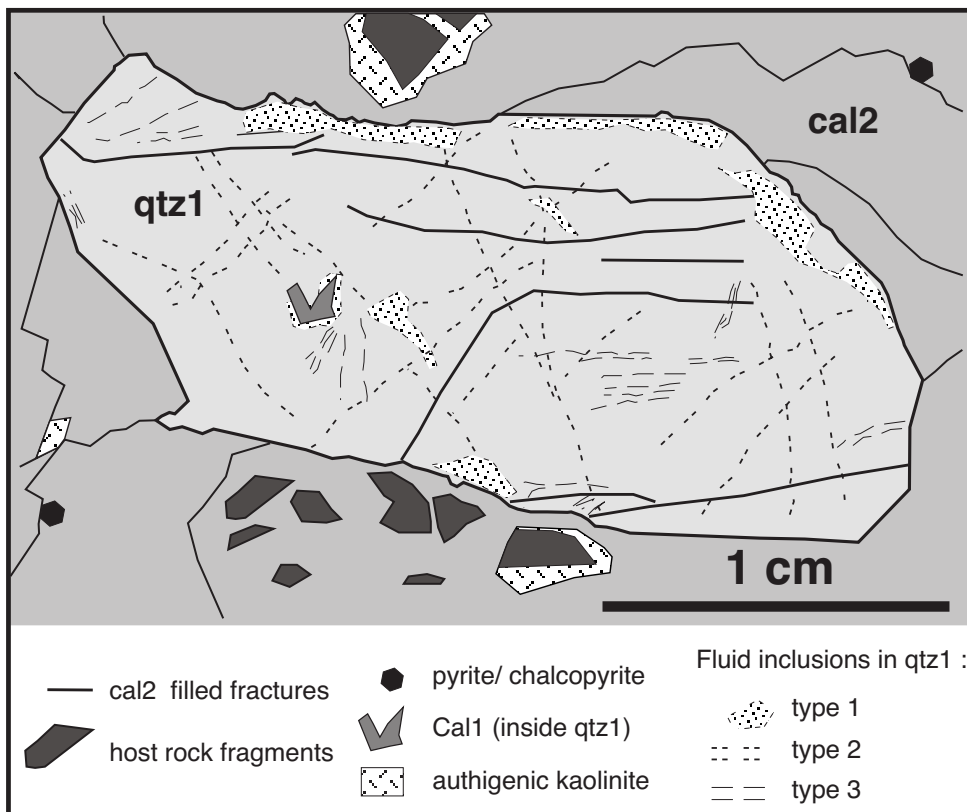
Figure 24. Sketch from part of a thin section showing the textural relations of the vein minerals and the distribution of fluid inclusion assemblages in qtz1.

Both type 1 and 2 inclusion assemblages show a wide range of filling degrees. The fluid compositions also have strong similarities (Table 4). The vapour phase is composed mostly of CH_4, CO_2 (slightly enriched in type 2 inclusions) and traces of C_2H_6, C_3H_8 and C_2H_4 (Fig. 26). Mole fractions mostly > 0.90 for CH_4 were calculated from the Raman spectra (Fig, 27a-b).
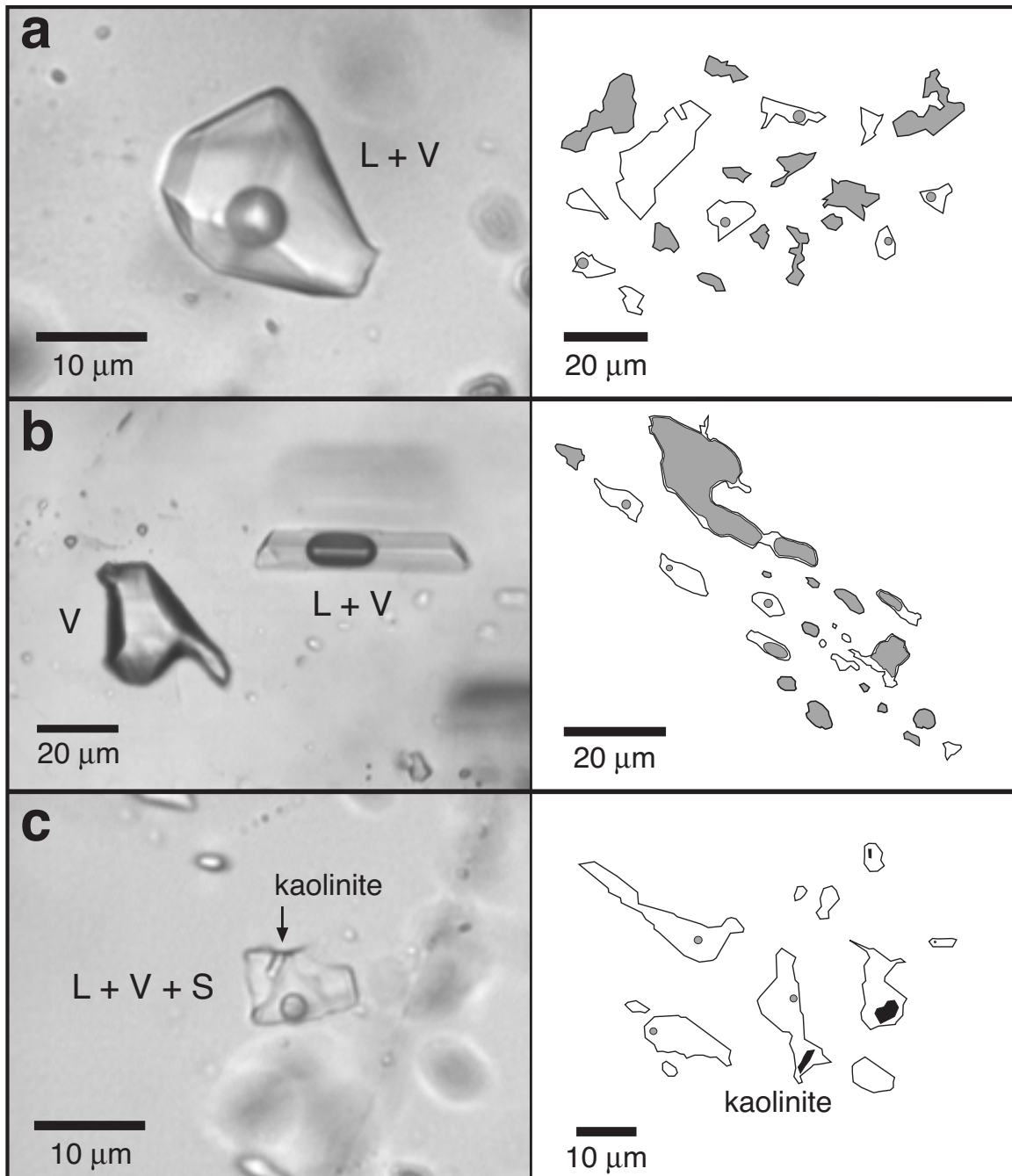
Figure 25. Photomicrographs and assemblage sketches of fluid inclusions, at room temperature, of (a) type 1, (b) type 2 and (c) type 3 in qtz1. Note the variations of aqueous and vapour phases content in type 1 and 2 assemblages, indicative of heterogeneous trapping.
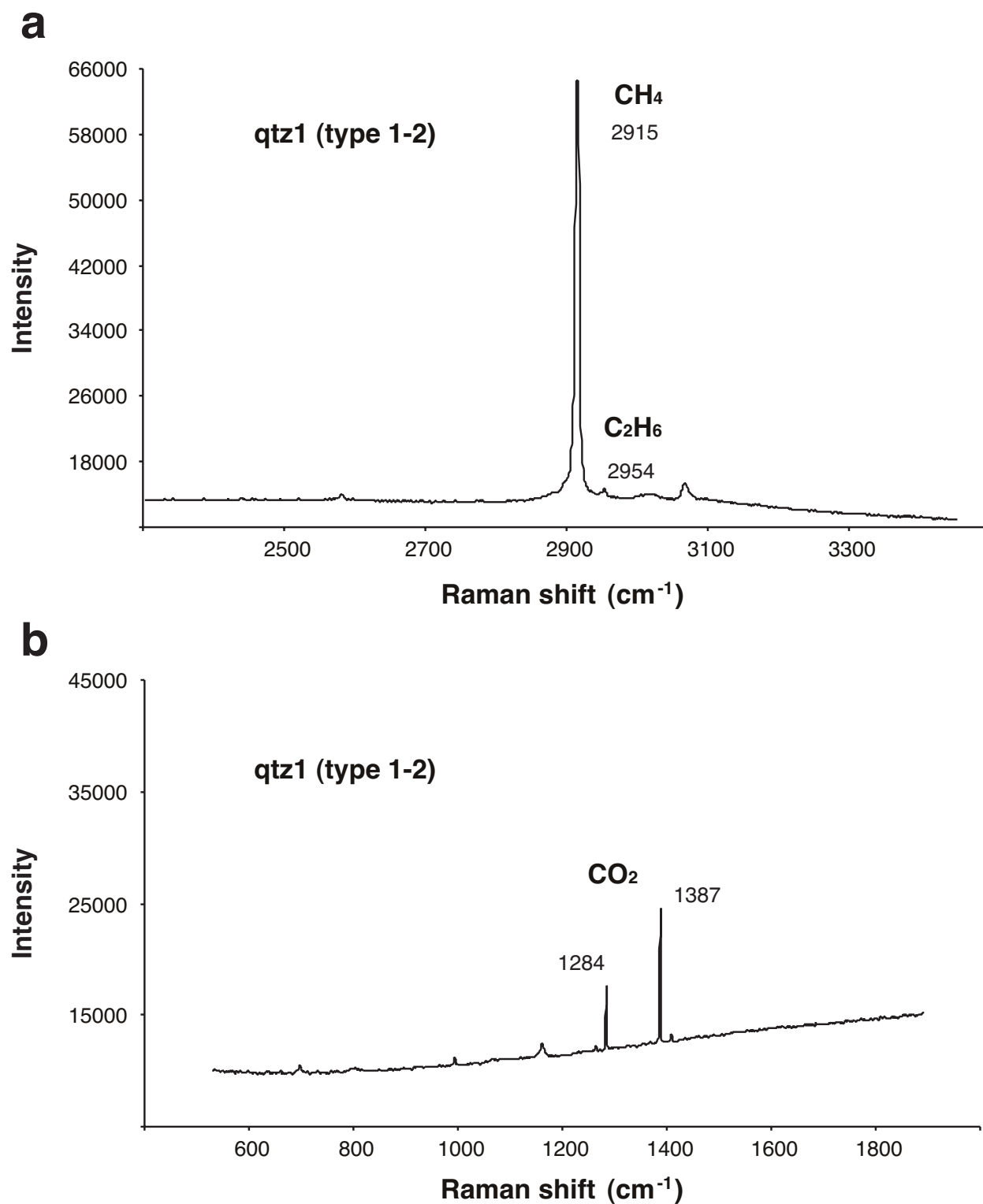
Figure 26. Main Raman peaks of the gas species present in the vapour phase of type 1 and 2 inclusions in qtz1: (a) CH_4 (v_1) and C_2H_6, (b) CO_2. Inclusion 42/2-1.
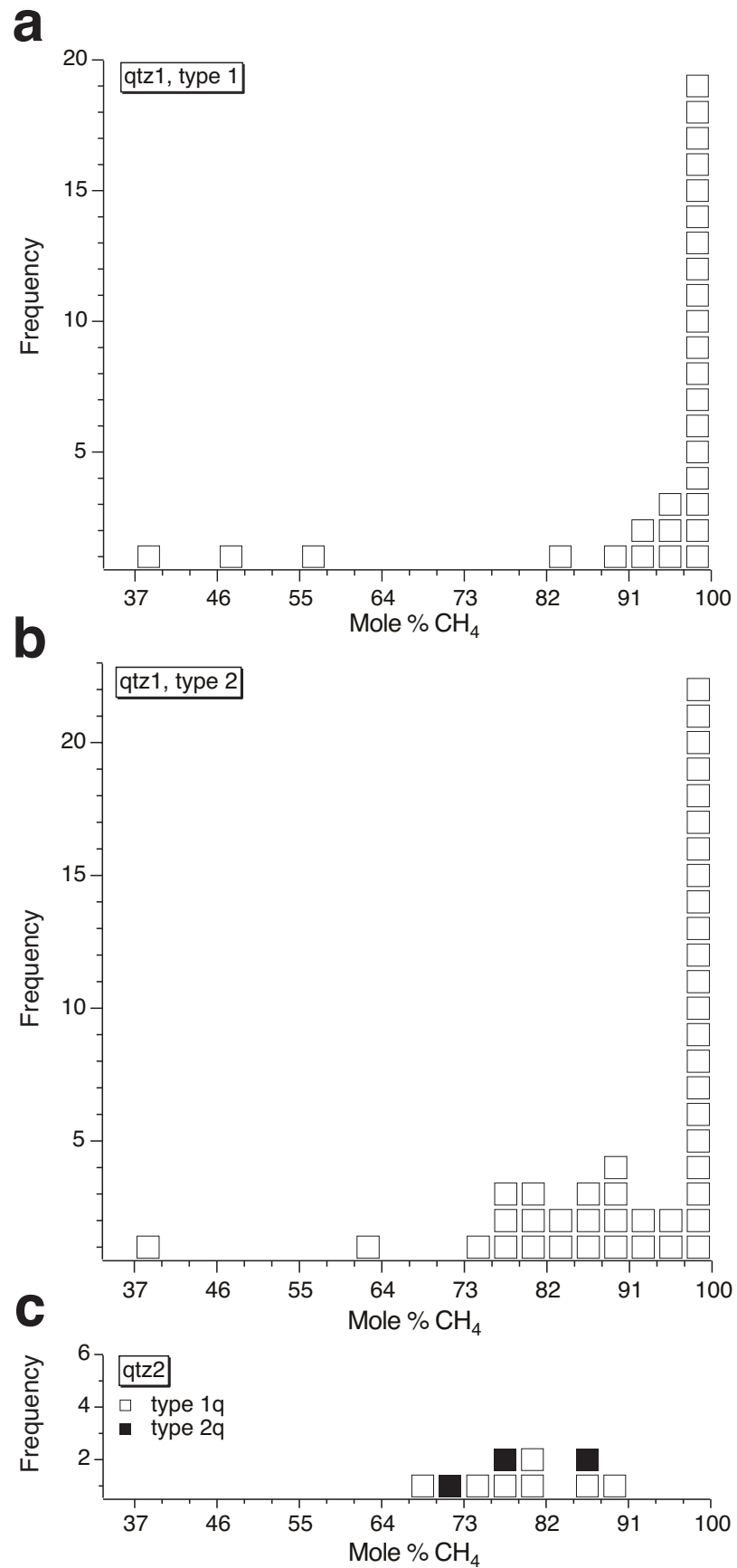
Figure 27. Histograms illustrating the composition of the CH_4 dominated vapour phase, expressed as mol %, for inclusions in qtz1 (a and b) and qtz2 (c). The drop in mole % CH_4 from type 1 to type 1q and 2q inclusions denotes a progressive increase in CO_2 content.

Documented phase transitions in vapour-rich fluid inclusions during micro-thermometry runs are illustrated in Fig. 28. Two groups are differentiated depending on total homogenisation of the CH_4-CO_2 phase into the vapour (Fig. 28a) or into the liquid state (Fig. 28b); corresponding to types H2 (V) and H2 (L) of van den Kerkhof (1990), respectively. Group (28b) inclusions have lower molar volumes (see Table 5, page 71). Melting temperatures of the CH_4-rich gas mixture from vapour-rich inclusions, between -90 and -80°C (Fig. 29), also indicate CO_2 mole fractions up to 0.10. The shift from type 1 to type 2 inclusions towards higher melting and homogenisation temperatures of the CH_4-CO_2 gas mixture indicates progressive enrichment in CO_2 and an increase in molar volume, respectively (see Table 5). In many gas-rich inclusions, thin water films wetting the inclusion walls were detected by Raman microspectrometry.

Figure 28. Documented phase transitions during micro-thermometric cooling-heating sequence in vapour-rich fluid inclusions of type 1 and 2 in qtz1. The temperature represented for each transition corresponds to the final disappearance of the respective phase. See explanations in the text.

Phase transitions in aqueous-rich inclusions are reported in Fig. 30. Differences between inclusions arise in the melting of the CH_4-clathrate phase after (Fig. 30a) or before (Fig. 30b) ice melting. For inclusions belonging to the second group, the CH_4-rich carbonic vapour phase has a very low molar volume and internal pressure.
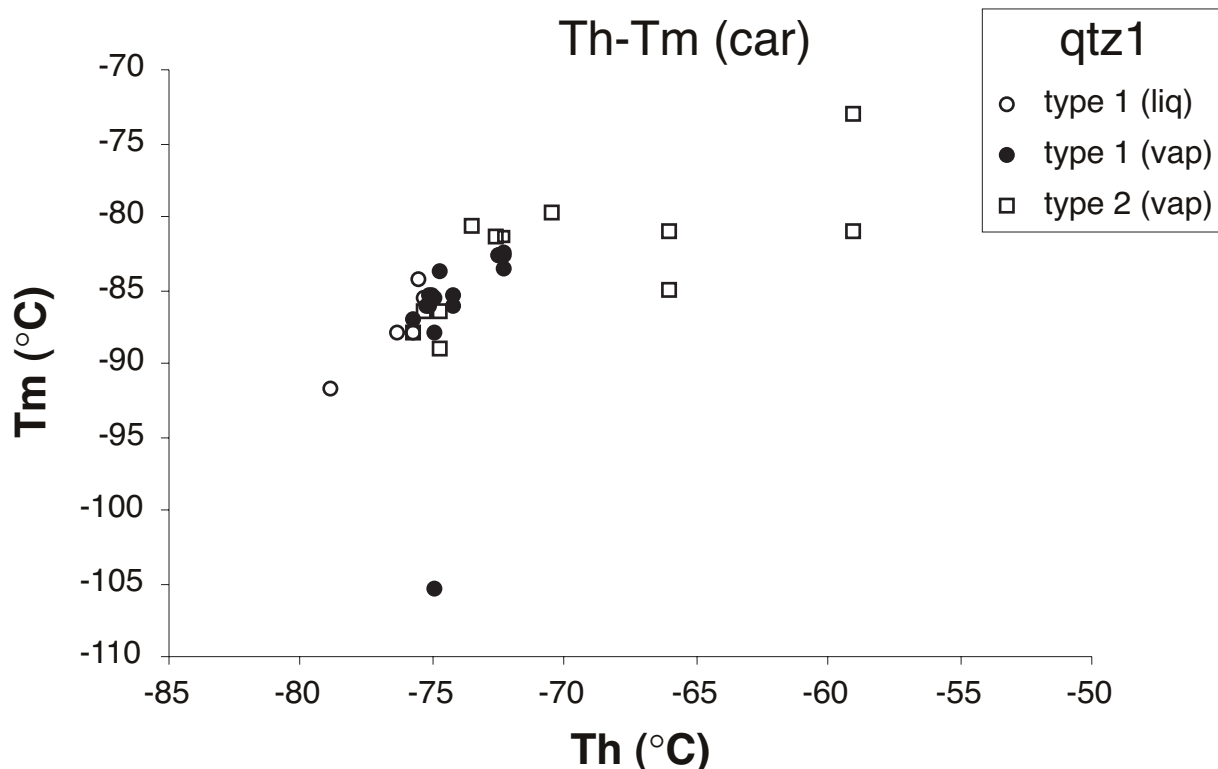
Figure 29. Plot of melting (Tm) versus homogenisation-temperatures (Th) of the vapour phase for vapour-rich inclusions in qtz1. car = carbonic CH_4-CO_2 mixture; vap = homogenisation into the vapour phase; liq = homogenisation into the liquid phase.

The aqueous inclusions have ice melting temperatures above -4 °C (Fig. 31a) and the estimated salinity varies between 2.9 and 5.9 eq.wt% NaCl (Table 5). Th's range from 73 to 110 °C for type 1, whereas they are slightly higher for type 2 inclusions, from 87 up to 129 °C (Fig. 31b). Locally, entrapped fragments of Mg-rich calcite are identified by Raman spectroscopy (Fig. 32a). The application of criteria given by Roedder (1984, p. 53-58) suggest that these solids are accidental inclusions rather than daughter minerals. Many inclusions of both type 1 and 2 assemblages show textural evidence for re-equilibration, analysed in detail in chapter 7.

Type 3 fluid inclusions are secondary in origin and distributed as small limited trails adjacent to microcracks within the crystals. They crosscut type 1 and 2 inclusion assemblages (Fig. 24). The inclusions are smaller in size (generally ≤ 20 µm) and their shapes tend to be highly irregular and generally flat, especially the larger inclusions (Fig. 25c). The vapour phase, which is seldom > 5 vol.% and not present in all inclusions, consists mostly of pure CH_4 (Fig. 33a), occasionally with minor amounts of CO_2. The aqueous phase contains NaCl in solution, with hydrohalite been detected by Raman at low temperatures (Fig. 33b), and at least one additional salt type. Fig. 34 (page 62) documents phase changes in these inclusions during microthermometry runs. Two types of melting behaviour are distinguished where ice is the first or the last phase to melt (Fig. 34a, b; respectively). This is interpreted to reflect differences in the ratio and ammount of

salt types in solution, with NaCl predominating on the first group of inclusions (Fig. 34a and Table 5). Ice total melting temperatures are generally below -25°C (Fig. 31a). Hypothetical compositions can be obtained by assuming a quaternary system of H_2O-CH_4-$CaCl_2$-NaCl. Total salinities, i.e. the summation of NaCl and $CaCl_2$, vary between 26.6 and 28.9 eq.wt%, where the weight ratio NaCl/$CaCl_2$ varies between 0.06 and 0.60 (Table 5). Total homogenisation temperatures, always into the liquid phase, range from 40° up to 98°C (Fig. 31c). Commonly these inclusions contain entrapped fragments of kaolinite, identified by Raman (Fig. 35a, page 63).

Figure 30. Documented phase transitions during microthermometric cooling-heating sequence in aqueous-rich fluid inclusions of type 1 and 2 in qtz1. The temperature represented for each transition corresponds to the final disappearance of the respective phase. See explanations in the text.

a

qtz1 final ice melting

type 1/2 (44)
type 3 (38)

Frequency (82)

Tm ice (°C)

b

qtz1 type1/2 Th (liquid)

Frequency (15)

Th (°C)

c

qtz1 type 3 Th (liquid)

Frequency (56)

sample 26
sample 31
sample 42

Th (°C)

Figure 31. Frequency-phase transition temperature histograms of aqueous-rich fluid inclusions in qtz1 measured by micro-thermometry. Data are grouped according to inclusion type: (a) final ice melting temperature, (b) homogenisation temperature (always into the liquid phase) of type 1 and 2 inclusions, (c) homogenisation temperatures (always into the liquid phase) of type 3 inclusions from the different analysed samples.
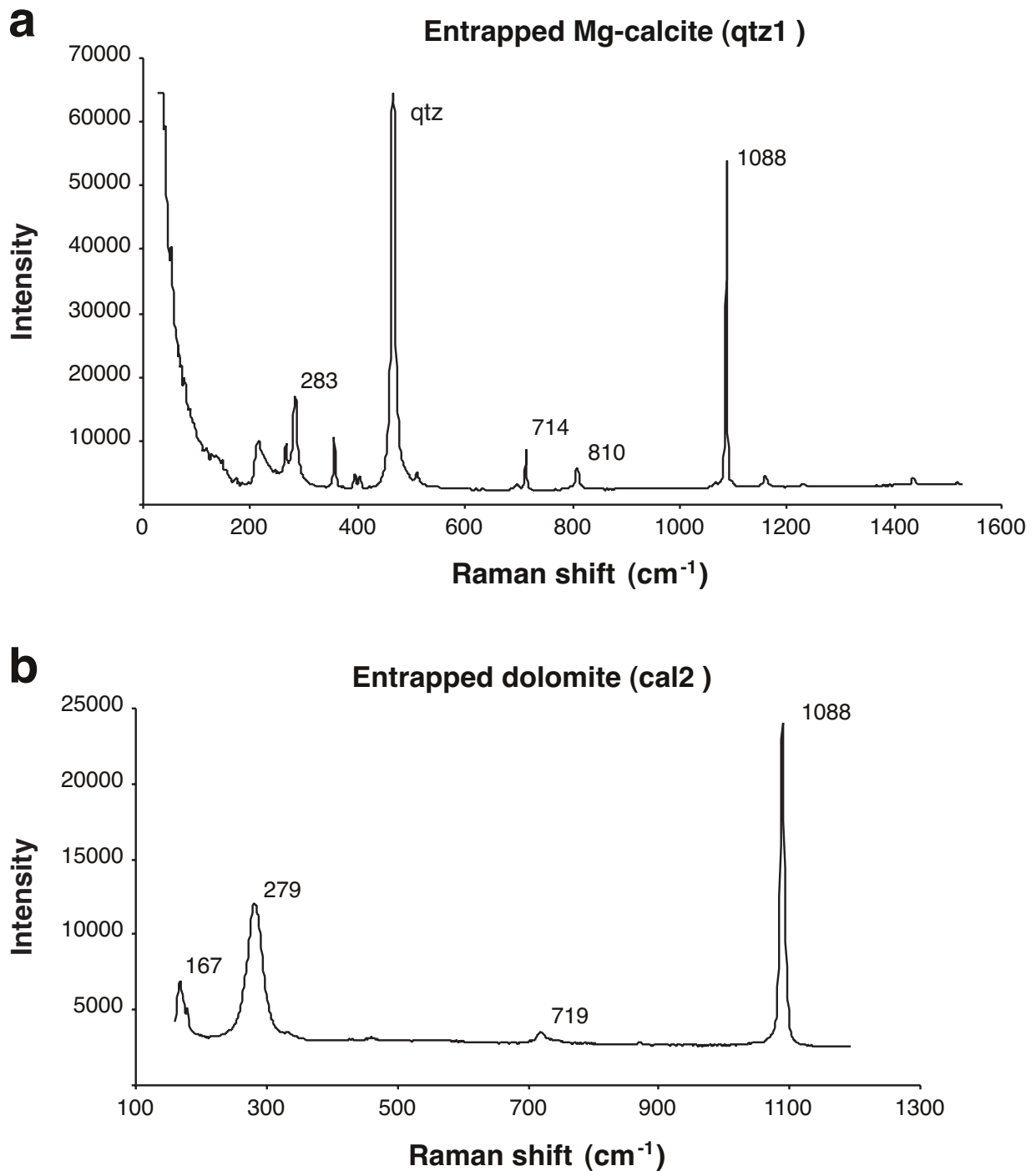
Figure 32. Main Raman peaks of mineral phases entrapped within fluid inclusions of the vein quartz and calcite. (a) Mg-calcite within type 2 inclusions, qtz1. Sample 28, inclusion 28/1-8. (b) Dolomite within 1c inclusions, cal2. Sample 6, inclusion 6-cal2-8.

a

b
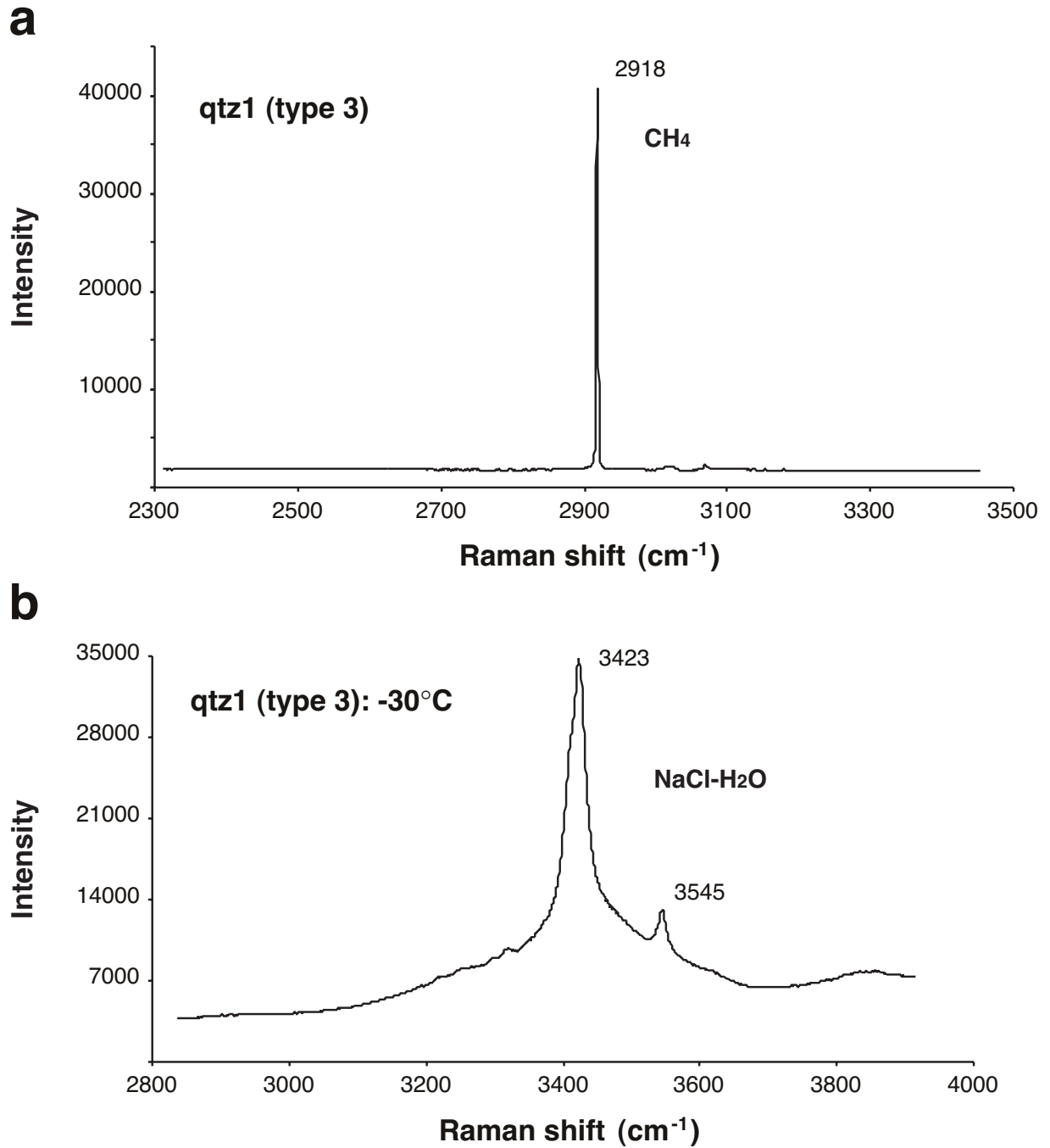
Figure 33. (a) Main Raman peak of CH_4 (ν_1), the principal gas species identified in the vapour phase of type 3 inclusions in qtz1. Inclusion 31/3-16. (b) Raman bands of hydrohalite (NaCl-H_2O) detected during microthermometric cooling of the aqueous solution in the same inclusion type (-30°C). Inclusion 26/3-22. Peak identification after Dubessy et al. (1982).

Figure 34. Documented phase transitions during microthermometric cooling-heating sequence of fluid inclusions of type 3 in qtz1. The temperature represented for each transition corresponds to the final disappearance of the respective phase. hh = hydrohalite ($NaCl-2H_2O$); hyd = unidentified salt hydrate, assumed as antarcticite ($CaCl_2-4H_2O$). See explanations in the text.
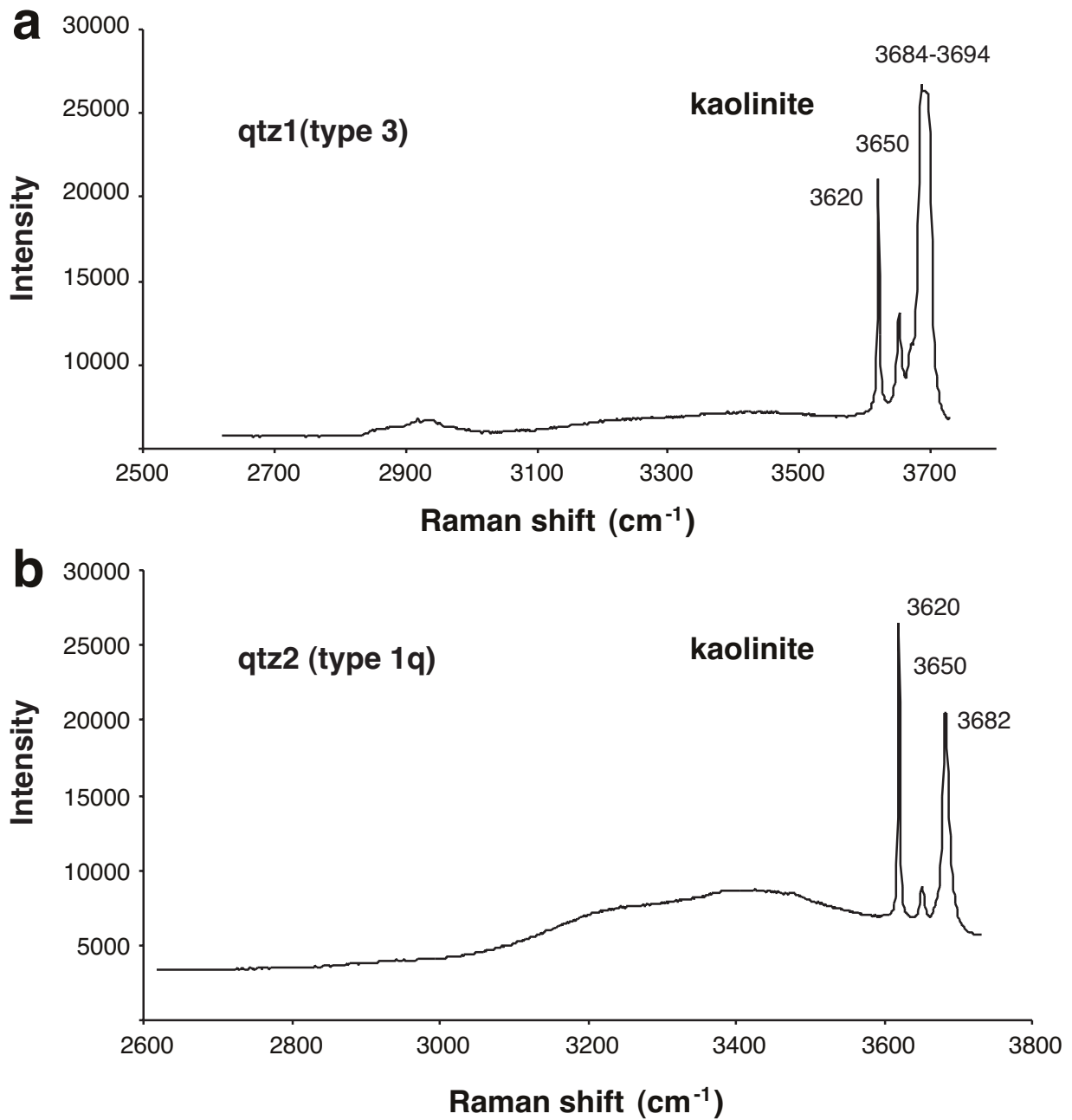
Figure 35. Main Raman peaks of the OH⁻ band of kaolinite entrapped in fluid inclusions of (a) type 3 in qtz1 (inclusion 31/3-4) and (b) type 1q in qtz2 (inclusion 51/1q-5). Peak identification after Johnston et al. (1985).

5.1.3. Blocky calcite (cal2) inclusions

Inclusions in many samples with cal2 were difficult to study due to the strong deformation and twinning experienced by most of the crystals, especially those in veins associated with faults. The least deformed crystals typically have a core, in which the trapped dolomite fragments are concentrated, and an outer rim of clear calcite (Fig. 36). Two inclusion types are distinguishable, whereby the re-equilibration features present in type 1 and 2 inclusions in qtz1 are clearly absent.
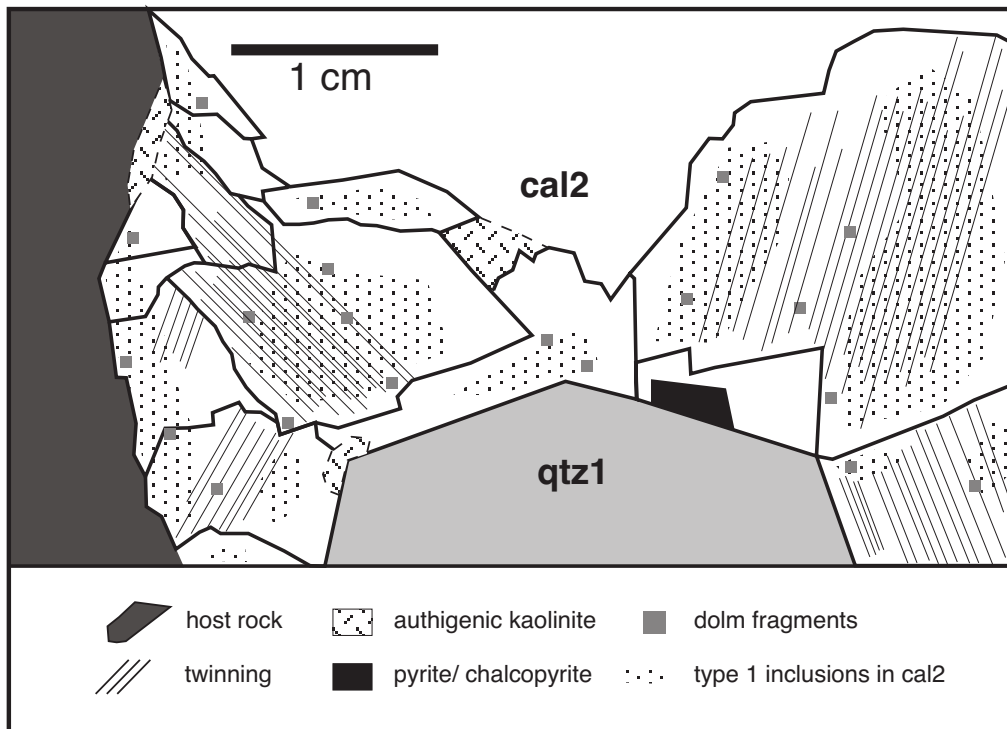
Figure 36. Sketch from part of a thin section showing the textural relations of the vein minerals and the distribution of fluid inclusion assemblages in cal2.
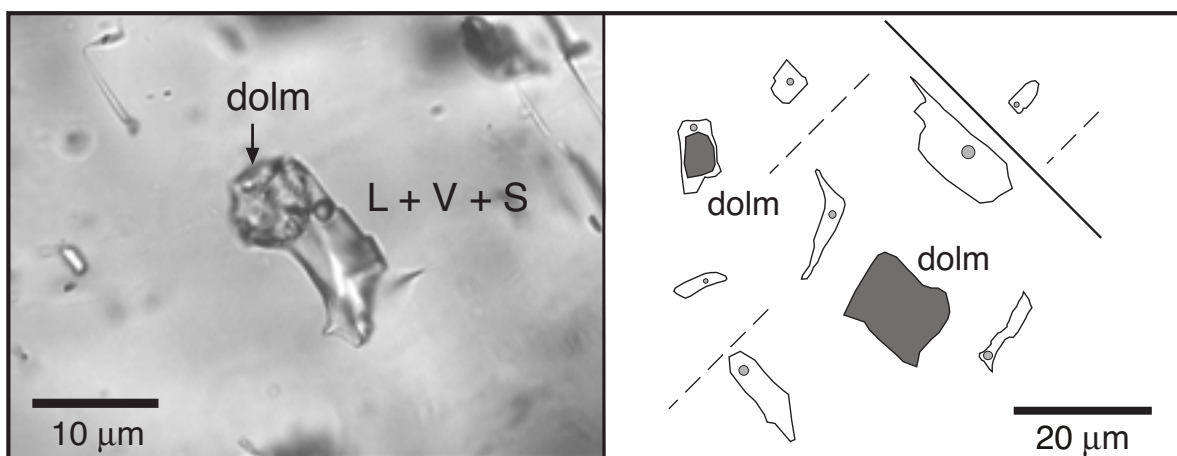
Figure 37. Photomicrograph and assemblage-sketch of type 1c inclusions in cal2 at room temperature. Entrapped dolomite fragments are observed in several aqueous-rich inclusions, providing evidence for the dedolomitisation produced during calcite precipitation. Lines in sketch represent twinning planes.
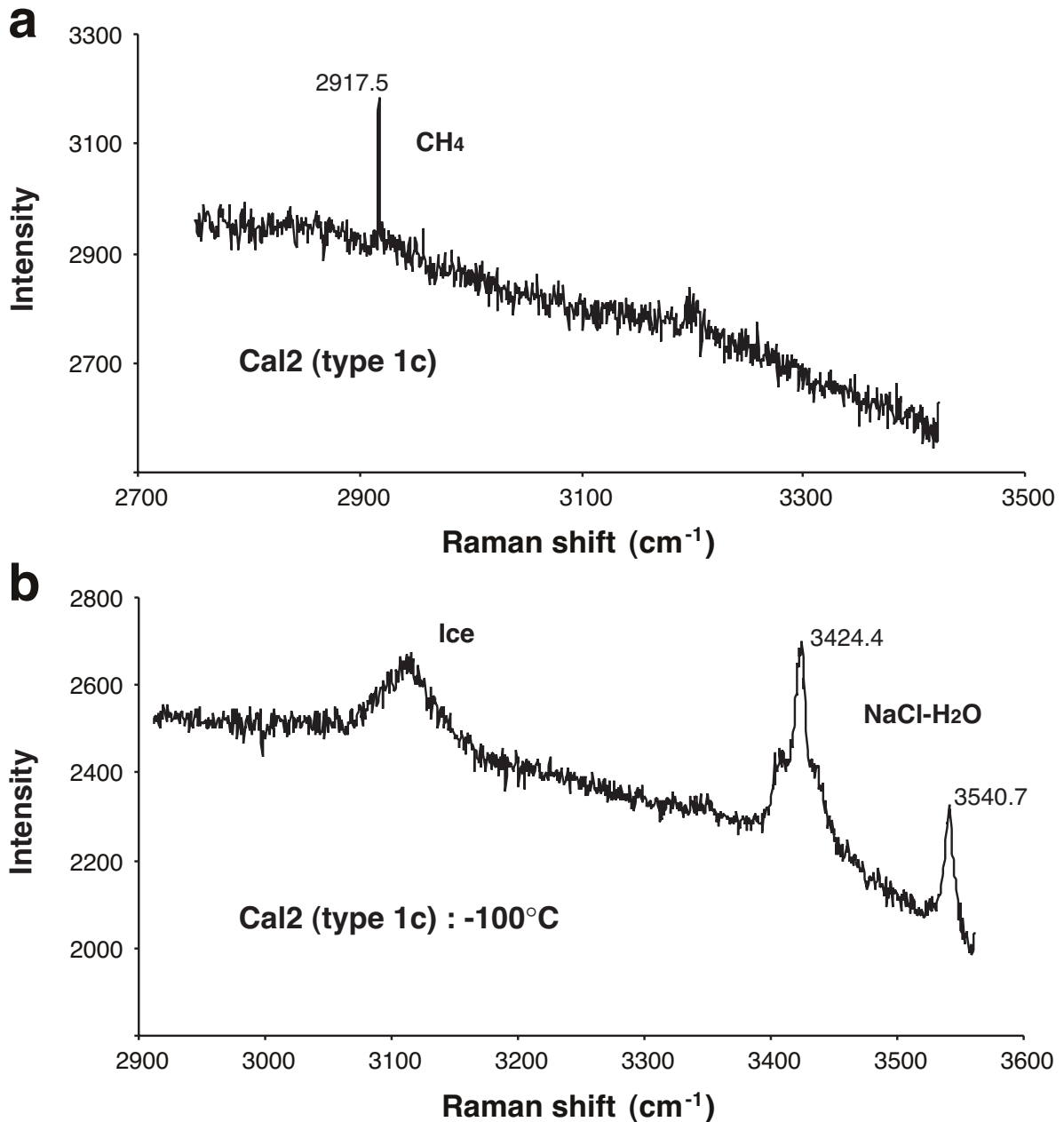
Figure 38. (a) Main Raman peak of CH_4, the only gas species identified in the vapour phase of type 1c inclusions in cal2. (b) Raman bands of hydrohalite ($NaCl-2H_2O$) detected during microthermometric cooling of the aqueous solution in the same inclusions ($-100°C$). Inclusion 26-cal2-22. Peak identification after Dubessy et al. (1982).

Type 1c inclusions occur mostly as clusters within the core of crystals and are primary in origin (Fig. 37). They have rounded walls, variable shapes and range from 5 up to 20 μm in size (locally larger). Inclusions are aqueous-rich, many with a CH_4 vapour bubble that never exceeds 10 % of the inclusion volume (Fig. 38a). The aqueous phase in type 1c inclusions contains a complex salt mixture (NaCl-rich) as reflected by the variable microthermometry phase transitions illustrated in Fig 39. Two types of melting behaviour are differentiated: ice melting after hydrohalite (Fig. 39a), with a second salt hydrate present, and ice melting before hydrohalite (Fig. 39b). As for type 3 inclusions in qtz1 this reflects

differences in the ratio of salt types in solution, NaCl predominating on the first group of inclusions (see Table 5). Melting temperatures of ice lie between -36° and -5°C (Fig. 40a). Hydrohalite, Raman identified (Fig. 38b), melts between -27° and -21°C and between -8° to -1°C, whereas other salt hydrates disappear at temperatures > -30°C (Table 4, page 51). For a quaternary system of H_2O-NaCl-$CaCl_2$-CH_4, total salinities, i.e. the summation of NaCl and $CaCl_2$, vary between 20.5 and 31.9 eq.wt% (Table 5, page 71). This range is similar to the salinities of type 3 inclusions in qtz1. The total homogenisation temperatures (always into the liquid phase) lie between 62° and 126°C (Fig. 40b). Some inclusions contain entrapped corroded crystals of dolomite, qualitatively identified by its Raman spectra (Fig. 32b).
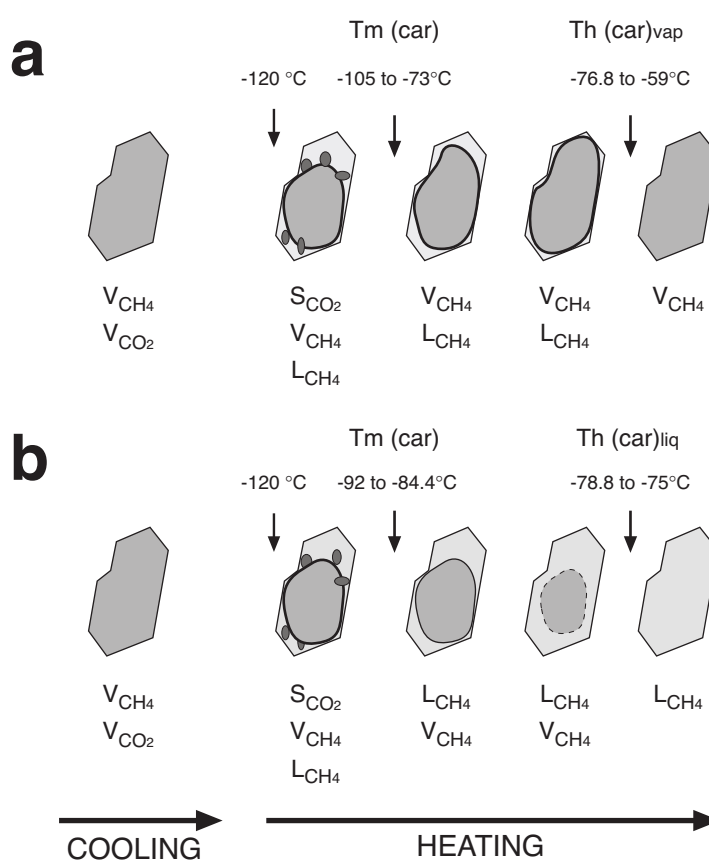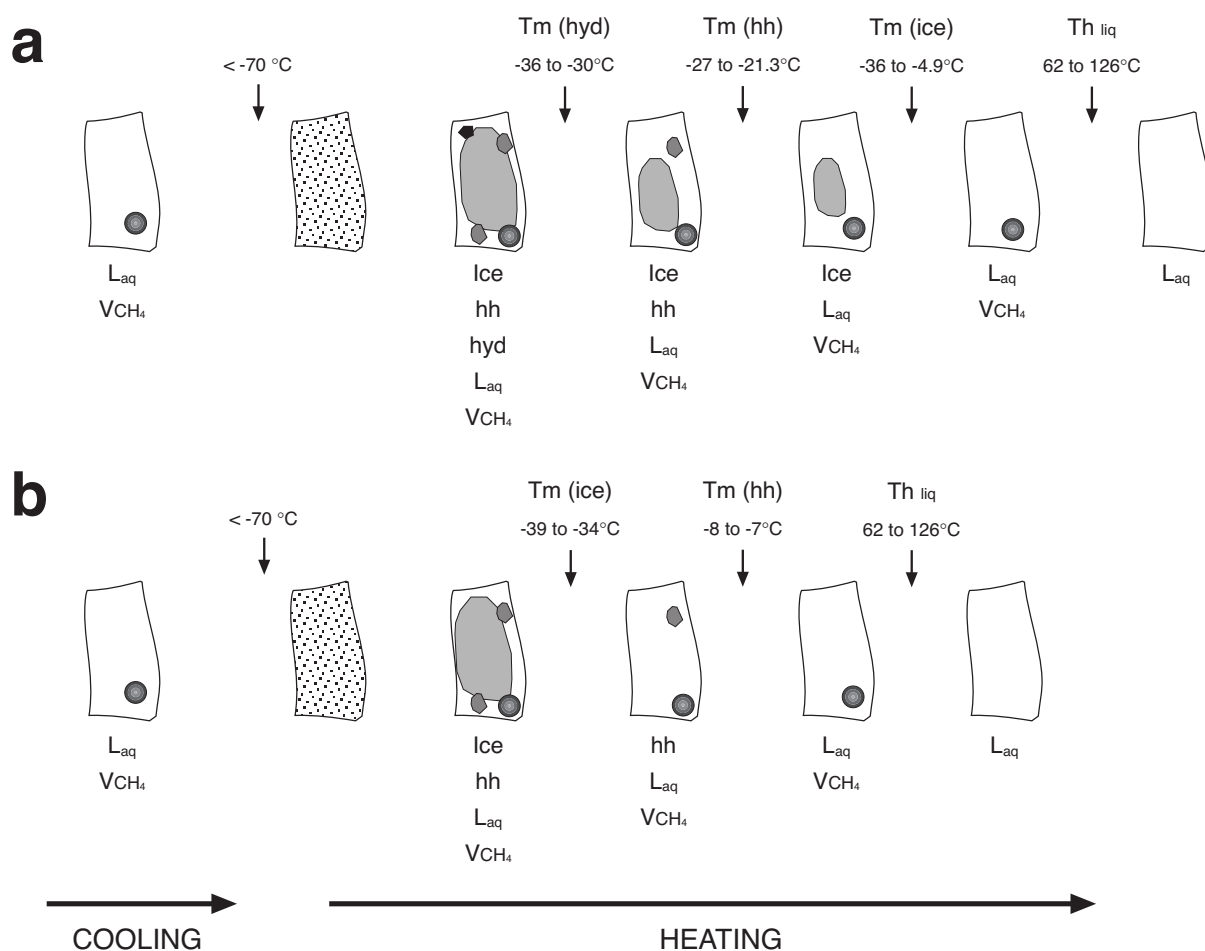

Figure 39. Documented phase transitions during microthermometric cooling-heating sequence of fluid inclusions of type 1c in cal2. The temperature represented for each transition corresponds to the final disappearance of the respective phase. hh = hydrohalite (NaCl-$2H_2O$); hyd = unknown salt hydrate (assumed to be antarcticite).

Type 2c inclusions are flat, variable in size and show sharp/square edges. They form trails of secondary inclusions, which lie close to and parallel twin planes. Inclusions are all liquid, and ice melting temperatures (Fig 40a) in experimentally stretched inclusions indicate that the aqueous phase is composed of almost pure water (up to 2.1 eq.wt%

NaCl). As a vapour phase is lacking, trapping temperatures are considered to be below 50°C (e.g. Goldstein and Reynolds, 1994).
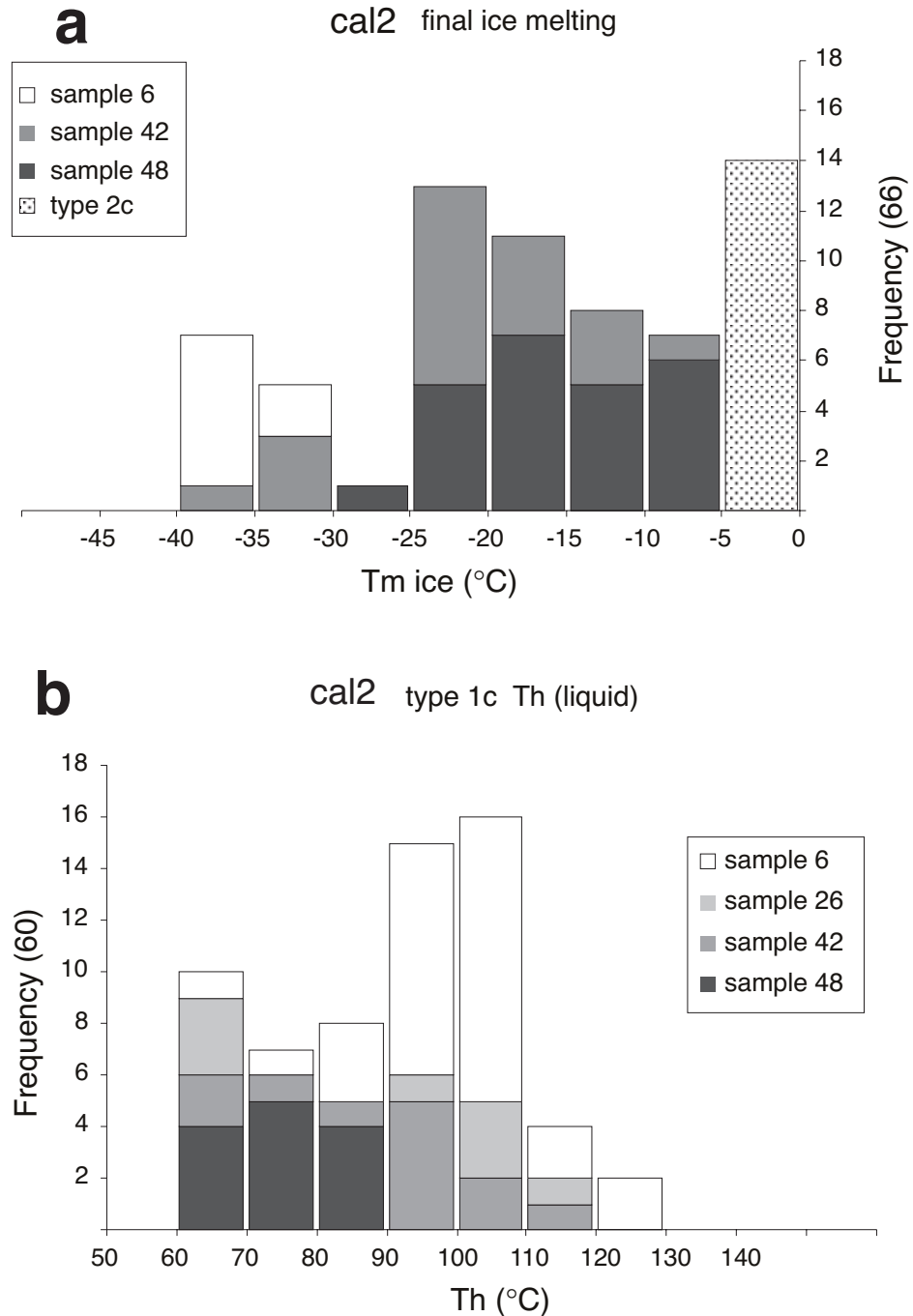
Figure 40. Frequency-phase transition temperature histograms of fluid inclusions in cal2 obtained by microthermometry. Data are grouped according to sample and inclusion type: (a) final ice melting temperature, (b) homogenisation temperatures (always into the liquid phase) of type 1c inclusions.

5.2. FLUID INCLUSIONS IN VEINS FROM THE DIORITES

A typical sample from the quartz mineralisations in the altered dioritic rocks was studied in detail (ign12, locality 12b). A summary of the data obtained can be viewed in Table 4 (page 51) and a complete database of the microthermometry and Raman microspectrometry results is included in the Appendix (Tables A3 to A13). Inclusions in hydrothermal quartz (qtz2) are distributed in several distinct assemblage types (Fig. 41).
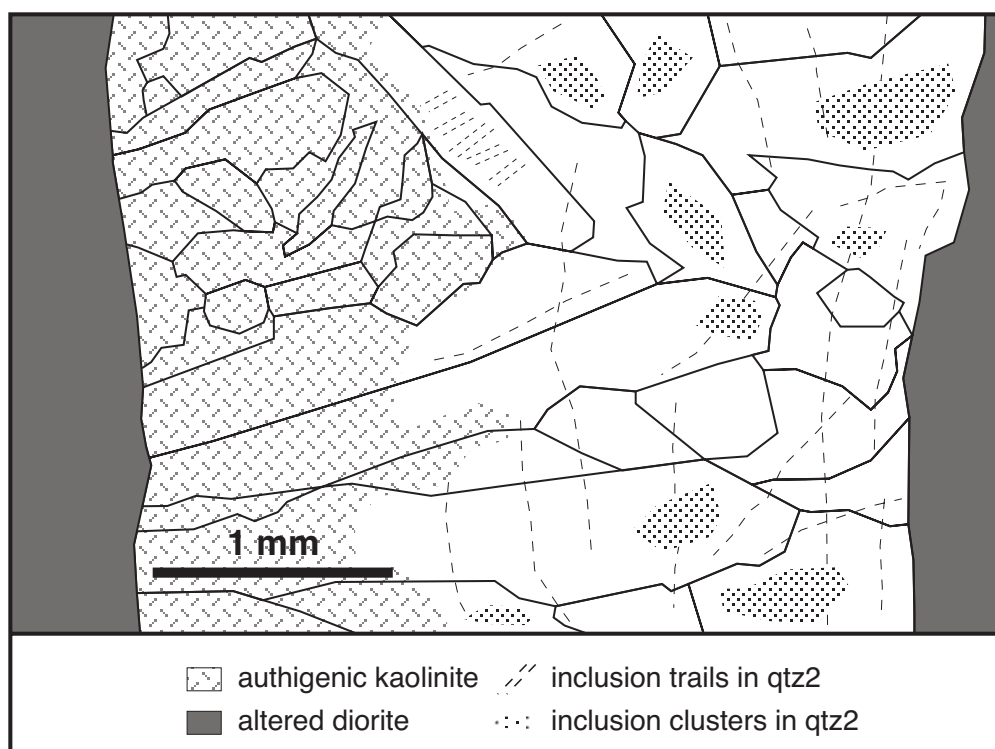
Figure 41. Sketch from part of a thin section showing the textural relations of the vein minerals and the distribution of fluid inclusion assemblages in qtz2.
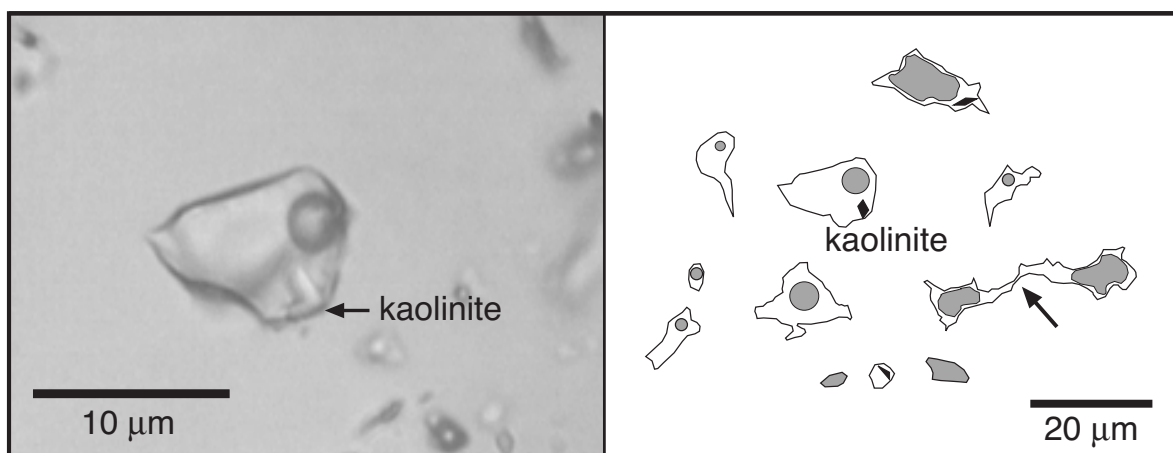
Figure 42. Type 1q inclusions in qtz2 at room temperature. The photo shows one of the numerous inclusions that have entrapped fragments of kaolinite. The sketch of an inclusion cluster provides evidence for heterogeneous trapping of two immiscible fluids and for necking down (see arrow).

The first generation consists of inclusions formed in clusters inside single crystals (type 1q). At least two types of secondary trails crosscut grains, lying at various angles to the vein walls (either perpendicular or oblique). These trails contain inclusions $< 2\mu m$, which are too small to study. Other inclusions occur in the pore filling quartz (type 2q) of the adjacent host rock, and were probably formed contemporaneous with the clusters inside the vein quartz.
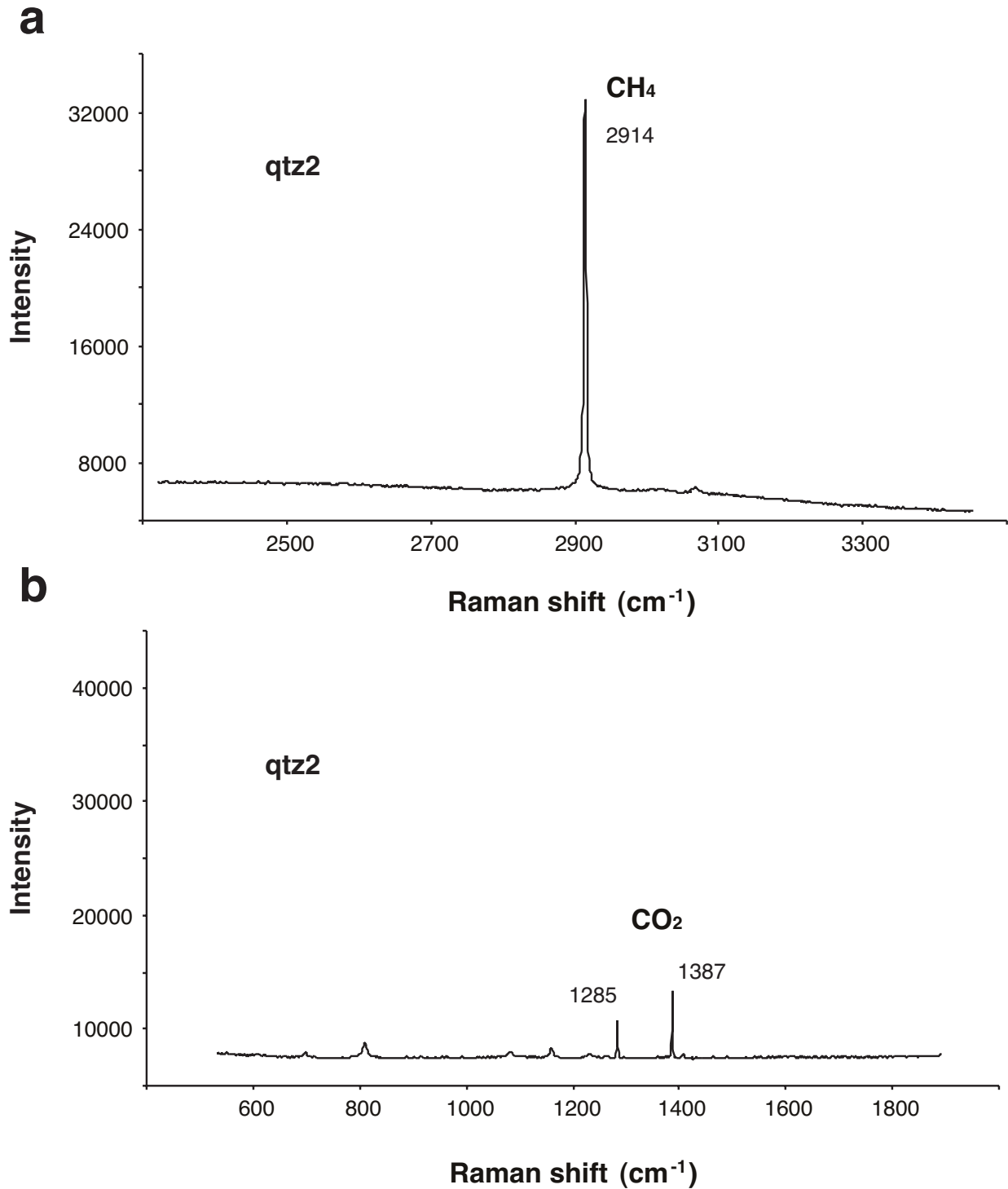
Figure 43. Main Raman peaks of the gas species present in the vapour phase of fluid inclusions in qtz2 : (a) CH_4 (ν_1) and (b) CO_2. Inclusion Ig/2q-6.

Both type 1q and 2q have semi-regular to irregular shapes with rounded walls (Fig. 42), although some are regularly shaped (negative crystal shape). Besides necking down, no other re-equilibration textural features were observed. In all the studied assemblages, inclusions are composed of a liquid and a vapour phase that coexist with highly variable filling degrees, ranging from 0.18 to 0.94 (Table 4). Type 2q inclusions in the pore filling quartz are mainly vapour-rich and have a higher gas content than type 1q. The vapour phase is always CH_4-rich but has a higher CO_2 content (mole fraction between 0.11 and 0.28) than inclusion types 1 and 2 in qtz1 (Figs. 43 and 27c). Documented phase transitions during microthermometry are represented in Fig. 44. Clathrate in type 1q inclusions melts at temperatures < -3°C, so molar volume of the vapour phase is lower in this type than for inclusions of type 2q. Ice melting temperatures are always > -3°C and the calculated salinity of aqueous type 1q and 2q inclusions varies between 0 and 2.5 eq.wt% NaCl (Table 5). Total Th_{liq} for type 1q inclusions ranges between 150 and 296°C. "Accidentally" entrapped kaolinite is commonly found in many inclusions of this type (Fig. 35b).
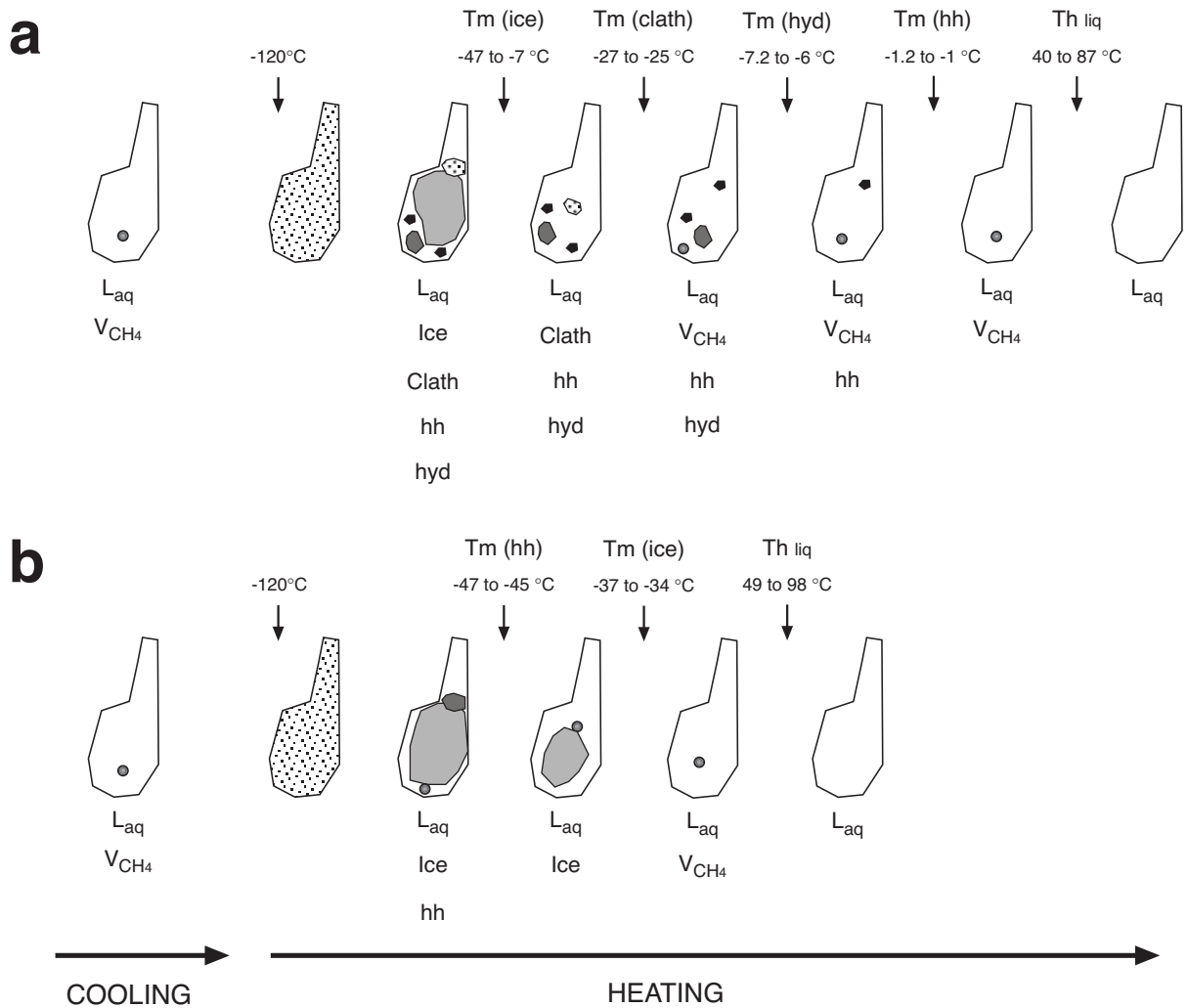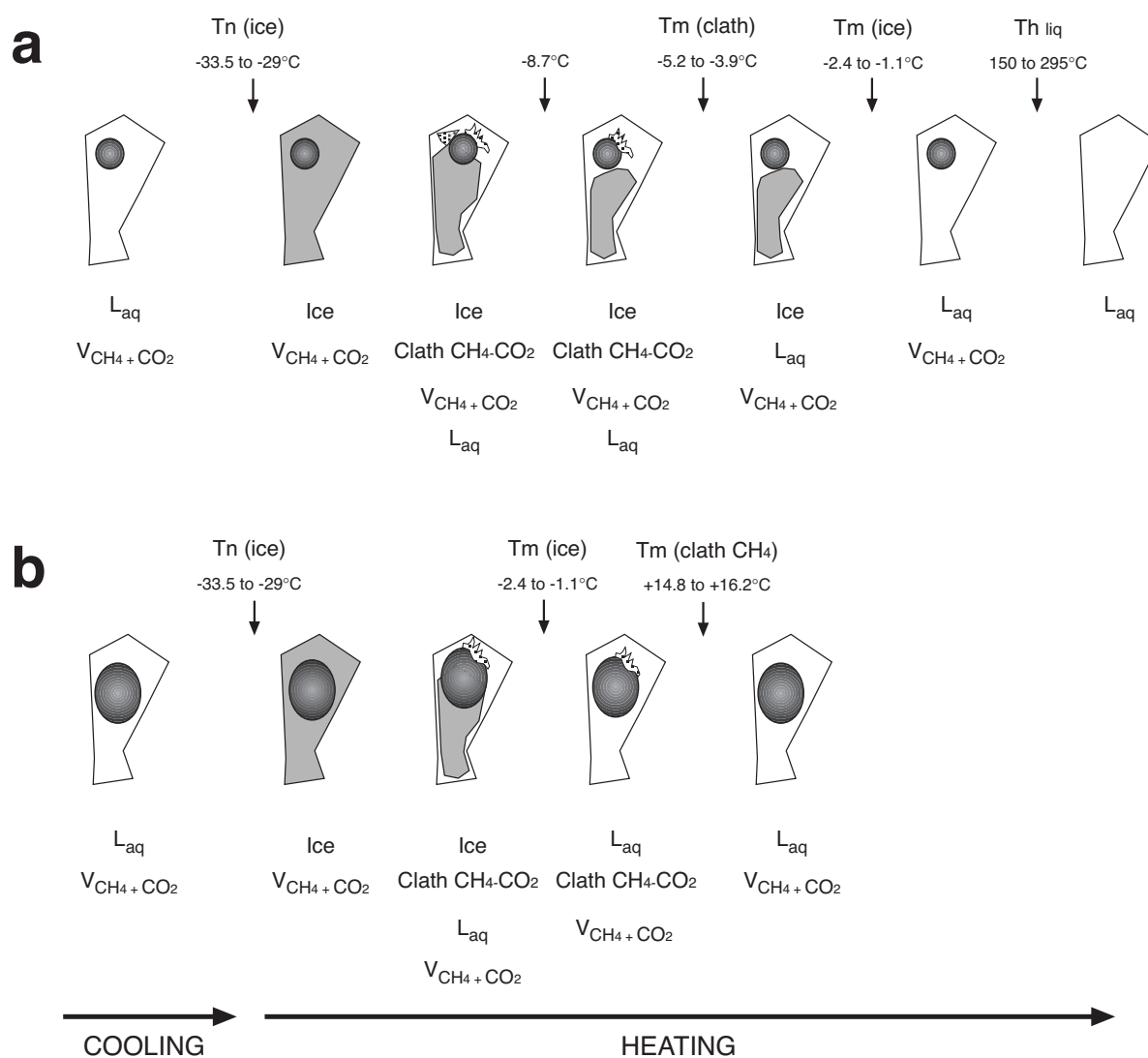

Figure 44. Documented phase transitions during microthermometric cooling-heating sequence of fluid inclusions in qtz2: (a) type 1q, (b) type 2q.

5.3. FLUID SYSTEMS AND TRAPPING CONDITIONS (P-T-V-X)

Using the analytical data on fluid composition obtained from the inclusions, the different fluid systems present during vein formation and their P-T trapping conditions are outlined as follows.

Inclusion Nr.	Mole Fractions						V_m cm³/mol	eq.wt% NaCl	eq.wt% $CaCl_2$
	H_2O	CH_4	CO_2	Na^+	Ca^{2+}	Cl^-			
qtz1 **type 1 (vap)**									
28.1-5	-	0.91	0.09	-	-	-	169.4	-	-
28/1-9[#]	-	0.95	0.05	-	-	-	80.0	-	-
28/1-16[#]	-	0.93	0.07	-	-	-	72.0	-	-
28/1-23[#]	-	0.92	0.08	-	-	-	69.0	-	-
42/1-1	-	0.98	0.02	-	-	-	150.4	-	-
42/1-2	-	0.98	0.02	-	-	-	231.6	-	-
type 2 (aq)									
26/2-36[*]	0.9799	0.0021	-	0.0090	-	0.0090	19.2	2.90	-
26/2-40[*]	0.9461	0.0176	-	0.0181	-	0.0181	33.5	5.86	-
31/2-7	0.9622	0.0048	0.0093	0.0119	-	0.0119	19.8	3.85	-
31/2-8	0.9326	0.0328	0.0172	0.0087	-	0.0087	25.9	2.94	-
type 2 (vap)									
42/2-1	-	0.80	0.20	-	-	-	461.6	-	-
42/2-2	-	0.79	0.21	-	-	-	505.8	-	-
42/2-3	-	0.84	0.16	-	-	-	498.5	-	-
42/2-4[§]	-	0.89 (0.87)	0.11 (0.13)	-	-	-	291.3	-	-
42/2-8[§]	-	0.98 (0.93)	0.02 (0.07)	-	-	-	150.4	-	-
42/2-9	-	0.89	0.11	-	-	-	541.1	-	-
42/2-10	-	0.86	0.14	-	-	-	244.8	-	-
42/2-11[§]	-	0.92 (0.85)	0.08 (0.15)	-	-	-	294.6	-	-
42/2-12[§]	-	0.86 (0.85)	0.14 (0.15)	-	-	-	290.6	-	-
42/2-13[§]	-	0.94 (0.85)	0.06 (0.15)	-	-	-	294.6	-	-
42/2-14[§]	-	0.92 (0.91)	0.08 (0.09)	-	-	-	123.7	-	-
type 3 (aq)									
26/3-21	0.8476	0.0005	-	0.0244	0.0344	0.0931	17.0	8.54	20
26/3-22	0.8476	0.0006	-	0.0383	0.0251	0.0884	17.2	12.78	15.41
26/3-23	0.8378	0.0004	-	0.0541	0.0179	0.0898	17.0	17.32	11.61
26/3-24	0.8445	0.0005	-	0.0446	0.0220	0.0885	17.0	14.62	13.82
42/3-1	0.8529	0.0006	-	0.0053	0.0453	0.0989	17.2	1.99	24.65
42/3-2	0.8487	0.0005	-	0.0046	0.0472	0.0990	16.9	1.73	25.53
42/3-13	0.8466	0.0005	-	0.0047	0.0479	0.1004	16.9	1.76	25.84
cal2 **type 1c**									
6/cal2-3	0.8424	0.0015	-	0.0205	0.0383	0.0972	17.9	7.32	21.91
6/cal2-22	0.8419	0.0013	-	0.0197	0.0391	0.0979	17.8	7.06	22.26
26/cal2-22	0.8447	0.0012	-	0.0358	0.0275	0.0908	17.7	7.32	21.91
48/cal2-1	0.8477	0.0008	-	0.0369	0.0369	0.0886	17.3	12.40	15.83
48/cal2-6	0.8295	0.0006	-	0.0350	0.0332	0.1016	17.1	12.05	19.83
48/cal2-9	0.8646	0.0006	-	0.0661	0.0008	0.0677	17.4	19.89	0.56
48/cal2-18	0.8755	0.0008	-	0.0331	0.0191	0.0713	17.5	10.93	11.87
48/cal2-20	0.8892	0.0007	-	0.0342	0.0138	0.0619	17.5	11.11	8.77
qtz2 **type 1q**									
51/1q-1	0.9793	0.0029	0.0029	0.0074	-	0.0074	22.1	2.41	-
51/1q-2	0.9899	0.0020	0.0027	0.0027	-	0.0027	20.4	0.88	-
51/1q-3	0.9709	0.0125	0.0050	0.0058	-	0.0058	36.1	1.91	-
type 2q									
51/2q-2	0.8191	0.1245	0.0513	0.0025	-	0.0025	34.1	1.00[$]	-
51/2q-4	0.6708	0.2360	0.0890	0.0021	-	0.0021	61.5	1.00[$]	-

Table 5. Calculated composition, bulk molar volume (V_m), eq.wt% NaCl and eq.wt% $CaCl_2$ of individual fluid inclusions in qtz1, cal2 and qtz2. Type 1 vapour-rich inclusions: # = molar volume graphically estimated with Fig.7 in Thiery et al. (1994). Type 2 vapour-rich inclusion: § = adjusted Raman values of mole fractions (in italics) to obtain a solution at the CH_4-CO_2 solvus according to Thiery et al. (1994). * = pure CH_4 vapour bubble is assumed, according to Raman data for most of type 2 inclusions in sample 26. In type 3 fluid inclusions of qtz1 and type 1 in cal2, V_m were calculated assuming a low density of the CH_4-rich vapour bubble, arbitrarily set to 1000 cm³mol⁻¹. Type 2q (qtz2) inclusions: $ = salinity is assumed to be 1.0 eq.wt% NaCl, which is an average value.

5.3.1. Primary H_2O-CH_4-CO_2-NaCl system in vein quartz (qtz1)

The H_2O-CH_4-CO_2 system (with minor amounts of NaCl), found in the primary type 1 and type 2 inclusions of qtz1, exhibits a large field of "liquid + vapour" immiscibility in P-T-X space. Experimental data on the fractionation components of the solvus show that the liquid compositions are H_2O-rich, whereas the vapour compositions are CH_4-CO_2 rich (Olds et al., 1942; Welsch, 1973; Price, 1979). Complete miscibility (i.e. one-phase state) is attained only at temperatures above 350 °C for pure binary system H_2O-CH_4, and above 270°C for H_2O- CO_2 (Fig. 45). NaCl is fractionated essentially into the H_2O-rich phase, so progressive addition of NaCl to mixtures has the effect of reducing aqueous solubility of CH_4 and expanding the field of immiscibility.

Aqueous-rich inclusions

No salt hydrates where observed during microthermometry and the salinity of the water-phase is low, so the composition of the aqueous inclusions can be modelled by an H_2O-CH_4-CO_2 system without salts, represented in Fig. 46. At the lowest temperature reached during microthermometry (-190°C), the inclusions consist of CH_4-CO_2-clathrate + CH_4-CO_2 vapour + ice. Upon progressive heating ice starts to melt at a point **(a)** above -30°C. Afterwards the inclusions follow two different paths along the equilibrium curve of coexisting clathrate + ice + water + vapour. In the first path, represented by the black stripped line, ice progressively melts until it finally disappears (crossing the stability field) and clathrate continues to melt with further heating until it in turn dissociates to water + vapour at point **(b)** (see Fig. 30a). Along the second path, not marked in Fig. 46, clathrate dissociates completely in the presence of ice, which finally disappears at higher temperatures (see Fig. 30b). Thereafter, heating drives the two-phase inclusions along the indicated isochore. The vapour bubble slowly condenses and eventually disappears at point **(c)**, Th, leaving the inclusions filled with liquid. Bulk fluid densities between 19.2 to 33.5 cm³mol⁻¹ were calculated for type 2 aqueous inclusions (Table 5).

Vapour-rich inclusions

As the solubility of quartz in water is very low at the recorded formation temperatures (Th), small amounts of water should be present in order to explain the entrapment of vapour-rich inclusions via dissolution-reprecipitation of the host quartz. Raman analyses have confirmed that H_2O is present as a separate phase in these inclusions, usually as a thin film surrounding the vapour phase and wetting the inclusion walls (see section 5.1.2). Therefore, the phase transition recorded by Th$_{car}$ (Fig. 28) does indeed represent partial homogenisation on a three-phase element, and the total homogenisation transition would occur at much higher, not measured, temperatures.
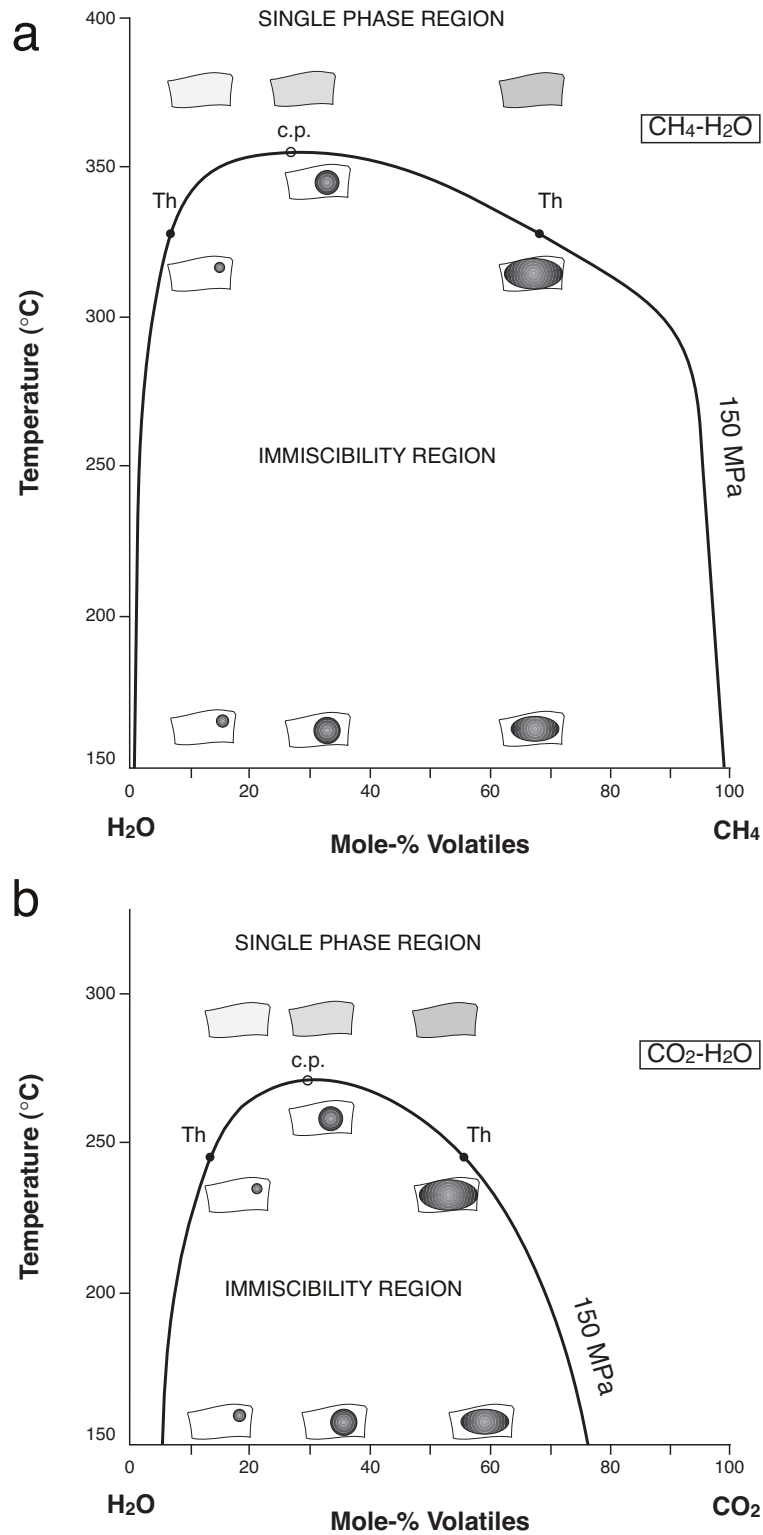
Figure 45. X-T diagrams showing the immiscibility fields, delimited by the solvus curve, for the systems (a) H_2O-CH_4 and (b) H_2O-CO_2 at 150 MPa. Note the different size of the immiscibility region for the two systems. Modified from Shepherd et al. (1985) and Mullis (1987).
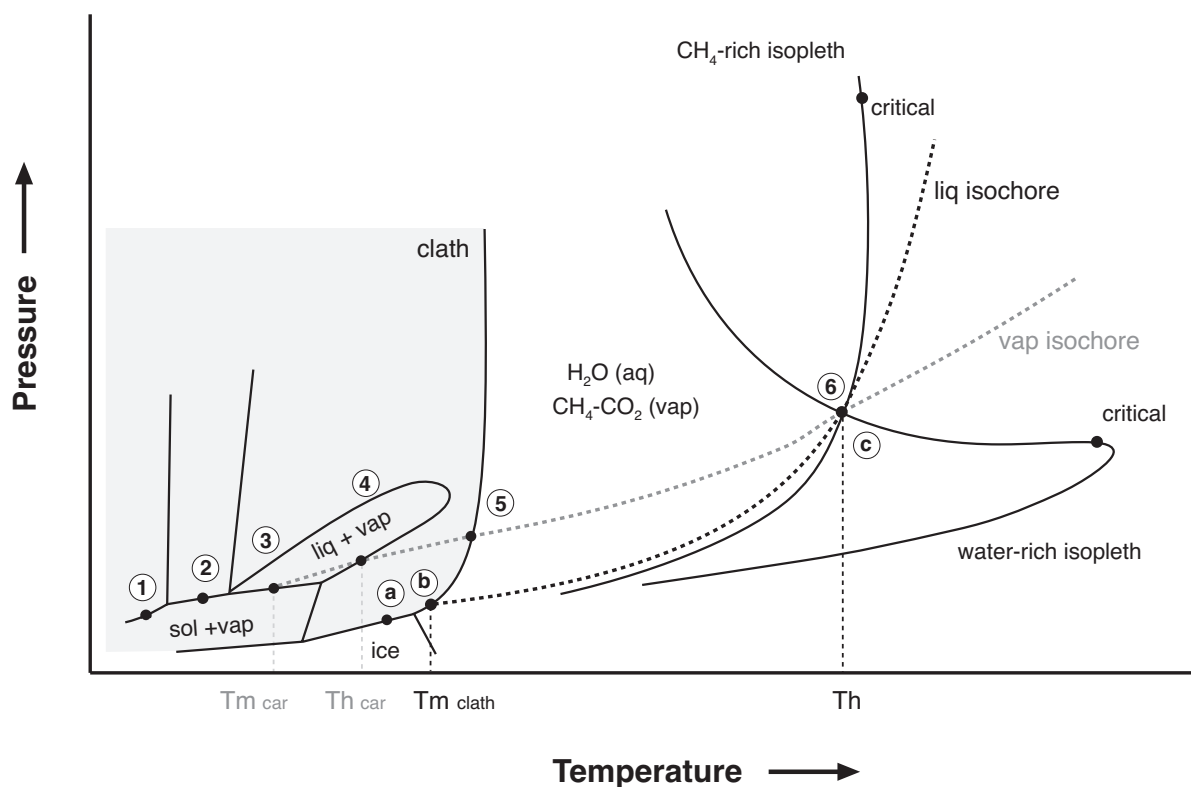
Figure 46. Schematic isoplethic phase diagram of equilibria in the system H_2O-CH_4 ($\pm CO_2$), representing the evolution with increasing temperature of vapour-rich (grey-stripped line) and aqueous-rich (black-stripped line) inclusions in vein quartz (qtz1 and qtz2) of the CMB. Shaded area delimits the stability field of clathrate. Modified from Bakker and Thiery (1994) and Diamond and Marshall (1994).

The evolution with increasing temperature of these inclusions is schematically illustrated in Fig. 46. At the lowest temperatures reached during microthermometry (e.g. point 1 at -120°C), the inclusions consist of solid CO_2 + CH_4 vapour + CH_4 liquid. Solid CH_4 should be stable rather than liquid, according to the phase diagram, but the degree of supercooling required to cause crystallisation is not attainable using the present liquid-nitrogen cooling technique. Consequently, no eutectic melting is seen upon heating the inclusions above point 1. Tiny amounts of CH_4-CO_2-clathrate should also be present, but none were observed. The bulk density of the methane fluid inclusions varies within individual samples, and hence the order of phase transitions observed during progressive heating also varies (Fig. 28). CO_2 melting is always the first phase transition observed upon heating inclusions (Tm_{car} at point 3 on the 3-phase element), and CH_4 liquid + vapour coexist until one of both phases disappears at point 4 (Th_{car}). In low-density inclusions the liquid phase evaporates on the bubble curve (Fig. 28a), meanwhile in dense inclusions it is the vapour phase that condenses completely (Fig. 28b). The two sequences of phase transitions observable upon heating the methane inclusions are thus seen to reflect a continuum from lower to higher densities of the CH_4-CO_2 phase. Thereafter, heating drives such inclusions through the vapour- or the liquid- CH_4-CO_2 + clathrate field, respectively, along the marked isochore (light grey line in Fig. 46). In principle, further heating should dissociate

clathrate to a discrete water phase plus CH_4-CO_2 liquid/vapour (e.g. Tm_{clath} at point 5). Similarly, final homogenisation of the inclusions via dissolution of the water in the volatile vapour or liquid should occur at higher temperature along the isochores (e.g. Th at point 6). In practice, however, neither Tm_{clath} nor Th transitions have been observed in the methane-rich inclusions from the CMB vein quartz.

Based on the Raman analyses and the above considerations on H_2O content, it is assumed that the V-X properties of all the analysed vapour-rich inclusions of type 1 and 2 in qtz1 can be modelled to a first approximation by binary CH_4-CO_2 mixtures. With the reduced thermodynamic variance of this system, the Tm_{CO2} (Tm_{car}) and Th_{CH4} (Th_{car}) measurements permit both the composition and molar volume of the inclusions to be calculated (Table 5). Molar volumes of the vapour-rich fluid range from 69 to 231.59 cm^3mol^{-1} for type 1 inclusions, and from 123.68 to 541.09 cm^3mol^{-1} for type 2 inclusions (Table 5, page 71).

Fluid immiscibility and pressure calculations

The petrographic evidence for partial contemporaneity of aqueous and methane fluid inclusions implies that two immiscible, conjugate fluids existed and were heterogeneously trapped in the veins of the clastic Stephanian rocks during qtz1 precipitation. The immiscible fluids comprised a low salinity aqueous solution and a CH_4-rich vapour phase. Mechanical mixtures of the coexisting liquid and vapour phases in the veins result in fluid inclusion assemblages with variable bulk compositions and densities, which are intermediate with respect to the pure end members. Such mixtures exhibit a range of homogenisation pressures and temperatures that are always higher than the end-member inclusions (Fig. 45). The fact that many coeval intermediate inclusion assemblages are present is strong evidence in support of heterogeneously trapped immiscible fluids. A further consequence of the P-T-V-X behaviour of fluid inclusion assemblages trapped on the solvus (Fig. 45) is that their respective temperatures and pressures of total homogenisation will be identical to the pressures and temperatures of entrapment in the vein environment (Ramboz et al., 1982; Diamond, 1990 and 2001). Moreover, internal pressures of vapour-rich and liquid-rich inclusions in immiscible systems are the same at trapping (Mullis, 1979; Diamond and Marshall, 1994). This is represented by the crossing of the "vapour" and "liquid" isochores at the same Th as shown in Fig. 46. Therefore, the P-T conditions of formation for type 1 and 2 fluid inclusions can be obtained at the intersection of the isochores calculated for vapour-rich inclusions with the measured Th in coeval aqueous-rich inclusions. The fluid pressures at formation conditions were relatively low, ranging from 15 to 56 MPa for type 1 and from 10 to 27 MPa for type 2 (Fig. 47).

75
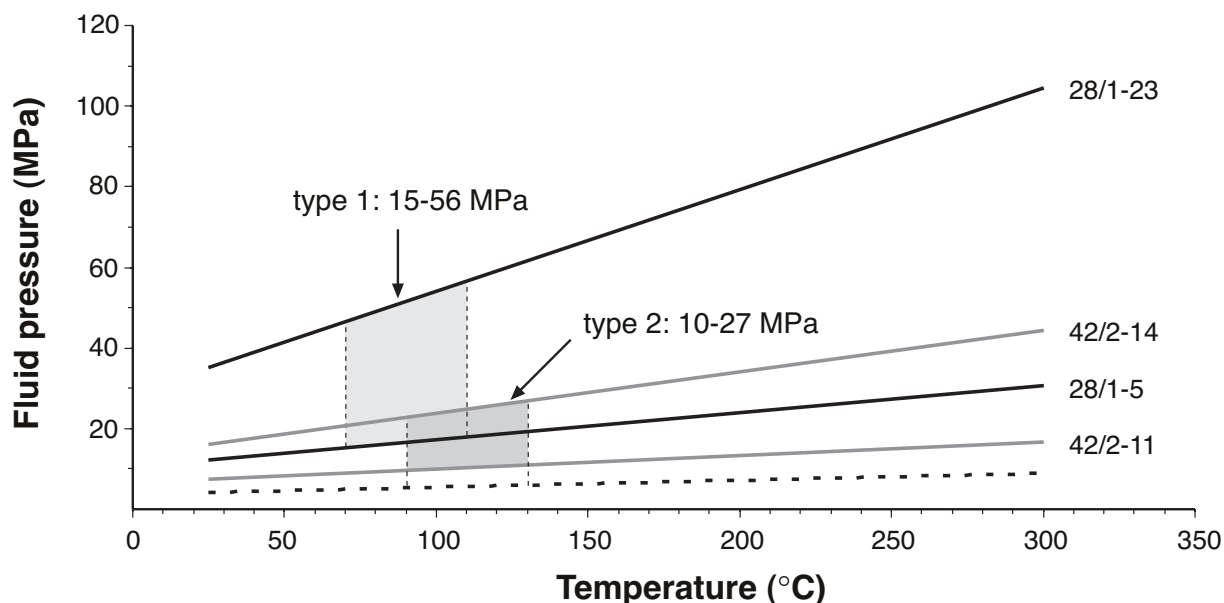
Figure 47. Temperature-pressure diagram with four isochores, representing the higher and the lower calculated molar volumes for vapour-rich inclusions of type 1 and 2 in qtz1 (samples 28 and 42), determined with Duan et al. (1992a, b, 1996). The trapping pressures are obtained from the homogenisation temperatures of coexistent, aqueous rich end member inclusions (Table 4). The lower dashed curve indicates the position of the isochores of vapour-rich inclusions with molar volumes above 400 cm^3mol^{-1}.

The predominance of such low trapping pressure conditions is supported by two other observations:

a) Methane clathrate melting occurred before ice in some aqueous-rich inclusions (Fig. 30b). This feature is indicative for high molar volumes of the vapour phase, as illustrated in Fig. 48. At the example temperature T_1 (-7°C) clathrate melts before ice, which is similar for a pure H_2O aqueous solution and a 5 wt.% NaCl aqueous solution. A high molar volume is obtained for the CH_4-rich vapour bubble (1000 cm^3mol^{-1}), independent of salinity. At T_2 (+8.5°C) ice is already melted at Q_1 temperatures and subsequently clathrate melts at a much higher CH_4 isochore: 333.6 cm^3mol^{-1} with a pure H_2O aqueous solution and 255.2 cm^3mol^{-1} with a 5 wt.% NaCl solution. Molar volumes up to 940 cm^3mol^{-1} have been estimated for the vapour phase in some aqueous-rich inclusions. The variation of density in vapour-rich inclusions, which ranges from 69 to 541 cm^3mol^{-1} (Table 5), is likely to reflect fluctuations in the pressure regime during crystallisation. Though the highest molar volumes (> 400 cm^3mol^{-1}) could also be the result of different degrees of stretching during subsequent heating and/or burial.
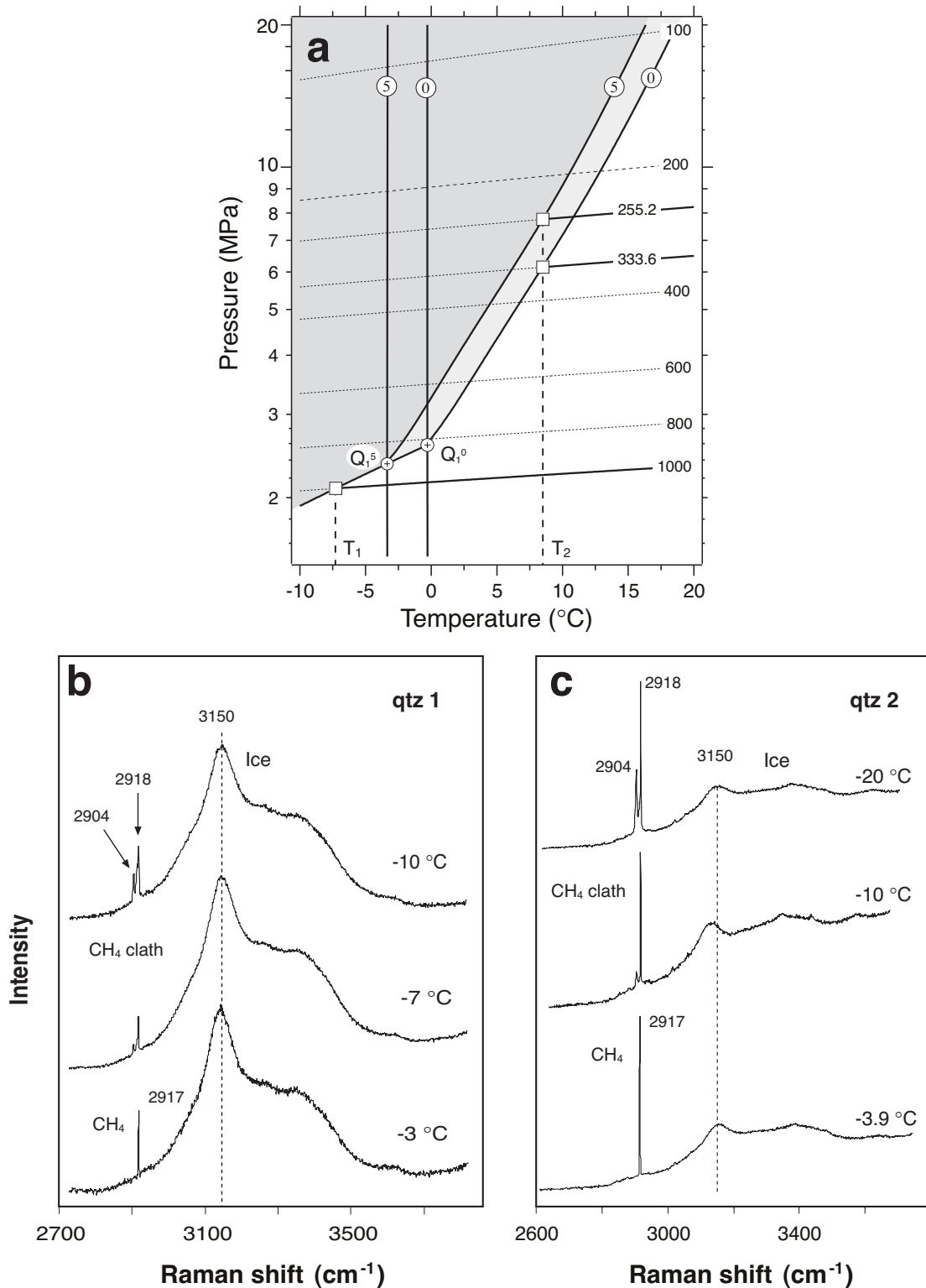
Figure 48. (a) Temperature-pressure diagram of the H_2O-CH_4-NaCl fluid system with the stability field of clathrate in a pure H_2O aqueous solution and a 5 wt.% NaCl aqueous solution (light shaded area), calculated from Bakker (1997). The vertical solid lines indicate the stability field of ice. Q_1^0 and Q_1^5 are the quadruple points 1 for the two solutions where four phases are at equilibrium in the inclusions. The dashed lines are isochores for CH_4 (numbers are molar volumes). (b) Sequence of Raman spectra showing the melting of CH_4-clathrate and ice in a type 2 inclusion of qtz1 (sample 26). At -3°C all the clathrate is melted but ice is still present. (c) Same phenomena in a type 1q inclusion from qtz2 in the dioritic rocks of the CMB (sample ign12).

b) Relative high values of the CH_4 and CO_2 Raman stretching vibration peaks are recorded in both type 1 and 2 vapour-rich inclusions. The magnitude of the Raman shift is pressure sensitive and can therefore be used as a semi-quantitative indicator of internal pressure in vapour-rich inclusions (Seitz et al., 1996).The higher the shift in the peak, the lower the internal fluid-pressure in the inclusion. The peak of the lower Fermi diad member of CO_2 (v_1) is not used, as it is sensitive to fluid composition and not only to pressure. Values of the CH_4 peak (v_1) are always above 2915 cm^{-1}, and those of the upper member of the Fermi diad of CO_2 ($2v_2$) are above 1387 cm^{-1} (Fig. 49).
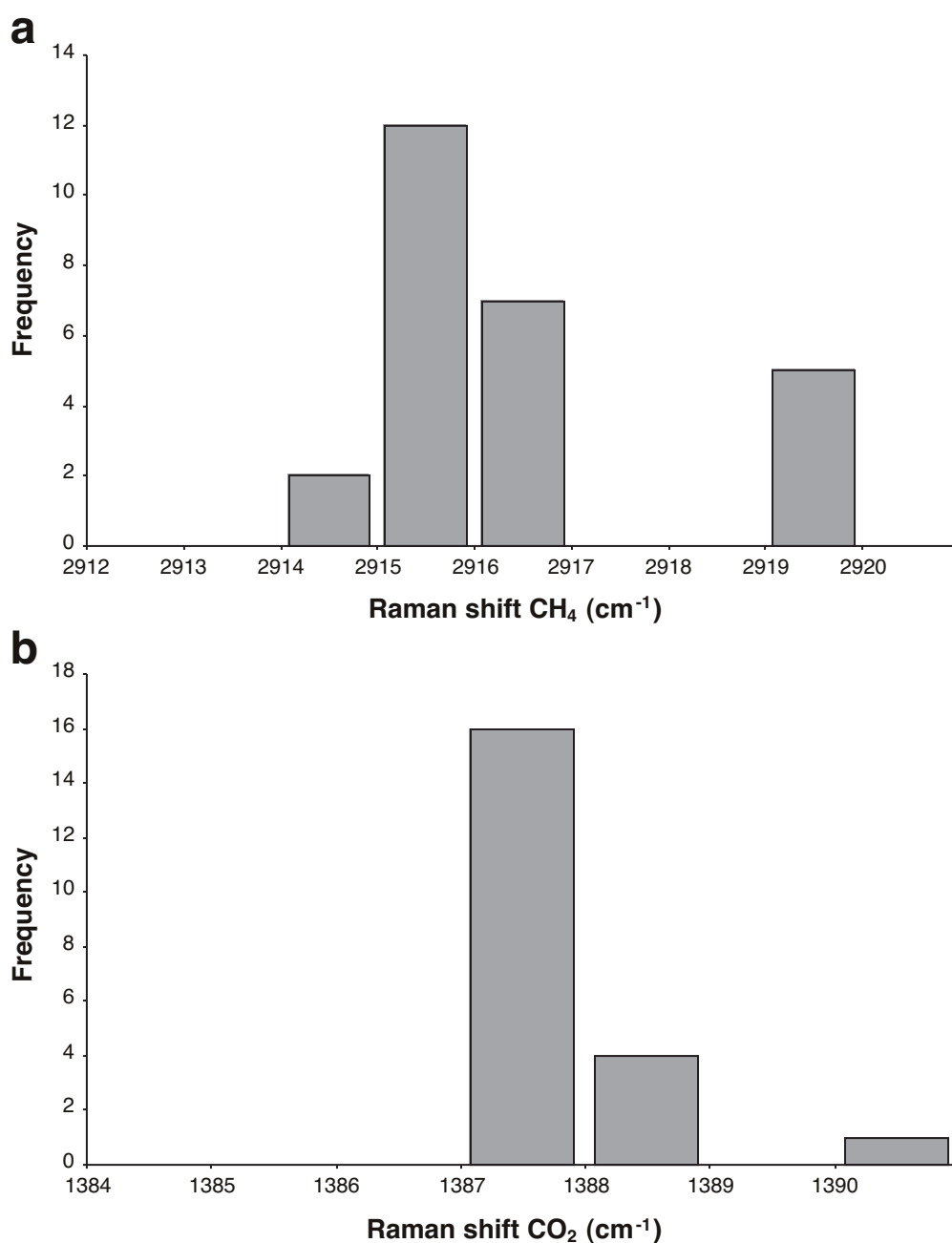
Figure 49. Frequency-Raman shift histogram obtained for vapour-rich inclusions of type 1 and 2 in vein quartz (qtz1): (a) v_1 peak of CH_4, (b) $2v_2$ peak of CO_2. Samples 28, 42 and 31. The shift values are mostly > 2915 cm^{-1} for CH_4 and ≥ 1387 cm^{-1} for CO_2.

This indicates that these inclusions have fluid internal pressures well below 10 MPa at room temperature, according to projections shown in Figs. 1 and 2 of Seitz et al. (1996). Nevertheless, due to considerable analytical error associated with these estimates the results can only be used qualitatively to support the low trapping pressures estimated above. Peak magnitudes in the vapour phase of aqueous-rich inclusions are generally above 2917 cm^{-1} for CH_4, but factors that influence the peak shift have not been investigated for these type of inclusions.

5.3.2. Secondary H_2O-NaCl-$CaCl_2$-CH_4 system in vein quartz (qtz1)

As seen from the petrographic evidence, a H_2O-NaCl-$CaCl_2$-CH_4 fluid was trapped in the vein quartz (qtz1) after its crystallisation. This system was not formed by heterogeneous trapping of two immiscible fluids, but from a relatively homogeneous brine with certain amounts of CH_4, detected by Raman in both the aqueous- and vapour-phases. The occasional detection of CO_2 in some type 3 inclusions is attributed to contamination during formation, as the inclusions in which this phase was detected always cut type 1 and 2 assemblages. The absence of vapour rich inclusions confirms that no methane rich end member was present during fluid trapping. As temperature falls below the bubble point curve of the system, a small vapour bubble nucleates in fluid inclusions. The presence of methane-bearing clathrates in these aqueous inclusions requires a minimum pressure roughly equal to that of the Q_1 point (2.7 MPa and 0°C in a salt free system). The melting of this phase before ice indicates that methane concentrations should be below 0.06 mol% (Dubessy et al., 2001). The high total salinity of the aqueous phase, 26.6 to 28.9 eq.wt%, also favours that the concentration of dissolved methane is low and imposes a problem in order to calculate the appropriate bubble point curve as it increases the immiscibility field (Fig. 50). The calculated methane concentration is below 0.01 mol% (Table 5). Therefore, Th can only be used as a minimum entrapment temperature for the fluid and no accurate pressure calculation can be made from equations of state or isopleth projections (Bakker, 1999).

The Th-Tm projection of fluid inclusion data, separately for each sample, shows that leakage and refilling, and/or stretching didnot affect the studied secondary inclusions. Besides, these plots outline straight away the differences of this fluid system with respect to the primary H_2O-CH_4-CO_2-NaCl system (Fig. 51). Calculated bulk fluid densities vary between 16.9 and 17.2 cm^3mol^{-1} (Table 5).
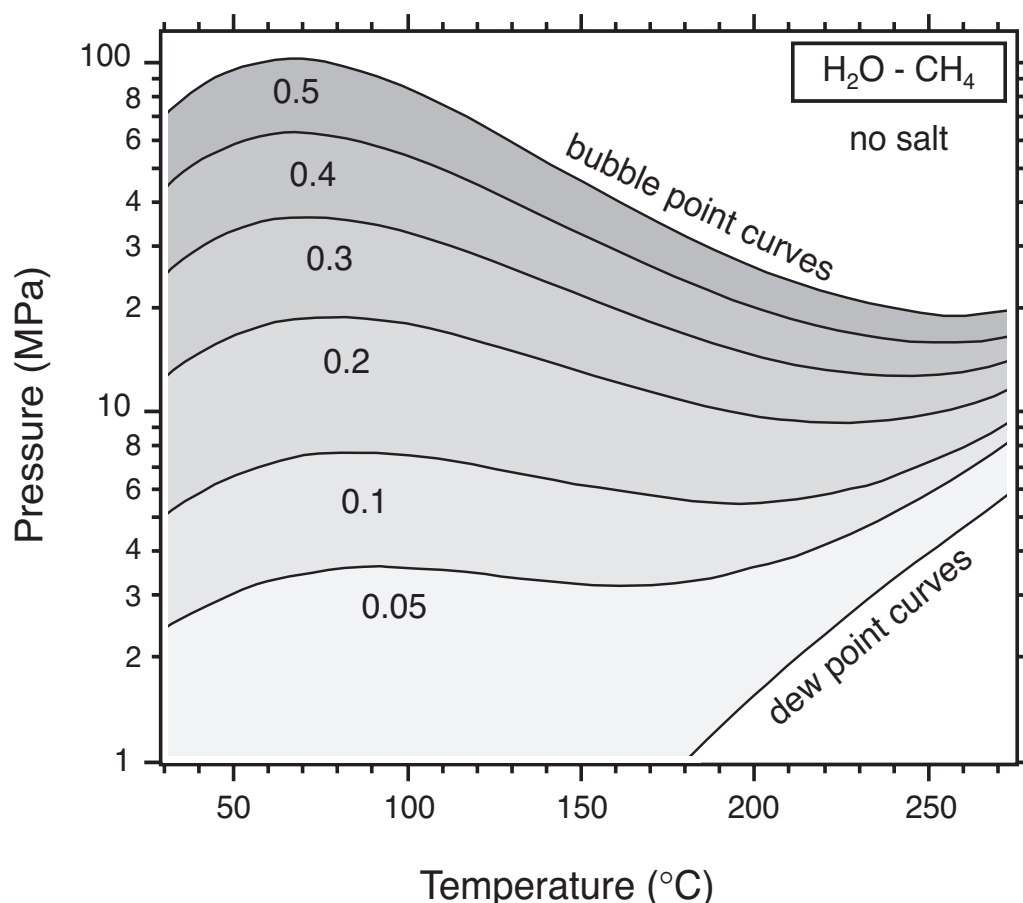
Figure 50. Temperature-pressure diagram with immiscibility fields of H_2O-CH_4 fluids with low bulk mole fraction of CH_4 (numbers are mole% CH_4). The solubility of CH_4 in H_2O is calculated with Henry's law, using a modified equation from Rettich et al. (1981), see Bakker (1998) for details. The CH_4-rich gaseous counterpart is calculated with the Redlich-Kwong equation of state. Above 100°C the curves are increasingly in error. The dew point curves of all 6 compositions coincides, close to the saturation curve of pure H_2O.

5.3.3. Primary H_2O-NaCl-$CaCl_2$-CH_4 system in vein calcite (cal2)

Due to the primary character of the type 1c inclusions in cal2 it is assumed that the fluid system within them was contemporaneous with de-dolomitisation and vein calcite precipitation. As for type 3 inclusions in qtz1, this fluid can also be described as a complex brine with minor amounts of dissolved CH_4, but it exhibits more significant variations in relative salt concentration and ice melting temperatures from sample to sample (Fig. 52). Differences in ice melting temperatures among the sample localities could represent local heterogeneity in cation sources and/or abundance in the solution, or different grades of mixing with low-salinity waters (see chapter 6).
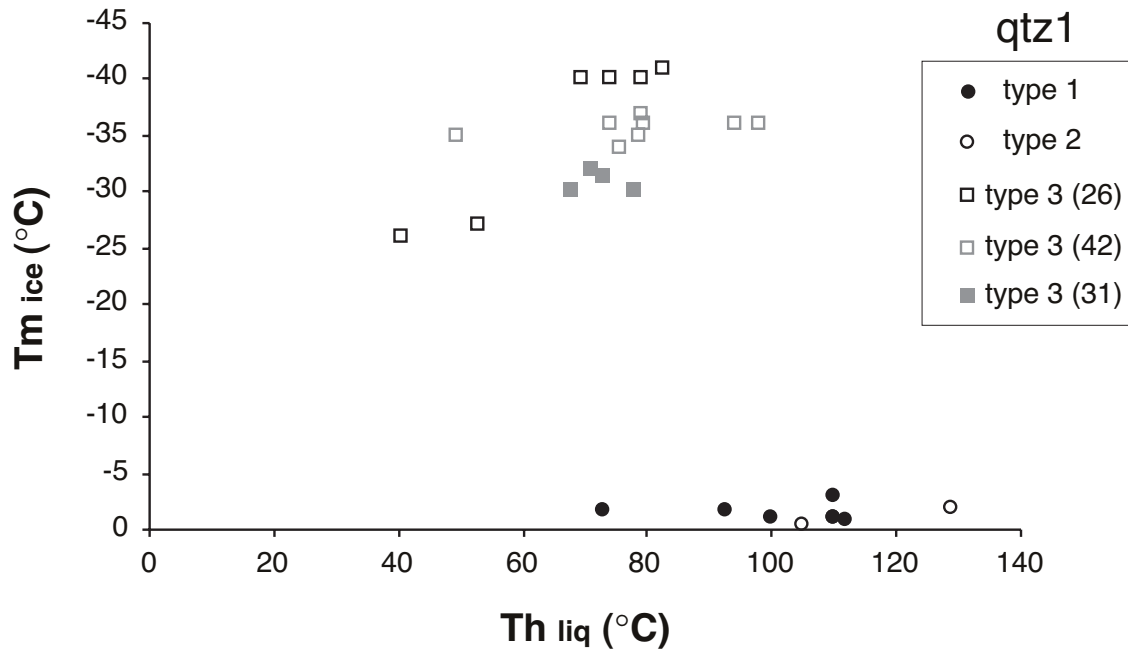
Figure 51. Final ice melting (Tm) versus total homogenisation (Th) temperatures of fluid inclusions in vein quartz from different localities of the CMB. The difference between type 1-2 and type 3 inclusions can be appreciated. Type 3 Tm have slight variations, though they are relatively uniform among localities and all are below -25°C.
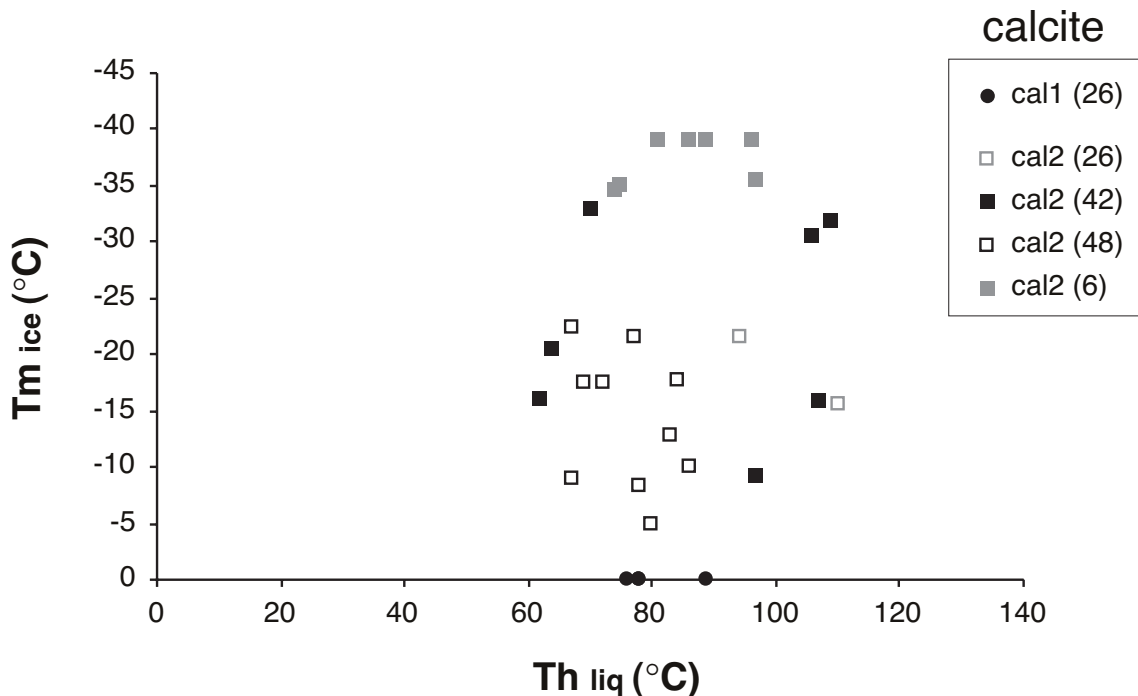
Figure 52. Final ice melting (Tm) versus total homogenisation (Th) temperatures of fluid inclusions in vein calcite from different localities (number in brackets) in the CMB and SB. Tm shows a wide spread of values, with the exception of sample 6 (SB).

The higher temperatures and salinities of this fluid system were attained in the SB (sample 6), where the Th range is small, with a well-defined mode between 90-110°C (Fig. 40b). Homogenisation temperatures in the CMB extend over a wider range of values (62 to 126°C) and vary from sample to sample. As the fluctuations in inclusions' vapour volume-fraction are small this can be attributed to a combination of general lower Th values and to inclusion stretching during microthermometric heating, common in calcite (Prezbindowsky and Larese, 1987). Stretching of inclusions leads to higher Th and therefore, for the samples of the CMB, the range of temperatures from 60° to 100°C is likely to better represent the minimum trapping conditions. Raman spectroscopy was severely hindered by fluorescence in most samples and no clathrate phase was detected or observed. The weakness of the CH_4 phase Raman signal (very few spectra could be taken) did not allow for estimations of the peak shift, resulting in similar difficulties in determining the trapping P-T conditions for this fluid. The molar volume of the vapour phase can only be inferred. Despite this, calculated bulk densities (and total salinities) are relatively homogeneous and vary between 17.1 and 17.7 cm^3mol^{-1} for the CMB samples, overlapping with those of the fluid trapped in type 3 secondary inclusions in qtz1, and between 17.8-17.9 cm^3mol^{-1} for the SB samples (Table 5, page 71).

Both type 3 inclusions and cal2 are associated with microcracking and remobilization of quartz within veins. The similarities of these fluid systems (overlapping homogenisation temperatures, fluid composition and bulk densities) suggest that they represent different manifestations of the same fluid event.

5.3.4. Primary H_2O-CH_4-CO_2-NaCl system in hydrothermal quartz (qtz2)

The fluid system present during qtz2 crystallisation has the same components as the one within primary inclusions in qtz1. The main two differences are the higher CO_2 content of the vapour-rich end member and the higher homogenisation temperatures (Fig. 27c and Table 4). The same criteria outlined for qtz1 suggest an immiscibility and heterogeneous trapping mechanism for these fluids. Calculated bulk densities for aqueous-rich inclusions are between 22 and 36 cm^3mol^{-1}. Trapping pressures were estimated at the intersection of Th temperatures with the isochores of liquid-rich inclusions. Vapour-rich isochores were also plotted to provide a further constraint (Fig. 53). Pressures range from 3 to 48 MPa. The same two phenomena as for the H_2O-CH_4-CO_2 ($\pm$ NaCl) system in qtz1, supporting low fluid trapping pressures, are also observed for inclusions in qtz2 (Fig. 48 and 49).
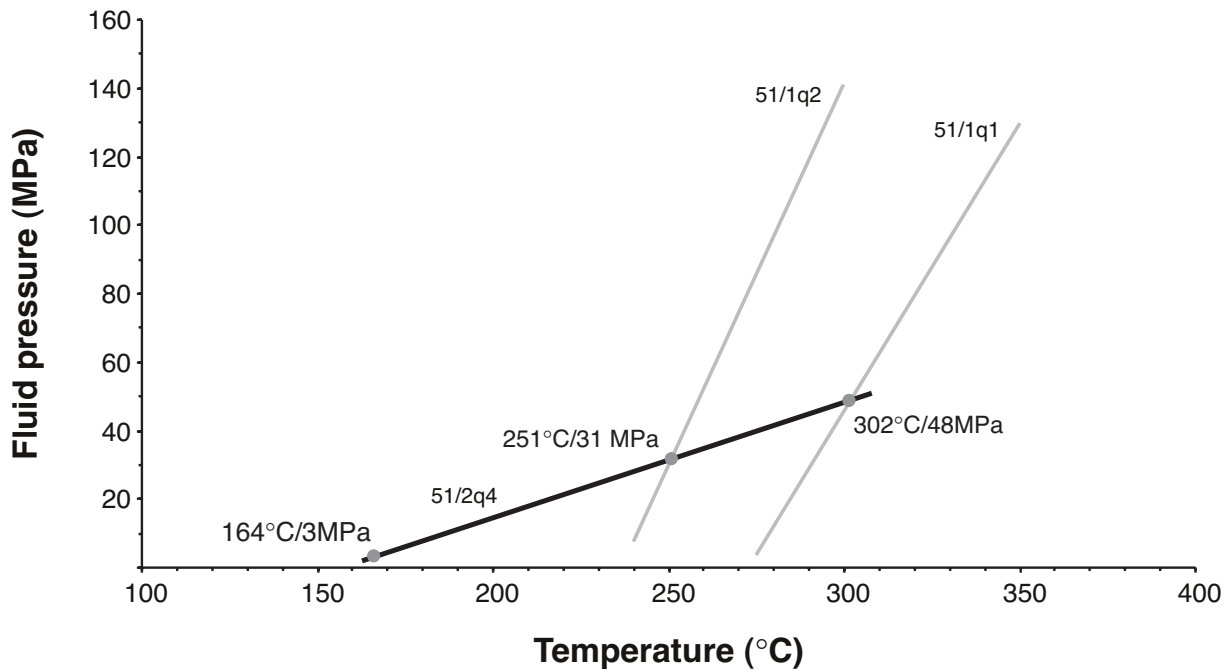
Figure 53. Temperature-pressure diagram showing the isochores calculated for 3 fluid inclusions in qtz2. Assuming fluid immiscibility in the system H_2O-CH_4-CO_2-NaCl, the intersection of the isochore for the vapour-rich inclusion with the other two, aqueous-rich, determines the upper range of pressures and temperatures of trapping (coincident with the Th measured for those inclusions). The lower value represents the minimum entrapment pressure corresponding to the lower range of Th_{liq}.

5.4. THE SEQUENCE OF FLUID EVENTS

Calculated fluid P-T conditions during the different stages of vein mineral growth represented by the recognised fluid systems are showed in Fig. 54. Characterisation of the veins as open fissures, their widespread distribution throughout the whole sediment sequence and basin and the low pressures of fluid entrapment (< 60 MPa), together with the absence of recognisable pressure trends with depth, indicate that hydrostatic pressure conditions prevailed during fissure formation and mineral precipitation. Fluid events and their associated characteristics and timing within these rocks are illustrated schematically in Fig. 55.

Following sedimentation in the Ciñera-Matallana basin, an early period of deformation and fracturing took place and small amounts of calcite (cal1) crystallised from a temperate, low salinity aqueous fluid at shallow depths within open fractures, which were predestined to host subsequent vein mineralisations. In the open fissures, quartz (qtz1) precipitated as large euhedral crystals in the presence of an immiscible fluid mixture, composed of a low salinity aqueous solution and a CH_4-rich vapour phase. Both fluid end-members were trapped heterogeneously in the large quartz crystals as type 1 and 2 fluid inclusions.
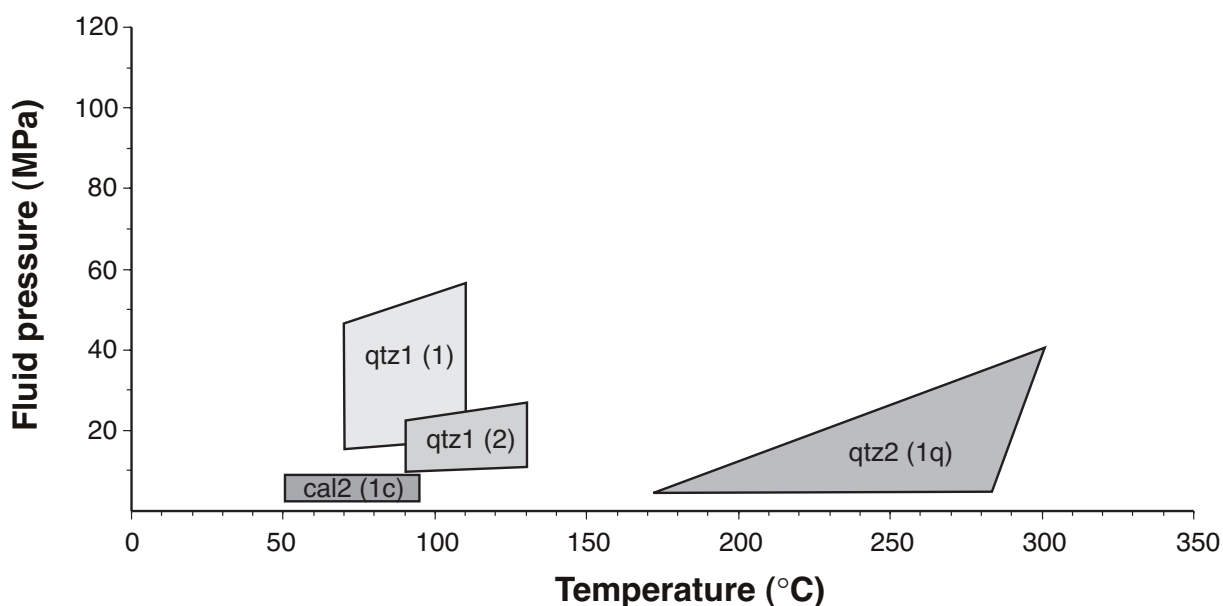
Figure 54. Diagram illustrating the estimated fluid pressure-temperature conditions for the different mineral phases investigated in the veins of the studied basins: (1) H_2O-CH_4-CO_2-NaCl in qtz1, (2) H_2O-CH_4-CO_2-NaCl in qtz2, (3) H_2O-NaCl-$CaCl_2$-CH_4 in cal2 and in secondary inclusions in qtz1. The position of the area for vein calcite (cal2) is inferred from other evidence, as no fluid-pressures could be estimated from the inclusion data.

P-T conditions evolved from 15-56 MPa and 73°-110°C for type 1 to 10-27 MPa and 87°-129°C for type 2 (Fig. 54). Inclusions of this last type also have progressively higher CO_2 content than type 1, further indicating an increase in temperature (Fig.27b). At a late stage of qtz1 growth, saddle dolomite (dolm) precipitated, partly enclosed as solid inclusions within qtz1. The formation conditions of the younger, relic dolm are not known, as only small crystals are preserved and even the largest fluid inclusions (< 2 μm) found are too small for analysis. Spötl and Pitman (1998) presented a revision of the published formation temperatures of saddle dolomite within sandstones obtained from fluid inclusions. They are approximately above 60°-80°C, with a maximum between 90 and 160°C. These same authors also associate this mineral phase with the input of saline palaeofluids.

Vein growth in the diorites constitutes a separate stage of mineral formation (qtz2 area in Fig. 54). The overall fluid properties of vein-quartz inclusions (qtz2) in these magmatic bodies are similar to the trends observed in the fluid inclusions of qtz1 (Fig. 55). However, in type 1q and 2q inclusions fluid conditions were between 164°-296°C and 3-48 MPa, CO_2 content in the vapour phase is always > 10 mol%, and re-equilibration textures are not observed in inclusions in qtz2. It therefore appears that the magmatic-related quartz represents a mineralisation product formed at high temperatures, which maybe related to a fluid event that caused the re-equilibration of inclusions in the fissure quartz (qtz1).

Finally, brittle reactivation of veins in the clastic rocks caused reopening and microcracking of the large quartz crystals. Calcite (cal2) precipitated at relative low temperatures, around 60° to 100°C, from a highly saline fluid preserved as primary inclusions (type 1c) in cal2, and probably as secondary type 3 inclusions in qtz1 as well (Fig. 55). Fluid pressure conditions could not be determined but the characteristics of the fluid system suggest they were low (< 20 MPa). Extensive dedolomitisation also took place associated with this event. This phase, together with the ongoing deformation that followed cal2 formation and the latest calcite (cal3), may have a much younger origin than the other minerals present in the veins.
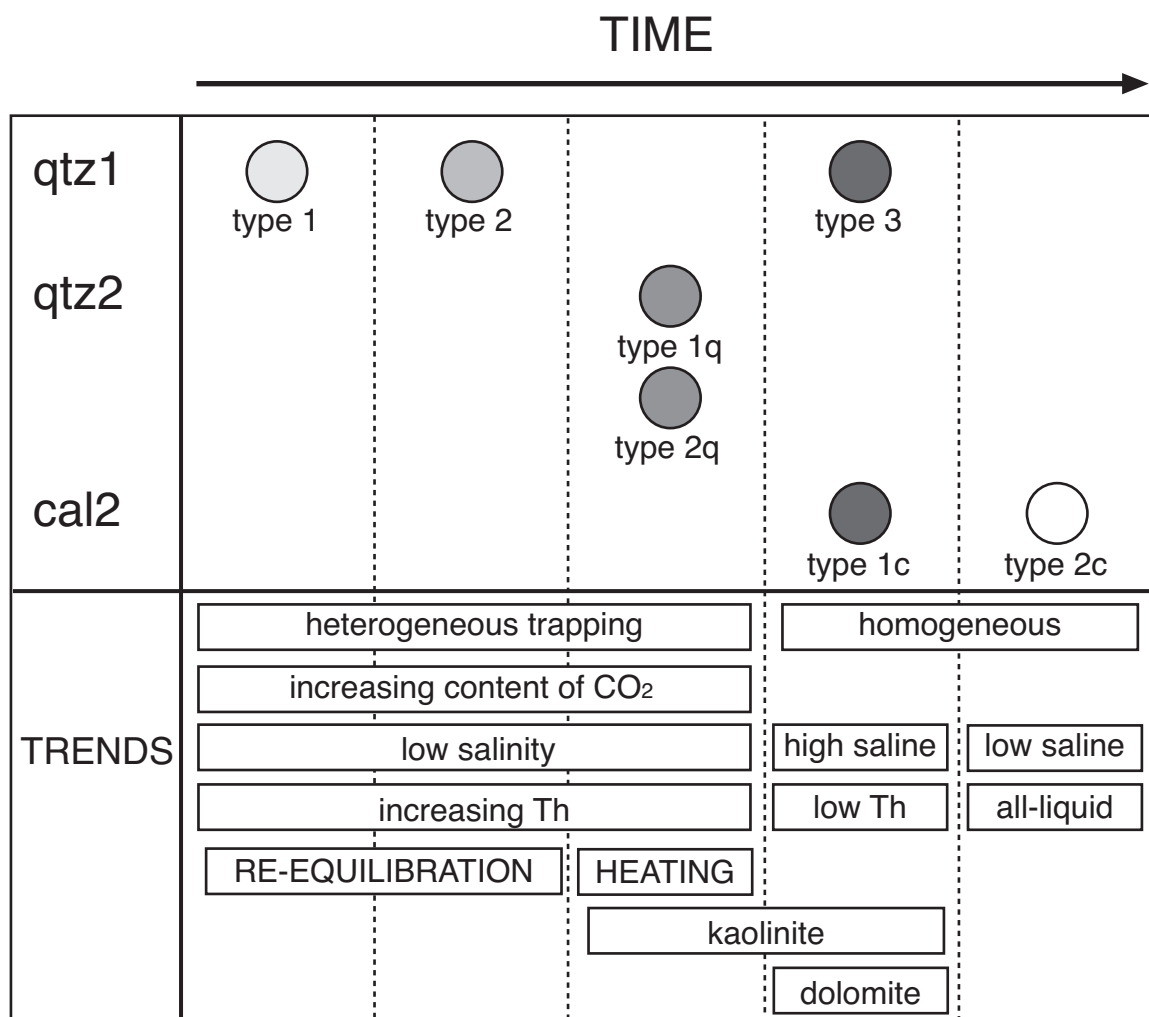
Figure 55. Schematic diagram illustrating the relations between vein mineralisation (qtz1, qtz2 and cal2) and fluid inclusion types. Trends indicate mode of trapping (heterogeneous or homogeneous), occurrence of re-equilibration textures, salinities, accidentally trapped minerals (kaolinite and dolomite), CO_2 contents and homogenisation temperatures.

CHAPTER 6: ORIGIN OF MINERAL PHASES AND FLUID SOURCES

After investigating the fluid types and trapping conditions associated with fissure mineral formation this chapter addresses the nature and possible sources of the fluid systems and minerals responsible for forming the studied veins. The aim here is to assess if the mineralisng fluids had a intrabasinal origin, i.e. derived from thermal maturation and dewatering of the basin rocks, or if they were externally-derived fluids, transported into the basin by fluid flow. In addition to the mineral, fluid chemistry and petrographic evidence, new data on carbonate stable isotopic composition and on the crystal growth mechanism of clay minerals are presented in this chapter. Each vein mineral phase and the co-existing fluids are treated separately within the time framework determined by the petrographic research and the fluid inclusion analysis. Potential mineral precipitation mechanisms are also discussed, which may be influenced by several interrelated factors: silica and carbonate sources, thermal history, transport mechanism, pore pressure history and local variations in lithology.

6.1. QUARTZ PRECIPITATION AND ORGANIC-DERIVED BASINAL FLUIDS

The level of organic matter maturation reached in the sediments of the CMB, according to the published data, falls largely within the catagenesis state in transition to the metagenesis zone. According to the review in Barnes et al. (1990), catagenesis occurs at temperatures from 50° to 150°C and pressures from 30 to 100 MPa. These conditions are largely coincident with the estimations of fluid P-T for the primary inclusions in the studied vein quartz. Within this P-T range the components of the fluid system H_2O-CH_4-CO_2 (with traces of C_2H_4, C_2H_6 and C_3H_8, and minor NaCl), present during quartz formation and from which quartz precipitated, could be largely derived from the thermal maturation of the organic matter in the coal seams. At this level of maturation coal macerals undergo a significant reduction in water content and volatiles, fully coincident with the generation of gas. Coal bed volume-reduction due to compaction processes also enhances fluid generation as well (Barnes et al., 1990). For temperatures > 80°C degradation of simple organic compounds (e.g. acetate) follows the reaction:

$$CH_3COOH + water \rightarrow CH_4 + CO_2 + carboxylic\ acid\ anions$$

Early carbonate precipitation is possible under these conditions (Morad, 1998), as reflected

by the early calcite relics (cal1) preserved within vein quartz. At T $\geq 100^\circ$C thermal degradation of carboxylic acids progressively produces more CH_4 and CO_2 and consequently a pH decrease (increase in ρCO_2) which also inhibits carbonate precipitation (Morad, 1998). The predominance of CH_4 over CO_2 in the vapour phase of the fluid system in qtz1 primary inclusions also reflects these conditions. CO_2 is generated preferentially at much higher temperatures related to thermal cracking reactions in the formation of meta-anthracites and coke. The solubility of quartz in water increases as result of:

- complexing by organic compounds, such as those produced during coal maturation (Bennet and Siegel, 1987; Fein, 2000)
- low salinity of the water, as reflected by the low salinity of the aqueous phase in primary fluid inclusions of qtz1 (Renard et al., 2000; and references within)

Sources of silica external to the basinal rocks are very unlikely in this setting. There exist three main arguments supporting an internal origin for the quartz brought into solution:

- most quartz-rich lithologies in the CMB contain veins, suggesting local transport
- fracture-related hydrothermal mineralisations in Devonian limestones adjacent to the basin do not contain quartz (samples 15-16, see appendix)
- the solubility of quartz is relatively low and vast quantities of water would be required to flow through the basin to accomplish the observed extent of quartz mineralisation in the CMB (Bjørlykke, 1994)

In clastic sedimentary environments, depending on the primary mineralogy and conditions of pressure and temperature, there are 3 possible internal SiO_2 sources derived from the detrital and authigenic fractions of the rock where vein formation occurs (Worden and Morad, 2000). These include:

1) intergranular pressure-dissolution of quartz grains
2) clay-mineral transformations (illitization of kaolinite and chloritization of smectite)
3) feldspar alteration reactions

In the study area, the host-lithologies of quartz-bearing veins are invariably sandstones where quartz grains are a major constituent of the detrital fraction, and XRD analysis of veins and adjacent clastic rocks denote the absence of feldspar and the presence of kaolinite, illite/smectite, and minor chlorite. Therefore, source (1) of SiO_2, and to a minor extent source (2); seem to have been dominant.

In clastic sedimentary sequences, quartz cementation from a fluid phase tends to occur at elevated temperatures because temperature has a major control on the solubility of quartz and the most important SiO_2 liberating reactions (Wood, 1986). As a result quartz is found as a major cement only in clastic rocks that have been heated above 80°C (Worden and Morad, 2000). However the main control on quartz precipitation in this setting seems to be governed by kinetics, although it is not clear whether quartz crystallises continuously over small rates or rapidly over short periods. Complex zonation of qtz1 in

the CMB unravelled by preliminary CL observations tends to support that crystallisation occurred in pulses (van den Kerkhof, pers. com.). In terms of chemistry, quartz crystallisation in water is slightly favoured by a pH increase, a low potassium concentration and by increasing salinity (NaCl). Pressure (effective stress) is potentially another important control whereby quartz tends to be concentrated in underpressured sites (Worden and Morad, 2000). The formation of fissures during early deformation and compaction processes in sandstone beds could have been the mechanism for generating local pressure gradients, allowing the flow of the H_2O-CH_4-CO_2 fluids from the coal seams and clastic rocks towards underpressured fracture (dilation) sites. The decrease in pressure (ρCO_2) during the fluid migration would have aided precipitation of quartz from solution. Such a mechanism would constitute a sort of "local" advection.

6.2 SADDLE DOLOMITE AND THE MATURATION OF THE CLASTIC ROCKS

As it is almost obliterated by later dedolomitisation, scarce data could be collected from the saddle dolomite preserved within vein samples. Nevertheless, the precipitation of this mineral after quartz in most of the studied veins has important implications for the fluid and thermal evolution of the basinal clastic rocks due to its special diagenetic significance (Radke and Mathis, 1980; Morrow et al., 1986). All the compositional and petrographic features of this dolm phase are typical of saddle dolomite described in other clastic sequences (Spötl and Pitman, 1998; and references within). As a rule, saddle dolomite is accepted as a potential high-temperature diagenetic geothermometer and as a reliable indicator of rock-brine interactions (Spötl and Pitman, 1998). It precipitates under conditions of extreme fluid supersaturation or in environments where surface-related activation energy barriers are significantly reduced (Radke and Mathis, 1980). The palaeofluids, according to published fluid inclusion data, are generally aqueous solutions dominated by NaCl + $CaCl_2 \pm MgCl_2 \pm KCl$ (total salinities of 18-25 eq.wt% NaCl), with low Eh and pH buffered to neutral (Spötl and Pitman, 1998). Growth rates are extremely rapid and bulk crystal composition is controlled by chemical and physical conditions prevailing in the precipitating solution.

The high concentration of Fe^{2+} (local source) present in the dolm samples of the studied coal basins could respond to decreasing amounts of dissolved Ca^{2+} and reflect the effect of increasing temperature in the basin rocks. The isotopic composition of the analysed samples (6 and 9) ranges from -9.5 to -8 $\delta^{18}O$‰ PDB and about +1 for $\delta^{13}C$‰ PDB (Fig. 56 and Table 6). Accepting formation temperatures between 100° and 150°C, SMOW values of the hypothetical precipitating fluid are above 0 ‰, typical of this dolomite type (Fig. 57). The low $\delta^{13}C$ values may also be attributed to an input of light carbon from thermally decarboxylized organic matter (organic carbon reservoir).
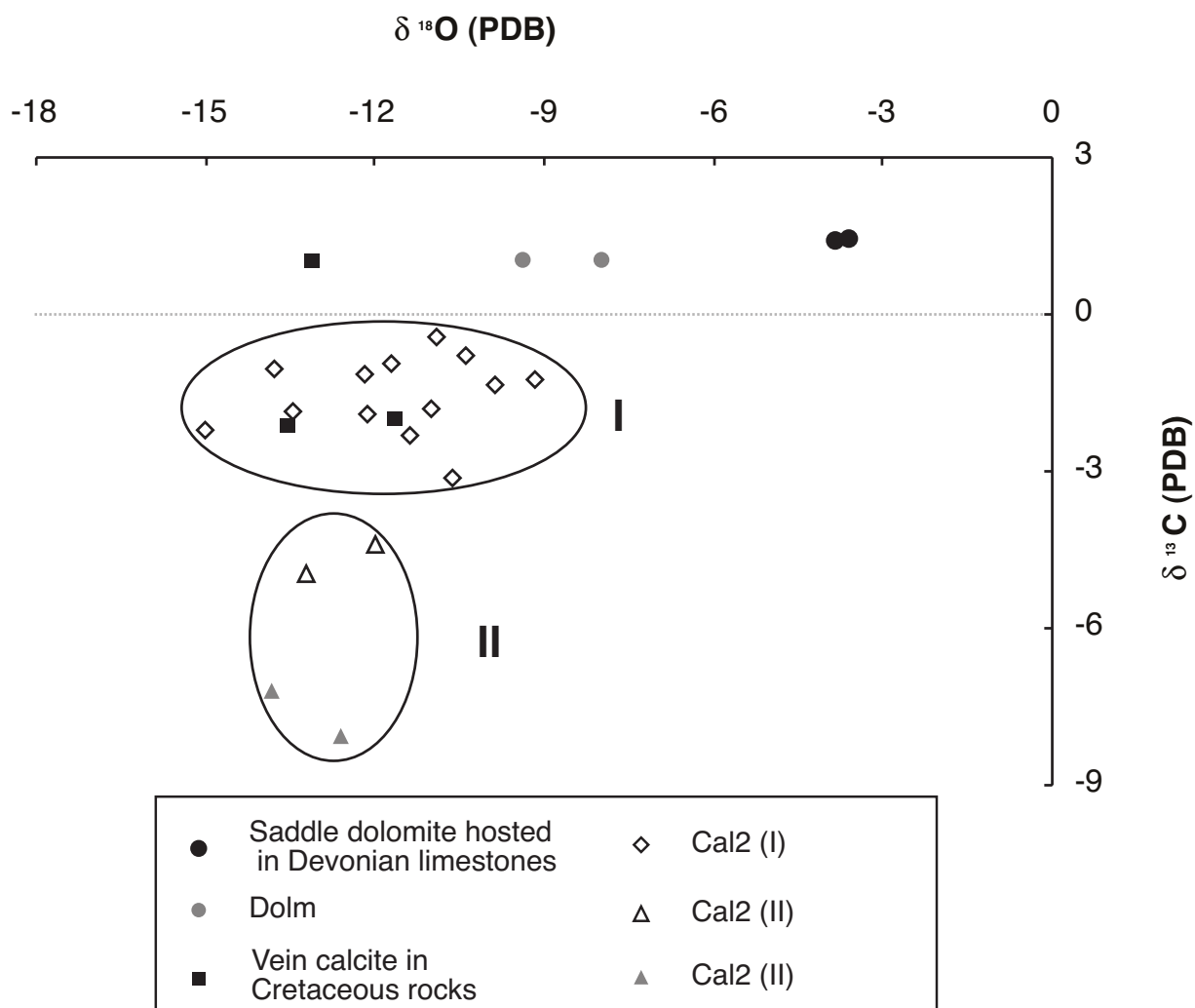
Figure 56. Plot of $\delta^{13}C$ vs. $\delta^{18}O$ (given in PDB) for carbonate vein minerals in the SB and CMB. Open squares and triangles correspond to averaged values for all measurements obtained from one locality (std. dev. = ± 1‰). Filled points correspond to individual vein samples. Saddle dolomite hosted in Devonian limestones belongs to two outcrops directly south of the Sabero-Gordón fault line. Sampled Cretaceous rocks delimit the NW margin of the SB.

The features depicted above, together with the fluid formation temperatures assumed from published data (100-150°C), could be explained by the following scenario. Under increasing temperature conditions, carbonates tend to precipitate while quartz remains in solution (Wood, 1986; Morad et al., 2000). From 120°C to 160°C (deep mesogenesis) thermal decarboxylation is mostly complete, reducing the generation of CH_4 and CO_2 (Morad, 1998). As a consequence, if veins remain open the still incoming H_2O-rich fluid will experience a decrease in ρCO_2 and an increase in the pH. During generation of organic acids dissociation processes putting Ca^{2+}, Mg^{2+}, Fe^{2+} and HCO_3^- into solution take place within the clastic fraction (Morad, 1998). In the stephanian basins this dissociation may have particularly occurred in mudrock lithologies (via clay mineral reactions), within the sandstone matrix and in conglomerate beds comprised mostly by limestone pebbles

(carbonate dissolution). Such reactions are enhanced at higher temperatures and the variety and concentration of dissolved salts increases thus inhibiting further dissolution of quartz. At this stage the alkalinity of waters is dominated by carbonate minerals, leading to precipitation of blocky ferroan dolomite cements.

As the dolomite crystals delimit external growth-zones in some qtz1-samples and also occur as a pore filling phase i.e. not associated wiht vein reactivation and dilation, this higher temperature event may be viewed as a continuum of a prograde rock maturation history.
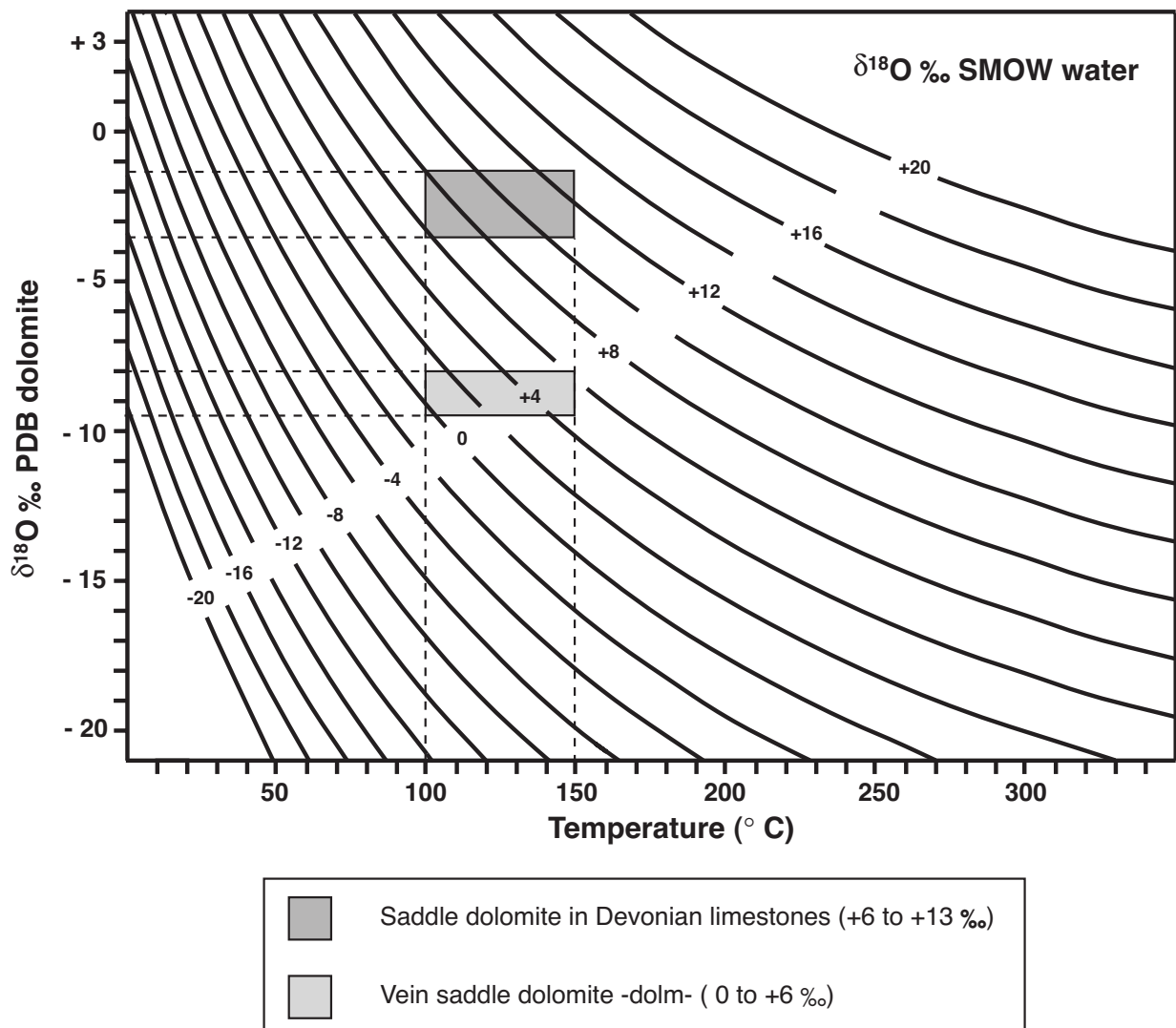
Figure 57. Estimated $\delta^{18}O‰$ SMOW values of the aqueous fluid from which dolm and saddle dolomite precipitated within Devonian limestones. Formula : 1000 ln α Dolomite = $T^{-2} \cdot 10^6 \cdot 3.20 - 3.30$ (in °Kelvin); after Land (1983).

6.3. THE ASSOCIATION OF DEDOLOMITISATION AND VEIN CALCITE

The vein calcite (cal2) was formed from an undersaturated Ca^{2+}-rich brine, at temperatures ranging from 60° to 100°C. Cal2 precipitation was also linked to an episode of tectonic reactivation and vein reopening accompanied by extensive dolm replacement.

Stable isotope measurements on cal2 were performed on 50 vein samples collected from the CMB and SB. Averaged values for each locality are given in Table 6 and plotted in Fig. 56. Oxygen isotopic values range from -9 to -15 $\delta^{18}O$‰ PDB. However, on the basis of $\delta^{13}C$ results two groups can be recognised, marked as I and II in Fig. 56. Group I presents carbon isotopic values ranging from -3 to -0.5 $\delta^{13}C$‰ PDB, whereas fraction II ranges from -4.5 to -8 $\delta^{13}C$‰ PDB. It is notable that all the samples at locality 14 fall into group II. Additionally, isotopic values of calcite veins in deformed overlying Cretaceous marine sediments have a Group I signature. All data for individual samples is presented in the appendix tables A14, A15 and A16.

| Locality | Sample vs. V-PDB | | Sample vs. V-SMOW |
	$\delta^{13}C$	$\delta^{18}O$	$\delta^{18}O$
1	-1.09	-13.75	16.73
2a	-1.82	-10.97	19.6
2b	-7.21	-13.81	16.67
3a	-2.35	-11.37	19.19
3b	-4.96	-13.18	17.32
4	-2.25	-14.99	15.46
5	-1.37	-9.86	20.74
6	-1.16	-12.16	18.38
8	-0.44	-10.88	19.69
9	-1.89	-13.42	17.07
10a	-0.97	-11.67	18.88
10b	-8.06	-12.6	17.92
11	-1.26	-9.16	21.47
12a	-3.17	-10.6	19.98
12c	-1.93	-12.1	18.44
13	-0.79	-10.39	20.2
14	-4.44	-11.96	18.58
1(dolm)	1.05	-8.00	22.66
2b(dolm)	1.01	-9.52	21.10

Table 6. List of averaged $\delta^{13}C$ and $\delta^{18}O$ isotopic values of calcite and dolomite (dolm) for the studied veins.

The ^{18}O-depleted values suggest that rock-dominated and/or deformation-related fluids were not significantly involved in supplying material for carbonate precipitation (Budai et al., 1984; Milliken, 2000). Also the oxygen isotopic composition is more depleted than it

would be expected for alteration of organic material under near-surface diagenetic conditions. Isotopic $\delta^{18}O$ values of the formation waters (calibrated in Standard Mean-Ocean Water values) were obtained for four different localities, plotted against the averaged homogenisation temperatures from fluid inclusions without pressure correction (Fig. 58). Results present a narrow range from +2 to -2 ‰SMOW, indicating a common fluid source for all samples, likely to represent modified seawater as the obtained water isotopic composition is still lighter than in modern brines (Clayton et al., 1966; Moore and Druckman, 1981).
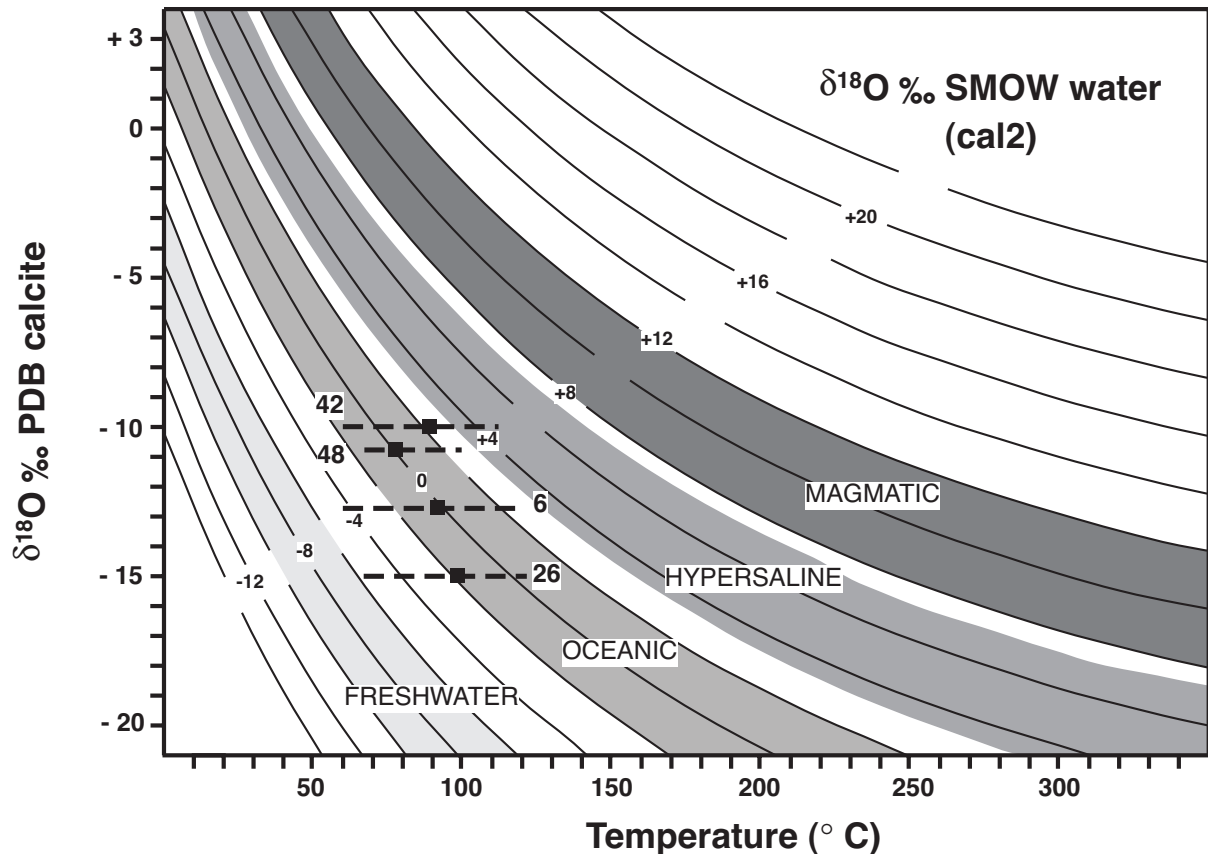
Calcite (cal2)	Th range (°C) ▬ ▬ ▬ ▬ ▬ ▬	Th (°C) ■	$\delta^{18}O$ ‰ PDB	$\delta^{18}O$ ‰ SMOW water
Sample 6	60-120	91	-12.74	0 (-4 to +2)
Sample 26	67-126	99	-15.0	-2 (-6 to +1)
Sample 42	62-123	91	-10.06	+2 (-2 to +5)
Sample 48	67-101	78	-10.81	0 (-1 to +3)

Figure 58. Estimated $\delta^{18}O$‰ SMOW values of the aqueous fluid from which cal2 precipitated, using the formula $1000 \ln \alpha$ Calcite $= T^{-2} \cdot 10^6 \cdot 2.78 - 2.89$ (in °Kelvin), after Friedman and O'Neil, (1977). Approximate values for the isotopic signature of the different water types (grey fields) are taken from Hoefs (1997).

The wide range of carbon isotope values for cal2 may reflect variations in the degree of mixing between fluids containing light organic carbon and heavy carbon derived from the dissolution of dolm. Group I of the replacing calcite presents oxygen depletion and has carbon isotopic compositions intermediate between early fracture dedolomite and group II. Carbon values may reflect a mixture of light, coal-derived carbon dioxide (group II) and heavy, dolomite-derived carbon. The $\delta^{13}C$ values of group II could be a result of physical mixing of calcite and dispersed carbonaceous matter trapped within the veins during powder extraction (see chapter 3). Excluding this effect, group II points may represent a more extensive local interaction between the fluid source and organic matter, though the fluid was still not extensively derived from or strongly buffered by the contact with organic matter.

Light oxygen and carbon compositions, combined with the close physical association of cal2 and dolm, strongly suggest that the replacement of dolomite occurred while the rocks were still buried and at relatively high temperatures (as indicated by fluid inclusions). Equivalent calcite cement phases have been commonly related to late fracturing and uplift; a situation experienced in both Stephanian basins during the Tertiary. The obtained isotopic values are roughly coincident with those reported for calcite related to dedolomitisation in similar late-orogenic clastic basins and they could reflect either higher formation temperatures or a depleted water contribution (Budai et al., 1984; Milliken, 2000).

The replacement of dolomite took place by dissolution, as seen from the fragments of dolomite entrapped within inclusions in vein calcite. Examining the conditions under which dedolomitisation can take place offers further insights into the features of the replacing fluid. The main prerequisites for calcitization of dolomite are (de Groot, 1967; Kastner, 1982):

      1) a high Ca^{2+}/Mg^{2+} ratio of the dolomite (as in saddle dolomite, dolm)

      2) a low ρCO_2 and pH < 7.8 of the incoming fluid

      3) a relatively high rate of fluid flow

Ca^{2+}-rich warm solutions have also been reported to cause dedolomitisation (Land and Prezbindowski, 1981) and these characteristics are fulfilled by the fluid system contained in the primary 1c inclusions in cal2. Moreover, the strong spatial affiliation of this calcite with the replacement of dolm points to a chemical system in which carbonate precipitation was not favoured outside the very local areas of pH buffering during dolomite dissolution:

$$CaMg(CO_3)_2 + 2Ca^{2+} + CO_2 \pm CH_4 \Leftrightarrow 2CaCO_3 + Mg^{2+}$$

That the fluids involved were prominently acidic is further confirmed by the coeval precipitation of disseminated pyrite and chalcopyrite. The iron content of cal2 can also be explained by dissociation of iron from the Fe-rich dolm, which in many samples presents a strong oxidation. The necessary extra Ca^{2+} could be incorporated into solution by pressure-dissolution of carbonate detrital components (e.g. conglomerate beds formed by limestone

pebbles), from Palaeozoic carbonate sequences adjacent to the basin and/or from overlying Cretaceous marine carbonates, during tectonic reactivation.

It is therefore considered likely that cal2 precipitated at conditions corresponding to shallow mesodiagenesis (Morad, 1998), by dissolution of pre-existing saddle dolomite within veins after peak temperatures in the Stephanian sequence were reached.

6.4. LATE CALCITE AND KAOLINITE CRYSTALLISATION

Characteristically, late calcite and kaolinite phases were formed by alteration of pre-existing vein minerals, and are significantly more abundant in fault-related veins than in fold-related ones.

The late calcite (cal3) generation of cement occurs as small crosscutting veins in both host rock and older fissure minerals. Isotopic data could not be obtained due to the small crystal size, which could not be sampled without impurities. Cal3 samples present no difference in CL colours with respect to those of cal2, but CL images illustrate parallel crack-wall zoning of this phase (Fig. 14h, page 40). Carbonate staining shows Fe^{2+} enrichment in cal3 in respect to cal2, suggesting that cal3 is the product of dissolution and recrystallisation of the previous calcite phase within microfractures formed during (minor) rock deformation following cal2 crystallisation, probably in the presence of certain amounts of fluid.

Pore-filling kaolinite (kln) is closely associated with the dissolution of previous vein minerals, preferentially carbonates, as well as wall-rock alteration. Authigenic kaolinite (low-temperature polytype) is abundant throughout the rock sequence in both basins (Galán et al., 1978; Frings, 2002). In humid environments, kaolinite forms by the dissolution of detrital aluminosilicates (e.g. feldspar, chlorite, muscovite; source of Al^{3+}) under acidic conditions. For example:

$$2KAlSi_3O_8 + 3H_2O \Rightarrow Al_2Si_2O_5(OH)_4 + 4SiO_2 + 2K(OH)$$
$$\text{(k-feldspar)} \qquad \qquad \text{(kaolinite)}$$
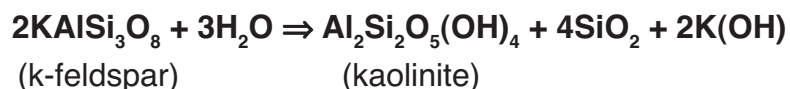
Information concerning kinetically controlled crystal growth processes allows the mechanism of kaolinite crystallisation to be assessed, in relation to its associated fluid phase (O'Hara and Reid, 1973). It has been proposed that crystal size distributions (CSDs) of clay minerals, calculated from X-ray scattering domain (crystallite) sizes, can be used to investigate crystal-growth mechanisms (Eberl et al., 1998). This method has been applied in this study to kaolinite-bearing vein samples. The analytical procedure follows the methodology of Eberl et al. (1996) and is summarised as follows. After a suitable XRD peak has been selected for analysis, peak intensities are first corrected (Fig. 59a) for the combined broadening effects of the Lorentz-polarisation (L_p) function and the layer scattering intensity
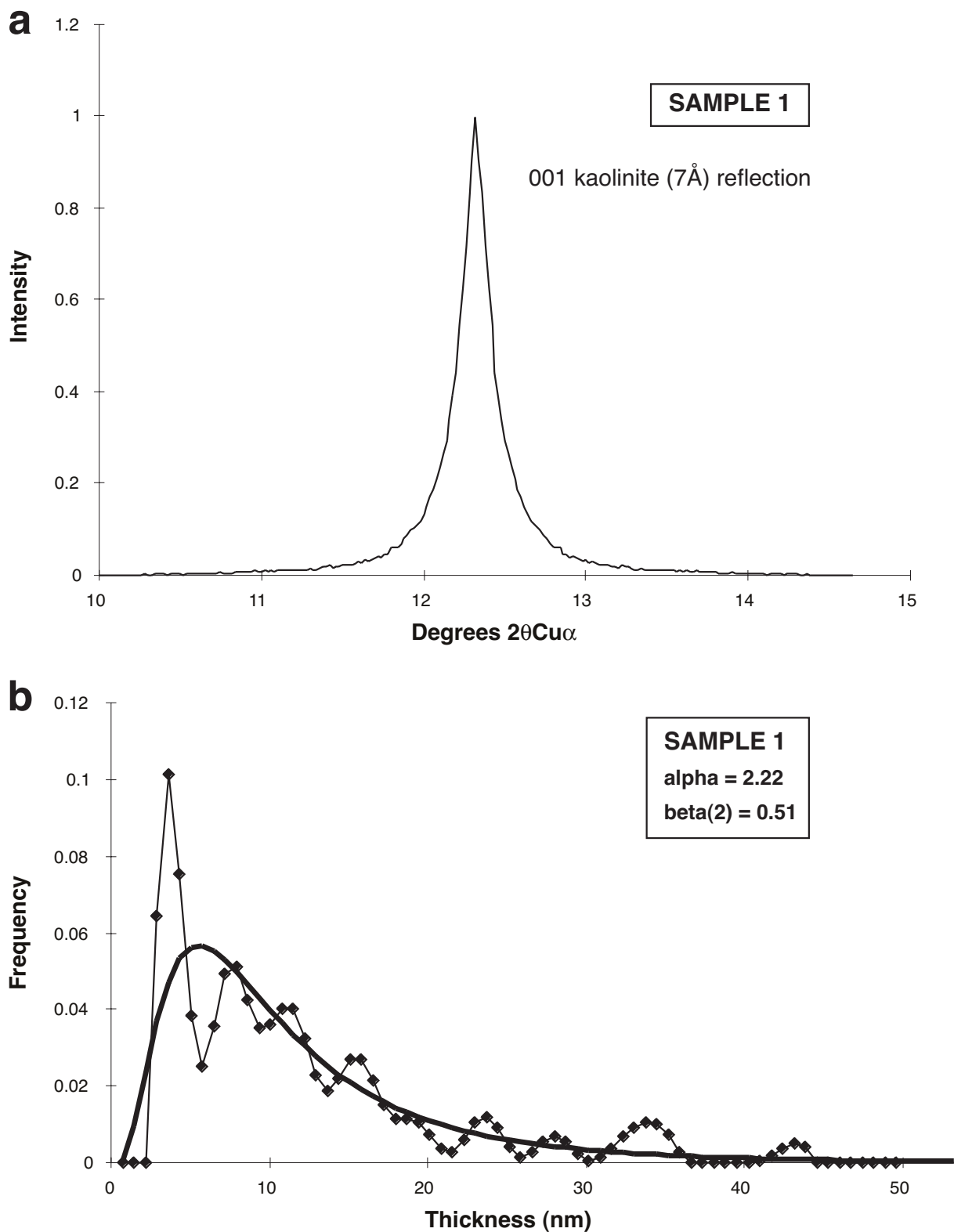
Figure 59. Example of the XRD 001 kaolinite (7Å) reflection and calculated X-ray scattering thickness crystallite size distributions for vein kaolinite. (a) sample 1, corrected peak using the program Mᴜᴅᴍᴀsᴛᴇʀ (Eberl et al., 1996). (b) Non log-normal crystallite thickness distribution, with parameters α and β^2. Solid black curve represents a theoretical log-normal distribution.

G^2 (square of the structure factor).

Then, following background subtraction and optional removal of the contribution of $K\alpha_2$ radiation, a Fourier analysis of the interference function is undertaken using the Bertaut-Warren-Averbach method, which calculates the distribution of thicknesses of X-ray scattering domains. The parameters α (mean of the natural logarithms of the crystal sizes) and β^2 (variance of the natural logarithms of the crystal sizes) describe the shape of the thickness distributions (Fig. 59b).

In the model of Eberl at al. (1998) crystal growth mechanisms can be interpreted from α-β^2 plots. Theoretical mechanisms are calculated using three simple equations: the Law of Proportionate Effect (LPE), a mass-balance equation and Ostwald ripening. Fig. 60 represents the simulated trends, corresponding to five growth mechanisms that show different trends in an α-β^2 plot:

(I) continuous nucleation and growth in an open system

(II) surface controlled growth in an open system

(III) supply controlled growth in an open system

(IV) supply- or surface-controlled Ostwald ripening in a closed system

(V) supply-controlled random ripening in a closed system.

According to Warr and Peacor (2002), the use of X-ray scattering domain (crystallite) sizes for determining crystal growth mechanisms relies on three important requirements:

1) domain-broadening information can be accurately extracted from X-ray diffraction profiles

2) the X-ray scattering domains correspond only to crystal growth surfaces

3) changes in the shape of size-distributions can be linked with established crystal-growth mechanism

Recent work has shown that the fulfilment of conditions 1) and 2) is complicated in polymineralic rocks due to a number of analytical limitations, particularly overlapping mineral reflections. Moreover, the crystal growth models outlined above represent time dependent crystal size changes, assuming fixed P-T fluid conditions, which differ by changing crystal growth parameters such as surface areas, supply of nutrients and interfacial energies. Nevertheless, in geological environments changes in mineral crystallisation are primarily driven by changes in P, T and composition in closed systems or by changes in fluid activity and solutes in open systems. Therefore, Warr and Peacor (2002) suggest using CSDs with caution when determining crystal growth mechanisms, and these should be preferentially applied to monomineralic clay samples of relatively simple geological histories. The following petrographic evidence suggests the kaolinite in these samples is suitable for analysis:

- mineral assemblages are simple, consisting of kaolinite, illite/smectite, calcite, quartz and minor chlorite
- overlapping reflections could be avoided by excluding samples containing chlorite
- the structural factor of kaolinite is well known

• there is no detrital kaolinite in the samples, as microscopically all kaolinite observed is authigenic

Results show that X-ray scattering domain size distributions for the selected samples are not lognormal (Fig. 59b). All the calculated α-β^2 values for kln are given in Table 7 and plotted in Fig. 60, and the change in shape produces an exponential curve, with a correlation coefficient of 0.7. This trend corresponds best with a crystal growth mechanism of continuous nucleation and growth in an open system, during which crystals nucleated at constant or accelerating rate and then grew according to the LPE with an unlimited fluid supply.
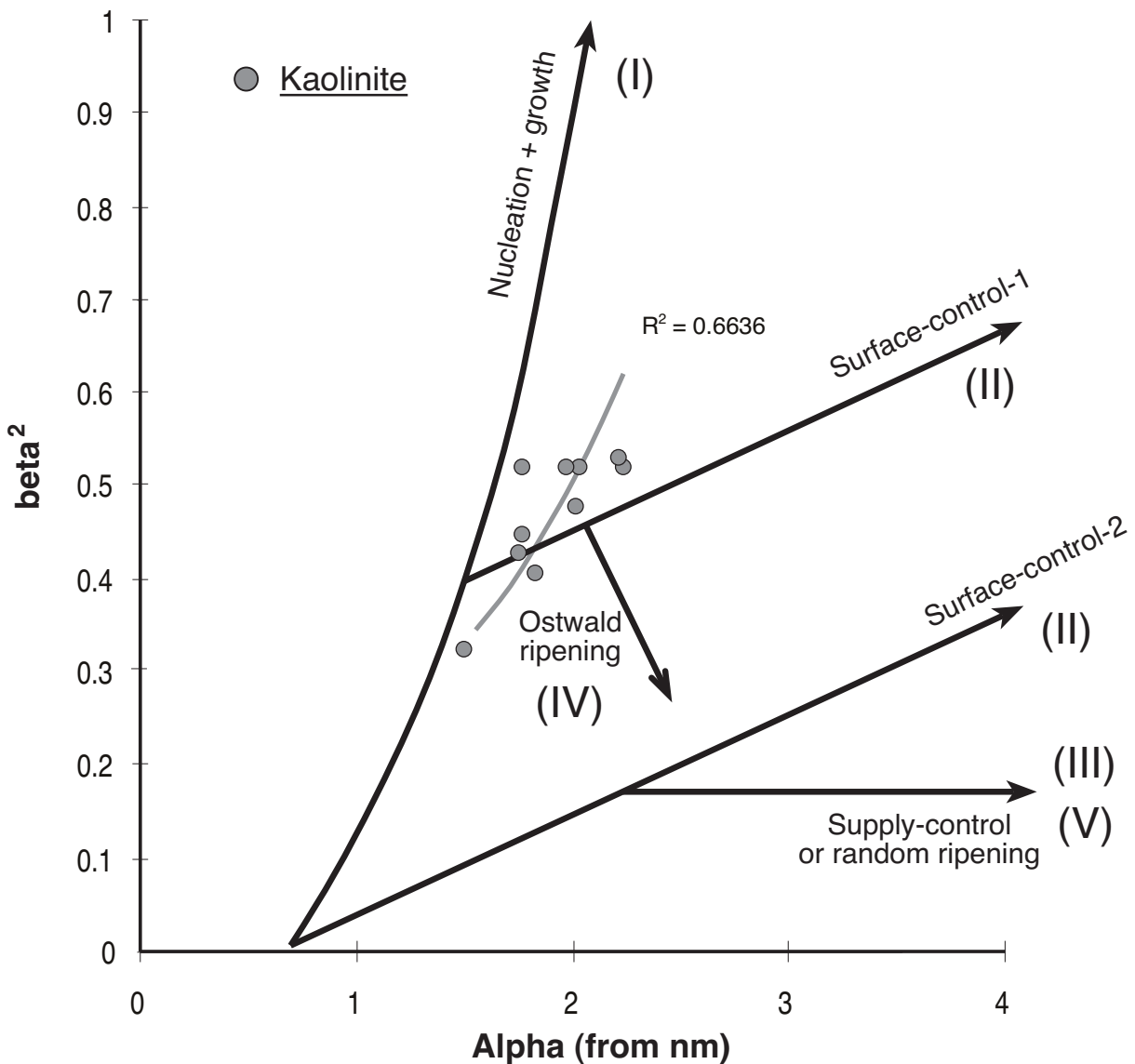
Figure 60. Predicted crystal size distributions (α-β^2) based on hypothetical crystal growth models using the program Galloper (Eberl et al., 1998). Plotted values correspond to samples of vein kaolinite (kln).

This crystal growth mechanism, together with the previous lines of evidence, suggest precipitation of the kln phase (together with cal3) during telogenetic alteration (sensu Morad et al., 2000), related to uplift, exposure and continuous meteoric water circulation through the basinal sequences. Alteration was especially intense along fault structures, which acted as preferential conduits for water, whereby kaolinite growth was favoured within the large pore spaces offered by the partly-filled fractures. This stage of fluid-rock interaction was accompanied by strong oxidation of organic matter within the coal seams (Méndez-Cecilia, 1985; Frings, 2002), which contributed to the acidification of circulating waters.

Sample	best mean	alpha	beta^2	CSD
CAN-01	11.7	2.22	0.51	not lognormal
CAN-02	9.6	2.03	0.51	not lognormal
CAN-06	7.7	1.76	0.51	not lognormal
CAN-07	11.8	2.21	0.52	not lognormal
CAN-08	7.7	1.83	0.4	not lognormal
CAN-10	7.2	1.74	0.42	not lognormal
CAN-24	7.3	1.76	0.44	not lognormal
CAN-28	9.5	2	0.47	not lognormal
CAN-30	9.5	2	0.51	not lognormal
CAN-45	5.6	1.62	0.22	not lognormal

Table 7. List of calculated α-β^2 parameters for samples of vein kaolinite (kln).

6.5 IMPLICATIONS FOR THE MINERAL GROWTH SEQUENCE

Based on the results presented here and on the earlier chapters, the mineral growth sequence in the Stephanian rocks can be subdivided in three stages. The first was related to the temperature rise before thermal peak conditions were achieved (stage 1), the second took place after the thermal peak, but still under burial conditions (stage 2), and the final stage occurred during the uplift and exhumation of the basin fill (stage 3).

The first stage was characterised by limited dilation of the veins, with a low vein to host rock ratio, and a close proximity between fluid and mineral sources. There are no signs for fluid-rock chemical disequilibrium related to mineral precipitation in the form of extensive wall-rock reactions, and advection-related mass-transport from an external circulating fluid would require extremely large amounts of fluids (Bjørlykke, 1994; Worden and Morad, 2000). It is considered more likely that vein materials were largely derived from the detrital fraction within the Stephanian rocks, and transported into solution in response to thermal, chemical and tectonic conditions. Therefore "local advection" of pore fluids, accompanied perhaps by diffusion, seems the most likely mass-transport mechanism.

Early transport was accompanied by rapid organic maturation during short-lived (hyper-thermal) temperature increments (Teichmüller et al., 1987; Uysal et al., 2000). The thermal increase was probably related to a combination of rapid burial and a high heat flux. During this stage a large amount of gas and water would have been liberated in response to organic-controlled reactions that dissolved silica and controlled quartz precipitation. Subsequently, still during the thermal rise, volatile generation declined (during prograde maturation) and mineral transformation reactions became predominant. Burial pore fluids underwent a progressive enrichment in cations within solution and a consequent rise in density. The amount of ions in solution inhibited gas solubility, reached fluid saturation and caused local precipitation of Ca-Mg-Fe (the less soluble ions) rich carbonate phase, namely the saddle dolomite (dolm).

Following thermal peak conditions, lower temperature diagenetic mineral dissolution-precipitation reactions controlled composition and mineral growth (stage 2). Mineral growth was related to vein reopening and dedolomitisation. A relative high fluid/rock ratio, and therefore an external fluid source, is considered likely but a definite origin for the fluid phase can not be determined. One possible source could have been the infiltration of marine water, subsequently modified, during tectonic subsidence of the area in the Cretaceous (Lobato et al., 1984).

Late alteration phases formed in response to low-T diagenetic and weathering reactions of the exposed and subjacent Stephanian rocks (stage 3). Alteration and clay mineral growth was controlled by a constant supply of meteoric water, which circulated preferentially along fault structures reaching the deeper parts of the stratigraphic section. Coal degradation and oxidation was associated with the acidification of the circulating waters, favouring mineral dissolution (Al^{3+} and Ca^{2+}) and carbonate-kaolinite precipitation, which may well be active at the present day.

6.6. HYDROTHERMAL ALTERATION AND QUARTZ GROWTH IN DIORITES

The formation of quartz veins within the diorite rocks of the studied basins constitutes a separate event in respect to the vein growth within the sedimentary sequence, and was related to the hydrothermal alteration of the magma intruding along coal seams. The alteration reactions of primary igneous minerals proceeded as irreversible, exothermic transformations, which generally denote temperatures below 300°C (Alt, 1999). Some of these reactions are:

HORNBLENDE $\Rightarrow$ chlorite + carbonate + hematite   BIOTITE $\Rightarrow$ chlorite ($\pm$ carbonate)

PLAGIOCLASE $\Rightarrow$ carbonate + epidote   CLINOPYROXENE $\Rightarrow$ actinolite + chlorite

In the case of the CMB and SB intrusions, dolomite was the main carbonate phase formed instead of calcite (Fig. 23a). The absence of glass and the fine-grained size of minerals are also indicative of subvolcanic conditions, i.e. pressures below 200 MPa (Winkler, 1979). The fluid phase necessary to activate most of these transformations was probably supplied by the abrupt transformation of coal to coke along the contact with the magma at temperatures between 200° and 300°C. The coke aureoles surrounding the intrusive bodies are generally several metres wide, and during formation liberated important amounts of water, CH_4 and CO_2. The mineral reactions described would have released minor amounts of silica into the "hot" circulating fluid, leading to precipitation of quartz in the available fissures during the latter stages of cooling. The related fluid composition and pressure-temperature conditions are reflected in the fluid system entrapped as primary inclusions in qtz2 (chapter 5).

Kaolinite is present within qtz2 veins in two different forms. A first type occurs as fragments trapped within primary fluid inclusions of the hydrothermal quartz and in very minor amounts in the igneous host rock (Fig. 23a). The high mole fraction of CO_2 in the fluid (> 0.1 in the vapour phase) would have favoured the formation of carbonates, minor clays, kaolinite and quartz; instead of the diagnostic Ca-Al minerals (Winkler, 1979; Schiffman and Day, 1999). The second type of kaolinite, clearly the more abundant, was related to a late low-temperature alteration of the hydrothermal quartz, probably cogenetic to the kln phase.

CHAPTER 7: FLUID INCLUSION RE-EQUILIBRATION

In the two previous chapters the different generations of fluids, their composition, P-T-X conditions and possible origin in the Sabero and Ciñera-Matallana basins have been outlined. An important feature not yet considered is the widespread occurrence of fluid inclusion re-equilibration in fissure quartz of the CMB. The low content of fissure quartz in the sampled veins of the SB prevented from any analysis of the fluid inclusions, therefore, the conclusions presented this chapter can not be extended to this basin.Fluid inclusions should not be considered as simple cavities filled with fluid, but as an integrative system which also comprises a part of the host mineral. The formation of fluid inclusions related textures is controlled by three main factors: external geological processes (e.g. changes in temperature-pressure), crystal dynamics of the host mineral and physico-chemical processes at the crystal-fluid interface. Textures are then highly useful in order to draw conclusions about the interaction between a fluid inclusion and its host mineral and of this mineral with its environment.

The observed re-equilibration textures of type 1 and 2 inclusions in qtz1 mark the onset of a specific event, which occurred at some stage following qtz1 crystallisation and before the second generation of blocky calcite (cal2). This chapter examines the fluid inclusion re-equilibration textures within the fissure quartz (qtz1) and demonstrates how they provide excellent indication of high heat flow conditions experienced by the clastic sediments within the high diagenetic to very low-grade metamorphic environment of the CMB.

7.1. DEFINITION OF RE-EQUILIBRATION

The ideal isochoric model for fluid inclusions assumes that they behave as compositionally and volumetrically closed systems after formation. When such conditions are fulfilled, the inclusions preserve the original parent fluid, which in many cases represents that associated with mineral growth. Re-equilibration is a term that encompasses any type of post-entrapment modification that takes place in fluid inclusions as a result of a departure from the P-T path of the original isochore for the inclusion (Fig. 61). This phenomenon has been a matter of intense investigation by fluid inclusion researchers due to the importance of evaluating any changes that may invalidate the interpretation of P-T-V-x formation conditions. Quartz, both natural and synthetic, has received by far the most attention (Pêcher, 1981; Gratier, 1982; Sterner and Bodnar, 1989; Bakker and Jansen, 1990).
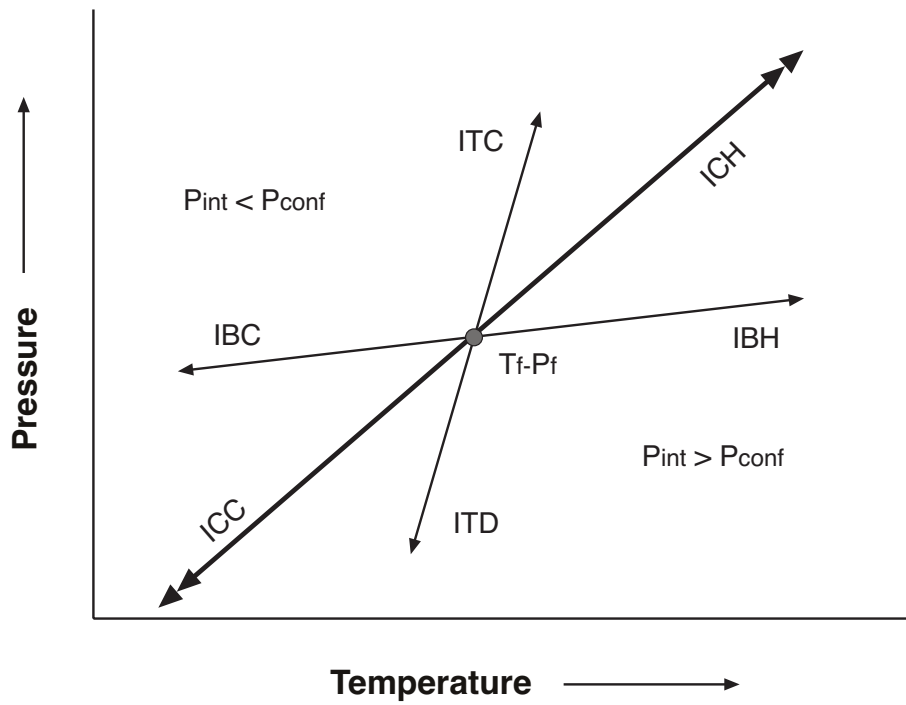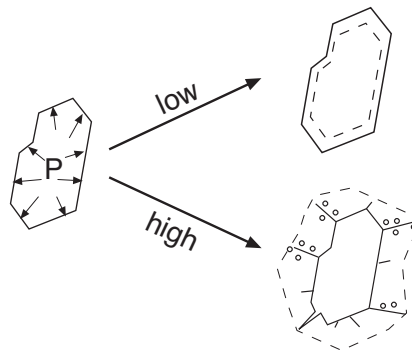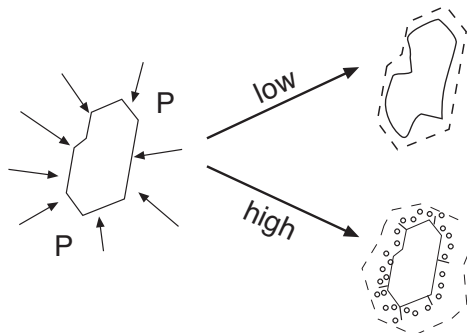
Figure 61. Schematic diagram illustrating the different P-T paths that fluid inclusions can experience after entrapment (T_f-P_f) and the expected textural modifications produced by the fluid re-equilibration to the surrounding conditions.

Re-equilibration of fluid inclusions follows several intermediate and progressive steps, namely, stretching, formation of irregular cavity walls, necking down, leakage and finally, partial and total decrepitation (e.g. Roedder, 1984). Experimental research has provided an insight into the variety of textural changes of fluid inclusions in natural rock. Such studies characterise the types of textures related to specific re-equilibration paths, and evaluate the relative importance of different factors that influence re-equilibration. Size and shape of the inclusion, its fluid composition and the physical and chemical properties of the host mineral have been shown to be important.

Textural variations caused by internal overpressure of fluid inclusions are considered to be limited. Stretching, i.e. inelastic deformation of the inclusion wall is not a feature that will be texturally preserved in natural rock (e.g. Bodnar and Bethke, 1984). Internal overpressure may cause a fluid filled cavity to explode (decrepitation), if it exceeds the lattice strength of the host mineral (Leroy, 1979; Gratier and Jenaton, 1984; Bodnar et al., 1989; Vityk et al., 1994 and 1995). Such brittle deformation changes the shape of the inclusion cavity creating cracks, which subsequently can be modified by recrystallisation to form characteristic textures, such as extremely irregular shapes and planes of satellite inclusions (i.e. decrepitation clusters). Pêcher (1981) and Bakker and Jansen (1991) documented the formation of cracks at higher confining pressures, produced both during internal overpressure and underpressure experiments, although some controversy exists as to the formation of decrepitation clusters under experimental conditions (Sterner and Bodnar, 1989).

Re-equilibration textures caused by internal underpressure are well documented and display a wide variety of morphologies. Progressive stages of modification are recognised as the parent inclusion is redistributed into the host mineral. Initially, scalloped textures may develop by intense dissolution of the walls, resulting in highly irregular and rough inclusion morphologies (Pêcher, 1981; Bakker and Jansen, 1991; Vityk et al., 1995; Vityk and Bodnar, 1995). Arc, hook, ring and semi-annular textures develop during advanced re-equilibration (Pêcher, 1981; Vityk and Bodnar, 1995). Audétat and Günther (1999) observed similar structures in natural samples, where the migration of inclusions was suggested to cause the formation of tails, giving the inclusions an arc-like appearance. Three dimensional inclusion clusters or haloes of small secondary inclusions result from further re-equilibration (e.g. Vityk and Bodnar, 1995). Such clusters are also reported as implosion haloes (e.g. Sterner and Bodnar, 1989) or sweat haloes (e.g. Audétat and Günther, 1999). During the most advanced stages of re-equilibration, highly irregular dendritic-like haloes develop with near closing of the parent inclusion (Sterner and Bodnar, 1989; Vityk and Bodnar, 1995). The original fluid of the parent inclusion is redistributed in an irregular shaped cloud of numerous small secondary inclusions.

Fluid inclusion studies of decrepitation features in natural samples have focused on case studies from ore deposits (Foley et al., 1989) and from high to medium grade metamorphic environments (Swanenberg, 1980, Boullier et al., 1991, Hurai and Horn,

1992; Vityk et al., 1996; Küster and Stöckhert, 1997). These studies address the use of decrepitated inclusions as indicators for thermal cracking of minerals (quartz) and as geobarometers for tectonic reconstruction in orogens. In contrast, decrepitation in diagenetic and very-low-grade metamorphic environments (sub-greenschist facies) has received little attention. Here, studies have focused on the resetting of homogenisation temperatures within calcite and quartz cements due to stretching of inclusions induced by overheating and burial (Goldstein, 1986; Burruss, 1987b; Osborne and Haszeldine, 1993 and 1995).

7.2. RE-EQUILIBRATION TEXTURES IN VEIN QUARTZ (QTZ1)

A wide range of re-equilibration textures can be observed in type 1 and 2 inclusions of vein quartz (qtz1) in the samples from the CMB basin (Fig. 62). Re-equilibration was, however, not uniform. Both unaffected and highly modified inclusions may occur within the same assemblage. A clear relationship has been observed between inclusion size and the intensity of re-equilibration, whereby larger inclusions are typically more affected. A range of intermediate stages of modification can be recognised in all qtz1 samples, including veins that do not contain the latter cal2 mineralisation phase (sample 31, Table 1). The only exception is sample 27, where only one textural variety was observed (Fig. 62c). The re-equilibration textures identified are summarised as follows.

Scalloped inclusion walls

This first group of inclusions is characterised by numerous irregularities, sharp edges and re-entrants in the inclusion walls, which suggests dissolution of the adjacent quartz. As a consequence inclusions become corroded, and adopt chaotic and irregular shapes. Therefore we use the term scalloped. This texture is predominant in large-sized inclusions that are both liquid and vapour rich (Fig. 62a).

Annular-ring textures

These exhibit a variety of shapes, which show no relation to whether the inclusion is aqueous or vapour-rich. A common feature to all is the smoothed, rounded and crystallographically defined inclusion walls. One type is the arch-hook shape, in which the ring is not totally closed (Fig. 62b). A second type consists of inclusions with a single, relatively small patch of enclosed crystallised quartz, pillaring the inclusion walls. A third type that occasionally occurs is comprised of tubular ring-shaped inclusions.
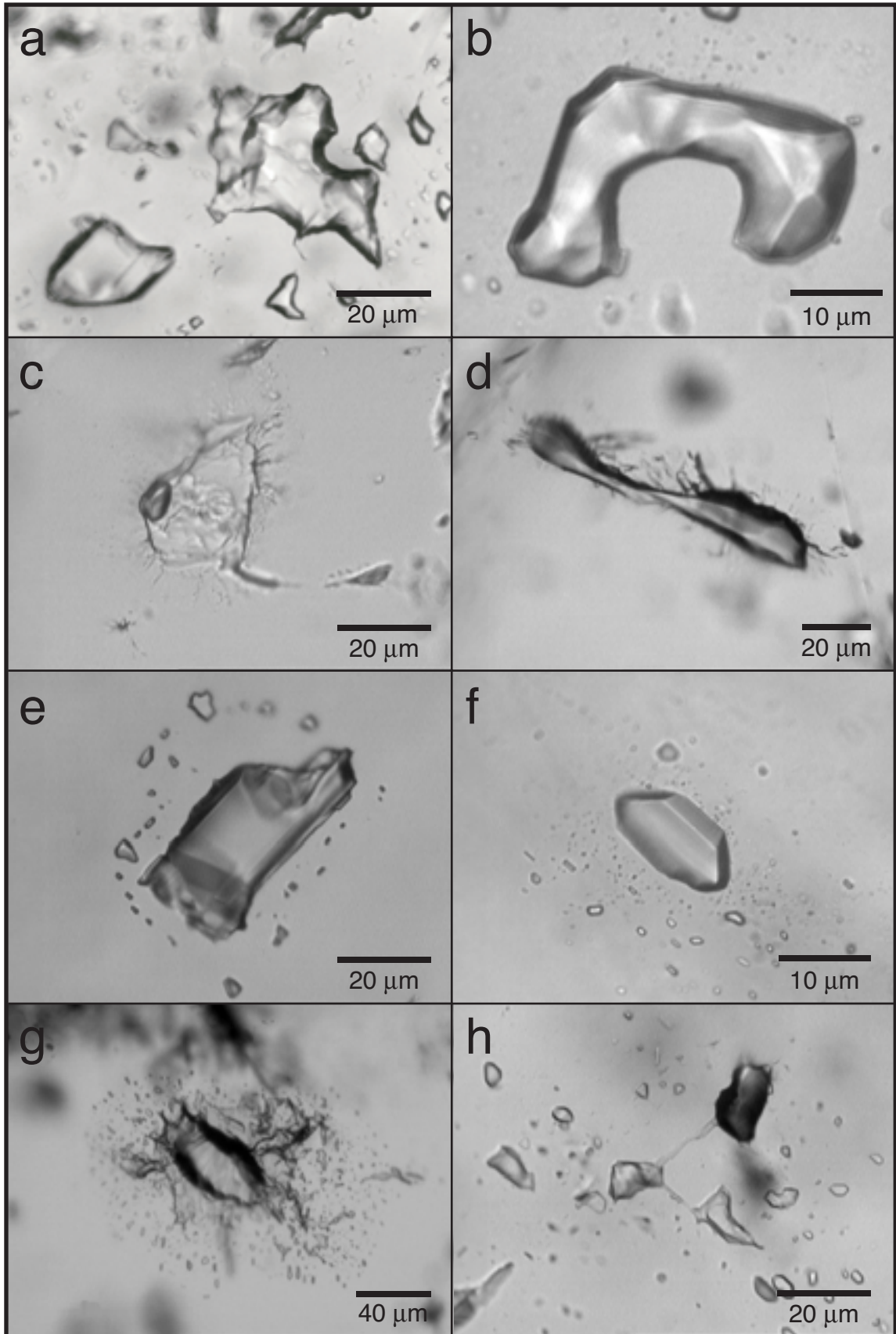
Figure 62. Photomicrographs summarising the different re-equilibration textures observed in type 1 and 2 fluid inclusions of qtz1 from sample 28, locality 5 (a, f, g, h); sample 27, locality 9 (c); and sample 42, locality 12a (b, d, e). See text for further explanation.

Hairy textures

These inclusions have numerous micro-tubes or micro-fractures, which radiate from the walls to give a hairy appearance. This texture occurs in both liquid-rich (Fig. 62c) and vapour-rich inclusions (Fig. 62d). In detail these tubes have highly irregular forms and very small diameters, and are generally filled with H_2O (Raman detected). The larger tubes and fractures typically occur around vapour-rich inclusions (Fig. 62d).

Haloes

Haloes are defined as a group of small daughter inclusions around a regular shaped parent inclusion (Fig. 62e & f). They consist of either planar or three-dimensional arrays of minute inclusions. In our examples, they occur preferentially around vapour-rich inclusions. The daughter inclusions may outline the initial shape of the parent inclusion (Fig. 62e), whereby both daughter and parent have negative crystal shapes and similar compositions. But compositional differences were also observed in parent-daughter combinations (Fig. 62f). Inclusions with semi-irregular wall shapes may also develop such haloes.

Decrepitation clusters

True decrepitation clusters consist of single planar fractures branching out from the inclusion walls in all directions and completely surround the parent inclusion (Fig. 62g). The fractures did not heal completely, giving a very irregular appearance to the parent inclusion. The numerous minute inclusions formed in the healed part of the fracture are also highly irregular, in contrast to the haloes in Fig 62e & f. These clusters show absence of re-crystallised inclusion-free quartz directly adjacent to the parent inclusion, and the fractured haloes are more oval in shape. Such textures are observed around both liquid-rich and vapour-rich inclusions.

Necking down

Typical necking-down textures are observed as small tubes of varying geometry that connect larger inclusions (Fig. 62h). Total separation of fluid phases may occur when the connecting tube is sealed, causing formation of all-liquid and all-vapour fluid inclusions. In the example shown in Fig. 62h, phase separation has nearly reached completion, as the darker vapour-rich part is connected by a narrow tube to the brighter aqueous-rich part.

7.3. CONDITIONS AND MECHANISMS OF RE-EQUILIBRATION

The variety of textures observed in qtz1 indicates that several mechanisms operated simultaneously during re-equilibration. Some of the previously described experimental re-equilibration textures (especially scalloped and annular-ring structures) have been formed at both internal over and underpressurised conditions. Variables other than temperature and pressure alone play an important role in the development of re-equilibration textures. Material properties of the host are usually completely ignored. Sterner et al. (1995) suggested that even chemical potentials of fluid components inside the inclusions might play an indirect role, at least in experimental studies.

In principle, two independent processes can change the morphology of individual fluid inclusions: 1. mechanical decrepitation, i.e. sudden change in the total inclusion volume by newly formed microcracks and/or dislocation arrays; 2. chemical dissolution and precipitation of quartz on the inclusion walls. In the first mechanism, chemical interaction between fluid and host mineral is excluded and the host mineral is considered as a homogeneous solid medium.

A first approach is to consider re-equilibration simply as a brittle mechanical phenomenon, described by physical variables such as pressure, temperature, inclusion shape and volume. In the case of fluid overpressure the inclusion acts as an internally pressurised crack (Lacazette, 1990). Fractures will generate and propagate from the inclusion walls if the internal pressure is above the host mineral lattice strength. These fractures tend to be planar and their orientation and intensity is governed by the mineral properties. Nevertheless, crack growth may occur at stress levels below those necessary to exceed lattice strength by mechanisms such as stress corrosion (by water), dissolution, diffusion, ion exchange and microplasticity, all of which may be affected by the chemical environment (e.g. Kronenberg et al., 1986)

Dissolution and precipitation of the host mineral (in this case quartz) is the main mechanism by which fluid inclusions form. Inside inclusions, this process does not cease after a pocket of fluid has been entrapped. Necking-down divides such pockets into many inclusions, which tend to obtain negative crystal shapes. This process depends on the solubility of the host mineral in the inclusion fluid, which is enhanced at higher pressures and temperatures. The cause for the subsequent formation of irregular walls is, however, unclear. As observed in internal underpressure experiments, fluid inclusions tend to be redistributed as irregular clouds of many small inclusions. Transport of fluid away from the parent inclusion may occur along microcracks or crystal defects, such as dislocations (Bakker and Jansen, 1994). Some components of that fluid, especially water, may be preferentially lost in response to gradients in pressure and/or water fugacity when re-equilibration takes place. Consequently, quartz is transported in the opposite direction, and the parent inclusion will tend to close. In the naturally re-equilibrated inclusions analysed in this study, it has been observed that water (Raman detected) is the predominant

component in decrepitation clusters, in radial tubes and fractures of the hairy textures, as well as in the haloes exemplified in Fig. 62f. Additionally, vapour-rich re-equilibrated inclusions show lower fluid densities than intact inclusions (lower Tm_{car}).

7.4. CAUSES OF FLUID INCLUSION RE-EQUILIBRATION IN THE CIÑERA-MATALLANA BASIN

Isochore calculations for type 1 and 2 aqueous inclusions in the fissure quartz (qtz1) indicate that in order to reach internal overpressures of about 100 MPa at low confining pressures, the surrounding temperature needs to rise about 50 to 60 °C for the aqueous-rich inclusions (Fig. 63). This overpressure is high enough to decrepitate inclusions larger than 30 μm (Bodnar et al., 1989; Lacazette, 1990). In the same temperature interval, vapour-rich inclusions can attain overpressures of only 10 to 15 MPa (Fig. 63). Internal underpressures in the inclusions, caused by further burial and/or cooling of the Stephanian sequence, would reach values of 56 MPa at most (maximum fluid trapping pressure), clearly not enough to induce significant textural re-equilibration.
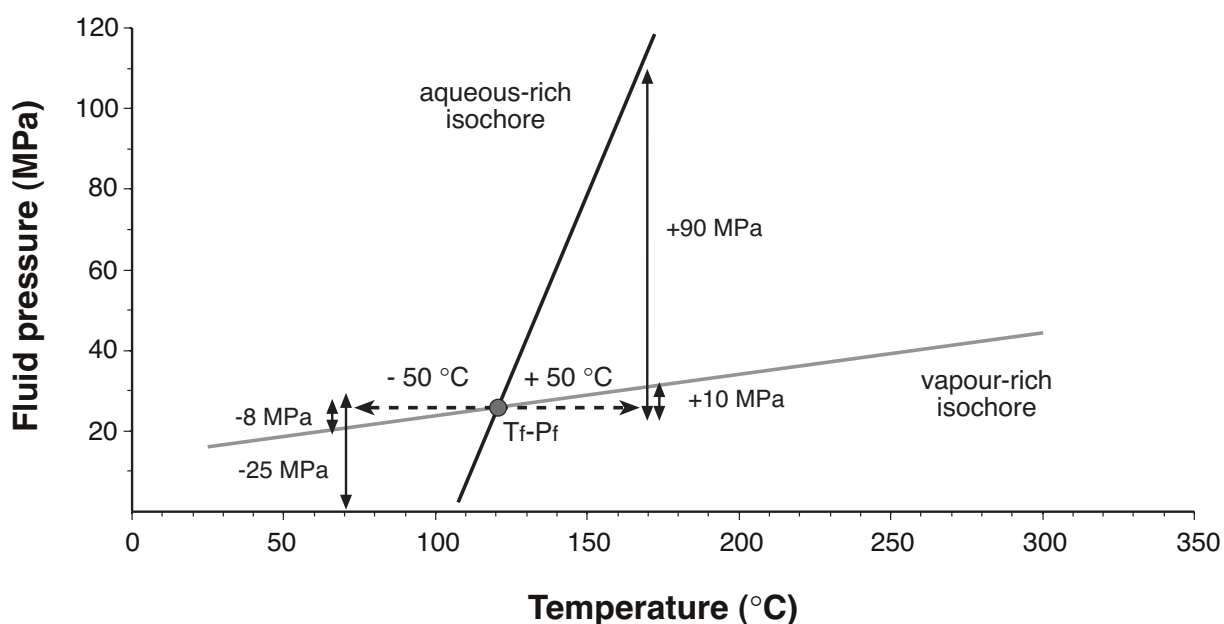
Figure 63. Temperature-pressure diagram illustrating the under- and overpressure experienced by aqueous- and vapour-rich inclusions of type 1 and 2 in qtz1 for a temperature drop/rise of 50°C from the original trapping conditions (T_f-P_f). Note that the internal pressure difference is much higher for aqueous- than for vapour-rich inclusions. Also the initial low trapping pressures limit the amount of possible underpressure.

Most of the fluid inclusion textures observed in vein quartz (qtz1) of the CM basin appear to have been formed initially by brittle fracturing of the host mineral, suggesting decrepitation was the main re-equilibration process. The factors that could produce re-equilibration/decrepitation features are discussed as follows.

Mechanical stress

External mechanical stress applied to the host crystal can produce re-equilibration of inclusions by inducing microfractures and dislocations to migrate towards the inclusion walls. As a result the fluid filled cavity may collapse, similarly to the effect of underpressure, and the fluid can be redistributed in the remaining parts of the inclusion. According to the constraints presented in chapter 5, deformation occurred after the formation of type 1 and 2 fluid inclusions. In many veins single crystals of qtz1 are extensively microcracked and the precipitation of cal2 within these cracks locally generated small, annealed fractures that extended into the host quartz and now form minute inclusion trails (Fig. 64a). This situation is exemplified in sample 27, where virtually all inclusions are re-equilibrated in the most deformed of qtz1 crystals and present a "hairy" texture type (Fig. 62c).
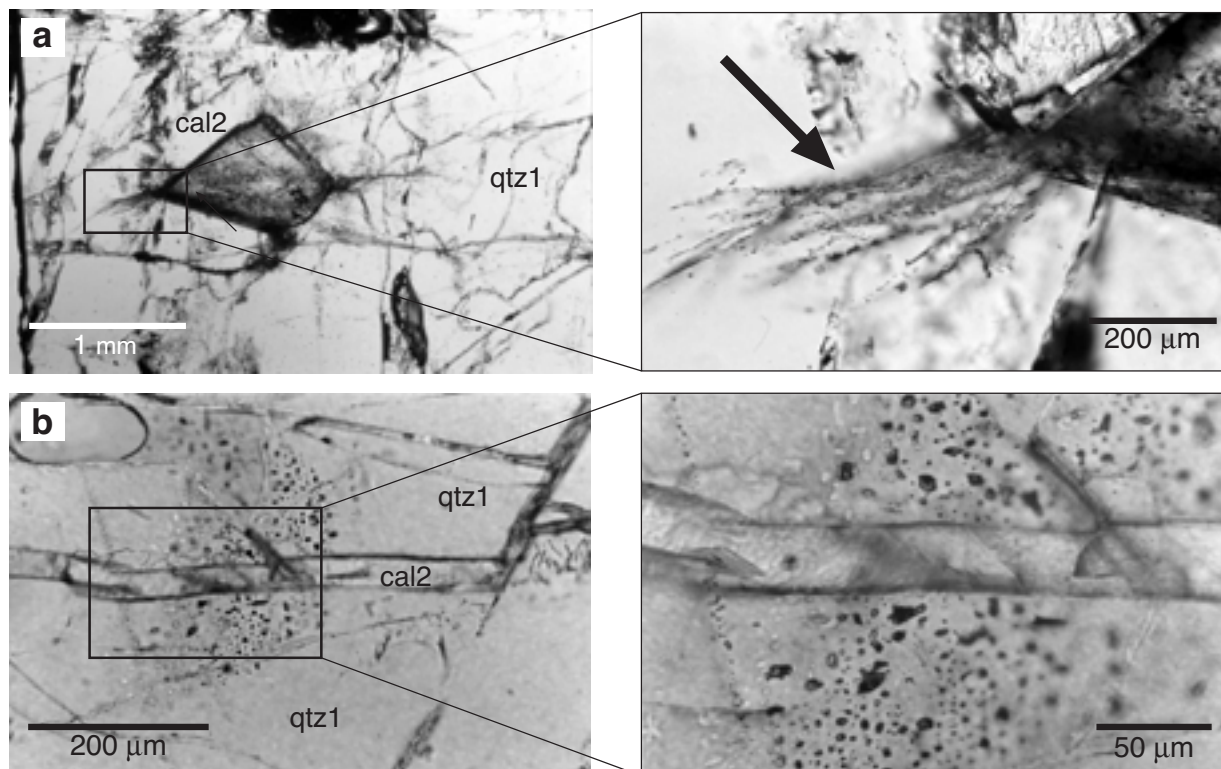
Figure 64. Photomicrographs showing the brittle deformation features in qtz1 accompanied by cal2 precipitation in the same veins. (a) Microfractures in qtz1, radiating from the contact between both mineral phases, decorated by small inclusions. Sample 60 (locality 15). (b) Cal2 filled microfracture crosscutting a cluster of primary type 1 inclusions. Inclusions close to the fracture walls have irregular shapes probably due to deformation induced re-equilibration. Sample 26 (locality 4).

Nevertheless, intracrystalline deformation features, such as twinning, pressure shadows, undulose extinction, and the development of subgrain boundaries, are rare or absent in most samples. Optical extinction between fracture planes is mostly sharp and uniform. In addition, re-equilibration textures are observed in both intensively cracked quartz and in virtually undeformed crystals (e.g. sample 31). Moreover, the main effect of brittle fracturing at this stage of development would be expected to cause refilling of original inclusions with the highly saline fluid responsible for cal2 precipitation (compositional re-equilibration). This feature is locally observed when the microcracks forming type 3 inclusions cut type 1 and 2 assemblages, but the inclusions affected can be clearly differentiated from other re-equilibrated ones (e.g. sample 31; appendix table). Therefore, it is considered that apart from cases of direct cross cutting (Fig. 64b), fracturing has not altered the properties of pre-existing fluid inclusions and external mechanical stress can be excluded as the principle cause of inclusion re-equilibration.

Decompression

A decrease in the confining pressure of the host quartz is a feature that may result from fast erosion and/or rapid uplift rates. The original fluid trapping pressures of primary inclusions (and hence for the mineral crystallisation) were low for qtz1, and ranged between 10 and 56 MPa. A fast uplift of the sequence caused by erosion and/or exhumation would not generate a pressure gradient high enough to induce extensive decrepitation, since a minimum pressure difference of 85 MPa is required in quartz to influence a fluid inclusion as large as 35 μm (e.g. Lacazette, 1990). The required pressure difference becomes much higher as the inclusion size decreases. The CMB basin is estimated to have reached a maximum thickness of 2500m (Villegas, pers. comm.; Frings, 2002), and it was overlain by a thin discordant sequence of Cretaceous cover, with a preserved thickness between 150 and 450 m in areas nearby (Lobato et al., 1984; and Alonso et al., 1990). This represents an extra burial confining pressure of 40 MPa at most, assuming lithostatic conditions and maximum thickness of sedimentary cover. Vein samples of qtz1 with decrepitated inclusions are reported throughout the stratigraphic sequence of the basin (Pastora to Bienvenidas Formations), and no difference has been observed in the intensity and character of the textures in relation to burial depth. These features also indicate that P-T paths that generate fluid underpressure within inclusions (cooling and burial) are not realistic causes of re-equilibration in this setting.

Heating

Maximum temperatures reached in the sedimentary succession can be estimated to have not exceeded 170-220 °C, based on the conversion of vitrinite reflectance values with the formula of Barker and Pawlewicz (1986) presented in Table 8. Such estimates are also in

agreement with the attained local anchizonal grades of metamorphism (Frings, 2002). Although the heating period was, geologically speaking, relatively short, the enhanced rock temperatures were high enough to generate minimum fluid overpressures of 50 to 140 MPa within the inclusions (Fig. 65). In such a case, the widespread re-equilibration of inclusions in the fissure quartz across the basin can be explained.

Formation	VR max	VR min	Max depth (m)	T max (°C)	T min (°C)
Matallana	1.31	1.31	200	174	174
Bienvenidas	1.66	1.303	400	199	173
San José	2.04	1.493	600	220	188
Pastora	2.66	1.676	1000	248	200
S. Francisco	2	1.527	600	218	190

Table 8. Correlation of VR with rock temperatures for the Ciñera-Matallana basin, according to the formula of Barker and Pawlewicz (1986): ln(Rm) = 0.0096 (T)-1.4. Rm is mean random vitrinite reflectance (in %) and T is maximum burial temperature. Reflectance data from Méndez-Cecilia (1985) measured on coal seams.
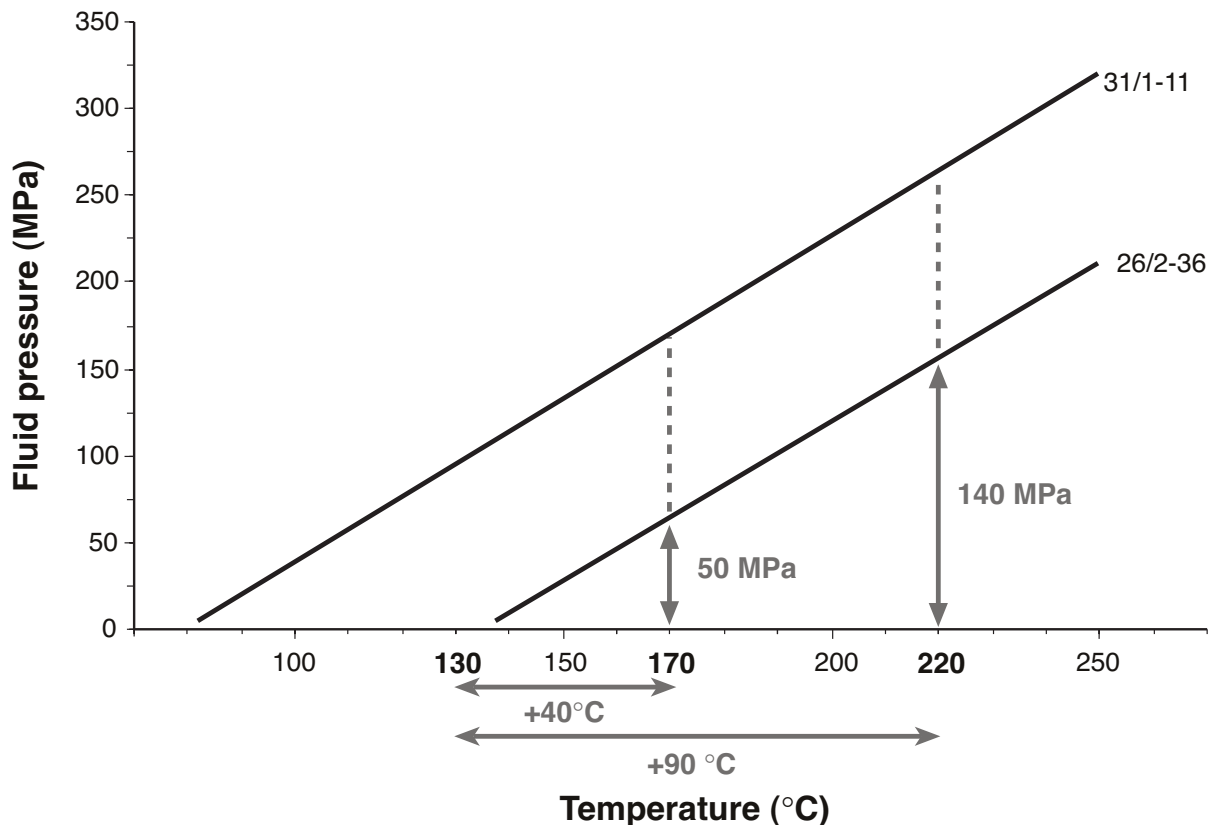
Figure 65. Temperature-pressure diagram with isochores for aqueous-rich fluid inclusions in qtz1 representing the lower (inclusion 31/1-11) and the higher (inclusion 26/2-36) homogenisation temperatures. Isochores were calculated for pure H_2O (Haar et al., 1984) as the low concentration of CH_4 and NaCl do not significantly affect their positions.

There are strong reasons for relating peak palaeotemperatures and therefore inclusion decrepitation to the high heat flow associated with Permian igneous activity. This line of evidence is of key importance for the discussion of possible mechanisms of heat transmission and for the reconstruction of the thermal-fluid history of the Stephanian basins (particularly of CMB), as analysed in detail in the next chapters.

CHAPTER 8: FLUID-TEMPERATURE DISTRIBUTION AND VEIN EVOLUTION

The results obtained in the previous chapters are here presented in the geological maps and stratigraphic columns of the two studied basins. The spatial distribution of fluid temperatures and re-equilibration textures along the CMB is important for considering possible sources and transmission mechanisms of heat. In addition, the spread on the geological maps of stable isotope data provides insights in the possible origin of the vein calcite and associated saline fluids. Finally, the fluid and mineral evolution of the two vein systems studied, reflecting the thermal maturation/diagenetic processes within the basinal rocks, is summarised in two diagrams.

8.1. FLUID TEMPERATURES IN CIÑERA-MATALLANA

Fig. 66 presents a summary of the fluid P-T-X data from the fluid system H_2O-CH_4-CO_2 ±NaCl, contemporaneous to vein quartz (qtz1) precipitation in the CMB. The distribution of vein quartz showing re-equilibrated inclusions is concentrated in a vertical section of 500 to 600 m, which ranges from the middle part of the Pastora Fm to the upper part of the Bienvenidas Fm. This section contains most of the coal seams present in the coalfield and all but two of the exposed diorite sills, which never outcrop above the uppermost San José Fm. The fluid data show no clear changes in pressure or temperature with depth, indicating similar conditions of quartz precipitation throughout the section. A notable discrepancy (about 70°C) occurs between the fluid inclusion homogenisation temperatures and the peak palaeotemperatures attained in the coal, according to R_0 measurements converted using the Barker and Pawlewicz (1986) formula. Therefore, both indicators can not be correlated in this setting to define thermal peak conditions, and this may imply that such method cannot be applied in inclusions of non-carbonate diagenetic minerals (Barker and Goldstein, 1990). Most veins are located in the vicinity of coal seams or organic-rich shales, which are the levels intruded preferentially by the diorites. This suggests that a link may exist between the occurrences of fluid inclusions decrepitation textures and the heat supplied by the magmatic bodies (see column in Fig. 66), although only in the Tabliza anticline mineralised fissures in the clastic sequence are found in the direct surroundings of diorite sills. The intrusives outcrop mainly on the western half of the basin, but the real extent of most sills laterally and at depth is unknown.
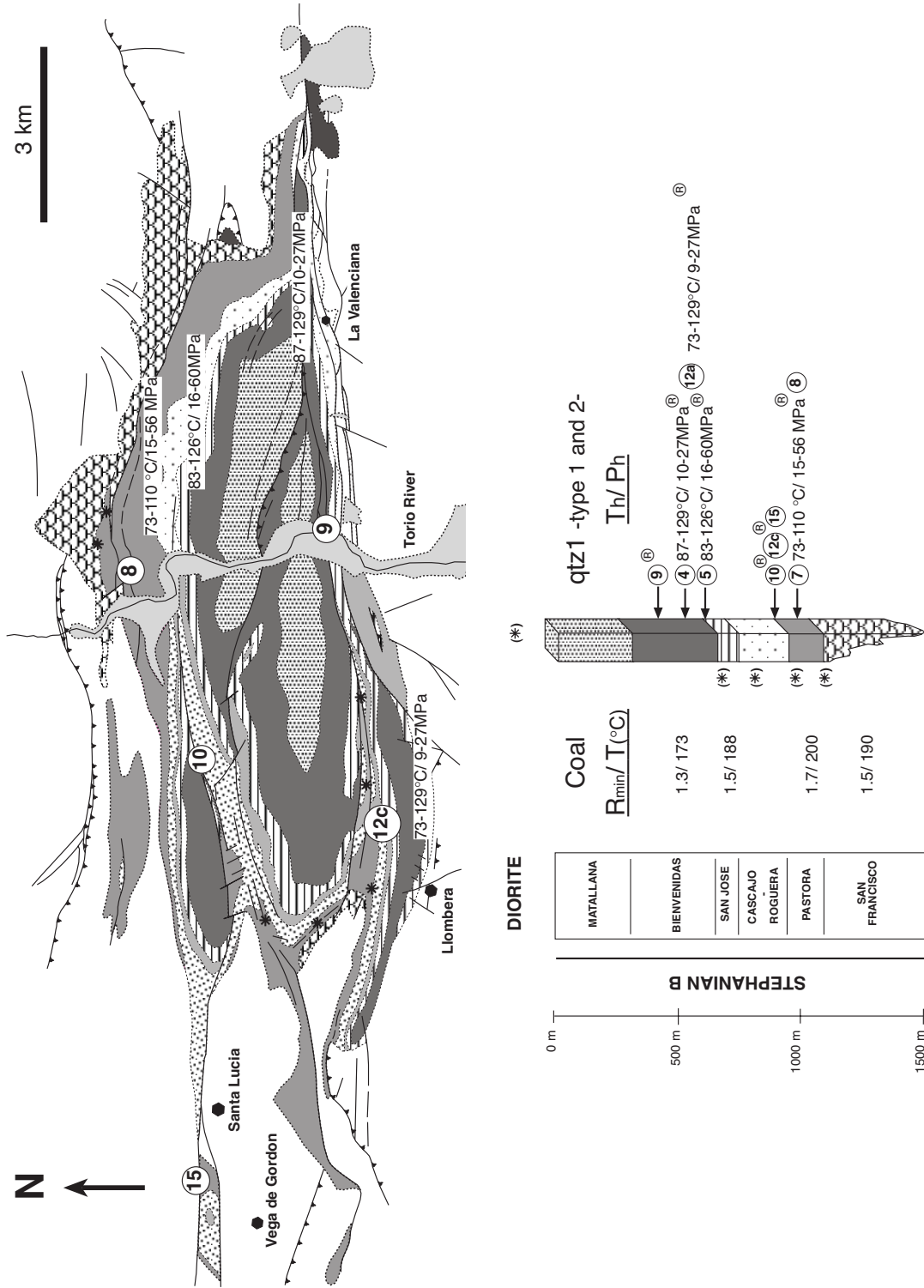
Figure 66. Distribution of entrapment temperatures (T_t) and pressures (P_t) of the H_2O-CH_4-CO_2±NaCl fluid system, contemporaneous with precipitation of vein quartz in the Stephanian clastic rocks of the CMB (type 1-2 inclusions in qtz1). ® = re-equilibration of fluid inclusions observed. In localities where no values are reported petrographic reconnaissance of the inclusion type and Raman identification of the fluid components was undertaken.
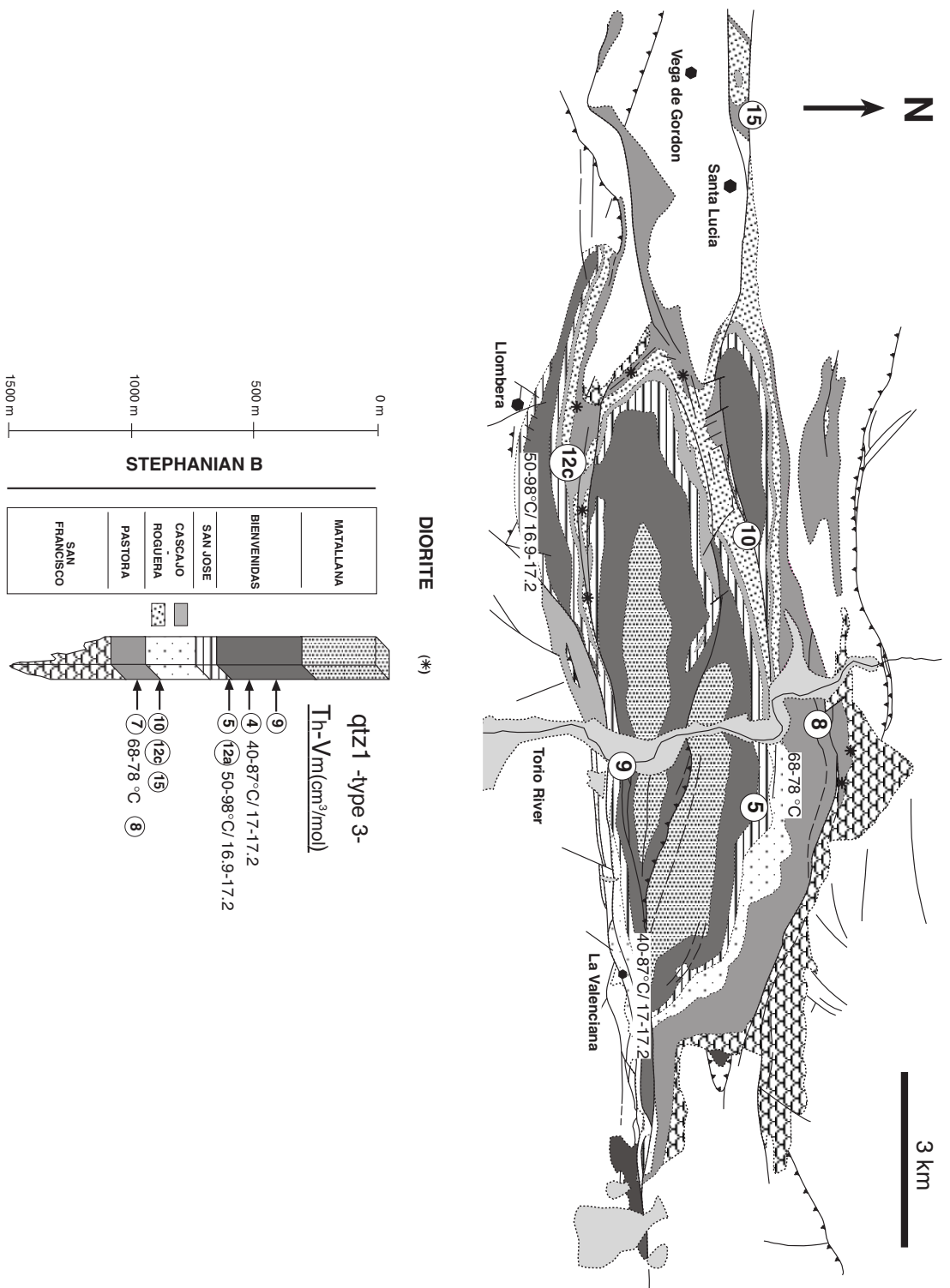
Figure 67. Distribution of homogenisation temperatures (T_h) and molar volumes (V_m) of the H_2O-$NaCl$-$CaCl_2$±CH_4 fluid system in vein quartz (qtz1) within the Stephanian clastic rocks of the CMB, entrapped as secondary inclusions (type 3).
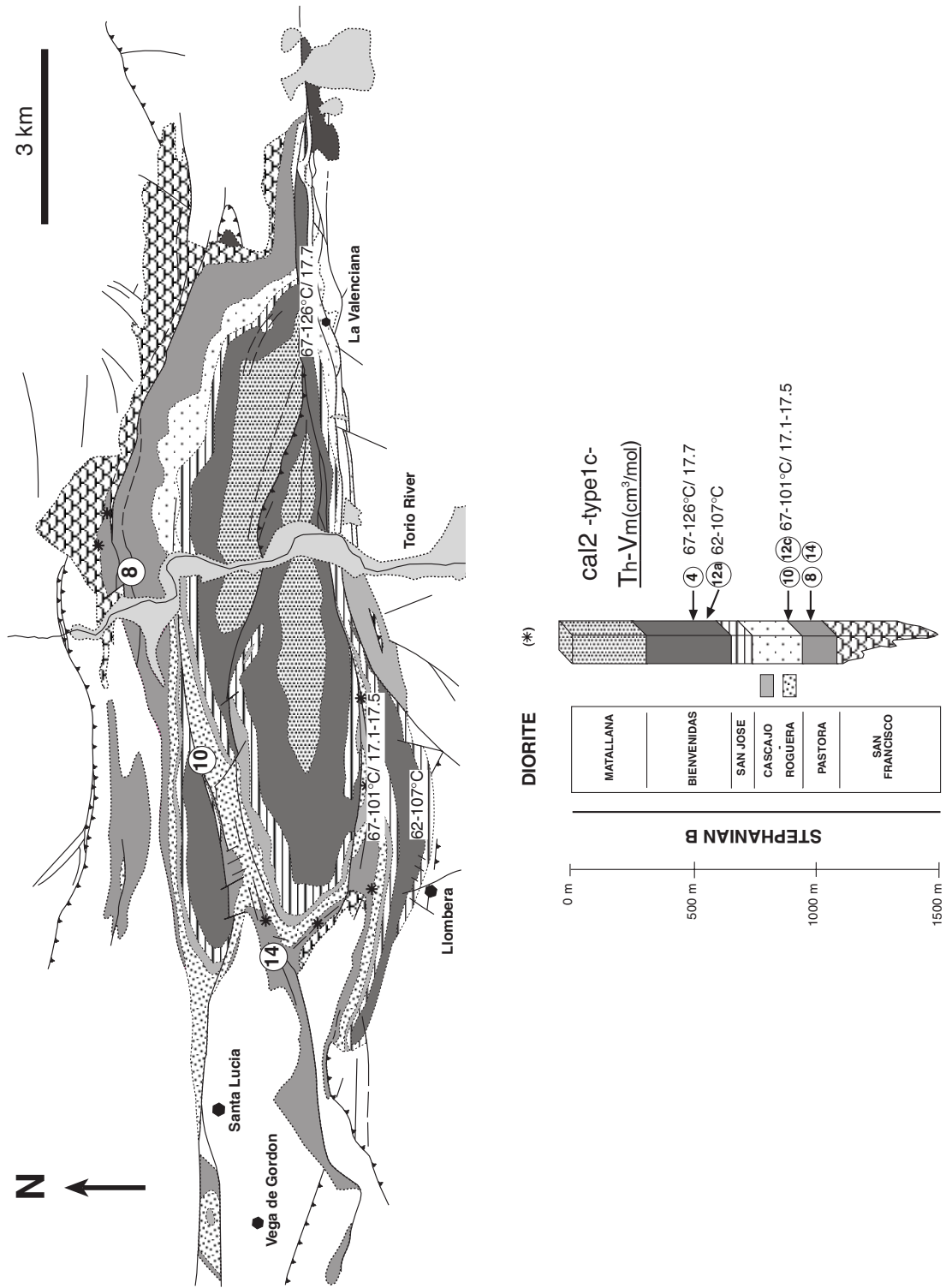
Figure 68. Distribution of homogenisation temperatures (T_h) and molar volumes (V_m) of the H_2O-NaCl-$CaCl_2$-CH_4 fluid system associated with precipitation of vein calcite (cal2) and dedolomitisation in the Stephanian clastic rocks of the CMB.

The secondary saline fluid system in qtz1 was not related with the conditions highlighted above. Fig. 67 reveals that uniform and low fluid temperatures were attained for the system H_2O-NaCl-$CaCl_2$-CH_4 along the basin and throughout the stratigraphic column, whereby no differences in fluid density can be observed with depth. Fig. 68 shows the same conditions for the primary H_2O-NaCl-$CaCl_2$-CH_4 fluid preserved in vein calcite (cal2).

8.2. A MARINE ORIGIN FOR THE VEIN CALCITE (cal2)

The isotopic data for cal2 in the CMB, summarised in Fig. 69, are regionally more extensive than the fluid P-T-X constraints and cover about 800m thickness of the clastic sequence. A slight increase in $\delta^{13}C$ and $\delta^{18}O$ values (± 1 ‰) with stratigraphic depth can be recognised, although this may reflect more exposure of the upper formations to meteoric water circulation (Hoefs, 1997). Oxygen isotopic values in cal2 are similar to those for late calcite veins collected from different older Palaeozoic formations in areas adjacent to the basin, but close to the discordance base (samples 14 to 22, see appendix). Despite these similarities, vein calcite in the surrounding Palaeozoic rocks is richer in heavy carbon content (about 0 ‰ PDB). The few scattered values in the SB, presented in Fig. 70, are too few to recognise any regional trends. It is, however, interesting to note that the isotopic values of calcite veins in Cretaceous mudstones and grainstones of marine origin along the western border of the basin are identical to those of cal2. In this area, the Stephanian rocks have been thrust over the previously overlying and discordant Cretaceous sequence along the La Llama Fault, and both units are significantly deformed (Helmig, 1965; Lobato et al., 1984; Alonso et al., 1995).

One of the main difficulties of establishing a reliable interpretation for the cal2 isotopic signature lies in the absence of any similarities with the stable isotope data for similar vein calcite in other areas of the CZ. Values for hydrothermal vein carbonates hosted in similar igneous intrusions emplaced in other Stephanian basins are $+0.9 \leq \delta^{13}C \leq +4.1$ ‰ PDB and $+17.6 \leq \delta^{18}O \leq +26.1$ ‰ SMOW for the Salamón Gold deposit (Crespo et al., 2000). Similarly, values of $-4.5 \leq \delta^{13}C \leq -2.0$ ‰ PDB and $+13.8 \leq \delta^{18}O \leq +20.3$ ‰ SMOW have been reported in the Burón Mine (Panaiagua, 1998). The late calcite phase (no dedolomitising), associated to the widespread dolomitization of Namurian carbonate formations has isotopic values of $-8 \leq \delta^{13}C \leq +1$ ‰ PDB and $-13 \leq \delta^{18}O \leq -5$ ‰ PDB (Gasparrini et al., 2002). The isotopic signature of cal2 also notably differs from "hydrothermal" carbonates described in similar settings such as the South Wales Coalfield (Alderton and Bevins, 1996) and the Bowen coal basin in Australia. In the later area cement calcite presents a wider range in carbon isotopic values $-11.4 \leq \delta^{13}C \leq +4.40$ ‰ PDB and consistently lighter oxygen signature $+5.9 \leq \delta^{18}O \leq +14.60$ ‰ SMOW (Uysal et al., 2000a).
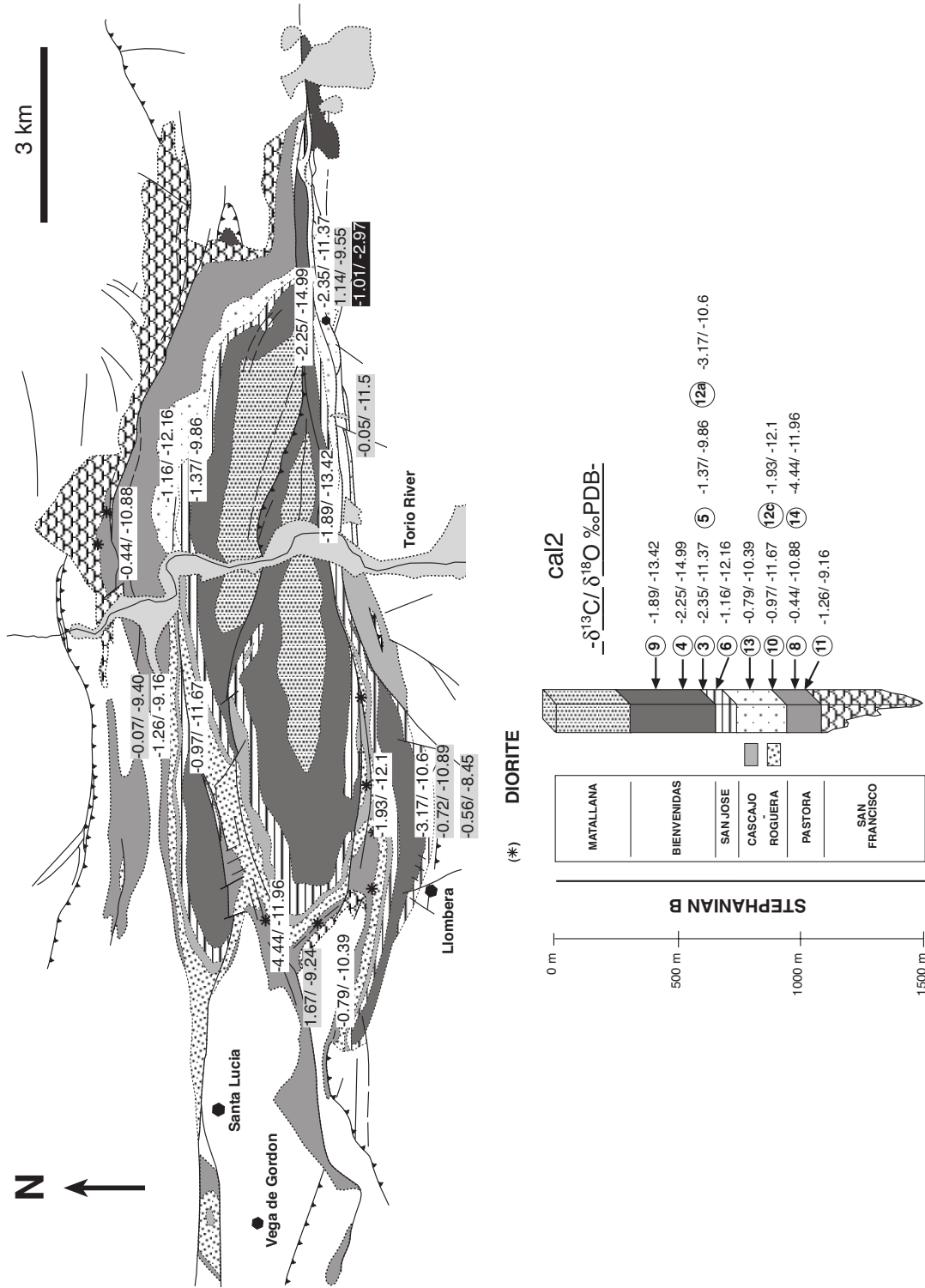
Figure 69. Distribution of carbon ($\delta^{13}C$) and oxygen ($\delta^{18}O$) isotopic values for vein calcite (cal2) in the CMB reported in ‰ vs. PDB (localities 3 to 14). The values placed outside the basin correspond to calcite (grey frames) and saddle dolomite (black frame) veins within Devonian and Carboniferous rocks (mostly carbonates) adjacent to the basin.
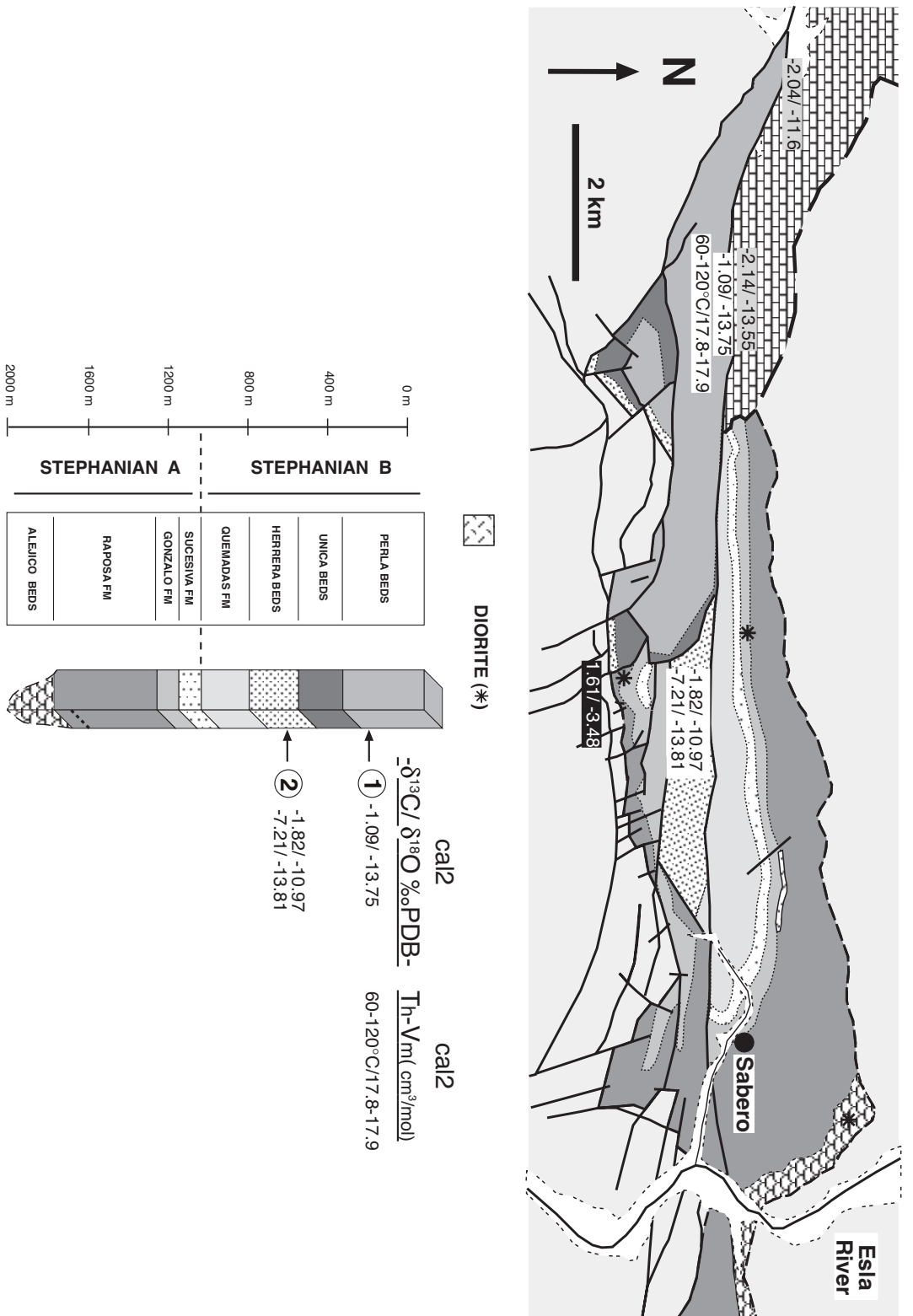
Figure 70. Distribution of carbon (δ¹³C) and oxygen (δ¹⁸O) isotopic values for vein calcite (cal2) in the SB, reported in ‰ vs. PDB (localities 1 and 2). The values placed outside the basin correspond to calcite (grey frames) and saddle dolomite (black frame) veins within Cretaceous and Devonian carbonates, respectively, adjacent to the basin. Also reported are the T_h and V_m of the H_2O-NaCl-$CaCl_2$-CH_4 system in locality 1.

Given this situation, the following scenario is proposed for the genesis of vein calcite. The temperate brine precipitating cal2, which has mean values around 0 ‰ SMOW for the precipitating fluid (Fig. 58, chapter 6), is suggested to have been derived from infiltrated and modified late Cretaceous marine water hosted in the underlying Stephanian clastic sequence. The temperature range of the fluid (Th) matches well with expected regional rock temperatures during Cretacous-Tertiary times by assuming about 1.5 km thickness for the Mesozoic cover and eroded Stephanian rocks and considering 33°C/km of geothermal gradient. This gradient has been adopted on the basis of present day borehole temperatures crossing the discordance between the Stephanian and older Palaeozoic rocks, and considering also the thermal stability of the crust beneath the southern margin of the CZ since the Cretaceous (Alonso et al., 1995). In the Matallana syncline (CMB), at a depth of 1140m, the temperature has been determined to be about 38°C (Villegas, 1996). The slightly higher fluid temperatures of cal2 in the SB would be expected due to the larger thickness of the clastic sequence in this basin.

8.3. FLUID AND THERMAL EVOLUTION OF THE STUDIED VEINS

Veins in the clastic Stephanian rocks

The evolution of the different minerals and associated fluid systems, in correspondence with the opening events in the veins of the clastic rocks of the CMB is illustrated in Fig. 71. No calcite or quartz cements with measurable inclusions were found in the host sandstones, even in areas close to the veins. Therefore, any fluid that has circulated through, or is derived from the clastic rocks is considered to be best represented in the studied mineralised fissures.Together with the fluid composition and conditions, the process responsible for the formation of each of the fluid systems is interpreted. At least seven different fluid types have been recognised, which can be related with at least two main vein-opening events. P-T-X characteristics of five of these fluids have been described in detail in chapter 5. The mineral sequence "quartz $\rightarrow$ dolomite $\rightarrow$ late calcite" has also been recognised in ore mineralisations in the south of the Cantabrian zone (Paniagua, 1998 and pers. comm.), and in coal basins of similar geological settings (South Wales and Appalachians).
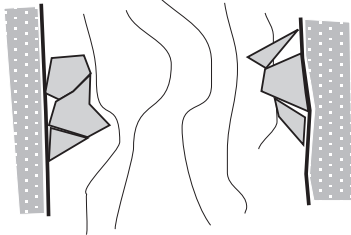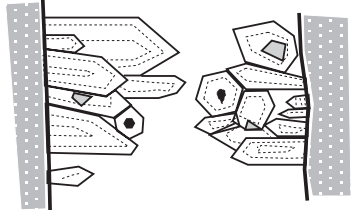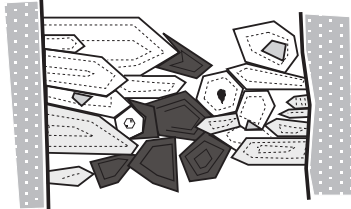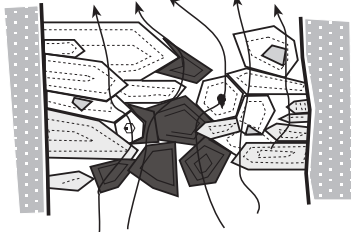
PHASE	FLUID SYSTEM	PROCESS

1   **cal1**

H_2O
76-90°C
18-18.6 cm^3/mol

Early sediment compaction and dewatering

2   **qtz1**

H_2O-CH_4-CO_2 (±NaCl)
90-130°C / 10-60 MPa

Dewatering, thermal maturation and decarboxilation of organic matter (coal)

3   **dolm**

H_2O + salts?
100-150°C?

Cation enriched pore fluid of sandstones and mudstones formed by thermal maturation of detrital components

4   **Fluid inclusion re-equlibration**

Steam + CH_4-CO_2 ?
Heated pore water?

Final maturation of coal driven by peak palaeothermal conditions associated with magmatic activity (diorite sills)

Figure 71. Development of mineralised fissures in the clastic Stephanian rocks of the CMB and SB.
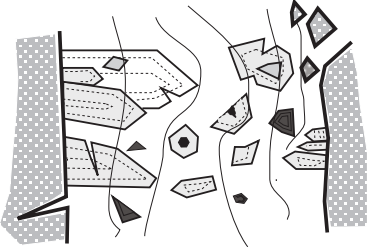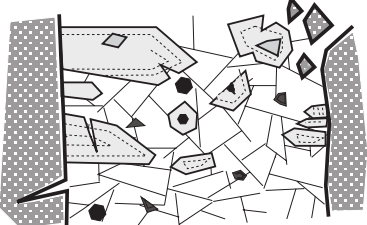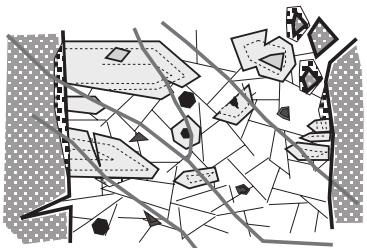
PHASE	**FLUID SYSTEM**	**PROCESS**
(5) **Vein re-activation** 	H_2O-$NaCl$-$CaCl_2$-CH_4 40 - 98°C 16.9-17.2 cm^3/mol	Host rock brecciation and microcracking of qtz1
(6) **cal2 - py** 	H_2O-$NaCl$-$CaCl_2$-CH_4 60 -100°C 17.1-17.9 cm^3/mol	Flow of heated and cation enriched fluid of marine origin Dissolution of dolm
(7) **cal3 - kln** 	$H_2O \pm NaCl$ < 50°C	Late telogenetic alteration associated to the uplift and exposure of the basin and circulation of meteoric waters

Figure 71 (continued).

Veins in the diorite rocks

Although more restricted in the basin's fluid-thermal history, a similar representation for the evolution of the hydrothermal quartz fissures (qtz2) in the diorite sill can be recognised and is summarised in Fig. 72. These veins provide a record of the highest fluid temperatures attained during the evolution of the Stephanian basins. Vein formation is subdivided in 4 phases, in which at least two different fluid systems have been identified, although only systems corresponding to peak temperatures could be characterised in detail.
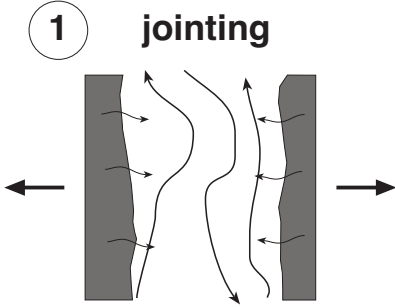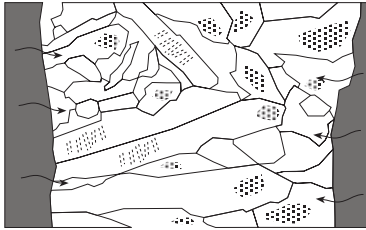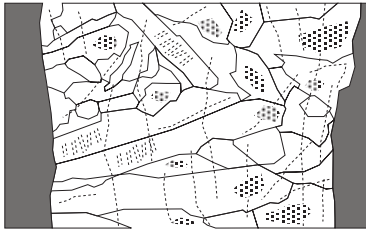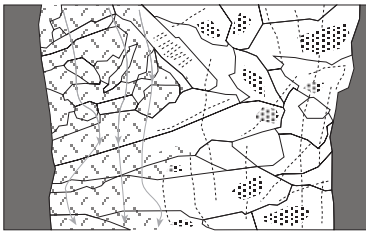
PHASE	FLUID SYSTEM	PROCESS

1 **jointing**

None

Progressive cooling of dioritic magma sills

2 **qtz2**

H_2O-CH_4-CO_2 ($\pm$NaCl)
160-296°C / 3-46 MPa

Formation of coke aureoles. Dewatering and degassing of coal induces alteration of magmatic minerals and puts silica into solution

3

H_2O-CH_4-CO_2 ($\pm$NaCl)

Formation of secondary inclusion trails. Continued fluid activity and vein deformation after quartz crystallisation

4 **Kaolinite**

$H_2O \pm$ NaCl?
< 50°C?

Late telogenetic alteration due to exposure and infiltration of meteoric water

Figure 72. Evolution of hydrothermal quartz (qtz2) veins within the dioritic sills of the CMB and SB.

125

CHAPTER 9: DISCUSSION AND TECTONO-THERMAL HISTORY

This chapter addresses two remaining questions. How were the fluid inclusions in the fissure quartz re-equilibrated? and, what are the implications of this event for the thermal evolution of the CMB and for the investigated fluid and mineral sequence preserved within the veins? Based on the constraints proposed, a reconstruction of the fluid-thermal events in relation to the geological history of the Stephanian Ciñera-Matallana basin is presented.

9.1. IMPLICATIONS OF RE-EQUILIBRATION FOR HEAT TRANSMISSION

In this study it has been argued that the re-equilibration of fluid inclusions in vein quartz (qtz1) is related to a thermal rise. Experimental data confirm that decrepitation is an almost instantaneous and sensitive phenomenon if the rise in temperature is sharp enough (see chapter 7). Both fluid inclusion decrepitation and organic matter maturation are irreversible phenomena and more sensitive to rapid and short-lived temperature rises than clay mineral reactions, which are often influenced by a number of other variables (Frey, 1987). If the temperature increased for only a short time span, it is likely that only these two processes register the full extension of the overheating. As the temperatures recorded by non-re-equilibrated fluid inclusions are lower than those obtained from the vitrinite reflectance, the thermal rise responsible for the final coal rank is suggested to have induced the re-equilibration of the vein quartz inclusions.

9.1.1. Factors affecting heat transmission

In areas where local extensional events take place, for example during the completion of an orogenic cycle as in the CZ, hyperthermal anomalies may cause maximum palaeo-temperatures, leading to mineral reactions and organic maturation grades that do not correspond with maximum burial conditions. These anomalies are commonly associated with hydrothermal fluid circulation, large igneous intrusions and regional / local high heat flow related to crustal thinning (Uysal et al., 2000; and references within). Heat can be transmitted either by conduction through solid rock, or by convection of a hydrothermal fluid through pore spaces and fractures. In sedimentary basins though, the effect of contact metamorphic environments, characterised by conductive heat transfer, on maturation level is often limited compared to that of hydrothermal environments. Large volumes of fluid are considered to transport heat more efficiently, resulting in more widespread thermal effects

(Parnell, 1994; Duddy et al., 1994).

The heat conductivity and the porosity/permeability of the rocks within any basin have an important control on the heat flow pattern (Duddy et al., 1994). Vertical and local variations in geothermal gradient commonly reflect changes in the heat conductivity of the sections where poorly conductive shaly formations, coals and carbonaceous shales are characterised by high geothermal gradients and high heat flow (Uysal et al., 2000). These lithologies tend to absorb the heat and act as a barrier for the vertical transfer of deeper heat flows towards the overlying formations. Their low porosity also makes them impervious to circulating fluids (Bjørlykke, 1994).

9.1.2. Evidence of fluid activity

The decrepitation of fluid inclusions in the vein quartz may have been caused by circulation of a hot fluid phase through the fissures and basinal host rocks of the CMB. But this study has revealed that fluid temperatures in later, deformation related fissure dolomite and calcite (dolm and cal2) were lower or within the same range ($\leq 100°C$) as those for vein quartz (qtz1). So, although these highly saline fluids left traces in the quartz, they can be excluded as a significant source of heat. Therefore, decrepitation must have occurred at some stage between the end of quartz formation and the precipitation of vein calcite.

It is nevertheless possible that a hot fluid phase circulated without apparently leaving associated signs of mineral growth, alteration or dissolution. Neither corrosion nor etching of the vein quartz (qtz1) is observed, although all these features could have been obliterated by the later calcite (cal2) mineralisation event. The absence of evidence for associated widespread host-rock hydrothermal alteration and mineral precipitation in fissures could be explained by the:

- lack of sufficient porosity-permeability in the clastic host-rocks, reduced as a consequence of ongoing clay mineralisation and diagenetic cementation
- local fluid buffering by the host rocks or vein minerals. Concentrated precipitation of dissolved minerals requires a change in the chemical environment by reactions with other fluids and minerals
- amount of fluid needed to transfer the heat was less than was needed to produce a mineralogical signature of a hydrothermal event (Yardley, pers. comm.)

That not even secondary inclusion trails containing traces of this hot fluid are preserved in qtz1 can be explained by the absence of pervasive deformation during this presumed fluid event. Without deformation, qtz1 crystals would not be able to form secondary fluid inclusion trails by crack healing. Dissolution and recrystallisation of vein quartz could have also taken place as a consequence of the circulation of this fluid. Preliminary optical-cathodoluminescence microscopy of the vein quartz seems to confirm that such processes may have occurred (van den Kerkhof, pers. comm.). CL-microscopy,

either optical or SEM, can reveal such features as internal structures, growth zoning and lattice defects of quartz (Boiron et al., 1992; Götze et al., 2001; Rusk and Reed, 2002).

9.1.3. The role of the diorites

The most important direct heat source in the geological history of the studied coal basins were the diorite sills. In this context, it is therefore of interest to consider how the magmatic bodies interacted with both the coal seams and the clastic rocks, and if there existed significant temperature gradients and heat transfer away from the sills. Studies on the influence of magmatic activity in the maturation of organic matter have been conducted in the Pannonian Basin in Hungary (Horváth et al., 1986), the Late Carboniferous of north Britain (Raymond and Murchison, 1991), the coalfields of South Africa (Snyman and Barclay, 1989) and the Bowen Basin in Australia (Uysal et al., 2000).

Conductive temperature gradients away from the intrusive bodies

Fig. 73 estimates the extent of conductive temperature gradients in coal seams away from an intrusive body, based on coal rank distribution. Reflectance values are taken from Méndez-Cecilia (1985) and Frings (2002). Initial magma temperatures for the intrusive dioritic material are estimated to be about 800° to 850°C. The mechanism of intrusion was in many cases a volume by volume replacement of coal within the seams by semi-concordant igneous bodies; a process that can only be achieved at relatively low confining pressures. This emplacement mechanism and the position of the sills along the central part of the seams are favoured by the fact that the coal had already reached the plastic phase during the degassing period (Méndez Cecilia, 1985). It was also estimated that the coal had about 0.9% random reflectance (sub-bituminous to high volatile bituminous) before the intrusion, based on the petrographic study of textures preserved in the coked coal. Temperatures attributed to these coal ranks are 110-130°C (Barker and Pawlewicz, 1986), which lyes within the range of those estimated from the primary inclusions in vein quartz. This suggests that the intrusions post-dated the sedimentation and early lithification, and post-dated the vein quartz preserved in the formations of the CMB. The regional geothermal gradient imposed a general rank upon the organic matter, which combined with the low thermal conductivity of coal, made it more susceptible to further alteration by the rise in temperature due to the dioritic intrusions. The heat affected non-coke coals in seams up to San José Fm and induced a rank increase up to about 2% reflectance (Fig. 73).

Where the igneous bodies intrude other lithologies (sandstones and shales) apart from coal, sills penetrate along stratification surfaces and small oblique fractures under pressure of the advancing head (Francis, 1982). The thermal effect of these relatively thin intrusions is very limited. Conductive heat transfer induced clay minerals reactions and illite growth only in areas immediately adjacent (< 1m) to the sill margins (Méndez-Cecilia,

1985; Villegas, 1996; Frings, 2002). This process has been termed "contact diagenesis" as the temperatures needed for mineral transformations are generally below 300°C and so reactions do not reach thermodynamic equilibrium. Under such conditions, the total porosity in sandstones remains unaffected because reactions mostly involve recrystallisation of original pore-filling minerals, so pre-existing pore fabrics are often well preserved (McKinley et al., 2001).
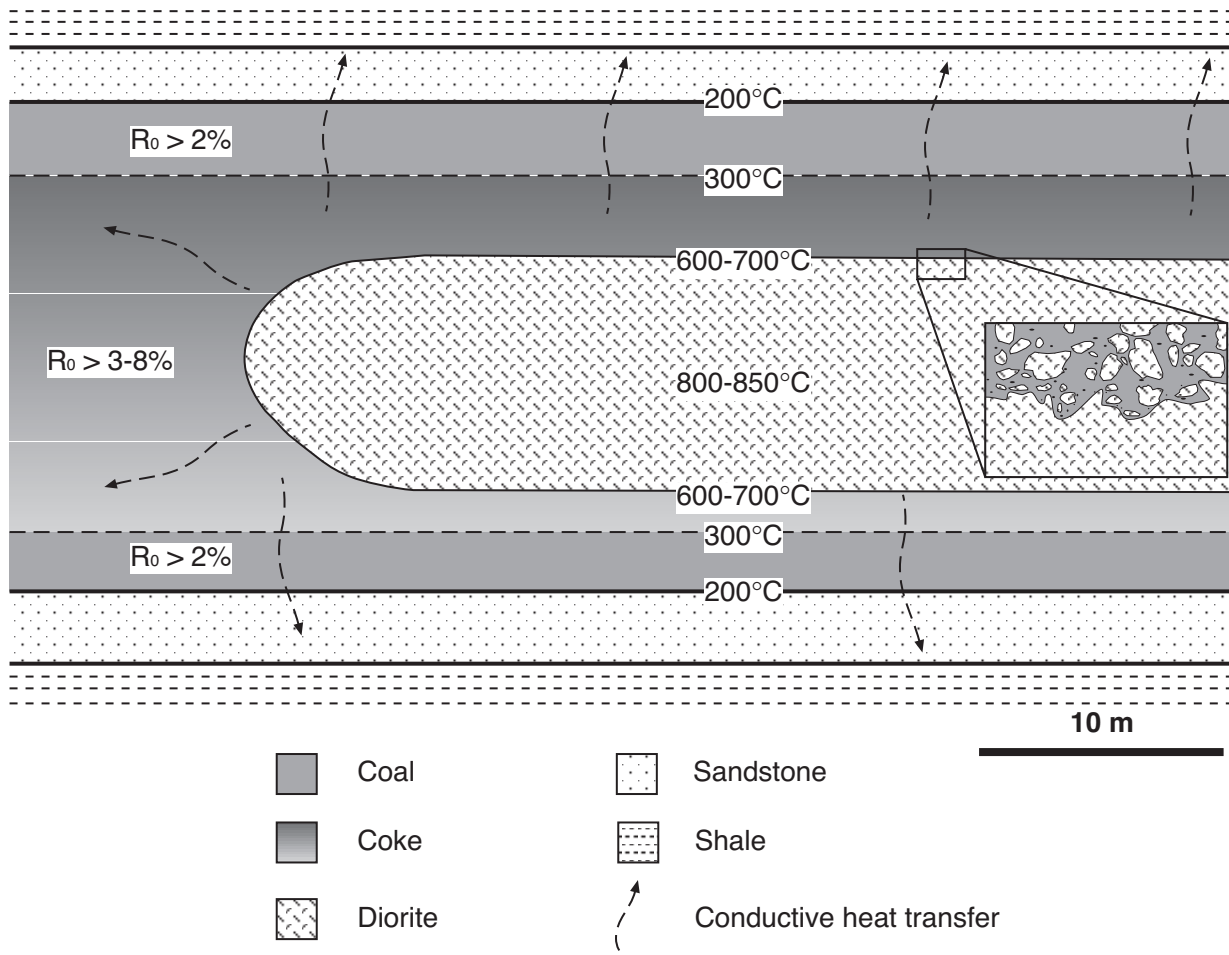
Figure 73. Approximation of the extent of coke aureoles (stripped lines) and conductive thermal transfer (arrows), based on palaeotemperatures estimated from vitrinite reflectance values (R_0) away from diorite sills. Inset shows the nature of the coke-diorite contact. See text for details.

Effect of water saturation

Another relevant aspect is that no clear relationship is observed between coke aureole thickness and the size of the intrusive bodies. Wide thermal aureoles within coal are favoured by magma intrusion into an essentially dry environment (Snyman and Barclay, 1989; and references within), and in such settings the extent of the aureole depends on the magma volume, temperature and the sill thickness. But if intrusions are emplaced at shallow levels into water-bearing sediments, rapid remobilization of the heat away from the vicinity of the

intrusive by fluid circulation can take place. In this case, important limiting factors on the thickness of the thermal aureoles are **(1)** the degree of consolidation and water saturation of the accumulating organic matter and sediments, and **(2)** the degree of maturation of the organic matter in the coals and sediments at the time of intrusion (Raymond and Murchison, 1991).

These relationships imply that at the estimated level of maturation reached before the onset of the magmatic activity in the CMB the coal was still partially saturated with water. This interpretation is also supported by the abundant contact irregularities (coke engulfing, magma veining, etc) and the mixing of sediment, organic matter and magma observed at the margins of some diorites (detail in Fig. 73), similar to that described in Kisch and Taylor (1966) and Kokelaar (1982). In such a setting, a steam and gas (CH_4-CO_2) envelope is generated during intrusion and much of the heat from the diorites was absorbed during the heating and evaporation of the fluid from the coal and associated clastic sediments. It is also conceivable that a chemical gradient caused a significant amount of the vapour and gas phases to migrate from the surrounding coke into the cooling dioritic magma (Fig. 74). This would further reduce the contact metamorphic effect of the intrusive on the coal and surrounding rocks, causing extensive mineral alteration and formation of "white traps" (Kisch and Taylor, 1966).

The fluid system related to the alteration of the igneous rocks, preserved in qtz2 veins, has trapping temperatures and pressures of 160-290°C and 3-48 MPa, respectively. The components of these fluids were essentially similar to those that caused the early fissure-quartz mineralisation in the clastic sedimentary rocks, confirming that they were derived from organic matter maturation. Their high CO_2 content conforms with the higher maturation temperatures reached by the coal in direct contact with the magma. That these quartz mineralisations only occur within the margins of deeply altered igneous bodies surrounded by coke aureoles suggests that advective mass transport by these hotter fluids was only local in extent (Fig. 74). But the excess of fluid produced by the maturation of coal in the outer margin of the aureoles would maintain P-T conditions similar to those of the preserved fluid in qtz2, and therefore transports an important amount of heat.

The degree of water saturation in the clastic sediments appears to have been much lower than that in the coal at the time of the intrusion, as no sediment fluidisation textures (sensu Kokelaar, 1982) have been observed in the clastic rocks at the contact with the sills. Although this factor is also influenced by the permeability of the specific host-rock. The dioritic rocks are also much less altered, with no quartz veins and, what is more significant, the host sandstones and shales present no signs of hydrothermal alteration.
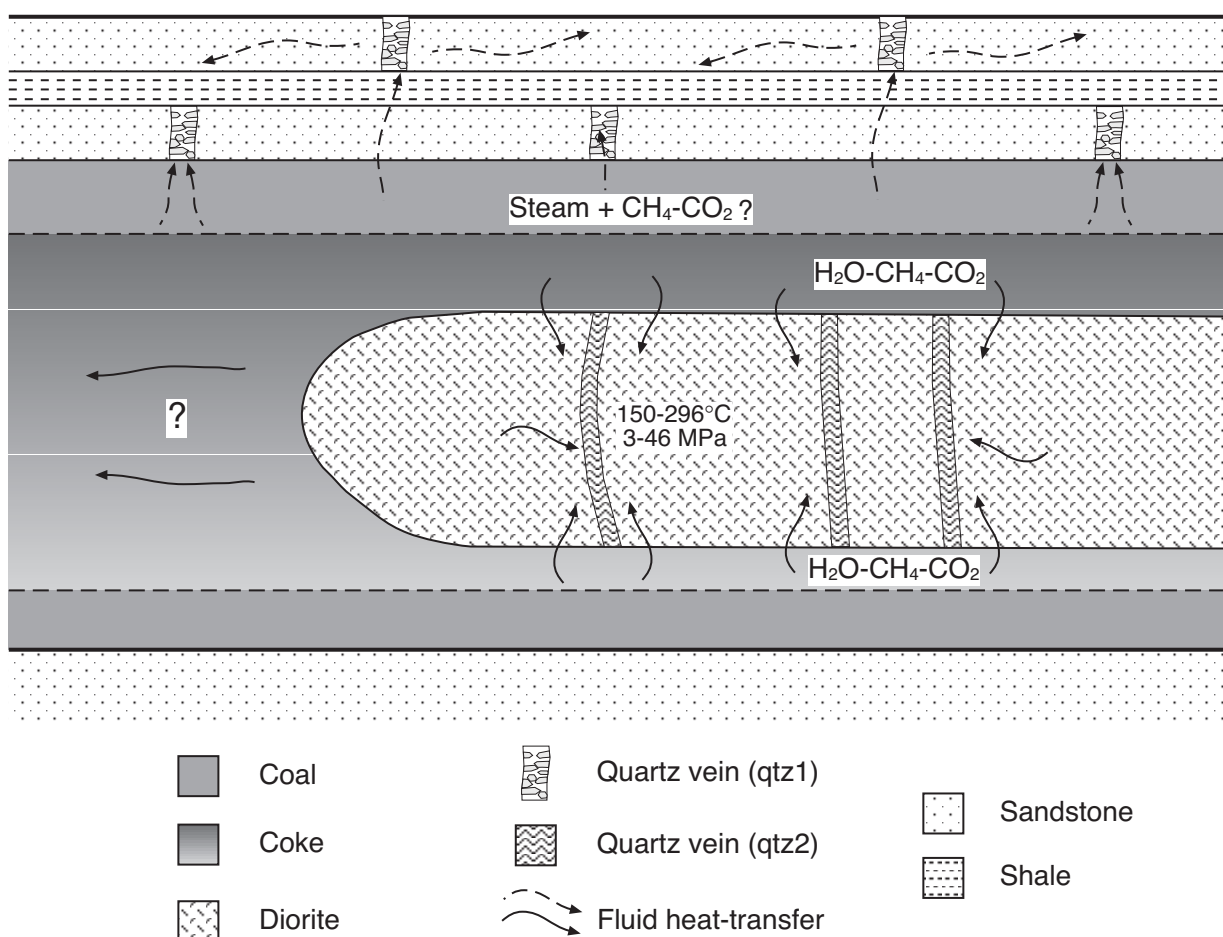
Figure 74. Effects of advective fluid transfer around and away from a diorite sill emplaced within a coal seam. Stripped arrows indicates the dispersion of fluid-heat transferred along pre-existing fissures, causing the re-equilibration of fluid inclusions in vein quartz. Solid arrows represent the hydrothermal fluid responsible for the late quartz (qtz2) precipitation and diorite alteration.

9.1.4. Mechanism of heat transmission

Having considering the factors that influenced heat transmission and the source of heat in the CMB, the mechanism for the re-equilibration of inclusions in fissure quartz is now outlined. The interpretation presented links the heating agent (fluid liberated by coal maturation), the heat transmission path (quartz bearing fissures) and the apparently limited effect of the thermal rise (fluid inclusion re-equilibration textures).

On the basis of the degree of organic maturation, the temperatures experienced by the coal up to the Bienvenidas Fm were high enough to induce inclusion decrepitation (Table 8, chapter 7). The intrusion of the diorite sills induced significant dehydration and degassing in the coal, which was still partially saturated in water. At the level of catagenesis reached by the non-coked coal in these formations (low volatile bituminous and semi-anthracites), macerals underwent a further and abrupt reduction in water content and volatiles, still coincident with the generation of gas ($\leq 200°C$).

The lithological and structural characteristics of the syncline units in the CMB indicate that each syncline constitutes a multilayer aquifer system of great thickness, which is heterogeneous and anisotropic on the local scale (Villegas, 1996). The overall permeability of the section is low, and the interbedded shale/coal levels and stratification surfaces compartmentalise the coarser clastic and more permeable rocks into sub-meter scale units with minimal fluid communication (Bjorlykke, 1994; McKinley et al, 2001). Nevertheless, the circulation of the steam and gas formed in the maturation "pulse" probably occurred along already existing tectonic structures, with enhanced permeability. The fracture network formed by faults and mineralised open fissures would facilitate the distribution of expelled organic maturation fluids and pore waters into permeable zones, and allow advective transmission of heat upwards and laterally along pressure gradients (Fig. 74).

The fluid generation and flow accompanying coalification would have lasted for a short time due to the small sizes of the magmatic sills, but is predicted to have had relatively widespread thermal effects. Heating would have been especially important in the fractured sandstone beds placed above the coal seams, because of their proximity to the coal and because they concentrate the largest amount of open mineralised fissures (Fig. 74). Overheating is suggested to have affected the quartz (qtz1) already formed in the fissures and induced fluid inclusion decrepitation. At depth the heat cannot be disseminated away from the fractures fast enough due to the low thermal conductivity of rocks (Bjorlykke, 1994). Only near the surface could the fluid flowing along fractures be cooled effectively. The overheating was probably coupled with a general increase in the basin's geothermal gradient, which may have affected the clastic host rocks as well by heating the remnant pore fluid and locally enabling clay mineral reactions, such as the formation of higher temperature 2M illite polytypes (Frings, 2002). Lateral variations in palaeogeothermal gradients and clay mineral crystallinity may reflect variable heat distributions due to the different proximity to coal seams and the extent of permeable fracture-rich zones, which presumably acted as heat reservoirs.

9.1.5. Implications

1) Fluids were the agents responsible for heat transmission at thermal peak conditions in the studied Stephanian basins. They induced an attenuation of contact metamorphic gradients around the diorite sills and transferred heat through the previously formed fissures at further distances away from the magmatic source. The fluids were not derived from a source external to the basins, but largely from thermal maturation of the organic matter within the coal seams during their intrusion by diorite sills.

2) The sequence of fluid evolution established from the veins is presented in a P-T-time diagram in Fig. 75. Initially (A) early lithification and maturation of the basin rocks, when fissure formation took place and quartz (qtz1) precipitated at 73-129°C and 10-60MPa (early stage 1 of chapter 6.5). Progressive maturation continued and the intrusion of the diorite sills marked thermal peak conditions (B), which induced re-equilibration of fluid inclusions in vein quartz and the alteration of the magmatic bodies with formation of local quartz (qtz2) mineralisations. The re-equilibration textures reflect the increase in temperature within the fissures, driven by dewatering and thermal maturation of the sediments during intrusion. The fluid temperatures and pressures estimated for qtz2 (160-290°C and 3-48 MPa) are considered to reflect the conditions of the transient thermal event. The P-T field represented in (C) corresponds with the formation conditions of vein calcite (cal2) and other late minerals (cal3 and kln), reflecting important fluid events but not related to the prograde maturation of the coal (stages 2 and 3 of chapter 6.5).
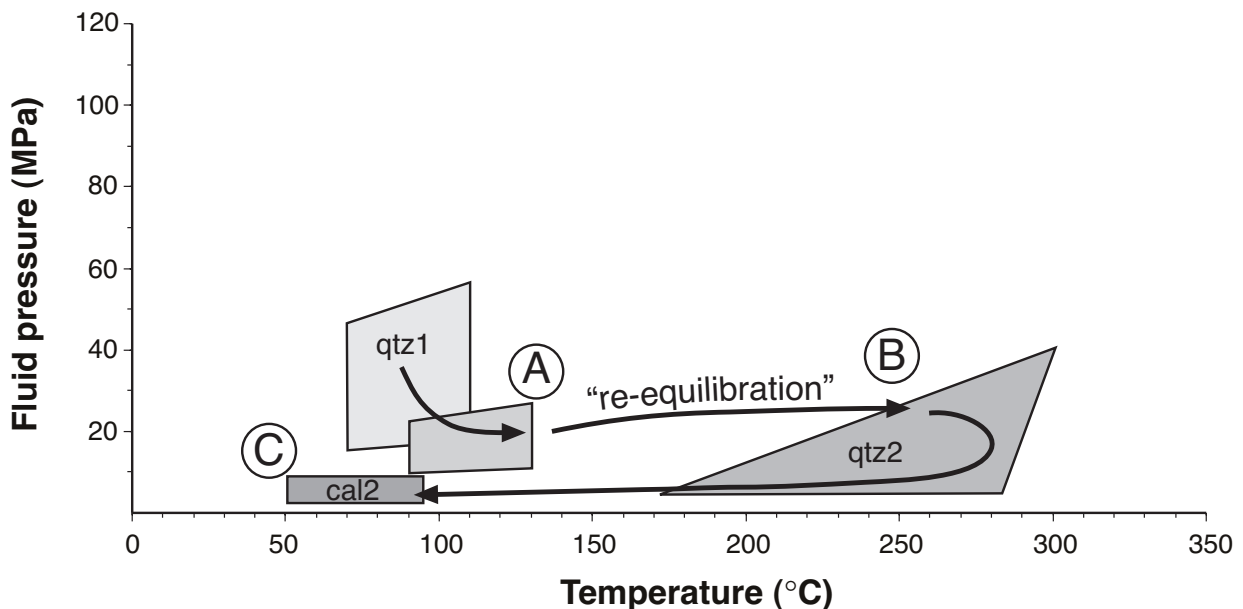
Figure 75. P-T-time evolution for the different fluid conditions preserved in the veins of the CMB, showing three principle phases (A to C).

3) Textural re-equilibration of fluid inclusions, when properly constrained, can provide an important marker for recognising transient (short-lived) thermal events in sequences where the transition from diagenesis to very low-temperature metamorphism is not sufficiently documented by other techniques.

9.2. TIMING OF VEIN FORMATION AND BASIN EVOLUTION

The geological evolution of the Ciñera-Matallana basin, in relation to the vein mineral growth sequence (chapters 6.5 and 8.3), is presented in 8 stages illustrated in Fig. 76. This evolution is not extended to the SB due to the low abundance of veins and the more restricted thermal effects of the magmatic intrusions. Figures are not to scale and present an idealisation of the outlined processes that occurred in the western half of the basin, along the cross-section I-II of Fig. 5 (page 14). For simplification, the eroded Stephanian rocks (about 1km) are not represented. The fluid, thermal and mineral evolution of the CMB is summarised as follows.

Basin development began with the onset of an extensional phase immediately following the completion of the Variscan Orogeny (Fig. 76a). Thinning of the continental crust originated transtension along the crustal scale fault of Sabero-Gordón, in the southern part of the Cantabrian arc. In the area of the Ciñera-Matallana Basin, fast deposition of more than 1,500 m of clastic material and coal, burial and episodic subsidence took place at least during Stephanian B times (298-294 Ma).
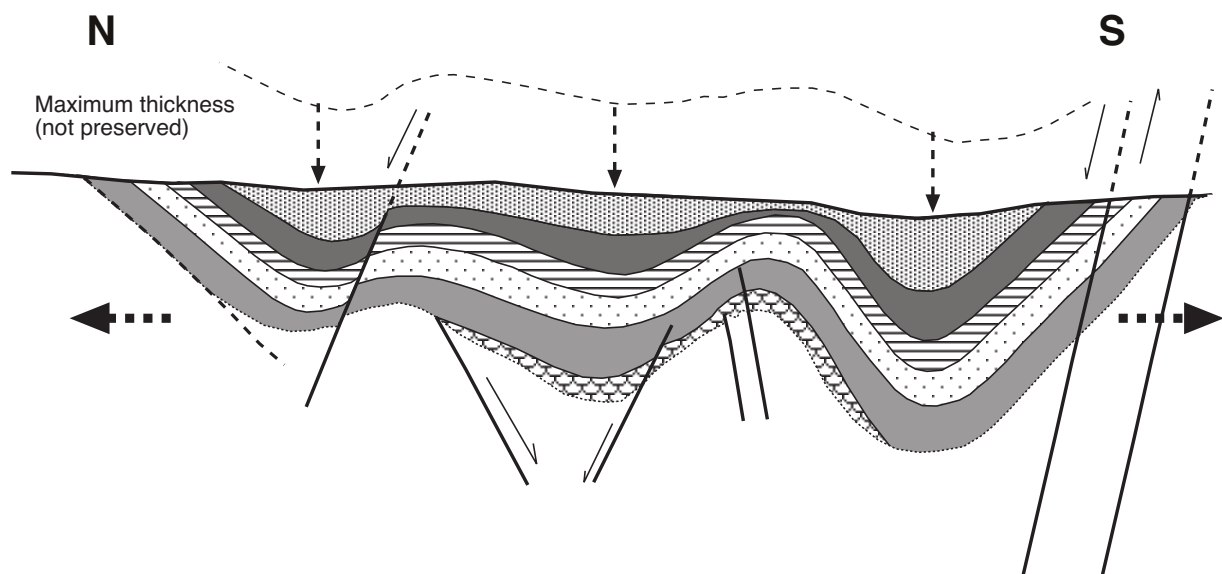
Figure 76a. Stephanian B (298-294 Ma). Sedimentation, subsidence and compaction.

Localised increases in heat flow occurred along the fault areas, due to the proximity of heat sources at depth (Fig. 76b). Incipient sediment compaction and lithification was accompanied by rapid thermal maturation (up to catagenesis) of coal as a consequence of the high palaeogeothermal gradients in the area. At the same time, early local transpressional movements along the Sabero-Gordón-Line produced tectonic compressional structures and associated bedding perpendicular fissures, particularly in zones adjacent to coal seams. Growth of early calcite (cal1) and quartz (qtz1) occurred during this phase from an immiscible mixture of low salinity water and a methane-rich vapour phase, at pressures and temperatures of 10-60 MPa and 73-129°C (stage 1).
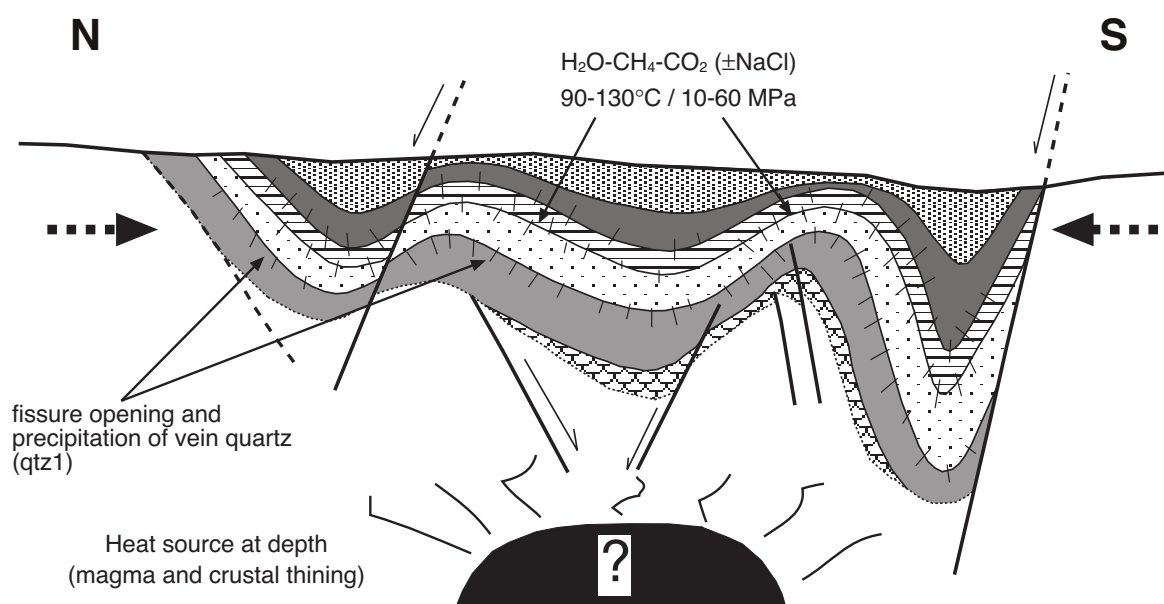
Figure 76b. Permian (290-260 Ma). Transpression and organic matter maturation, early stage 1 of vein evolution.

Temperature conditions continued to increase and were associated with diagenetic mineral reactions within basin rocks and the formation of saddle dolomite (dolm) into the fissures (Fig. 76c). Fluid conditions are not preserved, but precipitation of this mineral is associated with the input of saline palaeofluids and temperatures predicted to range from 100° to 150°C (late stage 1). Still during the Permian, the basin experienced a period of further heating due to magmatic activity. Diorite sills intruded the basinal rocks, predominantly along coal seams, and subsequent magmatic mineral alteration and formation of hydrothermal quartz (qtz2) occurred (Fig. 76d). Peak palaeotemperatures and final coal ranks were reached (transition of catagenesis to metagenesis) within the Stephanian rocks. The fluid generated during the enhanced degassing and dehydration of the coal circulated by advection through the fissure network, inducing the re-equilibration of fluid inclusions in vein quartz, probably still under a predominantly compressional regime. Fluid temperature and pressure conditions during the transient heating event are considered to have been about 160-290°C and 3-48 MPa.
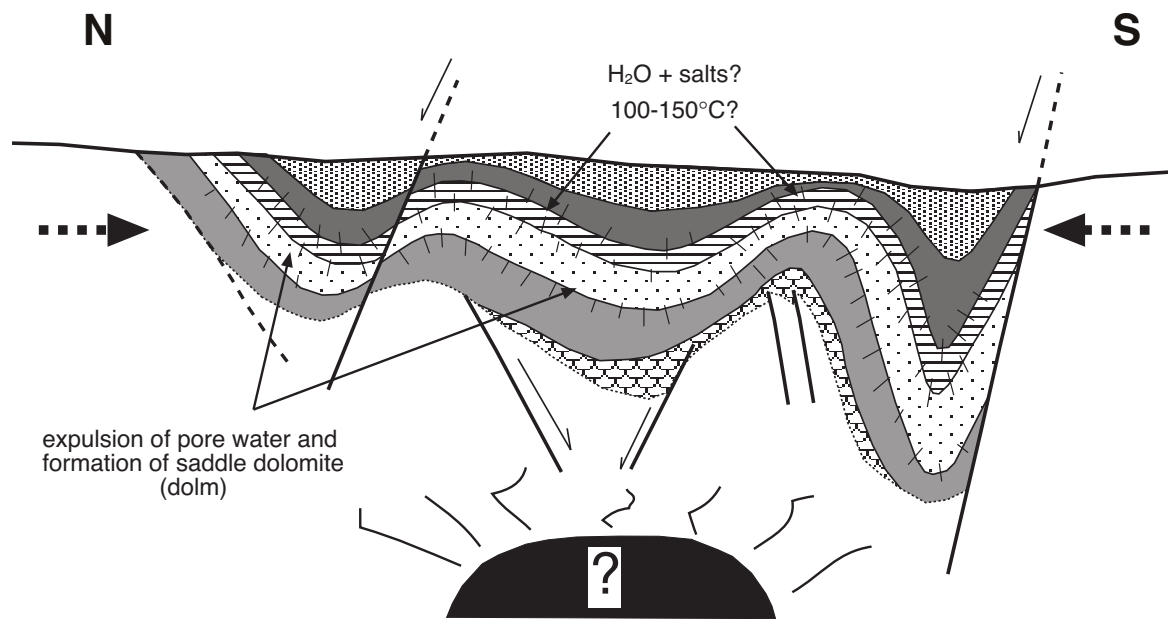
Figure 76c. Permian (290-260 Ma). Later maturation of clastic rocks, late stage 1 of vein evolution.
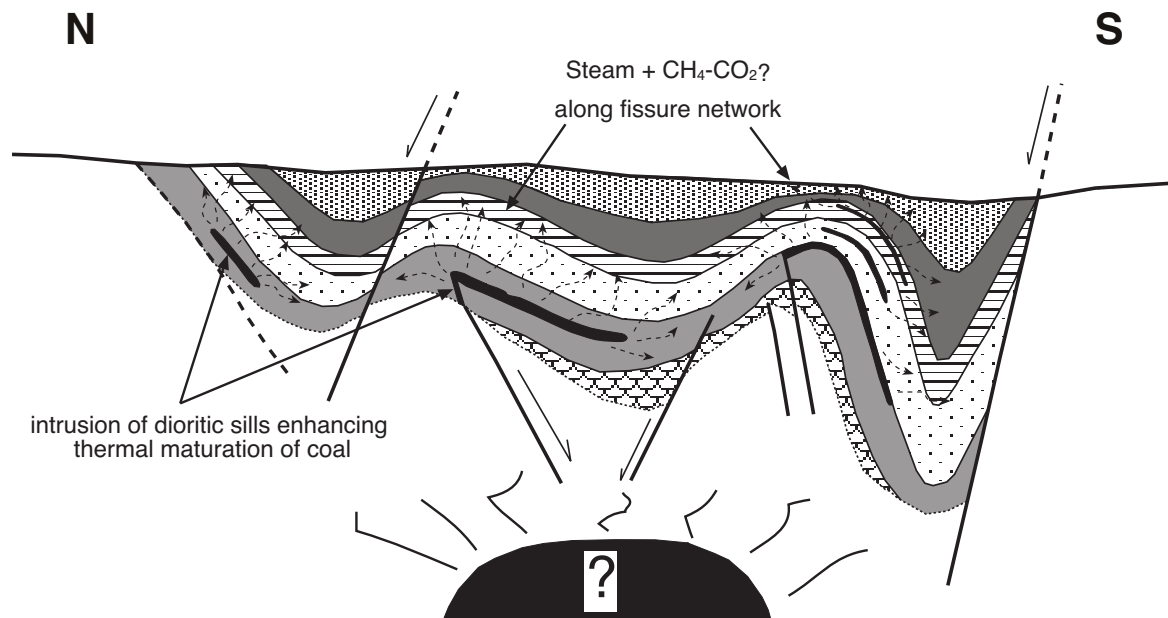
Figure 76d. Permian (290-260 Ma). Thermal peak conditions, re-equilibration of fluid inclusions within vein quartz.

There is no geological record in the south of the Cantabrian Zone from the end of Permian to Jurassic times (Fig. 76e), though the existence of a Permo-Triassic cover and associated further extensional activity has been postulated (Martínez-García, 1990; Alonso et al., 1995).
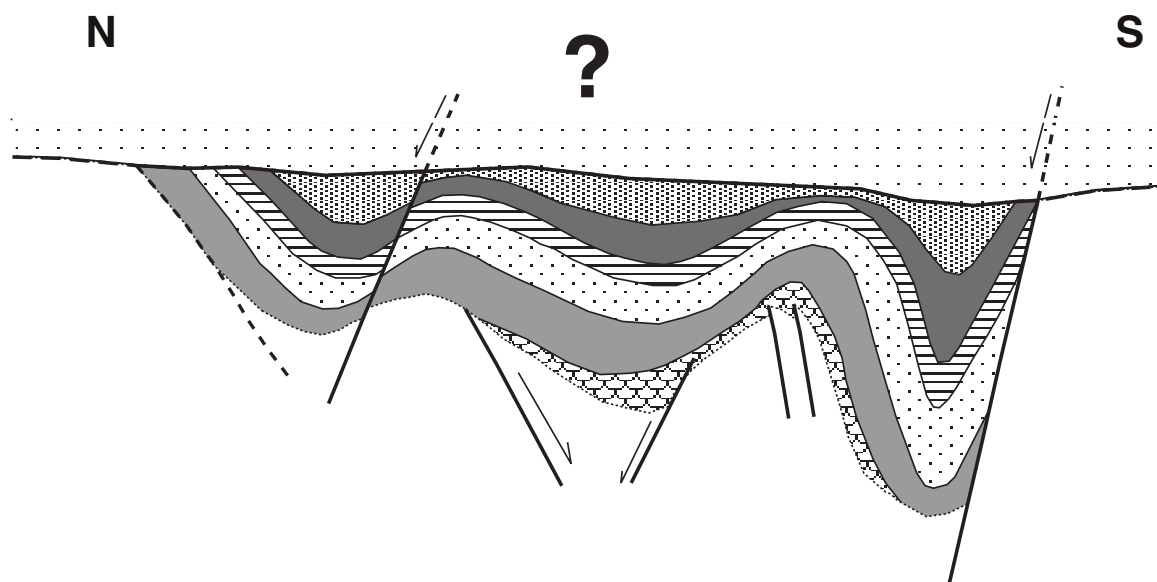
Figure 76e. Late Permian- Jurassic. No record of geological activity.

During the Upper Cretaceous, renewed extensional tectonic activity and subsidence took place, with a local depocentre located due east of the Ciñera-Matallana Basin (Lobato et al., 1984). A shallow marine sequence (calcarenites and mudstones) was deposited during Campanian to Santonian times (86-65 Ma) and during this period, marine water infiltrated the former clastic basin, saturating the Stephanian rocks (Fig. 76f). Following this extensional period, the Cantabrian Mountains experienced important uplift related to the Alpine orogenic cycle and to the formation of the adjacent Duero Basin during the Tertiary (Alonso et al., 1995). The reactivation of the Sabero-Gordón-Line generated renewed compression, forming the main N-transported thrusts in the Ciñera-Matallana Basin. Whereas the Stephanian rocks were still buried, the early marine waters, now brines with total salinities > 20 eq.wt%, were expelled through pre-existing mineralised fissures and newly formed veins at temperatures of 60° to 100°C (Fig. 76g). Vein re-opening and calcite (cal2) precipitation are proposed to have formed during this period, along with local pressure-solution phenomena in conglomerate beds containing carbonate clasts (stage 2). This interpretation remains unclear due to the absence of Permian to Jurassic rocks and to the lack of more data that relates the blocky calcite phase to the scarce veining of the Cretaceous sediments. Nevertheless the association of vein calcite with the re-activation and formation of the late tectonic structures and the isotopic evidence, though scarce, strongly suggests a Tertiary origin.

N

S

marine water infiltration

H₂O-NaCl-CaCl₂
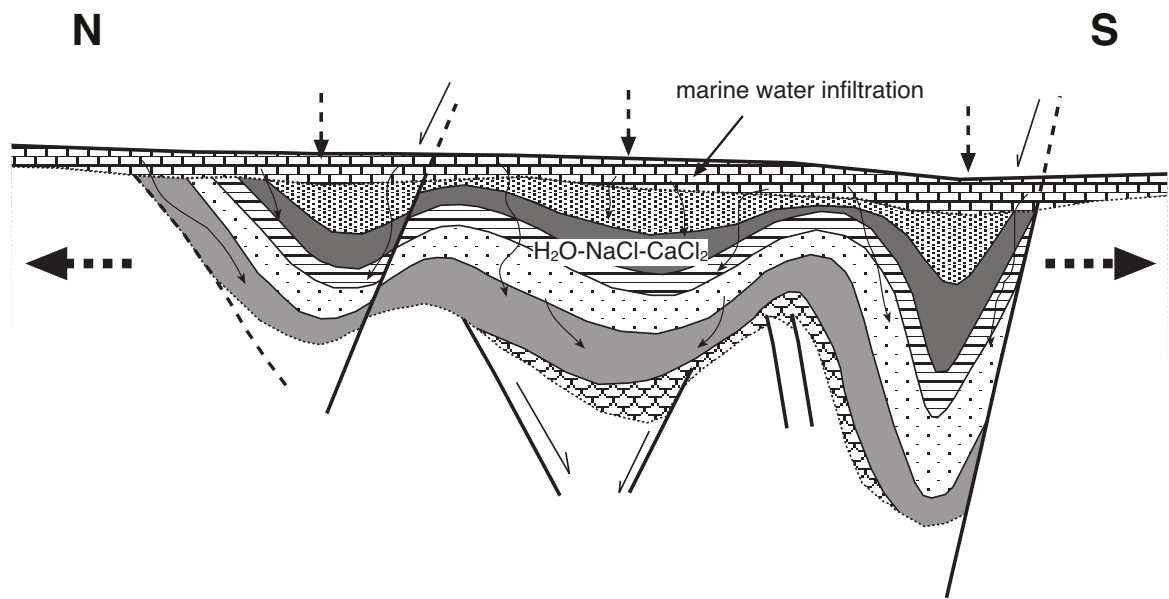
Figure 76f. Cretaceous (86-65 Ma). Subsidence and deposition of shallow marine sequence.

N

S

H₂O-NaCl-CaCl₂-CH₄
60 -100°C

expulsion of modified marine
water from saturated rocks along
re-activated fissures and formation
of vein calcite (cal2)

local pressure solution of
conglomerates with carbonate
clasts
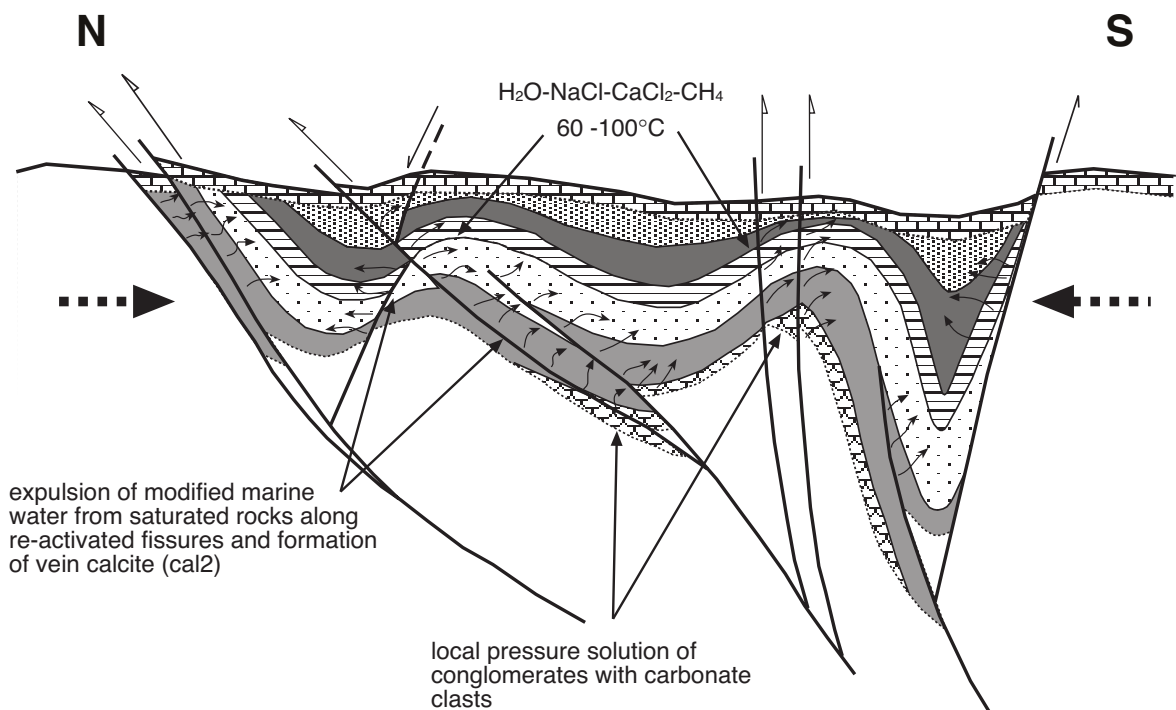
Figure 76g. Eocene- Miocene (50-20 Ma). Alpine compression and uplift, stage 2 of vein evolution.

From Miocene to present the basin underwent final tectonic uplift and subsequent erosion with exposure of the basinal rocks (Fig. 76h). A relative constant circulation of meteoric waters (< 50°C) through the basin occurred, preferentially directed along faults and mineralised fissures due to the low permeability of the Stephanian rocks. The formation of the late alteration minerals within the veins (late calcite and kaolinite) is related to this final phase (stage 3).
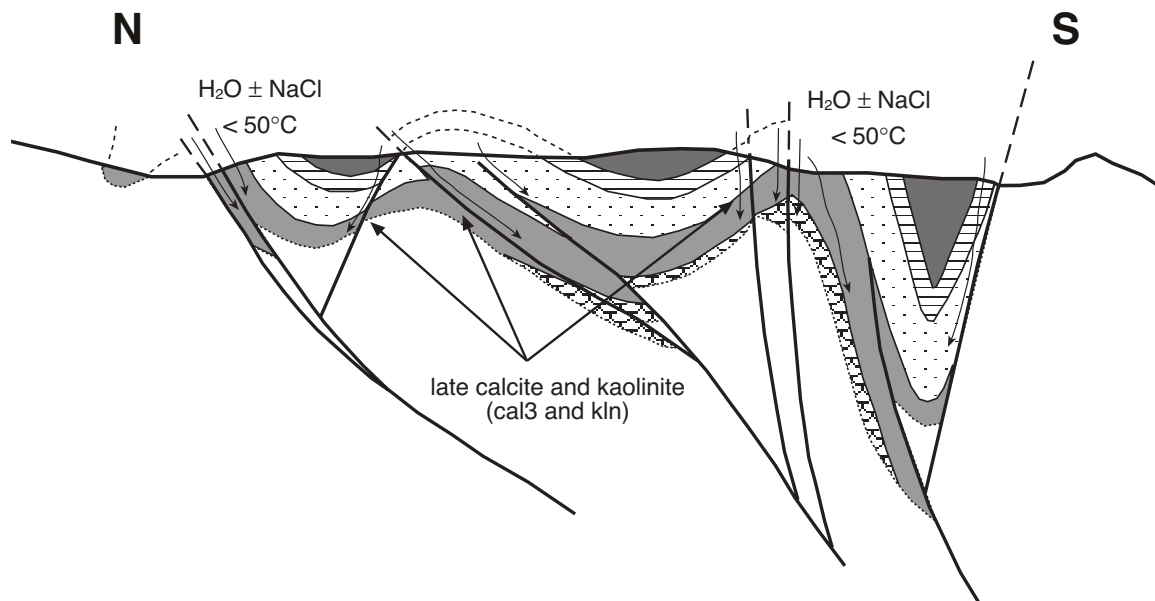
Figure 76h. Miocene- Holocene (20 Ma- present). Erosion and meteoric water infiltration, stage 3 of vein evolution.

CONCLUSIONS

1. Mineral precipitation in syntectonic veins within the Ciñera-Matallana and Sabero pull-apart coal basins records a complex fluid and thermal history. Fluids derived from the thermal maturation of the basin's rocks were responsible for heat transfer at temperature peak conditions in the Ciñera-Matallana coalfield.

2. The mineralised fissures (cm-wide) formed synchronous with folding and faulting in sandstone and conglomerate beds alternating with shales, organic rich pelites and coal-bearing strata. The mechanism responsible for fracture opening was bedding parallel slip.

3. The following mineral growth sequence is preserved within the veins: early calcite, euhedral quartz, saddle dolomite, ferroan blocky calcite, minor sulphides and authigenic kaolinite. Textural relations show that minerals grew within open fractures at various stages during the basins history.

4. Four mineralising fluid systems are preserved within fluid inclusions of vein minerals:

    1) H_2O in primary inclusions of early calcite at temperatures $< 90°C$ and molar volumes of 18-18.6 cm^3/mol

    2) H_2O-CH_4-CO_2 ($\pm$NaCl) heterogeneously trapped in primary and pseudosecondary inclusions of vein quartz. Fluid P-T conditions were 10-56 MP and 73°-129°C, and salinity was < 6 wt% NaCl

    3) H_2O-NaCl-$CaCl_2$-CH_4 in secondary inclusions of quartz and primary inclusions of vein calcite. Fluid temperatures were 60°-100°C, molar volumes ranged from 16.9 to 17.9 cm^3/mol and total salinities from 20.5 to 31.9 eq.wt%

    4) H_2O ($\pm$NaCl) at $T < 50°C$ in secondary inclusions of vein calcite, contemporaneous to the formation of late calcite and authigenic kaolinite

5. On the basis of fluid and mineral characteristics, three stages of vein growth can be recognised and related to basin evolution:

- Stage 1, early calcite, quartz and saddle dolomite formed in relation to burial and progressive rock (coal) maturation close to thermal peak conditions during Permian times. Materials for mineral precipitation were derived from the detrital fraction within the Stephanian rocks, and transported into solution by advection of large amounts of locally derived water and gas phases (CH_4-CO_2).

- Stage 2 reflects brittle reactivation of veins still under burial conditions. Lower temperature diagenetic dissolution-precipitation reactions (dedolomitisation) controlled calcite growth in relation to the infiltration of marine water, and was subsequently modified during tectonic subsidence in the Cretaceous and late tectonic reactivation in the Alpine Orogeny.
- Stage 3 is linked with the uplift and exhumation of the basin fill. Low-T diagenetic and weathering reactions of the Stephanian rocks result from a constant supply of meteoric water (T < 50°C), forming late calcite and kaolinite.

6. Small mineralisations of quartz and late kaolinite occur locally in diorite sills emplaced within the basins. An immiscible H_2O-CH_4-CO_2 ($\pm$ NaCl) fluid system is defined in primary inclusions of quartz. P-T conditions were 164°-296°C and 3-48 MPa, with $CO_2 > 10$ mol % and salinity < 2.5 wt% NaCl. The hydrothermal quartz crystallised due to extensive alteration of the igneous minerals as the magma intruded the coal seams.

7. Five textural types of re-equilibrated fluid inclusions are recognised and defined in the fissure quartz within the clastic rocks: scalloped, hairy, annular-ring shaped, haloes and decrepitation clusters. Each type represents a progressive order of inclusion modification. These textures resulted from a combination of brittle fracturing and dissolution and re-precipitation of quartz, with preferential loss of water, induced by a temperature rise within the veins and surrounding rocks.

8. The distribution of re-equilibrated inclusions in vein quartz throughout the entire basin reflects the extension of heat flow during thermal peak conditions. Short-lived high temperatures were related to the intrusion and alteration of the diorite sills into the basin, which enhanced further maturation of the coal and consequent degassing and dehydration. Heat was transferred by advective circulation of the released fluid along the already formed fissure network inducing inclusion re-equilibration.

LITERATURE LIST

Adams AE, Mackenzie WS, Guilford C (1984) Atlas of sedimentary rocks under the microscope. Longman Group, 104 pp.

Alderton DHM & Bevins RE (1996) P-T conditions in the South Wales Coalfield: evidence from coexisting hydrocarbon and aqueous fluid inclusions. Journal of the Geological Society, London, **153**, 265-275.

Aller J, Bastida F, (1987) Cleavage and its relation with metamorphic grade in the Cantabrian Zone (Hercynian of North-West Spain). Sciences Géologiques Bulletin, **40**, 255-272.

Alonso JL, Pulgar JA, García Ramos JC, Barba P (1995) Tertiary basins and alpine tectonics in the Cantabrian Mountains (NW Spain). In: Tertiary Basins of Spain (PF Friend & Dabrio CJ; Eds). Cambridge University Press, 214-227.

Alonso JL, Suárez Rodríguez A, Rodríguez Fernández LR, Farias P, Villegas, FJ (1990) Hoja del Mapa Geológico Nacional E. 1:50:000 **n° 103** (LA POLA DE GORDÓN). 2 Serie MAGNA. Instituto Geológico y Minero de España.

Alonso OE & Brime C (1990) Mineralogy, geochemistry, and origin of the underclays of the Central Coal Basin, Asturias, Spain. Clays and Clay Minerals, **38**, 265-276.

Alt JC (1999) Very low-grade hydrothermal metamorphism of basic igneous rocks. In: Low-Grade Metamorphism (Frey M & Robinson D; Eds). Blackwell Science, 169-201.

Andersen T, Frezzoti ML, Burke EAJ -Eds- (2001) Fluid Inclusions: Phase Relationships-Methods-Applications. Special Volume in honour of Jaques Touret. Lithos, **55**, 320 pp.

Audetat A & Günther D (1999) Mobility and H_2O-loss from fluid inclusions in natural quartz crystals. Contributions to Mineralogy and Petrology, **137**, 1-14.

Bakker RJ (1997) Clathrates: Computer programs to calculate fluid inclusion V-X properties using clathrate melting temperatures. Computers & Geosciences, **23**, 1-18.

Bakker RJ (1998) Improvements in clathrate modelling II: The H_2O-CO_2-CH_4-N_2-C_2H_6 fluid system. Geological Society Special Publications, **137**, 75-105.

Bakker RJ (1999) Adaption of Bowers & Helgeson (1983) equation of state to isochore and fugacity coefficient calculation in the H_2O-CO_2-CH_4-N_2-NaCl fluid system. Chemical Geology, **154**, 225-236.

Bakker RJ (2001a) Combined Raman Spectroscopy and low temperature Micro-thermometry. In: XVI ECROFI, European Current Research on Fluid Inclusions, Porto 2001. Abstracts (Noronha F, Dória A, Guedes A; Eds). Faculdade de Ciencias do Porto, Departamiento de Geologia. **Memória n° 7**, 15-18. University of Porto.

Bakker RJ (2001b) FLUIDS: new software package to handle microthermometric data and to calculate isochores. XVI ECROFI, European Current Research on Fluid Inclusions, Porto 2001. Abstracts (Noronha F, Doria A, Guedes A; Eds) Faculdade de Ciencias do Porto, Departamiento de Geologia, **Memoria n° 7**, 23-25. University of Porto.

Bakker RJ & Jansen JBH (1990) Preferential water leakage from fluid inclusions by means of mobile dislocations. Nature, **345**, 58-60.

Bakker RJ & Jansen JBH (1991) Experimental post-entrapment water loss from synthetic CO_2-H_2O inclusions in natural quartz. Geochimica et Cosmochimica Acta, **55**, 2215-2230.

Bakker RJ & Jansen JBH (1994) A mechanism for preferential H_2O leakage from fluid inclusions in quartz, based on TEM observations. Contributions to Mineralogy and Petrology, **116**, 7-20.

Bakker RJ & Thiery R (1994) Application of clathrates to fluid inclusions studies. In: IMA '94. Short Course on Fluid Inclusions in Minerals (de Vivo B & Frezzotti ML; Eds). Virginia Tech, 191-208.

Barker CE & Goldstein RH (1990) Fluid inclusion technique for determining maximum temperature in calcite and its comparison to the vitrinite reflectance geothermometer. Geology, **18**, 1003-1006.

Barker CE & Kopp OC -Eds- (1991) Luminescence Microscopy and Spectroscopy – Qualitative and quantitative applications. SEPM Short Course, **25**, 195pp.

Barker CE & Pawlewicz MJ (1986) The correlation of vitrinite reflectance with maximum temperature in humic organic matter. In: Palaeogeothermics (Buntebarth G & Stegena L; Eds). Springer (Heidelberg). Lecture Notes in Earth Sciences, **5**, 79-93.

Barnes MA, Barnes WC, Bustin RM (1990) Chemistry and diagenesis of organic matter in sediments and fossil fuels. In: Diagenesis (McIlreath IA & Morrow DW; Eds). Geoscience Canada reprint series, **4**, 189-204.

Bastida F, Brime C, Garcia-Lopez S, Sarmiento GN (1999) Tectono-thermal evolution in a region with thin-skinned tectonics; the western nappes in the Cantabrian Zone (Variscan Belt of NW Spain). International Journal of Earth Sciences, **88**, 38-48.

Bennet P & Siegel DI (1987) Increased solubility of quartz in water due to complexing by organic compounds. Nature, **326**, 684-686.

Bevins RE, White SC, Robinson D (1996) The South Wales Coalfield: low-grade metamorphism in a foreland basin setting? Geological Magazine, **133**, 739-749.

Bieg G & Burger K (1992) Preliminary study of tonsteins of the Pastora Formation (Stephanian B) of the Ciñera-Matallana Coalfield, north-western Spain. International Journal of Coal Geology, **21**, 139-160.

Bjørlykke K (1994) Fluid-flow processes and diagenesis in sedimentary basins. In: Geofluids: Origin, Migration and Evolution of Fluids in Sedimentary Basins (Parnell J; Ed). Geological Society Special Publication, **78**, 127-140.

Bodnar RJ (1993) Revised equation and table for determining the freezing point depression of H_2O-NaCl solutions. Geochimica et Cosmochimica Acta, **57**, 683-684.

Bodnar RJ & Bethke PM (1984) Systematics of stretching of fluid inclusions: I. Fluorite and sphalerite at one atmosphere confining pressure. Economic Geology and the Bulletin of the Society of Economic Geologists, **79**, 141-161.

Bodnar RJ, Binns PR, Hall DL (1989) Synthetic fluid inclusions VI. Quantitative evaluation of the decrepitation behaviour of fluid inclusions in quartz at one atmosphere confining pressure. Journal of Metamorphic Geology, **7**, 229-242.

Bohor BF & Tripplehorn DM (1993) Tonsteins: Altered volcanic-ash layers in coal-bearing sequences. Geological Society of America Special Paper, **285**, 44pp.

Boiron M, Essarraj S, Sellier E, Cathelineau M, Lespinasse M, Poty B (1992) Identification of fluid inclusions in relation to their host microstructural domains in quartz by cathodoluminescence. Geochimica et Cosmochimica Acta, **56**, 175-185.

Boullier AM, France-Lanord C, Dubessy J, Adamy J, Champenois M (1991) Linked fluid and tectonic evolution in the High Himalayan Mountains (Nepal). Contributions to Mineralogy and Petrology, **107**, 358-372.

Brime C (1985) A diagenesis to metamorphism transition in the Hercynian of NW Spain. Mineralogical Magazine, **49**, no.352, 481-484.

Brime C & Pérez-Estaún A (1980) A Diagenesis-metamorphism transition in the Cabo Peñas region. Cuadernos do Laboratorio Xeoloxico de Laxe, **1**, 85-97.

Brime C, García-López S, Bastida F, Valín ML, Sanz-López J, Aller J (2001) Transition from diagenesis to metamorphism near the front of the Variscan regional metamorphism (Cantabrian Zone, north-western Spain). Journal of Geology, **109**, 363-379.

Brindley GW & Brown G -Eds- (1980) Crystal Structures of Clay Minerals and Their X-ray Identification. Mineralogical Society, London, 495pp.

Brown G & Brindley GW (1980) X-ray Diffraction Procedures for Clay Mineral Identification. In: Crystal Structures of Clay Minerals and Their X-ray Identification (Brindley GW & Brown G; Eds-). Mineralogical Society, London, 305-360.

Budai JM, Lohmann KC, Owen RM (1984) Burial dedolomite in the Missisipian Madison Limestone, Wyoming and Utah thrust belt. Journal of Sedimentary Petrology, **54**, 276-288.

Burke EAJ (2001) Raman microspectrometry of fluid inclusions. Lithos, **55**, 139-158.

Burkhard M (1993) Calcite-twins, their geometry, appearance and significance as stress-strain markers and indicators of tectonic regime: a review. Journal of Structural Geology, **15**, 351-368.

Burley SD, Mullis J, Matter A (1989) Timing diagenesis in the Tartan Reservoir (UK North Sea): constraints from combined cathodoluminescence microscopy and fluid inclusion studies. Marine and Petroleum Geology, **6**, 98-120.

Burruss RC (1987a) Palaeotemperatures from fluid inclusions: advances in theory and technique. In: Thermal History of Sedimentary Basins, Methods and Case Histories (Naeser ND & McCulloh TH; Eds). American Association of Petroleum Geologists Special Publication, **41**, 121-131.

Burruss RC (1987b) Diagenetic palaeotemperatures from aqueous inclusions: re-equilibration of inclusions in carbonate cements by burial heating. Mineralogical Magazine, **51**, 477-481.

Carroll JJ, Slupsky JD, Mather AE (1991) The solubility of carbon dioxide in water at low pressure. Journal of Physical Chemistry Reference Data, **20**, 1201-1209.

Clayton RN, Friedman I, Graf DL, Mayeda TK, Meents WF, Shimp NF (1966) The origin of saline formation waters. Journal of Geophysical Research, **71**, 3869-3882.

Cole JE, Miliorizos M, Frodsham K, Gayer RA, Gillespie PA, Hartley AJ, White SC (1991) Variscan structures in the opencast coal sites of the South Wales Coalfield. Proceedings of the Ussher Society, **7**, 375-379.

Colmenero JR & Prado JG (1993) Coal basins in the Cantabrian Mountains, north-western Spain. International Journal of Coal Geology, **23**, 215-229.

Corretgé LG & Suárez O (1990) Cantabrian and Palentian Zones: Igneous rocks. In: Pre-Mesozoic Geology of Iberia (Dallmeyer RD & Martinez Garcia E, Eds). Springer (Heidelberg), 72-79.

Crespo JL, Moro MC, Fadón O, Cabrera R, Fernández A (2000) The Salamón gold deposit (León, Spain). Journal of Geochemical exploration, **71**, 191-208.

Daniels EJ, Altaner SP, Marshak S, Eggleston JR (1990) Hydrothermal alteration in anthracite from eastern Pennsylvania: implications for mechanisms of anthracite formation. Geology, **18**, 247-250.

de Groot K (1967) Experimental dedolomitisation. Journal of Sedimentary Petrology, **37**, 1216-1220.

Diamond LW (1990) Fluid inclusion evidence for P-V-T-X evolution of hydrothermal solutions in Late-Alpine gold-quartz veins at Brusson, Val d'Ayas, NW Italian Alps. American Journal of Science, 290, 912-958.

Diamond LW (2001) Review of the systematics of CO_2-H_2O fluid inclusions. Lithos, **55**, 69-99.

Diamond LW & Marshall DD (1994) Fluid inclusions in vein samples from boreholes at Wellenberg, Switzerland. Unpublished report, University of Bern.

Dickson JAD (1965) Carbonate identification and genesis as revealed by staining. Journal of Sedimentary Petrology, **36**, 491-505.

Duan Z, Møller N, Weare JH (1992a) An equation of state for the CH_4-CO_2-H_2O system: I. Pure systems from 0 to 1000°C and 0 to 8000 bar. Geochimica et Cosmochimica Acta, **56**, 2605-2617.

Duan Z, Møller N, Weare JH (1992b) An equation of state for the CH_4-CO_2- H_2O system: II. Mixtures from 50 to 1000°C and 0 to 1000 bar. Geochimica et Cosmochimica Acta, **56**, 2619-2631.

Duan Z, Møller N, Weare JH (1996) A general equation of state for supercritical fluid mixtures and molecular dynamics simulation of mixture P-V-T-X properties. Geochimica et Cosmochimica Acta, **60**, 1209-1216.

Dubessy J, Audeoud D, Wilkins R, Kosztolany C (1982) The use of the Raman Microprobe Mole in the determination of the electrolytes dissolved in the aqueous phase of fluid inclusions. Chemical Geology, **37**, 137-150.

Dubessy J, Poty B, Ramboz C (1989) Advances in C-O-H-N-S fluid geochemistry based on micro-Raman spectrometric analysis of fluid inclusions. European Journal of Mineralogy, **1**, 517-534.

Dubessy J, Buschaert S, Lamb W, Pironon J, Thiéry R (2001) Methane bearing aqueous fluid inclusions: Raman analysis, thermodynamic modelling and application to petroleum basins. Chemical Geology, **173**, 193-205.

Duddy IR, Green PF, Bray RJ, Hegarty KA (1994) Recognition of the thermal effects of fluid flow in sedimentary basins. In: Geofluids: Origin, Migration and Evolution of Fluids in Sedimentary Basins (Parnell J, Ed). Geological Society Special Publication, **78**, 325-345.

Eberl DD, Srodon J, Nüesch R (1996) MUDMASTER: a program for calculating crystallite size distributions and strain from the shapes of X-ray diffraction peaks. USGS Open File Report **96-171**, 44 pp.

Eberl D, Drits VA, Srodon J (1998) Deducing growth mechanisms for minerals from the shape of crystal size distributions. American Journal of Science, **298**, 499-533.

Ehrenberg SN, Aagaard P, Wilson MJ, Fraser AR, Duthie DML (1993) Depth-dependent transformation of kaolinite to dickite in sandstones of the Norwegian Continental Shelf. Clays and clay minerals, **28**,325-352.

Fein JB (2000) Experimental and field constraints on the role of silica-organic complexation and silica-microbial interactions during sediment diagenesis. Special Publications of the International Association of Sedimentologists, **29**, 119-127.

Fisher D & Byrne T (1990) The character and distribution of mineralised fractures in the Kodiak Formation, Alaska: implications for fluid flow in an underthrust sequence. Journal of Geophysical Research, **95**, 9069-9080.

Fitches WR (1987) Aspects of veining in the Welsh Lower Palaeozoic Basin. In: Deformation of Sediments and Sedimentary Rocks (Jones ME & Preston RMF; Eds). Geological Society Special Publications, **29**, 325-342.

Foley NK, Bethke PM, Rye RO (1989) A reinterpretation of the δD_{H_2O} of inclusion fluids in contemporaneous quartz and sphalerite, Creede mining district, Colorado. Economic Geology, **84**, 1966-1977.

Francis EH (1982) Emplacement mechanism of late Carboniferous tholeiite sill in northern Britain. Journal of the Geological Society, London, **139**, 1-20.

Frey M, Teichmüller M, Teichmüller R, Mullis J, Künzi B, Breitschimd A, Gruner U, Schwizer B (1980) Very low-grade metamorphism in external parts of the Central Alps: Illite crystalinity, coal rank and fluid inclusion data. Eclogae Geologae Helveticae, **73**, 173-203.

Frey M (1987) Very low-grade metamorphism of clastic sedimentary rocks. In: Low Temperature Metamorphism (Frey M; Ed). Blackie & Sons, Glasgow, 9-57.

Friedman I & O'Neill JR (1977) Compilation of stable isotope fractionation factors of geochemical interest. US Geological Survey Professional Paper, **440 K-K**, 12 pp.

Frings KH (2002) Palaeotemperature anomalies in late-Variscan coal basins, Ciñera-Matallana basin, Cantabrian Zone, NW Spain. GAEA heidelbergensis, **11**, 128pp.

Frodsham K & Gayer RA (1997) Variscan compressional structures within the main productive coal-bearing strata of South Wales. Journal of the Geological Society, London, **154**, 195-208.

Galán E, Aparicio A, Villegas FJ (1978) El metamorfismo de muy bajo grado (Anquimetamorfismo) de la Cuenca Carbonífera Ciñera-Matallana, León. Estudios Geológicos, **34**, 505-510.

García López S, Brime C, Bastida F, Sarmiento NG (1997) Simultaneous use of thermal indicators to analyse the transition from diagenesis to metamorphism: an example from the Variscan Belt of north-west Spain. Geological Magazine, **134**, 323-334.

García López S, Bastida F, Brime C, Aller J, Valín ML, Sanz-López J, Méndez CA, Menéndez-Álvarez JR (1999) Metamorphic episodes in the Cantabrian Zone and their structural context. Trabajos de Geología, **21**, 177-187.

Gardiner DJ & Graves PR -Eds- (1989) Practical Raman Spectroscopy. Springer, Berlin.

Garven G (1995) Continental-scale groundwater flow and geological processes. Annual Review of Earth and Planetary Sciences, **24**, 89-117.

Gasparrini M, Bechstädt T, Boni M (2001) Large scale hydrothermal dolomitization in the Southern Cantabrian Zone (NW Spain). In: Water-Rock Interaction 2001 (Cidu R; Ed). Swets & Zeitlinger Publishers, **Volume 1**, 165-168.

Gasparrini M, Bakker RJ, Bechstädt T, Boni M (2002) Massive hydrothermal dolomitization in the Cantabrian Zone (NW Spain): a Permian to Triassic event promoted by extensional tectonics? AAPG-IFP Hedberg Conference, Palermo. Abstracts (Roure F & Swennen R; Eds), s18.

Gayer RA, Cole JE, Frodsham K, , Hartley AJ, Hillier B, Miliorizos M, White SC (1991) The role of fluids in the evolution of the South Wales Coalfield foreland basin. Proceedings of the Ussher Society, **7**, 380-384.

Gayer RA, Fowler R and Davies G (1997) Coal rank variations with depth related to major thrust detachments in the South Wales coalfield: Implications for fluid flow and mineralisation. In: European coal geology and technology (Gayer RA & Pesek J; Eds). Geological Society Special Publication, **125**, 161-178.

Gayer RA, Garven G, Rickard D (1998) Fluid migration and coal-rank development in foreland basins. Geology, **26**, 679-682.

Goldstein RH (1986) Re-equilibration of fluid inclusions in low-temperature calcium carbonate cement. Geology, **14**, 792-795.

Goldstein RH & Reynolds TJ (1994) Systematics of fluid inclusions in diagenetic minerals. SEPM Short Course, **31**, 199 pp.

Gómez-Fernández F, Both RA, Mangas J, Arribas A (2000) Metallogenesis of Zn-Pb Carbonate-Hosted mineralisation in the south-eastern region of the Picos de Europa (Central Northern Spain) province: geologic, fluid inclusion, and stable isotope studies. Economic geology, **95**, 19-40.

Götze J, Plötze M, Habermann D (2001) Origin, spectral characteristics and practical applications of the cathodoluminescence of quartz – A review. Mineralogy and Petrology, **71**, 225-250.

Gratier JP (1982) Experimental and natural approach to the deformation of rocks by dissolution-crystallisation, with material transfer. Bulletin de Mineralogie, **105**, 291-300.

Gratier JP & Jenatton, L (1984) Deformation by solution-deposition, and re-equilibration of fluid inclusions in crystals depending on temperature, internal pressure and stress. Journal of Structural Geology, **6**, 189-200.

Grimmer JOW (2000) Fluidassoziierte Brekzien als Monitor dolomitisierender und dedolomitisierender Lösungströme in der Kantabrischen Zone (Nordspanien). Naturwissenschaftlich-Mathematischen Gesamtfakultät. Ruprecht-Karls-Universität Heidelberg, 148pp.

Haar L, Gallagher JS, Kell GS (1984) Steam Tables, thermodynamic and transport properties and computer programs for vapour and liquid state of water in SI units. Hemisphere Publishing.

Helmig HM (1965) The Geology of the Valderrueda, Tejerina, Ocejo and Sabero coal basins (Cantabrian mountains, Spain). Leidse Geologische Mededelingen, **32**, 75-149.

Heward AP (1978) Alluvial fan and lacustrine sediments from the Stephanian A and B (La Magdalena, Ciñera-Matallana and Sabero coalfields), northern Spain. Sedimentology, **25**, 451-483.

Hoefs J (1997) Stable Isotope Geochemistry. 4th Edition. Springer-Verlag, 202 pp.

Hollister LS & Crawford ML, Eds (1981) Fluid Inclusions: Applications to Petrology. Mineralogical Association of Canada Short Course Handbook, **6**, 304 pp.

Horváth F, Dövény P, Laczó I (1986) Geothermal effect of magmatism and its contribution to the maturation of organic matter in sedimentary basins. Lecture Notes in Earth Sciences, **5**, 173-183.

Hurai V & Horn E-E (1992) A boundary layer-induced immiscibility in naturally re-equilibrated H_2O-CO_2-NaCl inclusions from metamorphic quartz (Western Carpathians, Czechoslovakia) Contributions to Mineralogy and Petrology, **112**, 414-427.

Johnston CT, Sposito G, Birge RR (1985) Raman spectroscopy of kaolinite in aqueous suspension. Clays and Clay Minerals, **33**, 483-489.

Julivert M (1971) Décollement tectonics in the Hercinian Cordillera of NW Spain. American Journal of Science, **270**, 1-29.

Julivert M (1978) Hercynian orogeny and Carboniferous palaeogeography in north-western Spain: a model of deformation-sedimentation relationships. Zeitschrift der Deutschen Geologischen Gesellschaft, **129**, 565-592.

Kastner M (1982) When does dedolomitization occur and what controls it. 11th International Congress of Sedimentology (Abstracts). Hamilton, Ontario, Canada, 124.

Keller M & Krumm S (1993) Variscan versus Caledonian and Precambrian metamorphic events in the Cantabrian Mountains, Northern Spain. Zeitschrift der Deutschen Geologischen Gesellschaft, **144**, 88-103

Kisch HJ (1987) Correlation between indicators of very low-grade metamorphism. In: Low Temperature Metamorphism (Frey M; Ed). Blackie & Sons, Glasgow, 227-300.

Kisch HJ & Taylor GH (1966) Metamorphism and alteration near an intrusive-coal contact. Economic Geology, **61**, 343-361.

Kisch HJ & van den Kerkhof AM (1991) CH_4-rich inclusions from quartz veins in the Valley-and-Ridge province and the anthracite fields of the Pennsylvania Appalachians. American Mineralogist, **76**, 230-240.

Knight JA (1983) The stratigraphy of the Stephanian rocks of the Sabero Coalfield, León (NW Spain), and an investigation of the fossil flora: part I. The stratigraphy and general geology of the Sabero Coalfield. Paleontographica (Stuttgart), **Abt. B 187**, 1-88.

Knight JA, Burger K, Bieg G (2000) The pyroclastic tonsteins of the Sabero Coalfield, north-western Spain, and their relationship to the stratigraphy and structural geology. International Journal of Coal Geology, **44**, 187-226.

Kokelaar BP (1982) Fluidisation of wet sediments during the emplacement and cooling of various igneous bodies. Journal of the Geological Society, London, **139**, 21-33.

Kretz R (1983) Symbols for rock-forming minerals. American Mineralogist, **68**, 277-279.

Kronenberg AK, Kirby SH, Aines RD, Rossman GR (1986) Solubility and diffusional uptake of hydrogen in quartz at high water pressures; implications for hydrolytic weakening. Journal of Geophysical Research, B, Solid Earth and Planets, **91**, 12,723-12,741.

Krumgalz BS, Pogorelsky R, Pitzer KS (1996) Volumetric properties of single aqueous electrolytes from zero to saturation concentrations at 298.15 K represented by Pitzer's Ion-Interaction Equation. Journal of Physical Chemistry Reference Data, **25**, 663-689.

Küster M & Stöckhert B (1997) Density changes of fluid inclusions in high-pressure low-temperature metamorphic rocks from Crete: A thermobarometric approach based on the creep strength of host minerals. Lithos, **41**, 151-167.

Lacazette A (1990) Application of linear elastic fracture mechanics to the quantitative evaluation of fluid-inclusion decrepitation. Geology, **18**, 782-785.

Land LS (1983) The application of stable isotopes to studies of the origin of dolomite and to problems of diagenesis of clastic sediments. SEPM Short Course, **10**.

Land LS & Prezbindowski DR (1981) The origin and evolution of saline formation waters, lower Cretaceous carbonates, south-central Texas, USA. Journal of Hydrology, **54**, 51-74.

Lee BI & Kesler MG (1975) A generalised thermodynamic correlation based on three-parameter corresponding states. American Institute of Chemical Engineering Journal, **21**, 510-527.

Leroy J (1979) Gauging the internal pressure of fluid inclusions during decrepitation. Bulletin de Mineralogie, **102**, 584-593.

Lobato L, García Alcalde JL, Sánchez de Posada LC, Truyols J, Villegas FJ (1984) Hoja del Mapa Geológico Nacional E. 1:50.000 **n° 104** (BOÑAR). 2 Serie MAGNA. Instituto Geológico y Minero de España.

Luque C, Martínez-García E, Ruiz F (1990) Metallogenesis. In: Pre-Mesozoic geology of Iberia (Dallmeyer RD & Martínez-García E; Eds). Springer-Verlag, 80-87.

References

Machel HG & Burton EA (1991) Factors governing cathodoluminescence in calcite and dolomite, and their implications for studies of carbonate diagenesis. In: Luminescence Microscopy and Spectroscopy – Qualitative and quantitative applications (Barker CE and Kopp OC; Eds). SEPM Short Course, **25**, 37-57.

Machel HG, Mason RA, Mariano AN, Mucci A (1991) Causes and emission of luminescence in calcite and dolomite. In: Luminescence Microscopy and Spectroscopy – Qualitative and quantitative applications (Barker CE and Kopp OC; Eds). SEPM Short Course, **25**, 9-25.

Marcos A & Pulgar JA (1982) An approach to the tectonostratigraphic evolution in the Cantabrian Foreland thrust and fold belt, Hercynian Cordillera of NW Spain. Neues Jahrbuch. Geologie und Paläontologie, **163** (2), 256-260.

Marschik R (1992) Der Übergang von der Diagenese zur sehr niedergradigen Metamorphose im externen Varistikum (Kantabrische Zone), NW Spanien. Unpublished Diploma Thesis, University Heidelberg, 70 pp.

Martínez-García E (1990) Stephanian and Permian Basins. In: Pre-Mesozoic geology of Iberia (Dallmeyer RD & Martínez-García E; Eds). Springer-Verlag, 80-87.

McCaffrey KJW, Lonergan L, Wilkinson JJ -Eds- (1999) Fractures, Fluid Flow and Mineralization. Geological Society Special Publication, **155**, 330 pp.

McKinley JM, Worden R, Ruffell AH (2001) Contact diagenesis; the effect of an intrusion on reservoir quality in the Triassic Sherwood Sandstone Group, Northern Ireland. Journal of Sedimentary Research, **71**, 484-495.

McMillan PF (1989) Raman spectroscopy in mineralogy and geochemistry. Annual Reviews of Earth and Planetary Sciences, **17**, 225-283.

McMillan PF & Hofmeister AM (1988) Infrared and Raman spectroscopy. In: Spectroscopy Methods in Mineralogy and Geology. Reviews in Mineralogy, **18**, 99-159.

Méndez-Cecilia AJ (1985) Estudio de la evolución de los carbones de la cuenca Ciñera-Matalana, León. Unpublished PhD Thesis, University of Oviedo, 269 pp.

Milliken KL (1998) Carbonate diagenesis in non-marine sandstones at the western edge of the Alleghenian overthrust belt, southern Appalachians. Special Publications of the International Association of Sedimentologists, **26**, 87-105.

Moore CH & Druckman Y (1981) Burial diagenesis and porosity evolution, Upper Jurassic Smackover, Arkansas and Lousiana. Bulletin of the American Association of Petroleum Geologists, **65**, 597-628.

Moore DM & Reynolds RC (1997) X-ray diffraction and the identification and analysis of clay minerals. 2nd Edition. Oxford University Press, 378 pp.

Morad S. (1998) Carbonate cementation in sandstones: distribution pattern and geochemical evolution. Special Publications of the International Association of Sedimentologists, **26**, 1-26.

152

Morad S, Ketzer JM, de Ros LF (2000) Spatial and temporal distribution of diagenetic alterations in siliciclastic rocks: implications for mass transfer in sedimentary basins. Sedimentology, **47** (supplement 1), 95-120.

Morrow DW, Cumming GL, Koepnick RB (1986) Manetoe facies – a gas-bearing, megacrystalline, Devonian dolomite, Yukon and Northwest Territories. Canada. Bulletin of the American Association of Petroleum Geologists, **70**, 702-720.

Muchez P, Slobodnik M, Viaene WA, Keppens E (1995) Geochemical constraints on the origin and migration of palaeofluids at the northern margin of the Variscan Foreland, southern Belgium. Sedimentary Geology, **96**, 191-200.

Muchez P & Sintubin M (1997) Contrasting origin of palaeofluids in a strike-slip fault system. XIV ECROFI, European Current Research on Fluid Inclusions, Nancy 1997. 222-223.

Mullis J (1979) The system methane-water as a geologic thermometer and barometer from the external part of the Alps. Bulletin de Minéralogie, **102**, 526-536.

Mullis J (1987) Fluid inclusion studies during very low-grade metamorphism. In: Low Temperature Metamorphism (Frey M; Ed). Blackie & Sons, Glasgow, 162-199.

Mullis J, Dubessy J, Poty B, O'Neil J (1994) Fluid regimes during late stages of continental collision: Physical, chemical, and stable isotope measurements of fluid inclusions in fissure quartz from a geotraverse through the Central Alps, Switzerland. Geochimica et Cosmochimica Acta, **58**, 2239-2267.

Naden J (1996) CalcicBrine; a Microsoft Excel 5.0 add-in for calculating salinities from microthermometric data in the system $NaCl-CaCl_2-H_2O$. Program and Abstracts; Biennial Pan-American Conference on Research on Fluid Inclusions, **6**, 97-98.

O'Hara M & Reid RC (1973) Modelling Crystal Growth Rates from Solution. Englewood Cliffs, New Jersey, Prentice-Hall, 272 pp.

Olds RH, Sage BH, Lacey WN (1942) Phase equilibria in hydrocarbon systems: Composition of the dew-point gas in the methane-water system. AIChE Journal, **10**, 202.

Oliver J (1986) Fluids expelled tectonically from orogenic belts: Their role in hydrocarbon migration and other geologic phenomena. Geology, **14**, 99-102.

Osborne M & Haszeldine RS (1993) Evidence for resetting of fluid inclusion temperatures from quartz cements in oilfields. Marine and Petroleum Geology, **10**, 233-239.

Osborne M & Haszeldine RS (1995) Discussion: Evidence for resetting of fluid inclusion temperatures from quartz cements in oilfields. Marine and Petroleum Geology, **12**, 559-575.

Pagel M, Barbin V, Blanc P, Ohnenstetter D -Eds- (2000) Cathodoluminescence in Geosciences. Springer Verlag, 514 pp.

Paniagua A (1998) Gold showings and deposits of the Palentian Zone (NW Spain). In: Gold Exploration and Mining in NW Spain (Arias D, Martín-Izard A, Paniagua A; Eds). Facultad de Geología-Departamento de Geología. Universidad de Oviedo.

Paniagua A, Loredo J, Gracía-Iglesias J (1988) Epithermal (Cu-Co-Ni) mineralisation in the Aramo mine (Cantabrian Mountains, Spain): correlation between paragenetic and fluid inclusion data. Bulletin de Minéralogie, **111**, 383-391.

Paniagua A, Rodriguez-Pevida LS, Gutierrez-Villarias JL (1988a) Mineralizaciones As-Sb-Au asociadas a rocas igneas filonianas del NE de León: las minas de Burón. Boletín de la Sociedad Española de Mineralogía, **11**, 35-46.

Paniagua A, Fontboté L, Fenoll Hach-Alí P, Fallick AE, Moreiras DB, Corretgé LG (1993) Tectonic setting, mineralogical characteristics, geochemical signatures and age dating of a new type of epithermal carbonate-hosted, precious metal-five element deposits: the Villamanín area (Cantabrian Zone, Northern Spain). In: Current research in geology applied to ore deposits (Fenoll Hach-Alí, Torres-Ruiz, Gervilla; Eds). 2nd biennal SGA Meeting, Granada, 531-534.

Paniagua A, Loredo J, García-Iglesias J (1995). Epithermal carbonate-hosted Au-Cu-Ni-Co mineralisation at the Villamanín area (Cantabrian Zone, N Spain): fluid inclusion study versus paragenetic and sulfur isotopic data. XIII ECROFI, European Current Research on Fluid Inclusions, Barcelona 1995. Boletín de la Sociedad Española de Mineralogía, **18**, 172-173.

Paniagua A, Loredo J, Fenoll P, Rodríguez-Pevida LS (1997) Extrapolation at low temperatures of the arsenopyrite geothermometer contrasting with fluid inclusion data: the example of Salamón (Spain). XIV ECROFI, European Current Research on Fluid Inclusions, Nancy 1997. 255-256.

Parnell J -Ed- (1994) Geofluids: Origin, Migration and Evolution of Fluids in Sedimentary Basins. Geological Society Special Publication, **78**, 374 pp.

Paschier CW & Trouw RAJ (1998) Microtectonics. 2ndEdition. Springer-Verlag, 289 pp.

Pêcher A (1981) Experimental decrepitation and re-equilibration of fluid inclusions in synthetic quartz. Tectonophysics, **78**, 565-576.

Pérez-Estaun A, Bastida F, Alonso JL, Marquínez J, Aller J, Alvarez-Marrón J, Marcos A, Pulgar JA (1988) A thin-skinned tectonic model for an arcuate fold and thrust belt: the Cantabrian Zone (Variscan Ibero-Armorican Arc). Tectonics, **7** (3), 517-537.

Prezbindowsky DR & Larese RE (1987) Experimental stretching of fluid inclusions in calcite: implications for diagenetic studies. Geology, **15**, 333-336.

Price LC (1979) Aqueous solubility of methane at elevated pressures and temperatures. Bulletin of the American Association of Petroleum Geologists, **63**, 1527-1533.

Pulgar FJ, Alonso JL, Espina RG, Marín JA (1999) The alpine deformation in the Variscan basement of the Cantabrian Zone. Trabajos de Geología, **21**, 283-294.

Radke BM & Mathis RL (1980) On the formation and occurrence of saddle dolomite. Journal of Sedimentary Petrology, **50**, 1149-1168.

Ramboz C, Pichavant M and Weisbrod A (1982) Fluid immiscibility in natural processes. Use and misuse of fluid inclusion data. II. Interpretation of fluid inclusion data on terms of immiscibility. Chemical Geology, **37**, 29-48.

Raven JGM & Van der Pluijm BA (1986) Metamorphic fluids and transtension in the Cantabrian Mountains of northern Spain: an application of the conodont colour alteration index. Geological Magazine, **123**, 673-681.

Raymond AC & Murchison DG (1991) The relationship between organic maturation, the widths of thermal aureoles and the thicknesses of sills in the Midland Valley of Scotland and Northern England. Journal of the Geological Society, London, **148**, 215-218.

Renard F, Brosse E, Sommer F (2000) The different processes involved in the mechanism of pressure solution in quartz-rich rocks and their interactions. Special Publications of the International Association of Sedimentologists, **29**, 67-78.

Rettich TR, Handa YP, Battino R, Wilhelm E (1981) Solubility of gases in liquids: 13. High precision of Henry's constants for methane and ethane on liquid water at 275 to 328 K. Journal of Physical Chemistry, **85**, 3230-3237.

Roberts S & Beattie I (1995) Micro-Raman spectroscopy in the Earth Sciences. In: Microprobe Techniques in the Earth Sciences (Potts PJ, Bowless JFW, Reed SJB Cave MR; Eds). Chapman and Hall, London, 387-408.

Roedder E (1984) Fluid Inclusions. Reviews in Mineralogy, **12**, 646 pp.

Rosenbaum J & Sheppard SM (1986) An isotopic study of siderites, dolomites and ankerites at high temperatures. Geochimica et Cosmochimica Acta, **50**, 1147-1150.

Rusk B & Reed M (2002) Scanning electron microscope-cathodoluminescence analysis of quartz reveals complex growth histories in veins from the Butte porphyry copper deposit, Montana. Geology, **30**, 727-730.

Samson IM & Walker RT (2000) Cryogenic Raman Spectroscopic studies in the system $NaCl-CaCl_2-H_2O$ and implications for low-temperature phase behaviour in aqueous fluid inclusions. Canadian Mineralogist, **38**, 35-43.

Schiffman P & Day HW (1999) Petrological methods for the study of very low-grade metabasites. In: Low-Grade Metamorphism (Frey M & Robinson D; Eds). Blackwell Science, 108-142.

Seitz JC, Pasteris JD, Chou IM (1996) Raman spectroscopic characterisation of gas mixtures II: quantitative composition and pressure determination of the CO_2-CH_4 system. American Journal of Science, **296**, 577-600.

Setzmann U & Wagner W (1991) A new equation of state and tables of thermodynamic properties for methane covering the range from the melting line to 625°K at pressure up to 1000 MPa. Journal of Physical Chemistry Reference Data, **20**, 1061-115.

Sharp ZD (1999) Application of stable isotope geochemistry to low-grade metamorphic rocks. In: Low-Grade Metamorphism (Frey M & Robinson D; Eds). Blackwell Science, 227-260.

Shepherd T, Rankin AH, Alderton DHM (1985) A Practical Guide to Fluid Inclusion Studies. Blackie & Sons, Glasgow, 239 pp.

Sibson RH (1994) Crustal stress, faulting and fluid flow. In: Geofluids: Origin, Migration and Evolution of Fluids in Sedimentary Basins (Parnell J; Ed). Geological Society Special Publication, **78**, 69-84.

Snyman CP & Barclay J (1989) The coalification of South African coal. International Journal of Coal Geology, **13**, 375-390.

Soave G (1972) Equilibrium constants from a modified Redlich-Kwong equation of state. Chemical Engineering Science, **27**, 1197-1203.

Sorby HC (1858) On the microscopical structure of crystals indicating the origin of rocks and minerals. Quarterly Journal of the Geological Society, London, **14**, 453-500.

Spiro B, Tornos F, Shepherd TJ (1995) Stable Isotope characterisation of barren and mineralised tardi-Hercynian hydrothermal carbonates in the Cantabrian Zone (N Spain). In: Mineral Deposits: from their origin to environmental impacts (Pasava J, Kribek B & Zak K; Eds). Rotterdam, Balkema, 75-78.

Spötl C & Pitman JK (1998) Saddle (baroque) dolomite in carbonates and sandstones: a repraisal of a burial diagenetic concept. Special Publications of the International Association of Sedimentologists, **26**, 437-460.

Sterner SM & Bodnar RJ (1989) Synthetic fluid inclusions VII. Re-equilibration of fluid inclusions in quartz during laboratory-simulated metamorphic burial and uplift. Journal of Metamorphic Geology, **7**, 243-260.

Sterner SM, Hall DL, Keppler H (1995) Compositional re-equilibration of fluid inclusions in quartz. Contributions to Mineralogy and Petrology, **119**, 1-15.

Svensen H, Jamtveit B, Banks DA, Karlsen D (2001) Fluids and halogens at the diagenetic-metamorphic boundary: evidence from veins in continental basins, western Norway. Geofluids, **1**, 53-70.

Swanenberg HEC (1980) Fluid inclusions in high-grade metamorphic rocks from SW Norway. PhD Thesis, Geol. Ultraiectina, Univ. Utrecht, 25, 147 pp.

Swierczeswska A, Tokarski AK, Hurai V (2000) Joints and mineral veins during structural evolution: case study from the Outer Carpathians (Poland). Geological Quarterly, **44**, 333-339.

Teichmüller M (1987) Organic material and very low-grade metamorphism. In: Low Temperature Metamorphism (Frey M; Ed). Blackie & Sons, Glasgow, 114-161.

Teichmüller M & Teichmüller R (1986) Relations between coalification and palaeo-geothermics in Variscan and Alpidic foredeeps of western Europe. In: Palaeogeothermics (Buntebarth G & Stegena L; Eds). Springer (Heidelberg). Lecture Notes in Earth Sciences, **5**, 53-78.

Thiery R, Vidal J, Dubessy J (1994) Phase equilibria modelling applied to fluid inclusions; liquid-vapour equilibria and calculation of the molar volume in the CO_2-CH_4-N_2 system. Geochimica et Cosmochimica Acta, **58**, 1073-1082.

Tornos F & Spiro BF (2000) The geology and isotope geochemistry of the talc deposit of Puebla de Lillo (Cantabrian Zone, Northern Spain). Economic Geology, **95**, 1277-1296.

Uysal, IT, Glikson M, Golding SD, Audsley F (2000) The thermal history of the Bowen Basin, Queensland, Australia; vitrinite reflectance and clay mineralogy of Late Permian coal measures. Tectonophysics, **323**, 105-129.

Uysal, I T; Golding, S D; Glikson, M (2000a) Petrographic and isotope constraints on the origin of authigenic carbonate minerals and the associated fluid evolution in Late Permian coal measures, Bowen Basin (Queensland), Australia. Sedimentary Geology, **136**, 189-206.

Valley JW, Taylor HP, O'Neill JR -Eds- (1986) Stable Isotopes in High Temperature Geological Processes. Reviews in Mineralogy, **16**, 570 pp.

van den Kerkhof AM (1990) Isochoric phase diagrams in the systems CO_2-CH_4 and CO_2-N_2: Application to fluid inclusions. Geochimica et Cosmochimica Acta, **54**, 621-629.

van den Kerkhof AM & Hein UF (2001) Fluid inclusion petrography. Lithos, **55**, 27-47.

Villegas FJ (1996) Exploración e investigación de un nuevo yacimiento de carbón en la cuenca minera Cinera-Matallana (León). Unpublished PhD Thesis, Univ. Complutense Madrid, 417p.

Vityk MO & Bodnar RJ (1995) Textural evolution of synthetic fluid inclusions in quartz during re-equilibration, with application to tectonic reconstruction. Contributions to Mineralogy and Petrology, **121**, 309-323.

Vityk MO, Bodnar RJ, Schmidt CS (1994) Fluid inclusions as tectonothermobarometers: Relation between pressure-temperature history and re-equilibration morphology during crustal thickening. Geology, **22**, 731-734.

Vityk MO, Bodnar RJ, Dudok IG (1995) Natural and synthetic re-equilibration textures of fluid inclusions in quartz (Marmarosh Diamond): evidence for refilling under conditions of compressive loading. European Journal of Mineralogy, **7**, 1071-1087.

References

Vityk MO, Bodnar RJ, Dudok IG (1996) Fluid inclusions in "Marmarosh Diamonds": evidence for tectonic history of the Folded Carpathian mountains, Ukraine. Tectonophysics, **255**, 163-174.

Wachter E & Hayes JM (1985) Exchange of oxygen isotopes in carbon-dioxide - phosphoric acid systems. Chemical Geology, **52**, 365-374.

Wagner RH & Artieda JI (1970): La Cuenca Minera Ciñera-Matallana. S.A. Hullera Vasco Leonesa.

Wagner RH (1971) The stratigraphy and structure of the Ciñera-Matallana Coalfield (Province of León, NW Spain). Trabajos de Geología, **4**, 385-429.

Wagner W & Pruss A (1993) International equations for the saturation properties of ordinary water substances. Revised according to the international temperature scale of 1990. Addendum to Journal of Physical Chemistry Reference Data, **16**, 783-787.

Walderhaug O (1994) Temperatures of quartz cementation in Jurassic sandstones from the Norwegian continental shelf – Evidence from fluid inclusions. Journal of Sedimentary Research, **64**, 311-323.

Warr LN & Peacor DR (2002) Evaluation of X-ray diffraction methods for determining the crystal growth mechanisms of clay minerals in mudstones, shales and slates. Schweizerische Mineralogische und Petrographische Mitteilungen, **82**, 187-202.

Welsch H (1973) Die Systeme Xenon-Wasser und Methan-Wasser bei hohen Drücken und Temperaturen. Dissertation, Universität Karlsruhe.

Welton, Joann E (1984) SEM petrology atlas. AAPG methods in exploration series, **4**, 237 pp.

White SC (1991) Palaeo-geothermal profiling across the South Wales Coalfield. Proceedings of the Ussher Society, **7**, 368-374.

Wilson CJL (1994) Crystal growth during a single-stage opening event and its implications for syntectonic veins. Journal of Structural Geology, **16**, 1283-1296.

Winkler HGF (1979) Petrogenesis of metamorphic rocks. Springer-Verlag, 348 pp.

Wood JR (1986) Advective diagenesis: thermal mass transfer in systems containing quartz and calcite. In: Roles of organic matter in sediment diagenesis (Gautier DL; Ed). Society of economic palaeontologists and mineralogists (SEPM) Special Publications, **38**, 170-180.

Worden RH & Morad S (2000) Quartz cementation in oil field sandstones: a review of the key controversies. Special Publications of the International Association of Sedimentologists, **29**, 1-20.

LIST OF FIGURES

LIST OF TABLES

APPENDIX

Table A1. Sample list detailing the different methods applied in the investigation

Table A2. XRD analysis of veins in the sedimentary and igneous rocks

Table A3. Raman Laser microprobe spectrometric analyses of type 1 and 2 fluid inclusions in vein quartz (qtz1)

Table A4. Microthermometry data and volume fractions at room temperature of type 1 vapour-rich fluid inclusions in vein quartz (qtz1)

Table A5. Microthermometry data and volume fractions at room temperature of type 1 aqueous fluid inclusions in vein quartz (qtz1)

Table A6. Microthermometry data and volume fractions at room temperature of type 2 vapour-rich fluid inclusions in vein quartz (qtz1)

Table A7. Microthermometry data and volume fractions at room temperature of type 2 aqueous fluid inclusions in vein quartz (qtz1)

Table A8. Microthermometry data and volume fractions at room temperature of type 3 aqueous fluid inclusions in vein quartz (qtz1)

Table A9. Raman Laser microprobe spectroscopic analyses of the vapour phase of type 3 fluid inclusions in vein quartz (qtz1)

Table A10. Microthermometry data and volume fractions at room temperature of type 1c aqueous fluid inclusions in vein quartz (cal2)

Table A11. Microthermometry data and volume fractions at room temperature of type 1q and type 2q fluid inclusions in hydrothermal quartz (qtz2)

Table A12. Raman Laser microprobe spectroscopic analyses of the vapour phase of type 1q and type 2q fluid inclusions in hydrothermal quartz (qtz2)

Table A13. Raman stretching vibration peaks of gas phases, entrapped minerals and salt hydrates in fluid inclusions

Table A14. Carbon ($\delta^{13}C$) and oxygen ($\delta^{18}O$) stable isotope results for cal2 (SB)

Table A15. Carbon ($\delta^{13}C$) and oxygen ($\delta^{18}O$) stable isotope results for cal2 (CMB)

Table A16. Carbon ($\delta^{13}C$) and oxygen ($\delta^{18}O$) stable isotope results for calcite and dolomite

SAMPLE	LOCAL	FLINC	SECTION	CL	SEM	$d^{18}O/ d^{13}C$	XRD
1	1a	-	-	-	-	YES	YES
2	1a	-	-	-	-	YES	YES
3	1a	-	-	-	-	YES	-
4	1a	-	-	-	-	YES	-
5	1a	-	-		-	YES	YES
6	1b	1	1	YES	-	YES (2)	YES
7	2	-	-	-	-	YES	YES
8	2	-	-	-	-	YES (2)	YES
9	2	1	1	-	-	YES (2)	-
10	2	-	-	-	-	YES	YES
23	3	-	-	-	-	YES	YES
24	3	-	-	-	-	YES	YES
25	3	-	-	-	-	YES (2)	YES
26	4	2	3	YES	YES	YES (3)	YES
27	9	1	1	YES	YES	YES	YES
28	5	2	-	-	-	YES	YES
29	6	-	-	-	-	YES	YES
30	6	-	-	-	-	YES	YES
31	7	3	1	-	-	YES	-
32	8	2	1	YES	-	YES	YES
33	8	1	-	-	-	YES	YES
34	8	1	-	-	-	YES	YES
35	11	-	-	-	-	YES	YES
36	10	4	4	YES	YES	YES (5)	YES
37	10	1	-	-	-	YES	YES
38	10	-	-	-	-	YES	YES

Table A1. Sample list detailing the different methods applied in this investigation. Stephanian rocks of Sabero and Ciñera-Matallana. d = δ.

SAMPLE	LOCAL	FLINC	SECTION	CL	SEM	d¹⁸O/ d¹³C	XRD
39	12a	1	-	-	-	YES	-
40	12a	-	-	-	-	YES	-
41	12a	-	-	-	-	YES	-
42	12a	2	1	-	-	YES	-
43	12a	1	-	-	-	YES	-
44	12a	1	-	-	-	YES	-
45	12b	-	-	-	-	YES	YES
46	12c	-	-	-	-	YES (2)	YES
47	12c	-	1	-	-	YES	YES
48	12c	2	1	YES	-	YES	YES
49	12c	-	-	-	-	YES	YES
50	12c	-	-	-	-	YES	YES
51	12c	1	1	-	-	NO	YES
52	13	-	-	-	-	YES	YES
53	14	-	-	-	-	YES	YES
54	14	-	-	-	-	NO	YES
55	14	1	1	-	-	YES (2)	YES
56	14	-	-	-	-	YES	-
57	14	-	-	-	-	NO	-
58	14	-	-	-	-	YES	YES
59	14	-	-	-	-	YES	-
60	15	1	-	-	-	NO	YES

Table A1 (continued). Stephanian rocks of Ciñera-Matallana.

SAMPLE	LOCAL	FLINC	SECTION	CL	SEM	d^{18}O/ d^{13}C	XRD
11	cretac 1	1	1	-	-	YES (2)	-
12	cretac 1	-	-	-	-	YES	-
13	cretac 1	-	-	-	-	YES (2)	-
14	Portilla 1	1	2	YES	-	YES	-
15	Portilla 1	1	2	-	-	YES (3)	YES
16	Portilla 3	-	-	-	-	YES (2)	YES
17	Portilla 3	-	-	-	-	YES	-
18	Portilla 3	-	-	-	-	YES	-
19	Sta Lucia 12	-	-	-	-	YES (2)	-
20	Portilla12	1	1	-	-	YES	-
21	Sta lucia	-	-	-	-	YES	-
22	Emiliano 13	-	-	-	-	YES	-
IG Q C-M	12b	1	1	-	-	NO	-
IG Q SB	Alejico	1	1	-	-	NO	-

Table A1 (continued). Non Stephanian rocks.

Locality	Sample	Material	Mineral composition
1a	can1	HR+V	cal, kln, qtz, ill/sm
	can2	V+(HR)	cal, kln, ill/sm, qtz
	can5	V+HR	cal, qtz, kln, ill/sm, chl
1b	can6	V+(HR)	cal, kln, qtz, ill/sm, dol
2	can7	V	cal, kln, qtz, ill/sm
	can8	V+HR	cal, kln, qtz, ill/sm
	can10*	V+(HR)	cal, kln, qtz, ill/sm
3	can23*	V+(HR)	kln, cal, qtz, ill/sm, (dol)
	can24	V+SS	cal, kln, qtz, (ill/sm)
	can25*	V	cal, kln, qtz, ill/sm, gp
4	can26	V+SS	kln, ill/sm, qtz, cal, chl
5	can28	V+HR	cal, kln, qtz, ill/sm, dol
6	can29	V+HR	cal, kln, qtz, ill/sm, (chl)
	can30	HR+V	qtz, cal, kln, ill/sm, dol
8	can32	V+HR	cal, qtz, kln, gp, ill/sm, (chl)
	can33	V+HR	cal, qtz, kln
	can34*	V+HR	cal, kln, qtz, ill/sm, (chl)
9	can27	V+HR	kln, cal, ill/sm, qtz, chl
10	can36*	V+HR	cal, kln, qtz, ill/sm, (chl),
	can37*	V+(HR)	cal, kln, qtz, ill/sm, (chl)
	can38	V+(HR)	kln, cal, qtz, ill/sm, chl
11	can35*	V+HR	cal, qtz, ill/sm, kln, chl,
12	can45	V+HR	cal, qtz, kln, ill/sm
	can46*	V+SS	cal, qtz, kln, (ill/sm), (chl), (gp), (ab)
	can48	V+HR	cal, qtz, kln, ill/sm, (chlo),
	can49*	V+SS	kln, ill/sm, cal, chl, qtz, k-fs
	can50	V+SS	cal, ill/sm , qtz, kln, chlo
13	can52	V	cal, qtz, (kln), (ill)
14	can53	HR+V	cal, qtz, (ill)
	can54*	V + SS	kln, qtz, ill/sm, cal, (chl)
	can55	V+SS	qtz, cal, kln, ill/sm, (chl), (k-fs), (ab)
	can 57	V+SS	cal, qtz
	can58	V+HR	cal , qtz, ill/sm, kln, (chl)
15	can60	V	cal, kln, ill, chl, qtz, k-fs, ab
Alejico	Ign-Sb1*	V+HR	qtz, kln, ill/sm, chl, ep
Sotillos	Ign-Sb2	HR	ill, chl, act, pg, qtz, carb
12	Ign12*	V+HR	kln, chl, ill/sm, qtz, pg
14	Ign14*	HR	kln, ill, qtz, carb, chl

Table A2 (see next page).

Table A2. List of X-ray diffraction results for veins in the sedimentary and igneous rocks of Sabero and Ciñera-Matallana basins. All samples are texture preparates ($\Delta\theta < 2\mu m$). Samples marked with (*) have also been used in temperature tests for determining the kaolin mineral polytype, present in 32 out the 34 samples studied. V = vein minerals; HR = host rock; SS = slicken sides. Minerals are listed from higher to lower peak intensities (symbols after Kretz, 1983). Ab = albite; act = actinolite; cal = calcite; carb = carbonate; chl = chlorite; dol = dolomite; ep = epidote; gp = gypsum; ill/sm = illite/smectite; k-fs = k-feldspar; kln = kaolin; pg = plagioclase; qtz = quartz. A mineral listed in brackets indicates a very weak peak intensity.

Inclusion Nr.	Raman peak surface					Mole fraction			
	CH_4	CO_2 v_1	CO_2 $2v_2$	C_2H_6	C_3H_8	CH_4	CO_2	C_2H_6	C_3H_8
26/1-1	284					1			
26/1-2	206					1			
26/1-3	310					1			
26/1-4	262					1			
26/1-5	131					1			
26/1-6	18615			559	340	0.97		0.02	0.01
26/1-7	255					1			
26/1-8	266					1			
26/1-9	305					1			
26/1-10	721					1			
26/2-10	644					1			
26/2-11	582					1			
26/2-12	191					1			
26/2-13	373					1			
26/2-14	2379					1			
26/2-15	1199					1			
26/2-16	1521					1			
26/2-17	390					1			
26/2-18	332					1			
26/2-27	357					1			
26/2-29	1171					1			
26/2-31	485					1			
26/2-32	867					1			
26/2-33	286					1			
26/2-49	14364			351	452	0.98		0.01	0.01
26/2-50	15076			746	474	0.96		0.03	0.01
26/2-51	4982			129	81	0.98		0.01	0.01
28/1-1	5714					1			
28/1-2	2415					1			
28/1-3	44391	165	529			0.96	0.04		
28/1-4	2173					1			
28/1-5	202918	2222	4373	642		0.91	0.09	+	
28/1-6	202864	1262	2102			0.95	0.05		
28/1-7	579	243	383			0.24	0.76		
28/1-8	21621					1			
28/2-1	6678	384	859			0.64	0.36		
28/2-2	174712	2356	4025			0.90	0.10		
28/2-3	3097	659	911			0.40	0.60		
31/1-13	245239	2352	4015			0.93	0.07		
31/1-14	10544	1104	1586			0.57	0.43		
31/1-15	4117	652	757			0.49	0.51		
31/1-16	3958	1220				0.39	0.61		
31/1-17	209382	1984	3511			0.93	0.07		
31/1-18	11247	252	449			0.84	0.16		

Table A3. Raman laser microprobe spectroscopic analyses of type 1 and type 2 fluid inclusions in qtz1. The first number in the Inclusion Nr. refers to the sample number (see location in Table1 and Fig. 4 and 5) and the following number indicates the inclusion type, 1 or 2. All peak surface values are taken from spectra normalised to 30 seconds of excitation time, at room temperature. + = mole fraction of less then 0.01.

Inclusion Nr.	Raman peak surface					Mole fraction			
	CH_4	CO_2 v_1	CO_2 $2v_2$	C_2H_6	C_3H_8	CH_4	CO_2	C_2H_6	C_3H_8
31/2-7	41575	1694	2518			0.77	0.23		
31/2-8	122253	4437	7213			0.78	0.22		
31/2-9	19438	476	792			0.84	0.16		
31/2-7	41575	1694	2518			0.77	0.23		
31/2-8	122253	4437	7213			0.78	0.22		
31/2-9	19438	476	792			0.84	0.16		
31/2-10	19385	649	1342			0.76	0.24		
31/2-11	45920	1298	2158			0.82	0.18		
31/2-12	60002	1975	2874			0.80	0.20		
27/1-1	12623					1			
27/1-2	34941					1			
27/1-3	3741					1			
27/1-4	74122					1			
27/2-1	29929					1			
27/2-2	32528					1			
27/2-3	5761					1			
27/2-4	46127					1			
27/2-5	23275					1			
42/1-1	163175	487	708			0.98	0.02		
42/1-2	198533	423	685			0.98	0.02		
42/1-3	2617					1			
42/2-1	393781	11844	20632	3480		0.80	0.20	+	
42/2-2	322930	9408	18670	3198		0.79	0.21	+	
42/2-3	276922	6128	11805	2285		0.83	0.16	+	
42/2-4	439758	6816	11050	2992		0.89	0.11	+	
42/2-5	231372	1267	2071	874		0.96	0.04	+	
42/2-6	330404	6253	10652	1583		0.86	0.13	+	
42/2-7	272483			962		1		+	
42/2-8	144185	438	678			0.98	0.02		
42/2-9	44298	582	1220			0.89	0.11		
42/2-10	352127	6704	12096			0.86	0.14		
42/2-11	337736	3725	6524			0.92	0.08		
42/2-12	314138	6552	10802			0.86	0.14		
42/2-13	136723	1067	1600			0.94	0.06		
42/2-14	232116	2579	4092			0.92	0.08		

Table A3 (continued).

Inclusion Nr.	T_m (car) in °C	T_h (car) in °C	Volume fraction vapour
28/1-5	-83.6	-72.3	1
28/1-6	-82.7	-72.5	1
28/1-9	-91.9	-78.8 (liq)	1
28/1-10	-85.5	-75.1	1
28/1-11	-85.5	-74.2	1
28/1-12	-86.2	-74.2	1
28/1-13	n.o.	-76.4 (liq)	1
28/1-14	n.o.	-77.5 (liq)	1
28/1-15	n.o.	-75.3	1
28/1-16	-88.0	-76.3 (liq)	1
28/1-17	-88.0	-75.7 (liq)	1
28/1-18	-85.6	-74.9	1
28/1-19	-88.0	-74.9	1
28/1-20	-86.2	-75.1	1
28/1-21	-86.2	-75.2	1
28/1-22	-105.4	-74.9	1
28/1-23	-85.6	-75.3 (liq)	1
28/1-24	-84.4	-75.5 (liq)	1
28/1-25	-85.5	-75.0 (liq)	1
28/1-26	-87.0	-75.7	1
28/1-27	-82.8	-72.5	1
28/1-28	-82.8	-72.3	1
28/1-29	-82.7	-72.4	1
28/1-30	-82.5	-72.3	1
28/1-31	-83.9	-74.7	1

Table A4. Microthermometry data and volume fractions at room temperature for type 1 vapour-rich fluid inclusions in qtz1 (sample 28). car = CH_4-rich gas composition, with minor amounts of CO_2. Homogenisation of the CH_4-rich bubble occurs into the vapour phase, unless indicated in brackets (liq). n.o. = not observed.

Inclusion Nr.	T_m (ice) in °C	T_h (liq) in °C	Volume fraction vapour
31/1-1	-1.1	100	0.04
31/1-2	-1.1	110	0.05
31/1-3	-1.1	110	0.06
31/1-4	-2.9		0.26
31/1-5	-3.0	110	0.04
31/1-6	-2.9		0.05
31/1-7	-3.0		0.09
31/1-8	-3.5		0.13
31/1-9	-1.6	93	0.04
31/1-10	-1.0		0.02
31/1-11	-1.7	73	0.02
31/1-12	-1.6		0.07

Table A5. Microthermometry data and volume fractions at room temperature for type 1 aqueous fluid inclusions in qtz1 (sample 31). Total homogenisation occurs into the liquid phase.

Inclusion Nr.	T_m (car) in °C	T_h (car) in °C	Volume fraction vapour
28/2-4	n.o.	-75.9	1
28/2-5	n.o.	-74.9	1
28/2-6	n.o.	-74.3	1
28/2-7	n.o.	-74.7	1
28/2-8	n.o.	-76.8	1
28/2-9	n.o.	-75.7	1
28/2-10	n.o.	-76.8	1
28/2-11	-86.5	-74.7	1
28/2-12	-89.0	-74.7	1
28/2-13	-88.0	-75.7	1
28/2-14	-86.5	-75.3	1
28/2-15	-81.4	-72.3	1
28/2-16	-81.4	-72.3	1
28/2-17	-79.8	-70.4	1
28/2-18	-81.4	-72.6	1
28/2-19	-80.8	-73.5	1
42/2-1	-81.0	-59.0	1
42/2-2	-73.0	-59.0	1
42/2-3	-85.0	-66.0	1
42/2-4	-81.0	-66.0	1
42/2-8	n.o.	-75.0	0.5
42/2-9	n.o.	-76.0	1
42/2-10	n.o.	-63.0	1
42/2-11	n.o.	-62.1	1
42/2-12	n.o.	-62.0	1
42/2-13	n.o.	-62.1	1
42/2-14	n.o.	-71.0	1
42/2-15	n.o.	-76.0	1
42/2-16	n.o.	-70.7	1

Table A6. Microthermometry data and volume fractions at room temperature for type 2 vapour-rich fluid inclusions in qtz1 (samples 28 and 42). car = CH_4-rich gas composition, with minor amounts of CO_2. Homogenisation of all the CH_4-rich bubbles occurs into the vapour phase. n.o. = not observed.

Inclusion Nr.	T_m (cla) in °C	T_m (ice) in °C	T_h (liq) in °C	Volume fraction vapour
26/2-1		0.0		0.35
26/2-2		-0.6		0.05
26/2-3		0.3 (m)		0.05
26/2-4		-0.8		0.3
26/2-5		-0.7		0.1
26/2-6		-0.9		0.03
26/2-7		-0.9		0.11
26/2-8				0.3
26/2-9		-1.1		0.19
26/2-10		-2.1		0.9
26/2-11		0.5 (m)	105	0.04
26/2-12		0.2 (m)	125	0.07
26/2-13		-1		0.8
26/2-14		-0.1		0.04
26/2-15		-1		0.07
26/2-16			124	0.05
26/2-17			102	0.05
26/2-18			87	0.03
26/2-19			88	0.06
26/2-20			102	0.05
26/2-21				0.11
26/2-22			128	0.06
26/2-23		-0.9		0.1
26/2-24		-0.9		0.6
26/2-25		-0.6		0.45
26/2-26		-0.1		0.01
26/2-27				0.65
26/2-28		-1.0		0.07
26/2-29		-0.9		0.14
26/2-30		-0.9		0.06
26/2-31		-1.1		0.47
26/2-32		-1.1		0.34
26/2-33		2.0 (m)		0.06
26/2-34		-1.9		0.25
26/2-35		-0.9		0.01
26/2-36	-3.2	-2.0	129	0.07
26/2-37			102	0.06
26/2-38			118	0.09
26/2-39	-3.4	2.2 (m)		0.95
26/2-40	-5.0	-3.9		0.48
31/2-1		-1.7		0.04
31/2-2		-1.2		0.08
31/2-3		-1.0		0.06
31/2-4		-1.0		0.07
31/2-5		-1.5		0
31/2-6		0.0		0
31/2-7	8.5	-3.1		0.08
31/2-8	12.1	-3.0		0.33

Table A7. Microthermometry data and volume fractions at room temperature for type 2 aqueous fluid inclusions in qtz1 (samples 26 and 31). Total homogenisation occurs into the liquid phase. (cla) = clathrate. (m) = metastable melting in the absence of a vapour bubble.

173

Inclusion Nr.	T_m (ice) in °C	T_m (us) in °C	T_m (HH) in °C	T_h (liq) in °C	Volume fraction vapour
26/3-1	-39.4				0.05
26/3-2	-39.4				0.03
26/3-3	-39.4				0.05
26/3-4	-39.4				0.05
26/3-5	-39.4				0.05
26/3-6	-39.0				0.05
26/3-7	-39.0				0.05
26/3-8					0.05
26/3-9					0.05
26/3-10					0.05
26/3-11	-40.0			74	0.03
26/3-12	-40.2			74	0.02
26/3-13	-40.2			69	0.01
26/3-14	-40.2			78	0.04
26/3-15	-41.0			82	0.03
26/3-16	-40.0				0.05
26/3-17				55	
26/3-18				56	
26/3-19				87	
26/3-20				76	
26/3-21	-30.0#	-7.2	-2.0		0.01
26/3-22	-27.0#	-6.3	-1.2	53	0.02
26/3-23	-25.0#	-6.0	-1.2		0.01
26/3-24	-26.1#	-6.1	-1.2	40	0.01
26/3-25				80	0.01
26/3-26				81	0.01
26/3-27				44	0.01
26/3-28				50	0.01
26/3-29				53	0.01
26/3-30				53	0.01
26/3-31				54	0.01
26/3-32				56	0.01
26/3-33				53	0.01
26/3-34				65	0.01
26/3-35				57	0.01
26/3-36				56	0.01
26/3-37				53	0.01
26/3-38				53	0.01
26/3-39				64	0.01
26/3-40				60	0.01
26/3-41				55	0.01
26/3-42				57	0.01
26/3-43				53	0.01
26/3-44				47	0.01
26/3-45				59	0.01

Table A8. Microthermometry data and volume fractions at room temperature for type 3 aqueous fluid inclusions in qtz1 (samples 26, 31 and 42). Total homogenisation occurs in the liquid phase. (HH) = hydrohalite. (us) = unknown salt-hydrate. # = melting of clathrate at the same temperature as ice.

Inclusion Nr.	T_m (ice) in °C	T_m (us) in °C	T_m (HH) in °C	T_h (liq) in °C	Volume fraction vapour
31/3-1	-31.4			73	0.01
31/3-2	-30.0			68	0.02
31/3-3	-30.0			68	0.03
31/3-4	-30.0			78	0.04
31/3-5	-32.0			71	0.01
31/3-6	-24.8				0
31/3-7				72	0.03
31/3-8				72	0.03
31/3-9	-17.8				0.14
31/3-10	-14.5				0.05
31/3-11	-14.5				0
31/3-12	-17.0				0.06
31/3-13	-16.9				0.03
31/3-14	-7.2				0
42/3-1	-34.0		-45.0	75	0.02
42/3-2	-36.0		-47.0	79	0.01
42/3-3	-35.0			78	0.03
42/3-4	-35.0			49	0.01
42/3-5	-36.0			94	0.06
42/3-6	-36.0			98	0.05
42/3-7				95	0.01
42/3-8				92	0.01
42/3-9				96	0.02
42/3-10				97	0.01
42/3-11				87	0.01
42/3-12				72	0.01
42/3-13	-37.0		-47.0	79	0.01
42/3-14				95	0.06
42/3-15				-	0
42/3-16	-36.0			74	0.02
42/3-17				95	0.05
42/3-18				75	0.04

Table A8 (continued).

Inclusion Nr.	Raman peak surface			Mole fraction	
	CH_4	CO_2 v_1	CO_2 $2v_2$	CH_4	CO_2
26/3-22	622.1			1	
26/3-24	305			1	
26/3-46	157.3			1	
31/3-1	8760			1	
31/3-15	4855			1	
31/3-16	87959			1	
31/3-17	386	165	236	0.24	0.76
31/3-18	82013			1	
42/3-7	3176			1	
42/3-18	484			1	
42/3-19	242684	1373	2076	0.96	0.04

Table A9. Raman laser microprobe spectroscopic analyses of the vapour phase of type 3 fluid inclusions in qtz1. The first number of the Inclusion Nr. refers to the sample number (see location in Table 1). All peak surface values are taken from spectra normalised to 30 seconds of excitation time, at room temperature.

Inclusion Nr.	T_m (ice) in °C	T_m (us) in °C	T_m (HH) in °C	T_h (liq) in °C	Volume fraction vapour
6-cal2-1	-39.0			89.0	0.06
6-cal2-2	-35.4			97.0	0.06
6-cal2-3	-34.5		-7.5	74.0	0.07
6-cal2-4				86.0	0.07
6-cal2-5				100.0	0.06
6-cal2-6				103.0	0.07
6-cal2-7				93.0	0.06
6-cal2-8				68.0	0.03
6-cal2-9				86.0	0.04
6-cal2-10				91.0	0.04
6-cal2-11				97.0	0.05
6-cal2-12				93.0	0.05
6-cal2-13				99.0	0.06
6-cal2-14				75.8	0.04
6-cal2-15				120.0	0.07
6-cal2-19	-39.0			81.0	0.05
6-cal2-20	-39.0			86.0	0.06
6-cal2-21			-7.2	60.0	0.08
6-cal2-22	-34.9		-7.6	75.0	0.06
6-cal2-23	-39.0			96.0	0.10
6-cal2-24	-39.0				0.06
6-cal2-25				90.0	0.05
6-cal2-26				96.0	0.06
6-cal2-27				114.0	0.07
6-cal2-28				81.5	0.07
6-cal2-31				98.0	0.04
6-cal2-32				106.1	0.09
6-cal2-33				84.8	0.09
6-cal2-34				88.0	0.04
6-cal2-35				95.0	0.08
6-cal2-36			-7.6		0.05
26-cal2-1				67	0.02
26-cal2-2				100	0.03
26-cal2-3				126	0.06
26-cal2-4				80	0.01
26-cal2-7				110	0.04
26-cal2-8				72	0.01
26-cal2-10				70	0.02
26-cal2-11				114	0.05
26-cal2-12				98	0.03
26-cal2-14				97	0.03
26-cal2-15				94	0.02
26-cal2-16				95	0.02
26-cal2-17					0.3
26-cal2-18					0.09
26-cal2-19				93	0.09
26-cal2-20				124	0.22
26-cal2-21					0.13
26-cal2-22	-29.9		-1.4		0.05
26-cal2-23	-30.4		3.8		0.01
26-cal2-24					0.05
26-cal2-25	-15.5			110	0.04
26-cal2-26	-9.0				0
26-cal2-27				118	0.03
26-cal2-28				116	0.04

Table A10. Microthermometry data and volume fractions at room temperature for type 1c fluid inclusions in cal2 (samples 26, 42 and 48). Total homogenisation occurs into the liquid phase. (HH) = hydrohalite. (us) = unknown salt-hydrate.

Inclusion Nr.	T_m (ice) in °C	T_m (us) in °C	T_m (HH) in °C	T_h (liq) in °C	Volume fraction vapour
42-cal2-1	-16.0			62	0.02
42-cal2-2	-15.8				0.07
42-cal2-3	-15.7			107	0.07
42-cal2-4					0.09
42-cal2-5	-19.5				0.07
42-cal2-6				123	0.03
42-cal2-7	-13.5				0.04
42-cal2-8	-28.9				0.22
42-cal2-9	-23.6				0.05
42-cal2-11	-22.9				0.09
42-cal2-12	-15.4				0.05
42-cal2-13	-20.3			116	0.06
42-cal2-14	-23.0				0.05
42-cal2-15	-36.0				0.3
42-cal2-16	-14.7				0.05
42-cal2-17	-9.2			97	0.01
42-cal2-18	-32.8			70	0.02
42-cal2-19	-30.4			106	0.03
42-cal2-20	-31.7			109	0.04
42-cal2-21	-20.0				0.01
42-cal2-22	-19.0				0
42-cal2-23	-14.9				0.01
42-cal2-24	-16.3				0.01
42-cal2-25	-21.0				0.07
42-cal2-26	-20.5			64	0.01
42-cal2-27	-22.6				0.12
42-cal2-28	-15.6				0
48-cal2-1	-21.5	-30.2	-25.6	77	0.03
48-cal2-2				72	0.02
48-cal2-3				75	0.02
48-cal2-4	-8.4		-22.5	78	0.02
48-cal2-5	-10.0		-23.5	86	0.01
48-cal2-6	-12.9	-35.8	-23.6	83	0.02
48-cal2-7	-12.3				0.03
48-cal2-8	-11.5				0.01
48-cal2-9	-17.5		-21.4	72	0.02
48-cal2-10	-8.9			67	0.03
48-cal2-11	-17.3		-24.1		0.05
48-cal2-12				89	0.01
48-cal2-13	-17.6		-26	84	0.02
48-cal2-14	-6.2		-24.6		0.01
48-cal2-15	-4.9	-31.9	-24.9	80	0.02
48-cal2-16	-8.7				0.09
48-cal2-17				101	0.03
48-cal2-18	-22.3	-33.3	-26.6	67	0.03
48-cal2-19	-8.2		-24.6		0.06
48-cal2-20	-17.4	-33.8	-25.5	69	0.02
48-cal2-21	-19.5		-21,3		0.06
48-cal2-22	-22.0		-22.0		0.06
48-cal2-23	-24.6				0
48-cal2-24	-17.7		-23.6		0.2
48-cal2-25	-25.1		-26.6		0
48-cal2-26	-23.6		-27.1		0
48-cal2-27	-17.8				0
48-cal2-28	-13.2				0
48-cal2-29	-5.1			76	0.03

Table A10 (continued).

Inclusion Nr.	T_m (cla) in °C	T_m (ice) in °C	T_h (liq) in °C	Volume fraction vapour
Ig/1q-1	-5.2	-2.1	283	0.19
Ig/1q-2	-3.9	-1.2	280	0.12
Ig/1q-3	-4.1	-1.8		0.51
Ig/1q-4		-1.2	164	0.12
Ig/1q-5		-1.5	296	0.15
Ig/1q-6			155	0.08
Ig/1q-7			150	0.10
Ig/1q-8		-1.9		0.17
Ig/1q-9		-1.6		0.10
Ig/1q-10		-2.4		0.36
Ig/1q-11		-2.1		0.43
Ig/1q-12		-2.2		0.82
Ig/1q-13		-1.4		0.30
Ig/1q-14		-1.5		0.18
Ig/1q-15		-1.4		0.21
Ig/1q-16		-1.2		0.20
Ig/1q-17		-1.2		0.16
Ig/1q-18		-1.1		0.08
Ig/2q-1		-1.9		0.17
Ig/2q-2	16.2			0.56
Ig/2q-3				0.28
Ig/2q-4	14.8			0.80
Ig/2q-5		0.0		0.10

Table A11. Microthermometry data and volume fractions at room temperature for type 1q and type 2q fluid inclusions in qtz2 in altered dioritic igneous bodies (sample Ign 12). Total homogenisation occurs in the liquid phase. (cla) = clathrate.

Inclusion Nr	Raman peak surface			Mole fraction	
	CH_4	CO_2 v_1	CO_2 $2v_2$	CH_4	CO_2
lg/1q-1	21125	747	1089	0.79	0.21
lg/1q-3	17982	606	795	0.81	0.19
lg/1q-12	24216	629	1137	0.82	0.18
lg/1q-10	24868	946	1415	0.78	0.22
lg/1q-14	4231	175	305	0.89	0.11
lg/1q-16	51642	1093	1683	0.86	0.14
51/1q-20	39865	2131	3520	0.70	0.30
lg/2q-4	75322	3283	5597	0.74	0.26
lg/2q-6	121761	5560	9911	0.72	0.28
lg/2q-7	214987	3605	6296	0.88	0.12

Table A12. Raman laser microprobe spectroscopic analyses of the vapour phase for type 1q and type 2q fluid inclusions in qtz2 (sample lgn12). All peak surface values are taken from spectra normalised to 30 seconds of excitation time, at room temperature.

	Phase	Main peaks (cm^{-1})	Inclusion type	Sample
Gas	CH_4	2915-2918	1, 2, 3, 1c, 1-2q	-
	CO_2	1286,1388	1, 2, 1q	-
	C_2H_4	3021	1, 2	-
	C_2H_6	2954	1, 2	-
	C_3H_8	2890	1, 2	-
Mineral	kaolinite	3620, 3652, 3670, 3692	1q	Ign12
	kaolinite	335, 744, 3620, 3650, 3683	1q	Ign12
	kaolinite	334, 747	1q	Ign12
	kaolinite	3622, 3650, 3682	1q	Ign12
	kaolinite	3623, 3654, 3688	1q	Ign12
	kaolinite	336,438,458, 744, 1039, 3621, 3635, 3702	1q	Ign12
	kaolinite	3621, 3649, 3696	3	26
	kaolinite	3621, 3688	3	26
	kaolinite	335, 746, 1057, 3620, 3651, 3685	3	26
	kaolinite	3620, 3651, 3669, 3695	3	26
	Mg-calcite	806, 1070	2	28
	Mg-calcite	284, 713, 1087	2	28
	Mg-calcite	283, 714, 809, 1087	1	28
	Mg-calcite	283, 714, 810, 1088	1	28
	Calcite	714, 809, 1087	2	42
	Calcite	708, 808, 1083	2	31
	Carbonate	738, 808, 1037, 1370, 1405, 1425	2	28
	Dolomite	167, 279, 719, 1088	1c	6
	Dolomite	167, 280, 719, 1088	1c	48
Salt hydrate	Hydrohalite	3424, 3540	1c	26
	Hydrohalite	3424, 3544	3	36
	Hydrohalite	3423, 3545	3	36
	Hydrohalite	3424, 3543	3	26
	Hydrohalite	3424, 3543	3	26

Table A13. Raman stretching vibration peaks of gas phases, entrapped minerals and salt hydrates in fluid inclusions from vein minerals qtz1, cal2 and qtz2.

Sample	Sample vs. V-PDB				Sample vs. V-SMOW
	d¹³C	std.dev.	d¹⁸O	std.dev.	d¹⁸O
23 (3)	-4.68	0.01	-13.29	0.01	17.21
24 (3)	-2.87	0.03	-11.57	0.03	18.99
25A (3)	-1.82	0.01	-11.18	0.03	19.38
25B (3)	-5.23	0.03	-13.08	0.03	17.43
26A (4)	-2.31	0.02	-14.17	0.02	16.31
26B (4)	-2.10	0.02	-15.80	0.04	14.62
26C (4)	-2.33	0.02	-15.00	0.03	15.44
27 (9)	-1.89	0.01	-13.42	0.04	17.07
28 (5)	-1.37	0.01	-9.86	0.04	20.74
29B (6)	-1.00	0.01	-13.08	0.02	17.42
30B (6)	-1.32	0.01	-11.23	0.03	19.33
32A (8)	-0.04	0.02	-10.95	0.02	19.62
32B (8)	-0.52	0.02	-10.94	0.03	19.63
33 (8)	-0.58	0.01	-11.13	0.03	19.43
34 (8)	-0.62	0.02	-10.52	0.03	20.06
35 (11)	-1.26	0.03	-9.16	0.02	21.47
36A (10)	-0.36	0.02	-11.61	0.04	18.94
36B (10)	-0.70	0.03	-11.89	0.04	18.66
36C (10)	-0.76	0.02	-11.98	0.03	18.56
36E (10)	-2.44	0.02	-10.87	0.03	19.71
37 (10)	-0.58	0.02	-12.02	0.04	18.52
38 (10)	-8.06	0.01	-12.60	0.02	17.92
39 (12a)	-3.64	0.04	-9.52	0.04	21.10
40 (12a)	-3.28	0.02	-9.54	0.03	21.08
42 (12a)	-2.95	0.02	-10.06	0.04	20.54
44 (12a)	-2.80	0.02	-13.28	0.03	17.22
45 (12b)	-3.25	0.01	-11.55	0.01	19.01
46A (12c)	-1.77	0.02	-12.49	0.05	18.03
46B (12c)	-2.01	0.01	-13.10	0.03	17.41
47 (12c)	-1.60	0.02	-12.17	0.03	18.37
48 (12c)	-1.99	0.02	-10.81	0.04	19.77
49 (12c)	-1.28	0.03	-11.93	0.04	18.61
50 (12c)	-1.62	0.01	-12.63	0.01	17.89
52 (13)	-0.79	0.02	-10.39	0.06	20.20
53 (14)	-6.89	0.02	-13.45	0.04	17.05
55A (14)	-4.07	0.04	-11.33	0.03	19.23
55B (14)	-4.36	0.03	-11.16	0.04	19.41
56 (14)	-3.83	0.02	-11.56	0.02	18.99
58 (14)	-2.53	0.01	-11.61	0.03	18.94
59	-4.94	0.02	-12.67	0.03	17.85

Table A14. Carbon ($\delta^{13}C$) and oxygen ($\delta^{18}O$) stable isotope results for cal2, Ciñera-Matallana. d = δ.

Sample	Sample vs. V-PDB				Sample vs. V-SMOW
	$d^{13}C$	std.dev.	$d^{18}O$	std.dev.	$d^{18}O$
1 (1a)	-0.86	0.02	-11.92	0.04	18.62
2 (1a)	-1.22	0.02	-15.21	0.05	15.23
3 (1a)	-1.16	0.01	-14.97	0.02	15.48
4 (1a)	-0.48	0.02	-14.11	0.03	16.36
5 (1a)	-2.02	0.02	-13.58	0.03	16.91
6A (1b)	-0.81	0.02	-12.74	0.05	17.77
7 (2)	-1.37	0.03	-11.58	0.03	18.97
8A (2)	-2.26	0.02	-10.36	0.06	20.23
8B (2)	-6.89	0.03	-13.73	0.06	16.75
10 (2)	-7.52	0.02	-13.89	0.02	16.59
6B/dolm	1.05	0.00	-8.00	0.01	22.66
9B/dom	1.01	0.03	-9.52	0.06	21.10

Table A15. Carbon ($\delta^{13}C$) and oxygen ($\delta^{18}O$) stable isotope results for cal2, Sabero. d = δ.

Sample	Sample vs. V-PDB				Sample vs. V-SMOW
	$d^{13}C$	std.dev.	$d^{18}O$	std.dev.	$d^{18}O$
11a/cal	-2.14	0.01	-13.55	0.03	16.95
11b/cal	1.00	0.03	-12.91	0.03	17.60
12/rock	1.67	0.02	-4.97	0.02	25.78
13a/cal	-2.04	0.02	-11.60	0.05	18.95
13b/rock	0.50	0.02	-2.62	0.04	28.21
14/dolm	1.61	0.02	-3.48	0.01	27.33
15a/dolm	0.51	0.02	-1.33	0.05	29.54
15b/dolm	-1.01	0.01	-2.97	0.03	27.85
15c/dolm	-6.77	0.01	-7.60	0.03	23.08
16a/dolm	2.32	0.02	-6.26	0.03	24.46
16b/cal	-6.77	0.01	-10.38	0.02	20.21
17/cal/Port	1.14	0.01	-9.55	0.03	21.06
18/cal/Port	-0.05	0.02	-11.50	0.03	19.05
19a/cal/SL	-0.07	0.01	-9.40	0.03	21.22
19b/rock	1.23	0.01	-7.23	0.01	23.45
20/cal/Port	-0.56	0.02	-8.45	0.02	22.20
21/cal/SL	-0.72	0.03	-10.89	0.03	19.68
22/cal/SE	1.67	0.01	-9.24	0.03	21.38

Table A16. Carbon ($\delta^{13}C$) and oxygen ($\delta^{18}O$) stable isotope results for calcite and dolomite veins hosted in discordant Cretaceous carbonates (11 to 13) and underlying Devonian-Carboniferous rocks (14 to 22) both adjacent to Ciñera-Matallana and Sabero. d = δ.